Surface and Interfacial Study of Chemical Degradation in Polymer Composites and Coatings

A Dissertation Presented

by

Christopher Norman Young

to

The Graduate School

in Partial Fulfillment of the

Requirements

for the Degree of

Doctor of Philosophy

in

Materials Science and Engineering

Stony Brook University

August 2013

Stony Brook University
The Graduate School

Christopher Norman Young

We, the dissertation committee for the above candidate for the
Doctor of Philosophy degree, hereby recommend
acceptance of this dissertation.

Clive R. Clayton
Leading Professor, Department of Materials Science and Engineering

Gary P. Halada
Associate Professor, Department of Materials Science and Engineering

Charles M. Fortmann
Assistant Professor, Department of Materials Science and Engineering

James H. Wynne
Research Chemist, Naval Research Laboratory, Coatings Chemistry

This dissertation is accepted by the Graduate School

Charles Taber

Interim Dean of the Graduate School

Abstract of the Dissertation

Surface and Interfacial Study of Chemical Degradation in Polymer Composites and Coatings

by

Christopher Norman Young

Doctor of Philosophy

in

Materials Science and Engineering

Stony Brook University

2013

Polymeric composites and coatings are commonly employed in outdoor applications where they are subject to degradation under environmental and service conditions. Numerous mechanical studies have related both UV exposure and thermal damage to a reduction in mechanical performance. Chemical studies have predominantly focused on degradation of matrix resins and coatings by UV and by thermal exposure, while ignoring the vulnerability of the fiber/matrix interphase in composites. Low-grade thermal exposure has provided early indications of further damage, but the mechanism has not been extensively studied. Coatings have been developed to resist chemical exposure but their chemical interactions with solvents used in their removal are not well understood. Research was undertaken by employing complementary vibrational and x-ray spectroscopic techniques to investigate the surface and bulk chemistries of selected polymeric systems in order to develop models for the effects of exposure.

Carbon fiber / vinyl ester (CFVE) resin composites were studied to determine the chemical causes of the degradation in mechanical properties. The resin and composite systems were exposed to low-grade thermal damage and examined for chemical changes while also studying the mechanism of laser fluorescence as a means for early damage detection. Carbon fiber surface sizing was removed and analyzed in order to evaluate its stability against UV radiation, a known significant cause of mechanical degradation.

The mechanism by which polyurethane coatings are degraded and removed from substrates by commonly used military paint stripper was determined in order to facilitate future development of a more environmentally-friendly formulation. Particular focus was given to the interactions of methylene chloride and phenol with vulnerable moieties of the polymer chain. Other components in the reference paint stripper were found to enhance the performance of these active solvents. A new model to describe solvent-coating interactions was developed.

For my wife, Amy

and

For my parents, Norman and Darlene

Table of Contents

List of Tables

List of Equations

List of Figures

Acknowledgments

I cannot adequately thank my advisor, Dr. Clive R. Clayton, for his guidance, direction, and great patience throughout the years of research undertaken for this dissertation. I also thank Dr. Gary Halada for contributing significantly to my understanding and execution of spectroscopic methods. I extend my gratitude to Dr. Charles Fortmann for serving as a committee member, and for useful conversations on the interpretation of Raman effects. I further wish to thank Dr. James Wynne for mentorship throughout our studies on polyurethane coatings, for allowing me to intern at the Naval Research Laboratory, and for serving as my outside committee member.

Significant collaboration with other investigators was critical to the success of this research. Composites research was carried out in collaboration with principal investigator Dr. Richard Granata (Florida Atlantic University), Dr. William Scott (Computer Interface Instruments, Inc.), and Mr. Guy Connelly (Connelly Applied Research). Dr. Jon Longtin (SBU) provided significant assistance with laser ablation. Research on paint strippers was carried out in collaboration with principal investigator Dr. Young Han (NAVAIR), principal investigator Dr. James Wynne (NRL), Dr. James Yesinowski (NRL), Ms. Kelly Watson (NRL), Mr. Grant Daniels (NRL), and Mr. Jack Kelley (ARL). Assistance with the execution and interpretation of NEXAFS data was provided by Dr. Daniel Fischer (NIST) and Dr. Cherno Jaye (NIST) at the National Synchrotron Light Source at Brookhaven National Laboratory. Further assistance in data processing of NEXAFS spectra for analysis was provided in the form of custom

programming by Dr. Joseph Ortiz (SBU). Assistance with electron microscopy was offered by Dr. James Quinn (SBU).

This research was funded in two phases, by two funding agencies. The Office of Naval Research (ONR) provided funding for work related to composite materials through grants N00014-05-1-0341 and N00014-09-1-0317. The Strategic Environmental Research and Development Program (SERDP) provided funding for work related to paint stripping through grants WP-1682 and WP-2244.

Use of the National Synchrotron Light Source, Brookhaven National Laboratory, was supported by the U.S. Department of Energy, Office of Science, Office of Basic Energy Sciences, under Contract No. DE-AC02-98CH10886. Research carried out (in part) at the Center for Functional Nanomaterials, Brookhaven National Laboratory, which is supported by the U.S. Department of Energy, Office of Basic Energy Sciences, under Contract No. DE-AC02-98CH10886.

Other support was provided by the Naval Research Laboratory's Student Temporary Employment Program in the summer of 2010. Additional funding for this research was provided through a Department of Education grant to the Department of Materials Science and Engineering for a Graduate Assistantship in Areas of National Need (GAANN) Fellowship in AY2011-2012.

Lastly, I must thank my friends and family for their unwavering support throughout my academic career, without which I would not have made it this far.

Chapter 1: Introduction

Composite materials are seen as the next evolutionary step for structural materials in a number of applications. These materials combine lightweight, inexpensive filler fibers possessing desirable mechanical properties in a polymeric (or metallic) matrix to produce a component which is lighter and stronger than a purely metal part it might replace. It is for this reason that the United States military seeks to employ composite materials in a variety of upcoming applications.

While composites resist some means of degradation experienced by metal parts, they are not invulnerable to breakdown. Over the course of its service life, a composite material in military applications will face harsh exposure conditions. Intense sunlight, high humidity, salt water immersion, and high temperatures are all encountered on a regular basis. Materials may be selected specifically for their durability to such conditions, but the most durable material may not meet other performance requirements. While polymers may make an excellent matrix for composites, they are extremely vulnerable to the above-described effects. Sunlight can lead to material degradation within weeks due to the susceptibility of polymers to photo-cleavage. Many polymers have relatively low operating temperatures, making it much more likely that they will receive exposure above this temperature during the course of service, leading to premature failure. Moisture and salt water can penetrate and swell the matrix and can reach the fiber/matrix interface, causing disbondment.

Almost all materials employed in the field receive a protective coating of some sort prior to service in order to extend their service lifetime. Metals receive conversion coatings to resist corrosion and promote adhesion, followed by coating systems designed to protect the substrate from corrosion caused by the environment or other unsavory means. Polymeric composites receive similar (or identical) coatings to protect the resin from degradation, as the polymer is the weakest link in the composite system. The weathering performance of these coatings has been analyzed thoroughly, and their formulation has been augmented with fillers, stabilizers, radical scavengers, and other additives to maximize their stability. Such coatings are also easily chipped away during service, leaving the underlying substrate vulnerable to exposure. The weathering characteristics of many composite resins have also been studied and the effects of such exposure on their mechanical properties have been catalogued extensively in mechanical literature.

There is a chemical cause to the more severe effects of exposure, which comes about through fiber/matrix interfacial failure. Fibers are treated with a polymer dispersion called a sizing, which acts to improve adhesion between the fiber and the matrix. This sizing is not a well-understood system, and its durability has not been examined in public literature. Through the curing process, the fiber sizing and matrix resin intermix and (possibly) react to form the interphase, wherein the chemistry of the material is of great interest for predicting the durability of the composite. The fiber loading of the composite often leads to situations where fibers are in close contact with one another, creating sizing-rich interphase regions with different mechanical properties.

Analysis of the interphase region is challenging for several reasons. The chemistry of the sizing is often a proprietary trade secret, requiring the investigator to determine the chemical structure and construct a model of its proposed reactivity. Because the fiber sizing is such a thin coating, the interphase region is usually 500 nm or less in thickness, precluding the use of many common tools for polymer analysis. The interphase forms around the fiber in the composite, and the fiber itself often provides an overwhelmingly strong signature in spectroscopic analysis.

In light of these challenges, we must consider alternative methods of studying the chemistry of the sizing and revealing the interphase region for analysis. Many mechanical means of material removal are too imprecise to adequately control the depth, and common laser and ion etching techniques cause damage to the substrate on a scale greater than the thickness of the interphase region. Modern advances in laser technology have led to the development of a laser with femtosecond pulse duration, which operates with a unique model of energetic interaction with material. The duration of energy delivery is so short that the pulse removes electrons from atoms before energy can be phononically transferred to neighboring molecules, resulting in material ablation without chemical modification of the target by thermal damage.

There are many methods already employed to non-destructively measure the effects of exposure on composite materials, but many only detect late-stage damage. A testing method able to detect the early stages of exposure prior to thermal oxidation would be very useful in predicting the lifecycle of a material, and improving material selection for specific applications. The early stages of thermal damage at temperatures above T_g but below the regime of thermo-oxidative degradation are not well understood, and the causes of changes in mechanical properties are not well defined. Laser fluorescence has been useful in detecting such damage, but a chemical model for the changes seen in fluorescence has not been established.

Coatings which have been applied to substrates for protection eventually degrade to the point where they must be replaced. In the replacement process, the old coating is subjected to a mixture of solvents which have been engineered to soften the polymer and swell it to facilitate disbondment. These mixtures are highly effective, but their mechanism is not well understood. It is accepted that methylene chloride swells a polyurethane coating, but the nature of the interaction between methylene chloride and polymer which leads to such effective swelling has not been investigated. The addition of phenol results in easy destruction of a polyurethane coating, but the reaction pathway has not been explored.

These solvents are highly effective at coating removal, but they also present significant environmental and human health hazards. Methylene chloride is believed to be carcinogenic, and phenol is a corrosive irritant which is also neurotoxic. It is a priority in the Department of Defense to phase out the use of these solvents, but replacement solvents have shown poor performance. In order to develop a successful next-generation paint removing solvent, we must first understand the mechanisms which make the current solution so effective.

This dissertation involves the study of multiple means of degradation in polymeric systems. In composites, we will examine the chemistry and durability of a commercial carbon fiber sizing of interest to the United States Navy. We will explore the feasibility of employing ultrafast laser ablation to reveal the interphase in composite materials, while also interrogating the nature of the composite through slow-etch depth profiling. We will observe the chemical effects of low grade thermal damage on composites and resin, and relate the observed bulk and surface chemical changes to mechanical properties and to laser-induced fluorescence in order to better elucidate a means of non-destructive testing.

The durability of coating systems in industrial exposure conditions will also be examined. We will study the polymer-solvent interactions of polyurethane topcoats with paint-removing solutions to determine the mechanisms of action which make the current active ingredients (methylene chloride and phenol) so effective. We will investigate the effects of these solvents on the polymeric binder and evaluate the effects of coating additives on the degradation process. We will also discuss the utility of a specialized means of surface analysis called Near Edge X-ray Absorption Fine Structure (NEXAFS) spectroscopy and demonstrate the power of a large-area hyperspectral detector in examining solvent exposure effects.

While the polymeric systems studied and means of degradation are varied, the means of investigation are consistent. Raman and FTIR spectroscopy represent complementary vibrational techniques, while XPS and NEXAFS are complementary methods of surface analysis. Through the process, we will demonstrate the advantages and disadvantages of each technique in particular applications and further show the importance of studying each system with a full complement of analytical methods.

This dissertation represents a collaborative effort between the author at Stony Brook University and several groups: Florida Atlantic University, the Army Research Laboratory, the Naval Research Laboratory, Naval Air Systems Command, and Computer Interface Instrumentation, Inc. Each participant in this group has offered their significant expertise in the advancement of these projects, and their contributions of technical input, results, and interpretation is acknowledged and appreciated. These projects were funded as multi-year efforts by the Office of Naval Research and the Strategic Environmental Research and Development Program.

Chapter 2: Materials

2.1 Polyurethane systems

2.1.1 General coating system design of polyurethane topcoats

Military topcoat systems are often polyurethanes composed of polyisocyanates combined with polyester extenders. The use of aliphatic coatings provides superior colorfastness and resistance to weathering as compared to aromatic coatings, due to the inherent weakness to UV exposure in the latter [1]. Aliphatic coatings are generally polymerized by the reaction of an isocyanate end group with either an alcohol or an amine to produce either a urethane or urea linkage, respectively. Isocyanate groups can also react with water to produce a carbamic acid intermediate that decomposes into an amine for further reaction plus carbon dioxide gas. This reaction pathway is less desirable, as the production of CO_2 leads to the presence of gas voids and bubbles, while the production of the primary amine consumes isocyanate, which leads to a reduced crosslink density. These reactions are shown schematically in Figure 2-1. Bi-functionalization of the component monomer permits long-chain polymerization. A second component, generally containing polyols (as well as pigments, fillers, and other additives), is mixed in at the time of coating application, leading to step-growth polymerization.

$$\mathbf{R{-}NCO + R'{-}OH \rightarrow R{-}NH{-}CO{-}O{-}R'}$$

Isocyanate reaction with alcohol to produce urethane

$$\mathbf{R{-}NCO + R'{-}NH_2 \rightarrow R{-}NH{-}CO{-}NHR'}$$

Isocyanate reaction with amine to produce urea

$$\mathbf{R{-}NCO + H_2O \rightarrow R{-}NH{-}CO{-}O{-}H \rightarrow R{-}NH_2 + CO_2}$$

Isocyanate reaction with water ultimately producing amine and carbon dioxide

Figure 2-1 – Polymerization reaction pathways of isocyanates.

One drawback to these polyurethanes is the high toxicity of diisocyanate monomers [2]. Due to their low molecular weight and subsequent high vapor pressure, monomers are readily present in the vapor phase, posing a significant inhalation hazard. Polyisocyanates offer a suitable and less-hazardous means to avoid this hazard. While their effects are similar to those of the monomer, their higher molecular weight and lower vapor pressure substantially reduce the inhalation hazard, though contact hazards remain the same.

The aliphatic polyisocyanates used in military coating systems are generally derived from hexamethylene diisocyanate (HDI) monomers. Polyisocyanates are also based on other monomeric systems such as toluene diisocyanate (TDI) or isophorone diisocyanate (IPDI), which are used in the preparation of coatings with other desirable characteristics including radiation curability and powder application. Common polymer components come in a biuret, isocyanurate, or asymmetric trimer form. These polyisocyanates can be used with lower amounts of packaging solvent and can be tailored in component combination to obtain improved performance and weathering resistance.

A wide variety of additives are available to meet the required outdoor performance characteristics of the coating. Hindered amine light stabilizers (HALS) function as antioxidants and transition-metal complexing agents, providing protection against UV degradation; more direct antioxidants and radical scavengers based on hindered phenols may also be present. Pigmentation also affects the rate of photo-oxidation; while TiO_2 absorbs UV radiation better than most alternatives, it is also photocatalytic [3] and therefore must be further treated by coating with silica or alumina prior to use. Rutile-phase TiO_2 must also be used, as the anatase phase is more strongly catalytic. Other fillers, such as silica, may be used to enhance the mechanical performance. Further information on the varied sorts of fillers, additives, and pigments most often employed in coatings may be found in a number of texts on coating formulation [1, 4, 5].

More recent developments in coatings lay in the fields of self-decontamination, often through the incorporation of active fillers [6-12]; antifouling, both in the environmental effects of existing compounds [13-16] and the development of less-damaging replacements [17-19] [20]; and superhydrophobicity [21, 22]. Fillers may be incorporated as a straight additive, much like those found already in coatings, or they may be engineered for surface-segregation, which can enhance their effectiveness. A wide variety of other active fillers may be added to polymers and coatings to enhance other properties.

Coatings employed by the military have been optimized to meet a variety of constantly-evolving performance requirements. Formulations must demonstrate adequate optical, mechanical, and chemical properties in the face of weathering, heat, and incidental chemical exposure (e.g. [23, 24]). Furthermore, some coatings have also been designed to resist chemical warfare agents. Compounds such as mustard gas, first employed in World War I, produce sulfur and chlorine oxide compounds which cause rapid corrosion to exposed metals, in addition to representing a significant health hazard to soldiers. Coatings used in military applications have therefore been designed protect from exposure to such compounds and also permit later decontamination for continued use.

Military coating systems must pass a stringent set of tests prove their utility. In order to perform to this standard, the polyurethane binder is loaded with a significant amount of fillers and pigments. Like many high-performance coatings, the filler generally comprises half the total material of the coating. In some cases (such as MIL-DTL-53039, an Army topcoat used also in camouflage), the available ingredients are enumerated in the specification, wherein the possible pigments are listed for each specified color. As an example, to produce the color Aircraft White the primary hiding component must be titanium dioxide [23]. The coating must meet or exceed performance requirements in 32 separate categories, including storage stability, ease of application, optical character, and chemical agent resistance. EDS images have been published previously by this group, demonstrating the elemental content and distribution of some fillers and pigments in military coatings [25, 26].

The aging characteristics of polyurethanes have been characterized in the literature. Croll has extensively studied the degradation of polyurethane coatings [27-32] with an eye towards UV degradation and aging. Studies by Keene (from this research group) [25, 26, 33] have studied the penetrative effects of UV radiation on both topcoats and primers, and have also monitored the subsequent effects on the disposition and relocation of filler particles. However, the literature does not comprehensively discuss the nature of chemical reactions (rather than thermal or photo-oxidative reactions) with polyurethane. Several engineering tables exist which describe the level of resistance to different solvents, but there does not appear to be a thorough treatment of the nature of this resistance available.

2.1.2 Rationale for the usage of clear formulations in this work

Military coatings must meet stringent coloration and color-fastness specifications, as one primary use is for camouflage. This characteristic is at odds with the goals of our research because it is difficult to analyze such a polymer system with visible light techniques such as Raman spectroscopy. To demonstrate the problem, Raman spectra were collected from fully-formulated versions of current military topcoats using a standard 785 nm laser on a normal microscope. In addition to these, a 325 nm UV laser connected to a confocal microscope was employed to collect UV Raman data, representing the newest means of analysis available readily in the department.

The Raman spectrum shown in Figure 2-2(a) demonstrates several very strong, very sharp peaks between 1300 and 1450 cm^{-1}. While we might expect the binder to possess a strong peak at 1442 cm^{-1}, indicative of aliphatic chain CH_2 bending, this spectrum shows additional very strong peaks at 1394 and 1350 cm^{-1}, where such strong peaks are suggestive of azo pigments [34]. Peaks at 533, 922, and 1590 cm^{-1} suggest aromatic ring structures, the likes of which are not expected in an aliphatic polyurethane coating. Peaks at 590 and 440 cm^{-1} suggest the presence of TiO2 particles as well. The polymeric binder is expected to yield peaks around 1750 cm^{-1} (C=O) and 1090 cm^{-1} (C-C), yet these are not detected in the fully-formulated coating. While Raman spectroscopy could certainly be used to identify the composition of the pigmentation compounds in the coating, it provides only incomplete information on the chemistry of the binder [35]; a thorough investigation of the chemistry of coating pigmentation is outside the scope of this project, though the composition of binders and pigments would certainly influence the diffusion of paint removing solvents (which will be discussed shortly).

The use of a UV laser does not offer significant enhancement to the quality of our spectra. The spectrum from the UV laser shown in Figure 2-2(b) does show an additional peak over the visible-light sources, as it is able to resolve (faintly) the carbonyl peak at 1750 cm^{-1} (as will be discussed, an extremely important peak). However, there is a significant fluorescence background to this spectrum, as the laser burned the sample during analysis; the carbonyl peak that forms could be due to this oxidative degradation. Although fluorescence is suppressed when employing a UV laser in Raman spectroscopy, it is not completely eliminated, and the degree of fluorescence seen indicates that damage has been inflicted. Additionally, this analysis required several hours, as compared to the 60 seconds used to obtain the other spectra. From this, we have unfortunately concluded that UV Raman spectroscopy is not a useful technique for studying these samples.

A comparison among the spectra acquired from coating 85285 shows that the fully-formulated coating provides a very different result than the clear version, and that the binder cannot be readily discerned. In the Raman spectrum of the clear coating shown in Figure 2-2(c), a strong, sharp peak is observed at 1750 cm^{-1}, indicating the carbonyl found in urethane and urea linkages, which form through polymerization of the coating. Additional peaks correspond well to the expected chemical composition of the binder and will be discussed further in later chapters.

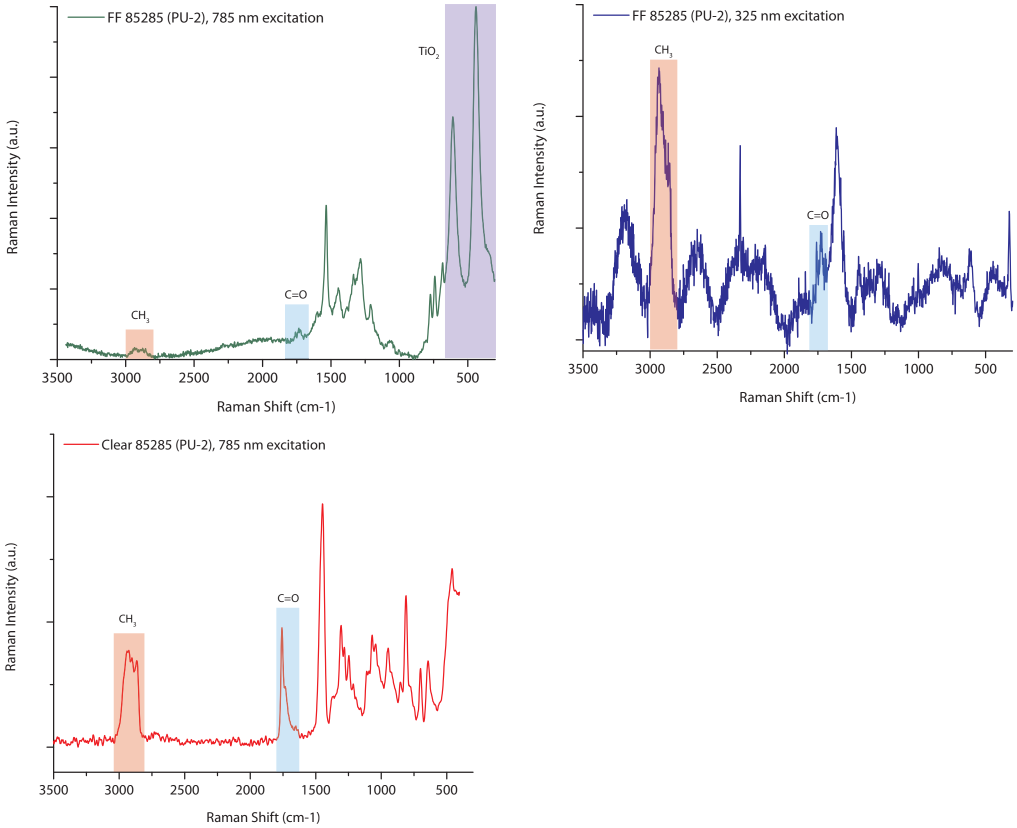

Figure 2-2 – Raman spectra of coatings (a, top left) fully-formulated 85285 analyzed with 785 nm excitation; (b, top right) fully-formulated 85285 analyzed with 325 nm excitation; (c, bottom left) clear 85285 analyzed with 785 nm excitation.

The absence of fillers does alter the properties of the coating. The presence of fillers and extenders, using anything from polymeric beads to diatomaceous earth (or more esoteric, purpose-driven compounds) creates a number of new interfaces which would have a significant effect on the rate of solvent diffusion. The swelling effect of the solvent would also function differently when faced with a number of inflexible barriers. However, since the purpose of this research is less about the mechanical means of disbondment and instead about the chemical changes caused in the binder, we feel this is a necessary trade-off. Ultimately, isolating the chemical changes will lead to a better understanding of disbondment.

A spectroscopic comparison of the clear and fully-formulated coatings provides useful context for relating our results from the clear coatings to the fully-formulated system. In Figure 2-3 we present the FTIR spectrum of both clear and fully-formulated Navy topcoat 85285. The majority of peaks are located in identical positions in the two samples, though the fully-formulated coating also shows several peaks which are not found the clear, indicating the pigments and other fillers of the system. FTIR offers substantially more information on the chemistry of the polymeric binder in the presence of pigmentation.

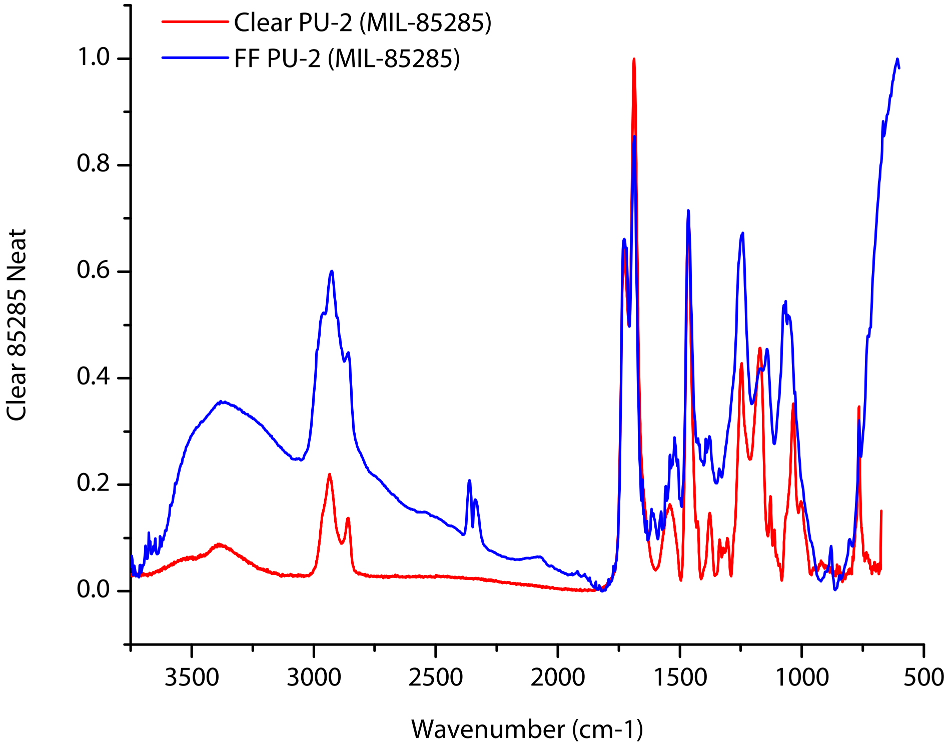

Figure 2-3 – ATR-FTIR spectra of clear and fully-formulated Navy topcoat 85285 (henceforth PU-2)

2.1.3 Coatings employed

The specific formulae of these coatings are not available for publication as they are derived from commercial coatings and thus covered under non-disclosure agreements. The chemical composition of the polymer and additives discussed will be based upon the requirements laid out in the relevant military specifications, with additional inferences drawn from spectral interpretation and collaborator guidance. Some additional information may also be referenced from past work done by Keene in this laboratory [25, 26].

Given the additional challenges to analysis introduced by the use of fully-formulated coatings, collaborators at the Army Research Laboratory (ARL) (Aberdeen, MD) also created coatings lacking pigmentation or fillers. The original formulae were adjusted to use additional solvents to produce the required viscosity for application to a substrate, and the amount of antifoam reagent was adjusted to minimize the presence of bubbles trapped in the cured coating. Ultimately, this enabled us to study only the polymeric binder, which is the weak link by which solvents swell and remove the coating. A more thorough discussion on the development of these clear coatings may be found in [36], as described by the formulators at ARL.

Samples were based on current topcoat specifications (MIL-PRF-85285 and MIL-DTL-53039, henceforth referred to by their specification numbers) employed by the U.S. Army and Navy. Coatings were provided in a fully-formulated form, with 85285 in light blue, and 53039 in tan. Coatings were also provided absent of any fillers or pigments, which produced clear films of polyurethane. All systems were provided on release paper to facilitate solvent exposure and analysis.

2.2 Paint removing solvents

2.2.1 Methods of paint removal

Polymer coatings provide excellent protection to substrates against corrosion, weathering, and impact, while also granting a variety of desirable properties. However, these coatings are not impervious to the same effects. As its performance degrades over time, the coating must be removed and reapplied in order to maintain the desired level of functionality. The efficient removal of paint coatings has long been performed by the application of solvent to soften the coating and reduce its adhesion to the substrate, followed by mechanical removal of the coating.

Paint strippers are made up from organic solvents, thickeners, anti-evaporants, and corrosion inhibitors, which combine in solution to provide an easily-applied mixture [37]. Compounds based on methylene chloride and phenol had been employed in military applications for many years, providing swift and efficient coating removal from nearly any geometry without corroding the substrate. However, in 1986 methylene chloride was added to the National Toxic Products list as a suspected carcinogen, resulting in a shift towards less-toxic solvents, and in 1990 the specification for this paint stripper (MIL-R-81294) was deactivated. The specification for next-generation paint removers (TT-R-2918A) calls for biodegradability and mild alkalinity in its compositional requirements in order to reduce its environmental footprint. The control formulation primarily consists of benzyl alcohol, water, ammonia, and anisole (along with the usual thickeners), offering a relatively innocuous blend of solvents with significantly reduced health hazards.

MIL-R-81294 was the gold standard for chemical paint removal and newer-generation paint strippers have been unable to equal its performance. The mixture of methylene chloride and phenol (with other solvents required for full formulation) performs polyurethane coating removal with a 15 minute dwell time (as per the specification). Newer paint removers based on TT-R-2918A call for a dwell time of 4 hours for stripping efficacy. Their performance may be enhanced by the addition of hydrogen peroxide, but this addition has been found to increase corrosion in aluminum substrates. While the environmental benefit of less-toxic paint removers cannot be discounted, the increased cost of removal in terms of time and manpower renders them an inefficient substitute for the original.

Non-chemical methods of paint removal have also been evaluated and employed. Water jets, media blasting, and lasers [38, 39] have all been used to remove paint, but each method has significant drawbacks. All are prone to causing substrate damage and require additional large-scale user protections (from toxic dust or hazardous laser scattering), and none are as efficient or effective as methylene chloride-based paint removers. Replacement non-solvent methods also require substantial retooling of existing service depots, thus incurring a significant increase in cost.

The mechanism by which methylene chloride and phenol remove the coating is not well understood or discussed in the literature. Recent work by Croll [40] has described the mechanism in terms of swelling and fracture resistance (through the Flory-Rehner and Griffith equations, respectively) to describe the means by which coatings lose adhesion to the substrate. However, this description fails to describe other irreversible changes we have observed which occur to the coating following exposure. In order to understand the mechanism by which MIL-R-81294 effectively removes paint we must first determine and recognize the purpose of each additive. This will allow the formulation of a simplified model solvent system to evaluate the reversible and irreversible chemical changes which result from solvent infiltration.

2.2.2 Rationale for the usage of proposed solvent systems

The control formulation of MIL-R-81294 is listed in Table 2-1. Briefly, the solvents considered important for coating removal are methylene chloride, ethanol, water, and phenol. Hydroxypropyl methylcellulose is added to enhance mixing and increase viscosity in the coating; an additional role played by this material will be discussed later. Sodium chromate treats the metal substrate. Toluene is used to dissolve the paraffin wax for addition, and paraffin wax is added to retard evaporation after application. Sodium petroleum sulfonate functions as a surfactant. In a simplified chemical analysis of solvent exposure, we believe we may safely discard toluene, paraffin, sodium chromate, and sodium petroleum sulfonate as being immaterial to the mechanism of action on the polymeric binder, due to their primary purpose relating to solvent retention.

Solvent interactions with polymers are often discussed through the context of Hansen Solubility Parameters [41], which quantify dispersion forces **(δ_d)**, dipolar interactions **(δ_p)**, and hydrogen bonding between molecules **(δ_h)**. The principle of "like dissolves like" applies to these values, and the closer one substance is to another in Hansen space (with these 3 parameters serving as coordinates) the more likely they are to dissolve one another. The Hansen solubility parameters of methylene chloride (**δ_d:** 18.2 MPa$^{0.5}$ **δ_p:** 6.3 MPa$^{0.5}$ **δ_h:** 6.1 MPa$^{0.5}$) [42] are very similar to those of polyurethane (**δ_d:** 18.0 MPa$^{0.5}$ **δ_p:** 6.3 MPa$^{0.5}$ **δ_h:** 6.3 MPa$^{0.5}$) [43], which offers an explanation for the effectiveness of this solvent on these polymers.

		Component Weight Percent			
		Methylene chloride	**Ethanol**	**Water**	**Phenol**
Solution	MIL-R-81294 control formulation[a]	60.6	5.8	7.8	15.8
	Methylene Chloride (A)	100	---	---	---
	Methylene chloride and ethanol (B)	91	9	---	---
	Methylene chloride, ethanol and water [b] (C)	82	8	10	---
	Methylene chloride, ethanol, water and phenol [b] (D)	67	6	9	18
	Ethanol and phenol	---	27	---	73
	Methylene chloride and phenol	79	---	---	21
	Methylene chloride, phenol and ethanol[c]	74	7	---	19
	Methylene chloride, phenol and water[c]	78	---	1	21

Table 2-1 – Formulations of control paint removal system and systems employed in this study.

a Also contains Methocel (1.2%), toluene (1.3%), sodium petroleum sulfonate (5.5%) and paraffin (1.9%)
b Methocel added to emulsify into a single phase

2.2.3 Solvents employed

Solutions containing mixtures of the 4 control formulation solvents of interest were assembled in varying combinations, and are listed in Table 2-1. Where solvents were found to be immiscible, hydroxypropyl methylcellulose (Methocel F4M PRG, DowWolff Cellulosics) was added in small amounts to enhance mixing. By studying mixtures in increasing complexity, we are able to probe the synergistic effects of the solvent combination. Using feedback from the initial set of experiments, additional mixtures were formulated to isolate specific effects which were observed.

2.3 Carbon fiber / vinyl ester composites

2.3.1 Considerations in the design of a fiber reinforced polymer system

Fiber-reinforced materials are commonly employed in situations with stringent mechanical requirements where weight is at a premium. Owing to their high strength-to-weight ratio, such composite materials have found applications in everything from tennis racquets to automobiles to naval vessels and aircraft.

There are three important considerations to the study of any composite material: the matrix resin, the reinforcing material, and the nature of the interface between the two. The properties of each material influence the ultimate performance of the composite, and the interface acts as a further multiplier of that effect.

Vinyl ester first appeared in the 1960’s as a replacement material for dental amalgam. It rose to popularity as a structural material in the 1980’s due to its superior resistance to water uptake compared to polyester, the common choice at the time. Vinyl ester chains contain far fewer ester moieties than polyesters, leading to an enhanced resistance to hydrolytic degradation.

Ester moieties are susceptible to hydrolytic degradation in both weak acids and bases, which tends to describe most natural sources of water. Mechanically, vinyl esters are superior to polyesters in strength, impact resistance, and cyclical loading capabilities, the latter two due to its increased ductility [44]. Chemically, vinyl ester is generated through the reaction of a diepoxide (such as DGEBA) with acrylic acid, which leaves vinyl end groups on the chain for subsequent crosslinking. The vinyl groups polymerize with each other, or with styrene to produce a matrix, which is shown in Figure 2-4.

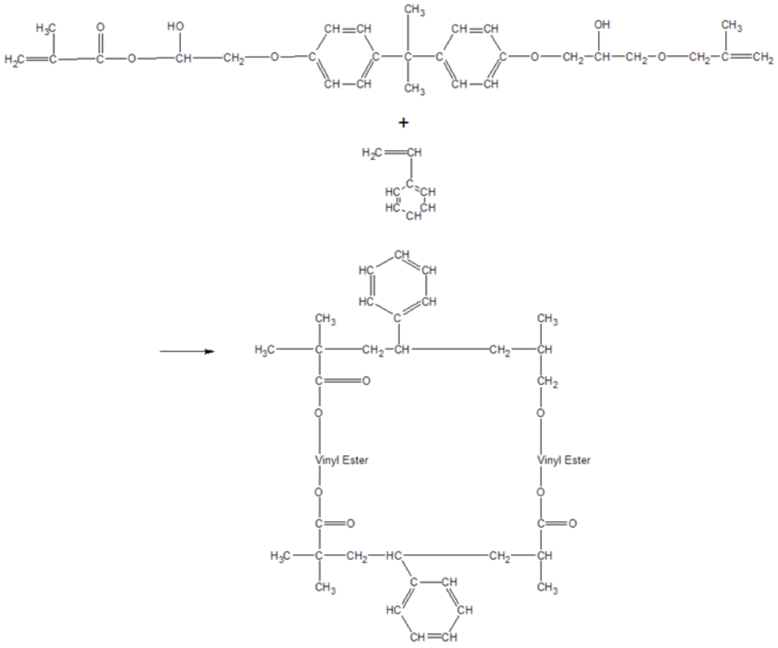

Figure 2-4 – Polymerization mechanism of vinyl ester with styrene.

Glass fibers have been employed as a reinforcement material for a long time as not only do they demonstrate good tensile strength, but they are inexpensive to produce, allowing for significant mechanical improvements at minimal cost. Newer fibers have been designed for high-performance applications. Kevlar fibers are made from aromatic polyamides, and have a high tensile strength due to their high degree of molecular orientation. These fibers are also very tough, which allows it to absorb more energy without breaking - hence their common use in body armor. Spectra fibers are made from highly oriented polyethylene, and show properties superior to Kevlar. Carbon fibers are the most common “high performance” fiber found in composites, as they strike a desirable balance of performance and cost. These fibers are extremely strong, even compared to Kevlar. They are also comparatively easy to produce in a large scale, as they exploit the inherent arrangement of highly ordered graphite [45].

Carbon fibers are commonly produced through the thermal treatment of polyacrylonitrile (PAN) fibers to the point of graphitization. Initially, the fibers are held under tension and heated to 200-300 °C to oxidize the material, producing a non-plastic material with a cyclic structure. Next, the fibers are carbonized at 1000 °C in nitrogen to remove substantial non-carbon impurities contained within; this does have the effect of incorporating nitrogen into the structure at the surface. Finally, the fibers are graphitized at temperatures ranging from 1500 to 3000 °C to form a graphite structure within the fibers. Fibers are then washed in an electrolytic bath to purge the surface of nitrogen and to add useful functional groups for fiber adhesion [46]. Ultimately, the carbon fiber consists of an assembly of graphite planes stacked together; the high degree of ordering within the graphite structure lends these fibers their great strength.

The adhesion between reinforcing fiber and matrix resin is an important factor in the strength of the resulting composite. An untreated carbon fiber may rely only on its inherent roughness and surface hydroxyl groups for adhesion, which provides only a limited benefit. A surface treatment known as a sizing is applied to the fiber, which has been chemically engineered to improve adhesion between fiber and matrix, thus yielding superior mechanical properties. The sizing also serves to protect the fiber during handling, helping to minimize breakage and fluffing as a result of mechanical friction during manufacturing.

2.3.2 Fiber sizings

Sizings have been studied extensively for glass and carbon fibers [47-49]. In general, they function by adhering to the fiber surface and diffusing into the resin, which creates a narrow zone around the fiber called the interphase [48, 50]. Prior to the application of sizing, a carbon fiber may be surface treated to enhance its adhesion [51, 52]. Given the highly surface-driven properties of this treatment, the common tool for chemical investigation has been XPS [53-55].

Sizings are chosen based on the resin in which the fibers will be embedded, as an appropriate match in chemistry will lead to improved performance [56]. Research has been conducted in the development of designer sizings to improve specific properties, such as fatigue resistance [57, 58] or high-temperature performance [59]. A chemical understanding of these property changes generally deals with the chemistry of the interphase. This is a complex region, wherein the sizing generally mixes and diffuses into, but does not cure with, the matrix polymer [48, 60]. FTIR microspectroscopy, XPS, and mechanical testing have all been used to probe changes in the interphase to demonstrate the effects of sizing and surface chemistry [50, 61-67]. A new class of sizings known as reactive finishes does react with the matrix, which leads to significant performance enhancements [68, 69]. A schematic drawing of the fiber-matrix interface may be found in Figure 2-5.

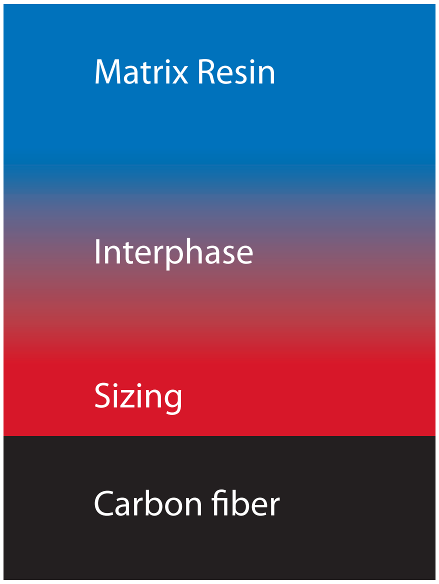

Figure 2-5 – Schematic representation of the carbon fiber - sizing - matrix interphase region

Fiber sizings are generally proprietary products, though we can infer characteristics based on knowledge from the literature. A properly-chosen sizing must be compatible with the matrix in which it will be embedded. It should inter-diffuse into that matrix during the curing process, if not outright react with it. The curing of the sizing may also be directly affected by the same promoters used in the resin. The amount of sizing used on the fiber must be adequate to improve adhesion, but not so high as to interfere with resin diffusion near the fiber surface [46]. Effectively, a fiber sizing may be considered a heterobifunctional crosslinker between the hydroxyl- and carbonyl-laden fiber surface and the resin. Several model systems have been examined, including PVP [50, 70, 71], LaRC PETI-5 [72], nano-silica [73], and vinyl ester emulsions [74]. These systems have generally been applied to the fibers post-purchase, after removing the existing sizing with acetone, methylene chloride, or chloroform. With that said, the sizings examined in the literature do not well resemble those found in patents.

The mechanical properties of neat resins and fibers are well understood and easily measured, leading to a strong understanding of the durability of these materials with respect to the degradative effects of water, heat, and sunlight [75-78]. However, the unique chemistry of the interphase means that the durability of composite materials is not well defined. Numerous studies have been conducted on the durability of composites to environmental degradation [59, 79-88], but these studies must by necessity focus on the chosen composite system of interest. While research has generally focused on the interphase as the point of vulnerability, there has been little research on the specific chemical durability of the sizing or interphase region.

2.3.3 Fibers and resins employed

Toray T700 carbon fibers with proprietary sizing system “F0E” and Ashland Derakane MOMENTUM 411-350 vinyl ester resin were combined in a VARTM process according to the manufacturer’s specifications to produce composite plates approximately 4mm thick. Neat resin was also processed to produce plates of similar thickness. Loose carbon fiber weave was also provided for analysis.

2.4 References

[1] C.H. Hare, Paint Film Degradation: Mechanisms and Control, SSPC: The Society for Protective Coatings, Pittsburgh, 2001.

[2] D. Bello, S.R. Woskie, R.P. Streicher, Y. Liu, M.H. Stowe, E.A. Eisen, M.J. Ellenbecker, J. Sparer, F. Youngs, M.R. Cullen, C.A. Redlich, Polyisocyanates in occupational environments: A critical review of exposure limits and metrics, American Journal of Industrial Medicine, 46 (2004) 480-491.

[3] J. Colmenares-Angulo, S. Zhao, C. Young, A. Orlov, The effects of thermal spray technique and post-deposition treatment on the photocatalytic activity of TiO2 coatings, Surface and Coatings Technology, 204 (2009) 423-427.

[4] C.H. Hare, Protective Coatings: Fundamentals of Chemistry and Composition, SSPC: The Society for Protective Coatings, Pittsburgh, 1998.

[5] Z.W. Wicks Jr., F.N. Jones, S.P. Pappas, Organic Coatings: Science and Technology, 2nd ed., Wiley-Interscience, New York, 1999.

[6] J.G. Lundin, S.L. Giles, R.F. Cozzens, J.H. Wynne, Analysis of surface segregating additives for self-decontaminating coatings, in, American Chemical Society, 2013, pp. COLL-280.

[7] N.C. Blacker, P.H. Findlay, D.C. Sherrington, Synthesis of CuII-complexed polymers and use as catalysts in the hydrolytic decontamination of sarin nerve agent, Polym. Adv. Technol., 12 (2001) 183-196.

[8] R.A. Brizzolara, D.M. Stamper, The effect of covalent surface immobilization on the bactericidal efficacy of a quaternary ammonium compound, Surf. Interface Anal., 39 (2007) 559-566.

[9] N. Grover, I.V. Borkar, C.Z. Dinu, R.S. Kane, J.S. Dordick, Laccase- and chloroperoxidase-nanotube paint composites with bactericidal and sporicidal activity, Enzyme Microb. Technol., 50 (2012) 271-279.

[10] R.R. Pant, J.L. Buckley, P.A. Fulmer, J.H. Wynne, D.M. McCluskey, J.P. Phillips, Hybrid siloxane epoxy coatings containing quaternary ammonium moieties, J. Appl. Polym. Sci., 110 (2008) 3080-3086.

[11] A.J. Russell, J.A. Berberich, G.F. Drevon, R.R. Koepsel, Biomaterials for mediation of chemical and biological warfare agents, Annu. Rev. Biomed. Eng., 5 (2003) 1-27.

[12] J.H. Wynne, P.A. Fulmer, D.M. McCluskey, N.M. Mackey, J.P. Buchanan, Synthesis and Development of a Multifunctional Self-Decontaminating Polyurethane Coating, ACS Appl. Mater. Interfaces, 3 (2011) 2005-2011.

[13] A. Turner, Marine pollution from antifouling paint particles, Mar Pollut Bull, 60 (2010) 159-171.

[14] R. Parks, M. Donnier-Marechal, P.E. Frickers, A. Turner, J.W. Readman, Antifouling biocides in discarded marine paint particles, Mar Pollut Bull, 60 (2010) 1226-1230.

[15] A. Turner, N. Singh, J.P. Richards, Bioaccessibility of metals in soils and dusts contaminated by marine antifouling paint particles, Environ Pollut, 157 (2009) 1526-1532.

[16] A. Turner, H. Pollock, M.T. Brown, Accumulation of Cu and Zn from antifouling paint particles by the marine macroalga, Ulva lactuca, Environ Pollut, 157 (2009) 2314-2319.

[17] F. Fay, D. Carteau, I. Linossier, M. Delbury, K. Vallee-Rehel, Joint-action of antifouling substances in copper-free paints, Colloids Surf., B, 102 (2013) 569-577.

[18] E.K. Oikonomou, Z. Iatridi, M. Moschakou, P. Damigos, G. Bokias, J.K. Kallitsis, Development of Cu2+- and/or phosphonium-based polymeric biocidal materials and their potential application in antifouling paints, Progress in Organic Coatings, 75 (2012) 190-199.

[19] F. Natalio, R. Andre, A.F. Hartog, B. Stoll, K.P. Jochum, R. Wever, W. Tremel, Vanadium pentoxide nanoparticles mimic vanadium haloperoxidases and thwart biofilm formation, Nat. Nanotechnol., 7 (2012) 530-535.

[20] S. Krishnan, R. Ayothi, A. Hexemer, J.A. Finlay, K.E. Sohn, R. Perry, C.K. Ober, E.J. Kramer, M.E. Callow, J.A. Callow, D.A. Fischer, Anti-Biofouling Properties of Comblike Block Copolymers with Amphiphilic Side Chains, Langmuir, 22 (2006) 5075-5086.

[21] R.J. Klein, D.A. Fischer, J.L. Lenhart, Thermal and Mechanical Aging of Self-Assembled Monolayers as Studied by Near Edge X-ray Absorption Fine Structure, Langmuir, 27 (2011) 12423-12433.

[22] J.D. Weir, R.G. Pirich, D.J. Leyble, L.G. Chorosinski, J.D. Gardner, Jr., S. Chu, Self-cleaning coating for protection against hazardous biopathogens and toxic chemical agents utilizing both super-hydrophobic effects and suitable oxide interfaces, in, Northrop Grumman Systems Corporation, USA . 2011, pp. 4pp.

[23] D.o. Defense, COATING, ALIPHATIC POLYURETHANE, SINGLE COMPONENT, CHEMICAL AGENT RESISTANT, in, Aberdeen, MD, 2011.

[24] D.o. Defense, COATING: POLYURETHANE, AIRCRAFT AND SUPPORT EQUIPMENT, in, NAWCAD, Lakehurst, NJ, 2012.

[25] L.T. Keene, G.P. Halada, C.R. Clayton, Failure of navy coating systems 1: chemical depth profiling of artificially and naturally weathered high-solids aliphatic poly(ester-urethane) military coating systems, Progress in Organic Coatings, 52 (2005) 173-186.

[26] L.T. Keene, M.J. Vasquez, C.R. Clayton, G.P. Halada, Failure of navy coating systems 2: failure pathways of artificially weathered navy coating systems applied to chromate conversion coated AA2024-T3 substrates, Progress in Organic Coatings, 52 (2005) 187-195.

[27] S.G. Croll, A.D. Skaja, Quantitative spectroscopy to determine the effects of photodegradation on a model polyester-urethane coating, Journal of Coatings Technology, 75 (2003) 85-94.

[28] A.D. Skaja, S.G. Croll, Quantitative ultraviolet spectroscopy in weathering of a model polyester–urethane coating, Polymer Degradation and Stability, 79 (2003) 123-131.

[29] X.F. Yang, J. Li, S.G. Croll, D.E. Tallman, G.P. Bierwagen, Degradation of low gloss polyurethane aircraft coatings under UV and prohesion alternating exposures, Polymer Degradation and Stability, 80 (2003) 51-58.

[30] X.F. Yang, D.E. Tallman, G.P. Bierwagen, S.G. Croll, S. Rohlik, Blistering and degradation of polyurethane coatings under different accelerated weathering tests, Polymer Degradation and Stability, 77 (2002) 103-109.

[31] X.F. Yang, D.E. Tallman, S.G. Croll, G.P. Bierwagen, Morphological changes in polyurethane coatings on exposure to water, Polymer Degradation and Stability, 77 (2002) 391-396.

[32] X.F. Yang, C. Vang, D.E. Tallman, G.P. Bierwagen, S.G. Croll, S. Rohlik, Weathering degradation of a polyurethane coating, Polymer Degradation and Stability, 74 (2001) 341-351.

[33] L.T. Keene, T. Fiero, C.R. Clayton, G.P. Halada, D. Cardoza, T. Weinacht, On the use of femtosecond laser ablation to facilitate spectroscopic depth profiling of heterogeneous polymeric coatings, Polym. Degrad. Stab., 89 (2005) 393-409.

[34] G. Socrates, Infrared Characteristic Group Frequencies: Tables and Charts, 2nd ed., John Wiley & Sons, Chichester, 1994.

[35] J. De Gelder, P. Vandenabeele, F. Govaert, L. Moens, Forensic analysis of automotive paints by Raman spectroscopy, Journal of Raman Spectroscopy, 36 (2005) 1059-1067.

[36] J.H. Wynne, K.E. Watson, J.P. Yesinowski, C.N. Young, C.R. Clayton, N. Nesteruk, J. Kelley, T. Braswell, Report on Scientific Basis for Paint Stripping: Mechanism of Methylene Chloride Based Paint Removers, in, Naval Research Laboratory, Washington, DC, 2011.

[37] DoD, MIL-R-81294D: REMOVER, PAINT, EPOXY, POLYSULFIDE, AND POLYURETHANE SYSTEMS, in, 1999.

[38] J. Durkee, Cleaning times: Paint stripping: It's just like parts cleaning, Metal Finishing, 107 (2009) 49-51.

[39] E. Groshart, Finishing in the green: Paint stripping—Without methylene chloride, Metal Finishing, 95 (1997) 55-57.

[40] S.G. Croll, Application of the Flory-Rehner equation and the Griffith fracture criterion to paint stripping, J. Coat. Technol. Res., 7 (2010) 49-55.

[41] C.M. Hansen, Hansen Solubility Parameters: A User's Handbook, Second Edition, Taylor & Francis, 2007.

[42] A.F.M. Barton, CRC handbook of solubility parameters and other cohesion parameters, CRC Press, 1983.

[43] A. Latnikova, D.O. Grigoriev, H. Möhwald, D.G. Shchukin, Capsules Made of Cross-Linked Polymers and Liquid Core: Possible Morphologies and Their Estimation on the Basis of Hansen Solubility Parameters, The Journal of Physical Chemistry C, 116 (2012) 8181-8187.

[44] P.A. Schweitzer, Mechanical and Corrosion-Resistant Properties of Plastics and Elastomers, 1 ed., Marcel Dekker, New York, 2000.

[45] D.D.L. Chung, Composite Materials: Science and Applications, Springer London, 2010.

[46] A.B. Strong, Fundamentals Of Composites Manufacturing: Materials, Methods and Applications, Society of Manufacturing Engineers, 2008.

[47] F. Santiago, A.N. Mansour, R.N. Lee, XPS study of sizing removal from carbon fibers, Surface and Interface Analysis, 10 (1987) 17-22.

[48] H. Al-Moussawi, E.K. Drown, L.T. Drzal, The silane/sizing composite interphase, Polymer Composites, 14 (1993) 195-200.

[49] C.L. Weitzsacker, M. Bellamy, P.M.A. Sherwood, Studies of the Effect of Size on Carbon Fiber Surfaces, Journal of Vacuum Science and Technology A, 12 (1994) 2392 - 2397.

[50] C.M.I. Laot, Spectroscopic Characterization of Molecular Interdiffusion at a Poly(Vinyl Pyrrolidone) / Vinyl Ester Interface, in: Chemical Engineering, Virginia Polytechnic Institute and State University, Blacksburg, 1997.

[51] L.T. Weng, C. Poleunis, P. Bertrand, V. Carlier, M. Sclavons, P. Franquinet, R. Legras, Sizing removal and functionalization of the carbon fiber surface studied by combined TOF SIMS and XPS, Journal of Adhesion Science and Technology, 9 (1995) 859-887.

[52] H. Oyama, J.P. Wightman, Surface characterization of PVP [poly(vinylpyrrolidone)-sized and oxygen plasma-treated carbon fibers, Surface and Interface Analysis, 26 (1998) 39-55.

[53] G.E. Hammer, L.T. Drzal, Graphite fiber surface analysis by x-ray photoelectron spectroscopy and polar/dispersive free energy analysis, Applications of Surface Science (1977-1985), 4 (1980) 340-355.

[54] A. Proctor, P.M.A. Sherwood, X-ray photoelectron spectroscopic studies of carbon fiber surfaces. III - Industrially treated fibers and the effect of heat and exposure to oxygen, Surface and Interface Analysis, 4 (1982) 212-219.

[55] A. Proctor, P.M.A. Sherwood, X-ray photoelectron spectroscopic studies of carbon fiber surfaces. I. Carbon fiber spectra and the effects of heat treatment, Journal of Electron Spectroscopy and Related Phenomena, 27 (1982) 39-56.

[56] G. Bogoeva-Gaceva, D. Burevski, A. Dekanski, A. Janevski, The effect of surface treatment on the interfacial properties in carbon fiber epoxy matrix composites, Journal of Materials Science, 30 (1995) 3543-3546.

[57] N.S. Broyles, S.V.D. K. N. E. Verghese, H. Li, R. M. Davis, J. J. Lesko and J. S. Riffle, Fatigue performance of carbon fibre/vinyl ester composites: the effect of two dissimilar polymeric sizing agents, Polymer, 39 (1998) 3417-3424.

[58] M.A.F. Robertson, M.B. Bump, K.E. Verghese, S.R. McCartney, J.J. Lesko, J.S. Riffle, I.C. Kim, T.H. Yoon, Designed interphase regions in carbon fiber reinforced vinyl ester matrix composites, Journal of Adhesion, 71 (1999) 395-416.

[59] R.E. Allred, S.P. Wesson, E.E. Shin, L. Inghram, L. McCorkle, D. Papadopoulos, D. Wheeler, J.K. Sutter, The influence of sizings on the durability of high-temperature polymer composites, High Performance Polymers, 15 (2003) 395-419.

[60] L.T. Drzal, K.J. Hook, R.K. Agrawal, Enhanced chemical bonding at the fiber-matrix interphase in microwave processed composites, Materials Research Society Symposium Proceedings, 189 (1991) 449-454.

[61] J.L. Koenig, F. Fondeur, Modern spectroscopic analysis of composite interphases, Adhes. Soc., Proc. Sixteenth Annu. Meet. Int. Symp. Interphase, (1993) 303-305.

[62] C.D. Arvanitopoulos, J.L. Koenig, Infrared spectral imaging of the interphase of epoxy-glass fiber-reinforced composites under wet conditions, Applied Spectroscopy, 50 (1996) 11-18.

[63] C.D. Arvanitopoulos, J.L. Koenig, FT-IR microspectroscopic investigation of the interphase of epoxy resin-glass fiber-reinforced composites, Applied Spectroscopy, 50 (1996) 1-10.

[64] C.L. Weitzsacker, M. Xie, L.T. Drazal, Using XPS to investigate fiber/matrix chemical interactions in carbon-fiber-reinforced composites, Surface and Interface Analysis, 25 (1997) 53-63.

[65] C. Perruchot, J.F. Watts, C. Lowe, R.G. White, P.J. Cumpson, Angle-resolved XPS characterization of urea formaldehyde-epoxy systems, Surf. Interface Anal., 33 (2002) 869-878.

[66] A. Al-Ostaz, H. Al-Moussawi, L.T. Drzal, Characterization of the interphase in glass sphere reinforced polymers, Composites, Part B: Engineering, 35B (2004) 393-412.

[67] A.C. Prickett, P.E. Vickers, P.A. Smith, J.F. Watts, The interphase chemistry of carbon fiber composite materials, Adhesion '99, International Conference on Adhesion and Adhesives, 7th, Cambridge, United Kingdom, Sept. 15-17, 1999, (1999) 369-373.

[68] R.E. Allred, A.E. Hoyt Haight, J.M. Gosau, S.P. Wesson, Aqueous-based emulsion reactive finishes for improving carbon/vinyl ester interfacial bonding, International SAMPE Symposium and Exhibition, 50 (2005) 741-756.

[69] R.E. Allred, S.P. Wesson, A.E. Hoyt Haight, J.W. Whitehead, Reactive finishes for improved interfacial properties in carbon/vinyl ester laminates, International SAMPE Symposium and Exhibition, 49 (2004) 2059-2072.

[70] N.S. Broyles, Thermoplastic Sizings: Effects on Processing, Mechanical Performance, and Interphase Formation in Pultruded Carbon Fiber/Vinyl-Ester Composites, in: Chemical Engineering, Virginia Polytechnic Institute and State University, Blacksburg, VA, 1999, pp. 328.

[71] P. Bartolomeo, J.F. Chailan, J.L. Vernet, Dielectric investigation of interphase formation in composite materials. Part 1. Ionic conductivity and permittivity exploration, Journal of Polymer Science, Part B: Polymer Physics, 38 (2000) 2154-2161.

[72] D. Cho, Y. Choi, J.-H. Chang, L.T. Drzal, Interphase sizing temperature effect of LaRC PETI-5 on the dynamic mechanical thermal properties of carbon fiber/BMI composites, Composite Interfaces, 13 (2006) 215-229.

[73] Y. Yang, C.-X. Lu, X.-L. Su, G.-P. Wu, X.-K. Wang, Effect of nano-SiO2 modified emulsion sizing on the interfacial adhesion of carbon fibers reinforced composites, Materials Letters, 61 (2007) 3601-3604.

[74] J. Liu, H. Ge, J. Chen, D. Wang, H. Liu, The preparation of emulsion type sizing agent for carbon fiber and the properties of carbon fiber/vinyl ester resin composites, Journal of Applied Polymer Science, 124 (2012) 864-872.

[75] L.W. Jelinski, J.J. Dumais, A.L. Cholli, T.S. Ellis, F.E. Karasz, Nature of the water-epoxy interaction, Macromolecules, 18 (1985) 1091-1095.

[76] J.-L. Gardette, B. Mailhot, J. Lemaire, Photooxidation mechanisms of styrenic polymers, Polymer Degradation and Stability, 48 (1995) 457-470.

[77] A.W. Signor, M.R. VanLandingham, J.W. Chin, Effects of ultraviolet radiation exposure on vinyl ester resins: characterization of chemical, physical and mechanical damage, Polymer Degradation and Stability, 79 (2002) 359-368.

[78] S. Agrawal, A. Mishra, J.S.P. Rai, Effect of diluents on the decomposition behavior of vinyl ester resin, J. Appl. Polym. Sci., 87 (2003) 1952-1956.

[79] B.G. Kumar, R.P. Singh, T. Nakamura, Degradation of carbon fiber-reinforced epoxy composites by ultraviolet radiation and condensation, Journal of Composite Materials, 36 (2002) 2713-2733.

[80] L. Wu, K. Murphy, V.M. Karbhari, J.S. Zhang, Short-term effects of sea water on E-glass/vinylester composites, J. Appl. Polym. Sci., 84 (2002) 2760-2767.

[81] V.M. Karbhari, S. Zhang, E-Glass/Vinylester Composites in Aqueous Environments - I: Experimental Results, Applied Composite Materials, 10 (2003) 19-48.

[82] K.-B. Shin, C.-G. Kim, C.-S. Hong, Correlation of accelerated aging test to natural aging test on graphite-epoxy composite materials, Journal of Reinforced Plastics and Composites, 22 (2003) 849-861.

[83] A. Kootsookos, A.P. Mouritz, Seawater durability of glass- and carbon-polymer composites, Composites Science and Technology, 64 (2004) 1503-1511.

[84] Y. Miyano, M. Nakada, N. Sekine, Accelerated testing for long-term durability of GFRP laminates for marine use, Composites, Part B: Engineering, 35B (2004) 497-502.

[85] K.N.E. Verghese, N.S. Broyles, J.J. Lesko, R.M. Davis, J.S. Riffle, Pultruded Carbon Fiber/Vinyl Ester Composites Processed with Different Fiber Sizing Agents. Part II: Enviro-Mechanical Durability, J. Mater. Civ. Eng., 17 (2005) 334-342.

[86] A.P. Mouritz, A.G. Gibson, Fire properties of polymer composite materials, Springer London, Limited, 2006.

[87] B.C. Ray, Temperature effect during humid aging on interfaces of glass and carbon fibers reinforced epoxy composites, Journal of Colloid and Interface Science, 298 (2006) 111-117.

[88] R. Martin, Ageing of Composites, 1st ed., Woodhead Publishing Limited, Cambridge, England, 2008.

Chapter 3: Methods of Analysis

3.1 FTIR and Raman Spectroscopy

3.1.1 FTIR spectroscopy

Vibrational spectroscopy represents one of the most well-defined areas of non-destructive chemical analysis. Arising from the excitation of specific molecular bonds, it is capable of characterizing most samples in a qualitative and quantitative fashion. We will briefly discuss the mechanisms of two complementary methods to illustrate the power of these tools.

Infrared spectroscopy has its roots in the 19th century with the first observations of IR spectra from the sun. Since then, with the invention of the Michelson interferometer and the development of inexpensive lasers, Fourier Transform Infrared (FTIR) spectroscopy has risen to prominence as a fast, easy tool to characterize molecules and materials. Samples can be in the solid, liquid, or gaseous phase for analysis, and an overwhelming catalogue of reference spectra have been assembled over the past decades (*e.g.* [1], which itself references dozens of papers in each chapter and offers almost 70 sources of additional reading), leading to rapid identification of unknowns. A superior understanding of quantum mechanics has led to a solid theoretical model for the cause of IR absorbance, which extends modeling as an additional tool for the determination of more complex systems, such as biological complexes (*e.g.* [2]) or catalysts (*e.g.* [3]).

Infrared spectroscopy operates due to the principle of anharmonic oscillation between molecules. Molecules may be considered to be made up of balls of particular masses connected by springs of particular force constants. The frequency of oscillation therefore derives from Hooke's law, and becomes

$$\tilde{\nu} = \frac{1}{2\pi c}\sqrt{\frac{k}{\mu}}$$

Equation 3-1 – Frequency of oscillation of interatomic bonds.

where k is the force constant of the bond and μ is the reduced mass of the atoms being considered in this oscillation. From this equation, we may make general observations concerning the behavior of spectra. The wavenumber of a vibration increases as the spring constant of the bond increases, and the wavenumber decreases with increasing mass of the participating atoms. Electronically, IR vibrations are induced when an electron is excited to the first vibrational energy level. A schematic of FTIR spectroscopy may be found in Figure 3-1.

Quantum mechanical selection rules determine how a molecule vibrates under IR radiation. For a given vibration to be IR active the molecular electric dipole moment must change during vibration, as it is the electric field component of the radiation which induces vibration. While diatomic gases will not vibrate due to a lack of dipole, other molecules which initially have zero dipole may vibrate in such a way as to generate one, such as through antisymmetric stretching as in CO_2. A more comprehensive discussion of the physics behind infrared spectroscopy may be found in physical chemistry [4] or spectroscopy texts [5].

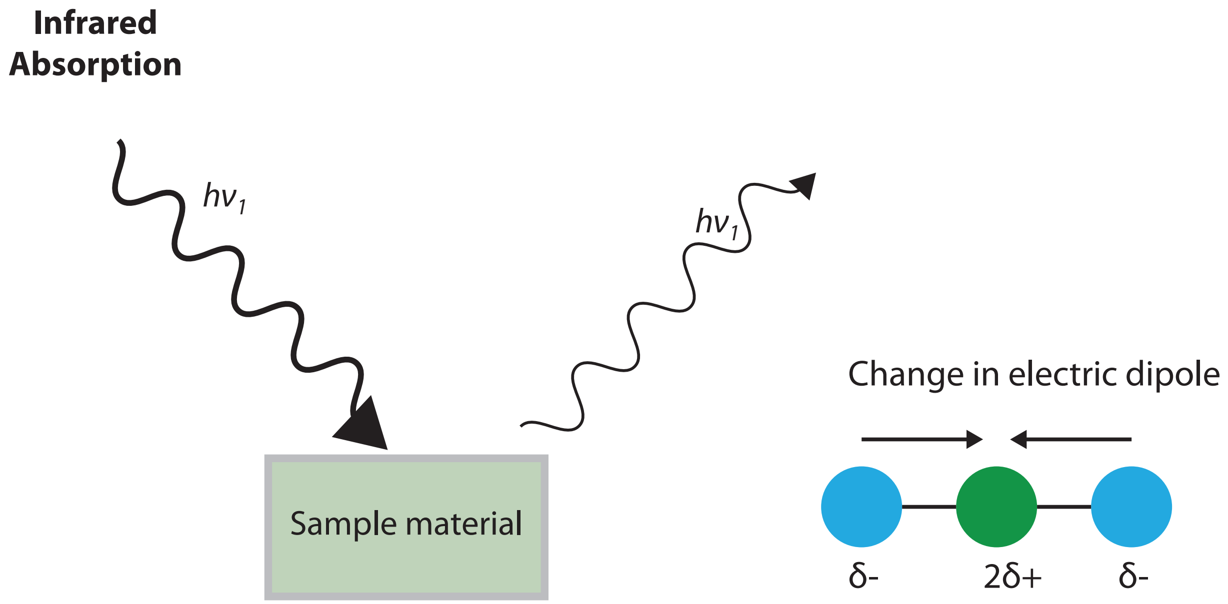

Figure 3-1 - Schematic representation of FTIR spectroscopy, and the subsequent effects on molecular electric dipole.

3.1.2 Raman spectroscopy

In 1928, C.V. Raman first observed and published evidence of a new type of radiation from samples [6] which he observed from a sample illuminated by filtered sunlight. A spectrum could be detected within a small range of wavelengths distinctly separated from those of the illuminating light. The later invention of the laser led to significant increases in the utility of this method by providing high-intensity, monochromatic light at the sample. Raman spectroscopy has many advantages as a characterization method, one of which was highlighted by Raman himself: spectra may be collected through the container in which a sample is stored, thus requiring little (if any) sample preparation. As such, the test is almost completely non-destructive (although laser damage may occur, as discussed in Chapter 2.)

The Raman effect occurs through a mechanism similar to fluorescence. The energy of the stimulating light source is chosen to be below the first excited electronic state, leading to any energy absorption exciting the electron to a virtual excited state. Subsequent relaxation of this electron to the first vibrational state leads to emission of a photon with slightly shifted energy, which produces a line in the Raman spectrum. The emission which results from this type of relaxation is called Stokes radiation. If an electron is already in the first vibrational state and is excited, then relaxes to the ground state, such an emission is referred to as anti-Stokes [7]. A schematic depiction of Raman spectroscopy may be found in Figure 3-2.

The selection rule for Raman activity indicates that the vibration must change the polarizability of the molecule. This may be visualized as an induced change in the shape of the electron cloud of the molecule being probed at the two extremes of motion in the vibration. A mathematical treatment of this effect utilizes a tensor to describe polarizability, an excellent description of which is available in [7].

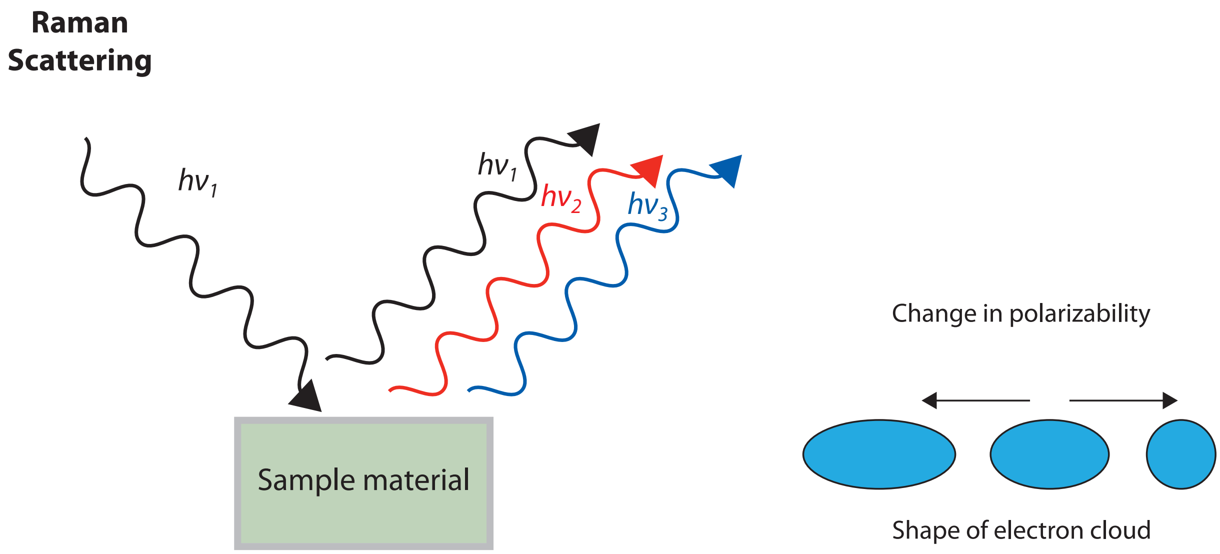

Figure 3-2 - Schematic depiction of Raman scattering, and the physical effect on the electron cloud which occurs in Raman-active vibrations.

3.1.3 Complementary nature

FTIR and Raman spectroscopy are complementary techniques, based on the physics of their selection rules. In the former, a bond must be polar; in the latter, a bond must be polarizable. It follows that FTIR will be more sensitive to functional groups of polymers, as they tend to be polar, and Raman is more sensitive to backbone chains and double bonds, as they are often more electron-rich. The selection rules also lead to an exclusion rule: if a molecule has a center of inversion, then any vibrations can be either IR or Raman active, but not both. This rule directly demonstrates the complementary nature of these two techniques.

3.1.4 Sampling methods available in vibrational spectroscopy

Sample preparation required for FTIR allows for the analysis of all phases of a material and can range from minimal to moderately extensive. Solids may be ground into a pellet with KBr, a substance which does not absorb in the IR region, to permit analysis of a very small quantity. Specular and diffuse reflectance from sample surfaces may also be measured. With Attenuated Total Reflectance (ATR), samples may be placed into contact with a specially-shaped crystal (often ZnSe, Ge, or diamond) through which IR light is passed, which causes an evanescent wave effect in the sample, Thin samples may be analyzed directly by transmission. A microscope may be employed to analyze small regions through transmission, reflection, and ATR (using a small crystal). Liquids may be analyzed in many of the same ways , such as through reflectance, transmission (when held between two transparent windows), or direct contact with a crystal by ATR. Gases may be analyzed at extremely low concentrations (measured in ppb, if necessary) using long path cells, in which radiation is bounced between two mirrors providing an effective path length on the order of tens of meters. Photoacoustic FTIR spectroscopy is well-suited to solid samples and fine particles; the depth of analysis may be controlled by varying the speed of the mirror in the interferometer.

Raman spectroscopy requires no sample preparation whatsoever – with a spectrometer of appropriate dimensions, one need not even remove the sample from its vessel. That said, it can be advantageous to place a liquid sample into a quartz cuvette, as quartz is both transparent and Raman inactive within the range of organic samples. Microspectroscopy is of great utility in Raman analysis, as the use of a laser permits excitation spot sizes of less than 1 μm^2. Analysis of gases is also possible with this method.

3.1.5 Methods employed in this work

FTIR and Raman spectroscopy were both employed in the course of this research. As discussed in the Materials section, the ability to employ Raman spectroscopy dictated an important restriction in our coatings formulation. A Thermo Nicolet Almega dispersive Raman spectrometer with paired microscope and excitation lasers at 785 nm and 532 nm was used to collect spectra from samples, as was a WiTec alpha-500 confocal Raman microspectrometer with excitation laser at 532 nm. The latter instrument is housed at the Center for Functional Nanomaterials at Brookhaven National Laboratory in Upton, NY. Most sample analysis did not require additional preparation, but the investigation of solvated coatings called for creative measures to protect the (Almega) instrument from methylene chloride. The key to the investigation was that the sample needed to still retain sufficient solvent, but when saturated the coating outgassed at a rapid pace. By placing the coating inside a quartz cuvette, adhering it to a face of said cuvette, and laying it on its side, we were able to analyze the solvated sample while capturing most of the outgassed solvent due to the Teflon cap of the cuvette. Any solvent vapors which escaped were also no longer immediately beneath the objective lens, thus protecting the sensitive optics from damage.

Over the course of this research, several FTIR benches were used to perform this basic method of analysis. Thermo Nicolet Magna 560, Thermo Nicolet 6700, and Thermo Nicolet iS-50 FTIR spectrometers were used, with a Continuum microscope paired to the 560 and iS-50.

Benches were used for ATR, with attachments bearing ZnSe, Ge, and diamond crystals. With the microscope, both reflection (single-bounce through a thin film on a gold slide) and diamond micro-ATR were used to investigate smaller regions of interest.

3.2 XPS

3.2.1 Background

X-ray Photoelectron Spectroscopy (XPS) relies on the well-defined photoelectric effect, which describes the mechanism by which x-rays are able to eject electrons from the surface of a sample. The spectrometer measures the kinetic energy of emitted electrons, and using the formula

$$\mathrm{KE} = h\nu - \mathrm{BE} - \phi$$

Equation 3-2 – Relation of the photoelectric effect.

where KE is the kinetic energy, BE is the binding energy, $h\nu$ is the energy of the impinging x-ray, and ϕ is the work function of the spectrometer, we may determine the binding energy of emitted electrons. The binding energy differs for electrons from each element, and from the different electron orbitals. XPS exploits this difference to observe elemental composition of the sample. Additionally, the binding energy is sensitive to chemical bonding, which yields small shifts in the binding energy; the use of appropriate atomic sensitivity factors permits quantification of bonds, allowing for the development of an empirical formula of the material [8].

Soft x-rays provide energy suitable for XPS analysis. In the laboratory setting, sources are generally Al Kα (1486.6 eV) or Mg Kα (1253.6 eV). These sources have a somewhat broad energy width (on the order of >1 eV), which lowers resolution; the use of monochromated Al Kα

(1486.7 eV) provides narrower excitation lines and enhanced resolution. Synchrotrons provide tunable, monochromatic sources of x-rays with much higher intensity and narrow linewidth. With a tunable range, the energy of the x-rays may be lowered considerably, which increases the interaction cross-section with the material and yields a better signal-to-noise ratio. The escape depth of such soft electrons is extremely short – on the order of 10 nm or less, depending on the angle of takeoff, which makes this technique extremely surface sensitive.

3.2.2 Methods employed

In this work, we employed a VG Scientific ESCA-3 x-ray spectrometer with an Mg source. Later, the x-ray gun was replaced with one from a PHI system, and utilized an Al source. The change of guns led to changes in spot size, working distance, and overall flux, which will account for changes in noise levels in the spectra presented. Spectra were processed in CasaXPS, generally using literature values as inputs for curve fitting parameters.

3.3 NEXAFS spectroscopy

3.3.1 A brief introduction to NEXAFS

Following the elucidation of the electron shell model for atoms by Bohr, X-ray absorption spectroscopy found use in the analysis of matter. In addition to the absorption edge itself, two additional regions were observed: a fine structure near the edge, known as the Kossel structure (as it was first explained in theory by Kossel), and a structure extending well past the edge, known as the Kronig structure (again named for the scientist involved in explaining the theory). The Kronig structure has become better known as extended X-ray absorption fine structure (EXAFS). EXAFS has been used and studied for some time and developed into a powerful technique for the analysis of material structure in the 1970s [9]. More recently, the near edge structural information from this technique has been known as either the X-ray absorption near edge structure (XANES), or near edge X-ray absorption fine structure (NEXAFS), depending on application – XANES is used to describe solids and "bulk" analysis, while NEXAFS is used to describe surface applications of this information. While surface applications of EXAFS do exist (and are referred to as SEXAFS), NEXAFS has come to specifically refer to "K-shell excitation spectra of low-Z molecules adsorbed on surfaces" [10].

Data from the energy region about the ionization edge is collected during EXAFS for all atoms under investigation, but the complexity of this region led to this information being discarded. The exceptions to this were low-Z molecules with binding energies below 750 eV, which was an energy range that could be independently investigated using inner shell electron energy loss spectroscopy (ISEELS) to better understand the nature of absorptions. Through ISEELS, the absorption transitions of gases were readily analyzed, since there was no requirement for synchrotron radiation in order to conduct the experiment. Later applications went on to analyze thin films and surfaces.

Data obtained through ISEELS is generally in excellent agreement with those obtained by NEXAFS, which has provided a useful library of reference spectra for comparison of analytes. With ISEELS and NEXAFS analysis of simple and component molecules [11-14], one can assemble a complete spectral interpretation of a system by using reference spectra to model each component. This so-called "building block method" permits the analysis of increasingly complex systems.

3.3.2 Methods employed

NEXAFS spectroscopy was performed at beamline U7A at the National Synchrotron Light Source at Brookhaven National Laboratory in Upton, NY. Monochromated x-rays were scanned through the binding energy regions of interest to measure absorption. Two detectors were used: the first measured partial electron yield and fluorescence yield with a spot size on the order of 500 x 500 um; the second measured partial electron yield over a very large area (12x15 mm) with 480,000 points in a hyperspectral data format.

3.3.3 Pre- and post-edge correction and normalization in NEXAFS spectroscopy

The spectrum obtained through NEXAFS spectroscopy contains a number of peaks and bands corresponding to electronic absorptions and excitations. In order to obtain more quantifiable information, the spectrum must be corrected and normalized. There are three common aspects to spectral correction: pre-edge subtraction, post-edge normalization, and normalization with respect to the reference intensity.

Pre-edge correction removes the acquired background intensity. We look for a binding energy region below any pre-edge features where the intensity is consistent, and use this to establish a baseline for subtraction. As a result, the intensity of the spectrum just before any pre-edge features is set to zero. Without further normalization, the edge jump height may be used to assess the density of atoms being probed [15]. With a fixed detector bias voltage, an increased edge jump height indicates an increased density of the atom of interest. We will exploit this analysis in the investigation of exposed polymers.

Post-edge correction utilizes an energy region well beyond the edge jump features as a value against which to normalize the spectrum, causing the intensity at higher binding energies to trail off to 1. Dividing the intensity of the spectrum by this higher energy eliminates the effects of atomic density; rather, variations in intensity will now be related to the density of bonding states or orientation effects of the atom in question [15].

NEXAFS spectroscopy requires the use of a synchrotron to produce a coherent beam of x-rays of sufficient intensity and polarization to generate the spectrum. As it is designed, the National Synchrotron Light Source, a second-generation synchrotron, refills its electron storage ring at regular intervals, which is followed by a constant decline in the energy available. By measuring the intensity of the beam with a reference detector (here, a highly transmissive gold mesh), we can normalize the spectrum against the intensity of the beam at each data point, providing accurate spectral information.

3.3.4 Peak fitting in NEXAFS spectroscopy

The peaks in NEXAFS spectroscopy are fit in a similar fashion to those of any other forms of spectroscopy. Gaussian line shapes with flexibly Lorentzian components (producing a Voigt shape) are fit and added to produce the resultant spectrum. The edge jump is accounted for by an arctangent line shape, and subsequently subtracted. The FWHM of π^* peaks fitted in NEXAFS are generally narrow (on the order of 1 eV or less) and limited by the resolution of the monochromator used, while the FWHM of σ^* peaks are much broader, on the order of a few eV [16].

The fit of the background merits additional discussion. This line shape represents the ionization potential of a given molecular bond. However, the ionization potential differs between bonds to different atoms. In a complex polymer system, it is impossible to assign a single ionization value in a spectrum. Unfortunately, given the complexity of the system and its proprietary formulation, it is also impossible to properly assign a weighted number of ionization potentials. Accordingly, we make a best guess in our systems by assigning a single arctan line shape of broader-than-usual FWHM.

3.3.5 Dichroic ratio of polymers by NEXAFS spectroscopy

The dichroic ratio is defined as the ratio of the amount of polarized light absorbed when normal to the surface, versus the amount absorbed when parallel to the surface [17]. In a highly-oriented sample, the absorbance of particular bonds will change relative to the angle of analysis, as the interaction cross-section changes. Dichroic ratio analysis has been commonly used in FTIR and Raman spectroscopy to observe the direction of vibrational modes and thus the orientation of the functional groups of interest. This technique is invaluable for investigations of monolayers and engineered surfaces, as it can provide information on the adhesion of polymers to the substrate, or to the proper orientation of surface moieties where segregation is desired. Orientation information can also be used to evaluate the degradation of polymeric systems due to weathering, exposure, or other causes [18]. In this work, the dichroic ratio was measured using X-rays in NEXAFS spectroscopy, a process which has been employed extensively by others [15, 19-23].

In order to observe the orientation of molecules, the source of light used must be polarized. In vibrational spectroscopy, this is often accomplished by polarizing grid or plate, which offers somewhat polarized transmission at a cost of intensity. At beamline U7A at the National Synchrotron Light Source at Brookhaven National Laboratory (Upton, NY), the incident x-ray beam is approximately 85-90% polarized. Samples are rotated within the plane of incidence with respect to the beam to obtain angular dependence information.

Generally, the formula to calculate the dichroic ratio is given by

$$DR = \frac{I_{90}}{I_0}$$

Equation 3-3 – Dichroic ratio of an ordered polymer analyzed using polarized light.

where I_{90} is the intensity obtained at normal incidence, and I_0 is the intensity obtained from incident light parallel to the surface. Practically speaking, one cannot measure the absorbance parallel to the surface. However, we may extract intensity information in another fashion. The absorbance of an X-ray and subsequent electronic transition to a final orbital state is directly proportional to $\cos^2 \theta$ [10], where θ is the angle between the electric field vector of the incoming radiation and the direction of the final state molecular orbital, or the "direction" of the bond. Trigonometric calculations describe the azimuthal angular dependency of the bond being probed, but given the complexity of the system being analyzed, adequate symmetry is assumed across the large area in order to discount the effect. As a result, for a bond in the plane of the electric field vector, the intensity is simply related to $\cos^2 \theta$. A rigorous derivation of this relation is available by Stohr in [10]. Calculation of the dichroic ratio is performed through a linear fit of the intensity of the relevant peak versus $\cos^2 \theta$ of the angle of incidence, followed by extrapolation of this fit to 0 and 90 degrees, with these intensities used in the standard formula above. The quality of fit may be enhanced by measuring intensity at more angles. Accordingly, several angles are measured, beginning at 90 degrees and reaching as low as is experimentally possible, often a 20 degree glancing angle.

In a highly-oriented system, the absorbance of each peak will be highly dependent on the angle of analysis. In many applications, samples are prepared to produce a specific orientation. Self-assembled monolayers [23-26] and other highly-oriented systems produce a very strong dichroic effect, resulting in relatively large dichroic ratio numbers. A value of 1 indicates a strong orientation normal to the surface, while values approaching -1 suggest a high degree of orientation in the plane of the sample. Values near 0 suggest an isotropic distribution with no order. When dealing with surfaces which are not specifically oriented, values for the dichroic ratio are much smaller. Wallace *et al.* considered a dichroic ratio greater than 0.01 to connote an "ordered" structure in the phenyl rings of polystyrene [27], while Liu *et al.* observed values near 0.2 in the phenyl rings of polystyrene after rubbing with velour (a process which induces surface orientation in polystyrene films) [23].

In smooth, well-ordered systems, the terms in the dichroic ratio may be expanded geometrically to obtain the bond angle of a given molecular orbital. In a rough, heterogeneous system such as a polyurethane topcoat, the definition of surface bond angle measurement loses some meaning, as the value will be dramatically affected by the high degree of isotropy throughout the region of interest. A more useful approach is to gauge the average degree of orientation within a particular region. The samples we have studied consist of long chains polymerized *in situ* to create a material ranging from tens of microns to millimeters in thickness. The direction of polymerization is not controlled, nor are the chains or functionalities deliberately anchored to any surface. With the high degree of randomness inherent in the material, we expect that any observed dichroic ratio will have a fairly low value, indicating a relatively weak trend. It has been reported by Lenhart *et al*. that angle-dependent changes may be on the order of 10-30% of the intensity of the spectrum [15]. When order is imposed on these systems through (*e.g.*) mechanical forces, the effect is observable [23, 27]. By exposing the coating systems to the solvents used in paint stripping, we hope to assess any indications of chain mobility and rearrangement of the polymer due to exposure.

3.4 References

[1] Socrates G. Infrared Characteristic Group Frequencies: Tables and Charts. 2nd ed. Chichester: John Wiley & Sons; 1994.

[2] Tian J, Liu J, He W, Hu Z, Yao X, Chen X. Probing the Binding of Scutellarin to Human Serum Albumin by Circular Dichroism, Fluorescence Spectroscopy, FTIR, and Molecular Modeling Method. Biomacromolecules. 2004;5:1956-61.

[3] Janssen A, Niederer JPM, Hoëlderich WF. Investigation of rhodium complexes in micro- and mesoporous materials by computer modeling, FTIR, and 31P MAS NMR. Catalysis Letters. 1997;48:165-71.

[4] Atkins P, de Paula J. Physical Chemistry. 8th ed. New York: W. H. Freeman and Co.; 2006.

[5] Gauglitz G, Vo-Dinh T. Handbook of Spectroscopy: Wiley; 2006.

[6] Raman CV. A New Radiation. Indian Journal of Physics. 1928;2:387-98.

[7] Ferraro JR. Introductory Raman spectroscopy. 2nd ed. ed. Academic Press: Amsterdam ;; 2003.

[8] Moulder JF, Stickle WF, Sobol PE, Bomben KD. Handbook of X-ray Photoelectron Spectroscopy. 2nd ed. Eden Prairie, MN, USA: Physical Electronics, Inc.; 1995.

[9] Teo BK, Joy DC. EXAFS spectroscopy, techniques and applications. Plenum Press: New York; 1981.

[10] Stöhr J. NEXAFS Spectroscopy: Springer; 1992.

[11] Francis JT, Hitchcock AP. Inner-shell spectroscopy of p-benzoquinone, hydroquinone, and phenol: distinguishing quinoid and benzenoid structures. The Journal of Physical Chemistry. 1992;96:6598-610.

[12] Tinone MCK, Tanaka K, Maruyama J, Ueno N, Imamura M, Matsubayashi N. Inner-shell excitation and site specific fragmentation of poly(methylmethacrylate) thin film. The Journal of Chemical Physics. 1994;100:5988-95.

[13] Urquhart SG, Smith AP, Ade HW, Hitchcock AP, Rightor EG, Lidy W. Near-Edge X-ray Absorption Fine Structure Spectroscopy of MDI and TDI Polyurethane Polymers. The Journal of Physical Chemistry B. 1999;103:4603-10.

[14] Dhez O, Ade H, Urquhart SG. Calibrated NEXAFS spectra of some common polymers. Journal of Electron Spectroscopy and Related Phenomena. 2003;128:85-96.

[15] Lenhart JL, Fischer DA, Chantawansri TL, Andzelm JW. Surface Orientation of Polystyrene Based Polymers: Steric Effects from Pendant Groups on the Phenyl Ring. Langmuir. 2012;28:15713-24.

[16] Lam RSK, Metzler RA, Gilbert PUPA, Beniash E. Anisotropy of Chemical Bonds in Collagen Molecules Studied by X-ray Absorption Near-Edge Structure (XANES) Spectroscopy. ACS Chemical Biology. 2011;7:476-80.

[17] Nishikida K, Nishio E, Hannah RW. Selected Applications of Modern Ft-Ir Techniques: Kodansha and Gordon and Breach; 1995.

[18] White JR, Turnbull A. Weathering of polymers: mechanisms of degradation and stabilization, testing strategies and modeling. Journal of Materials Science. 1994;29:584-613.

[19] Klein RJ, Fischer DA, Lenhart JL. Thermal and Mechanical Aging of Self-Assembled Monolayers as Studied by Near Edge X-ray Absorption Fine Structure. Langmuir. 2011;27:12423-33.

[20] Holch F. Investigation of Intermolecular Interaction in Organic Thin Films by means of NEXAFS Spectroscopy. Wurzburg: Julius–Maximilians Universität Würzburg; 2009.

[21] Hemraj-Benny T, Banerjee S, Sambasivan S, Balasubramanian M, Fischer DA, Eres G, et al. Near-Edge X-ray Absorption Fine Structure Spectroscopy as a Tool for Investigating Nanomaterials. Small. 2006;2:26-35.

[22] Scholl A, Fink R, Umbach E, Mitchell GE, Urquhart SG, Ade H. Towards a detailed understanding of the NEXAFS spectra of bulk polyethylene copolymers and related alkanes. Chemical Physics Letters. 2003;370:834-41.

[23] Liu Y, Russell TP, Samant MG, Stöhr J, Brown HR, Cossy-Favre A, et al. Surface Relaxations in Polymers. Macromolecules. 1997;30:7768-71.

[24] Cerruti M, Rhodes C, Losego M, Efremenko A, Maria J-P, Fischer D, et al. Influence of indium–tin oxide surface structure on the ordering and coverage of carboxylic acid and thiol monolayers. Journal of Physics D: Applied Physics. 2007;40:4212.

[25] Li Z, Zhang L, Resasco DE, Mun BS, Requejo FG. Angle-resolved x-ray absorption near edge structure study of vertically aligned single-walled carbon nanotubes. Applied Physics Letters. 2007;90:103115-3.

[26] Banerjee S, Hemraj-Benny T, Sambasivan S, Fischer DA, Misewich JA, Wong SS. Near-Edge X-ray Absorption Fine Structure Investigations of Order in Carbon Nanotube-Based Systems†. The Journal of Physical Chemistry B. 2005;109:8489-95.

[27] Wallace WE, Fischer DA, Efimenko K, Wu W-L, Genzer J. Polymer Chain Relaxation: Surface Outpaces Bulk. Macromolecules. 2001;34:5081-2.

Chapter 4: Carbon Fiber Sizing Analysis

4.1 Introduction

Sizing is a low-concentration polymer dispersion applied to fibers used in composites in order to facilitate interfacial interactions between the fiber and polymer matrix. In this work, we will examine the chemistry and durability of the fiber sizing used on Toray T700 fibers for vinyl ester composites, which is a proprietary polymer system coded as system “F.” A survey of patent literature indicates that common components in carbon fiber sizings by this manufacturer have been disclosed as consisting of polyoxyalkylenes, esters, and urethanes, in some varied combinations of concentration [1, 2]. This provides a starting point from which to begin our investigation of the sizing. From an outside perspective, one might expect such a material to be more strongly attached to both the fiber and sizing, in order to improve the interfacial properties; indeed, more specialized treatments exist which react with both fiber and matrix , serving as heterobifunctional cross-linkers between the two which have been shown to outperform the standard fiber treatment in our system of interest [3-5]. In this literature, it has been determined that Toray sizing F is not a reactive finish.

From the same work by Allred, we know that Toray F is readily extracted through the use of boiling chloroform, suggesting that it may be vulnerable to other organic solvents as well. Chloroform is a proven solvent, but its relatively high boiling point (61.2 °C) could require a process which leads to thermal damage of the sizing, which we must avoid. Accordingly, we have sought a solvent with similar capabilities for dissolution of organic molecules but at a lower temperature – methylene chloride (with a boiling point of 39.2 °C) met these requirements.

4.2 Materials and methods

The sizing of interest comes from Toray T700 carbon fibers coated with system F sizing, which is designed for compatibility with Derakane MOMENTUM 411-350 vinyl ester resin. The sizing was extracted using the Soxhlet warm solvent reflux method, which gently removes soluble components by evaporating and condensing the solvent over the solid sample several times. Several grams of carbon fiber were placed in the extractor and refluxed for up to 12 h with methylene chloride to ensure maximum sizing removal. The sizing-rich solvent was then pipetted onto an appropriate substrate and allowed to dry, in order to cast a thin sizing film for analysis.

The coating was analyzed using Raman and FTIR microspectroscopy. Raman analysis was conducted using the Thermo Nicolet Almega Raman microscope at 10x magnification using 532 nm and 785 nm lasers for excitation. FTIR microspectroscopy was conducted using the Thermo Nicolet Magna 560 FTIR spectrometer coupled to the Continuum microscope, with a 15x objective in specular reflectance mode. Sized and unsized fibers were analyzed using a VG ESCA-3 XPS system, with a pass energy of 50 eV. Sizing samples were placed in a Q-Panel Q-Sun 1000 accelerated weathering chamber for 500h, with intensity set at 0.7 W/m^2 at 340 nm, to simulate noontime exposure in the northern hemisphere.

4.3 Results

4.3.1 Neat sizing

The Raman spectrum of neat, as-deposited sizing (532 nm excitation) is shown in Figure 4-1. A few characteristic peaks are evident. A peak at 1442 cm^{-1} indicates the presence of CH_2 scissoring, while the peak at 1302 cm^{-1} indicates CH_2 twisting, thus suggesting a polymer chain. A small peak is visible at 1653 cm^{-1}, which suggests a C=C arrangement in fairly low molar quantity. The Raman spectrum obtained using 785 nm excitation is shown in Figure 4-2. A peak is present at 1723 cm^{-1}, indicating a likely ester carbonyl; additional peaks between 1050 and 1250 cm^{-1}corroborate an ester determination. The peaks at 1640 and 1610 cm^{-1} represent non-aromatic C=C. Overlaid in this figure is the spectrum of resin, which bears a number of similarities to the sizing. Noteworthy differences include the presence of aromatic CH at 3060 cm^{-1}, and a very strong ring breathing mode around 1000 cm^{-1}. In order to investigate the sizing/matrix interphase region, it must be possible to differentiate between the two components. As can be seen in this image, there is a great deal of similarity of functional groups between the sizing and resin, which would complicate Raman analysis. However, the urethane linkage employed in this sizing offers discernible evidence for interphase analysis.

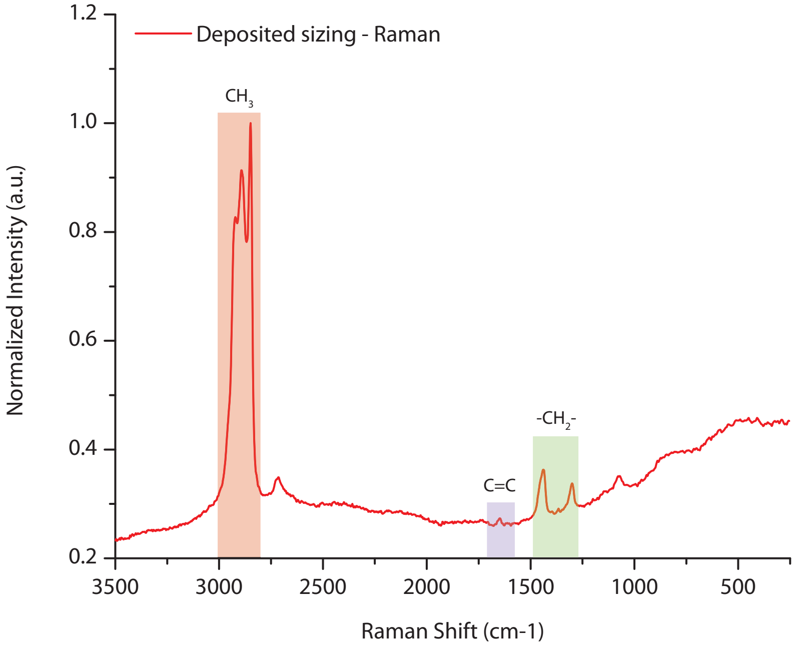

Figure 4-1 – Raman spectrum of extracted and deposited sizing F from T700 carbon fibers, with 532 nm laser excitation.

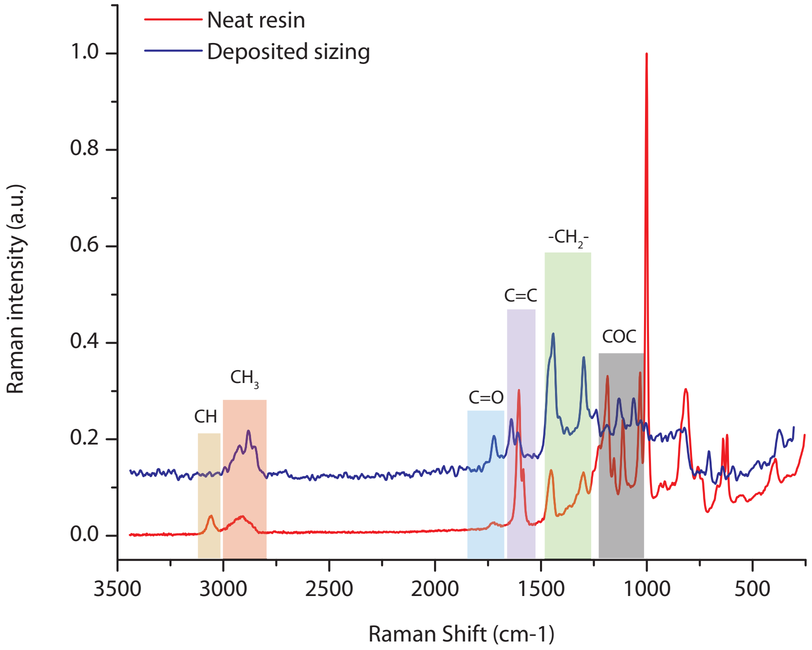

Figure 4-2 – Raman spectrum of deposited sizing and neat VE resin, 785nm excitation.

The FTIR spectrum of sizing is presented in Figure 4-3. A major peak at 1737 cm^{-1} indicates an ester carbonyl with only a low degree of hydrogen bonding (based on the width of the peak on the lower-wavenumber side), while the peaks located between 1050 and 1250 cm^{-1} represent C-O-C stretching. Relatively strong absorbance around 1465 cm^{-1} confirms the presence of substantial CH_2 seen in Raman. The trio of peaks at 1515, 1530, and 1550 cm^{-1} indicate Amide II. The lack of peaks in the C-H range just above 3000 cm^{-1} eliminates the possibility of an aromatic compound. A peak at 3365 cm^{-1} indicates an N-H stretch. Sharp peaks at 2855 and 2920 cm^{-1} indicate the well-defined presence of CH_2 stretches, again suggestive of a long chain, while the shoulder peak at 2955 cm^{-1} indicates CH_3 end groups, suggesting a branched polymer. Peaks at 1326 and 1027 cm^{-1} indicate symmetric and asymmetric C-O vibrations.

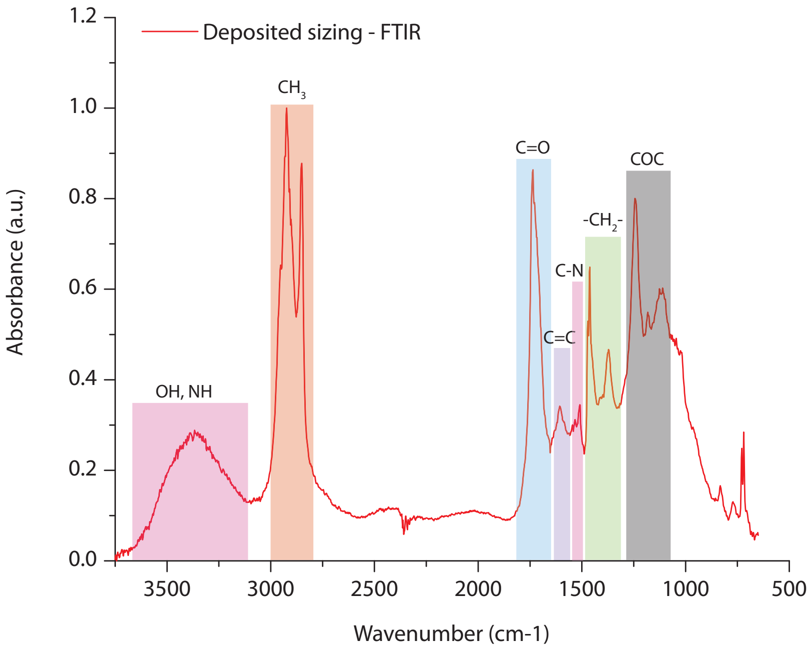

Figure 4-3 – FTIR reflection mode spectrum of deposited sizing.

XPS spectra with peak fits are presented in Figure 4-4. The vibrations seen above, particularly by FTIR, are well-represented in the x-ray data. C1s data shows a majority of C-C/C-H moieties, with the addition of **C**-O and O-**C**=O functionalities, while O1s confirms these fits with **O**-C and **O**-C=O. The N1s spectrum fits a single, relatively weak peak for **N**-H. These spectra are in excellent agreement with the vibrational results.

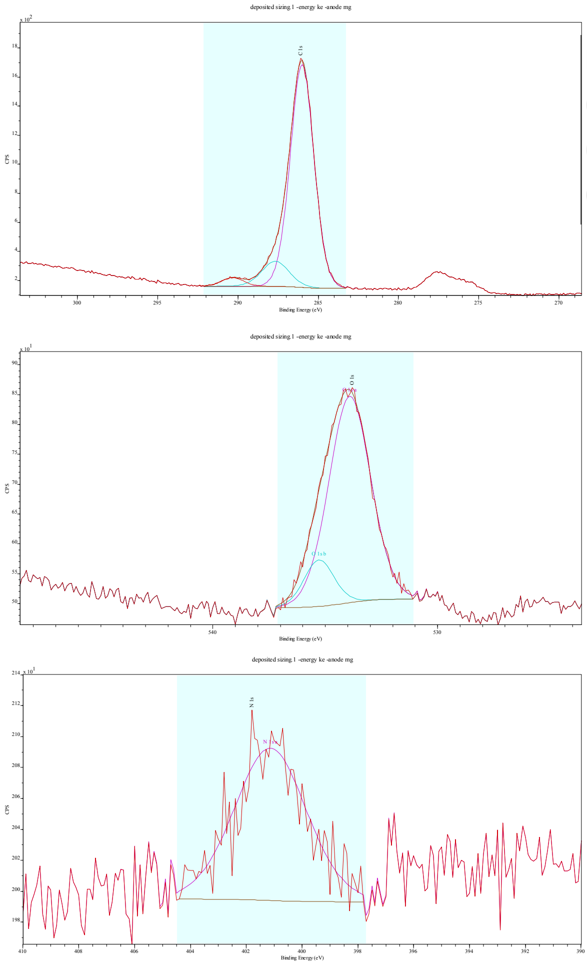

Fit	Label	Uncal. eV	At. %	Cal. eV
C-C	**C1s a**	286	85.61%	284.5
C-O	**C1s b**	287.67	11.32%	286.2
O=C-O	**C1s c**	290.33	3.07%	288.8

Fit	Label	Uncal. eV	At. %	Cal. eV
C-O	**O1s a**	533.92	85.92%	532.4
O=C-O	**O1s b**	535.28	14.08%	533.8

Fit	Label	Uncal. eV	At. %	Cal. eV
-NH-	**N1s a**	400.92	100%	399.4

Figure 4-4 – XPS spectra with curve fits and peak assignments for deposited sizing.

Considering the peak assignments above, it is reasonable to conclude that the sizing seen here is not dissimilar to those described in patent literature, with segments consisting largely of CH_2, C-O-C, and C=O, with a urethane conformation, combined with a branched structure containing methyl end groups. While a complete structural determination cannot readily be made without NMR, we have defined several the functional groups present. This provides us with appropriate perspective to evaluate the durability of the material.

4.3.2 Sized and desized fibers

A comparison of sized and desized fibers under XPS analysis is presented in Figure 4-5. The changes seen in the spectrum provide additional confirmation of the successful removal of the sizing, and are in agreement with the fits above. Following removal of the sizing, the C1s spectrum shows significant narrowing corresponding to a decrease in **C**-O compared to **C**-C/**C**=C, and a decrease in the second peak indicative of carbonyl functionality. O1s shows a corresponding change as well, plus the addition of a new peak due to the indium foil used for sample mounting, which was unfortunately exposed during analysis. The loss in the N1s peak shows that some residual nitrogen remains at the surface of the fiber from the manufacturing process, but is ordinarily covered by sizing. From these spectra, we may conclude that the sizing has been fully removed and redeposited.

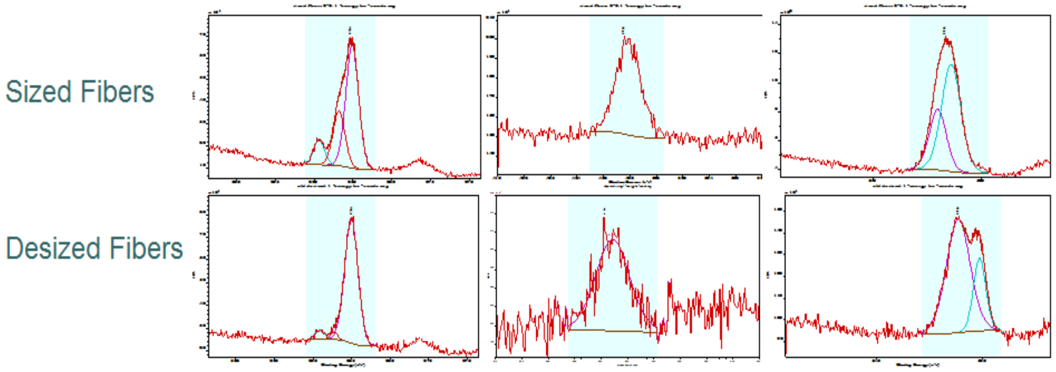

Figure 4-5 – XPS spectra of sized and unsized fibers focusing on C1s (left), N1s (center), and O1s (right).

4.3.3 UV-damaged sizing

Given the general chemistry of the sizing, we may expect photodegradation to especially impact the urethane linkage, based on the literature [6-8]. In Figure 4-6, we show the FTIR spectrum of sizing after UV exposure. There have been significant changes to the material after just 500 hours of exposure. First and foremost, the majority of the spectrum shows significantly reduced intensity compared to the peaks for CH_2 at 2925 and 2850 cm^{-1}, possibly due to a phase change. With extensive UV exposure at relatively high temperatures (60 °C), it is not impossible that the sizing would begin curing. This further suggests that in addition to the sizing molecule itself, there are other components to the sizing which are more resilient to irradiation. The literature referenced above does suggest that a sizing may consist of several components in combination. If this is the case, then we will be unable to differentiate the vulnerable aspects of this molecule from those others present in the sizing, leading us to consider everything as a single system. It may also be that the chain length of methylene repeats in the polymer is very high, leading to a less-constrained system spectroscopically. Further investigation of the extracted sizing via chromatography and NMR would be required to make these distinctions.

Given the complexity of the system, it is best to draw attention to the appreciable differences which we observe after exposure. The peak at 2960 cm^{-1} for CH_3 end groups is significantly depleted, suggesting that the branched nature of the polymer may have been damaged. The ratio of free to hydrogen-bound carbonyl functionalities (at 1743 and 1717 cm^{-1}, respectively) decreases, indicating more extensive hydrogen bonding as a result of crosslinking. The primary peak for Amide II at 1515 cm^{-1} also shows strong depletion. Taken together, these latter two changes suggest cleavage of the observed urethane, accompanied by increased hydrogen-bonding and chain crosslinking. Other works have shown the high susceptibility of Amide II to UV-induced cleavage [7].

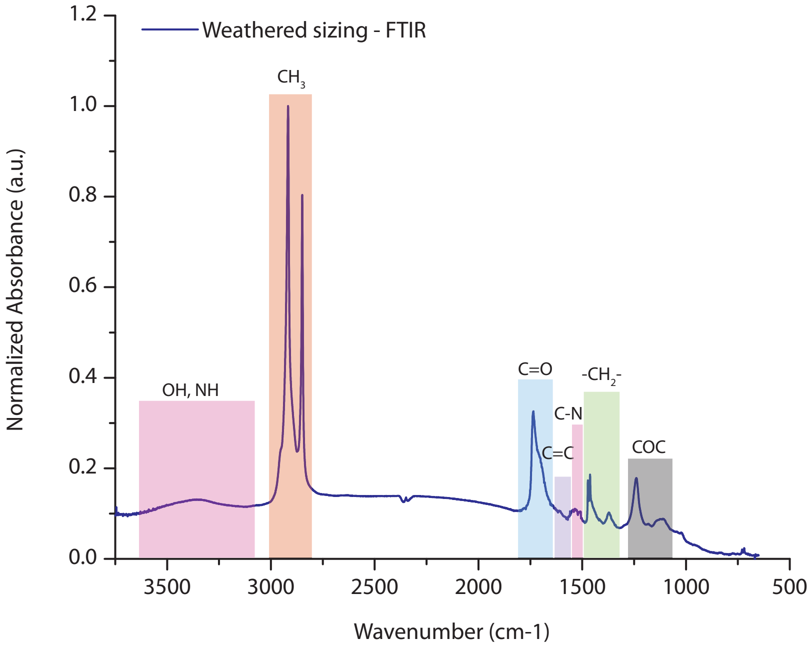

Figure 4-6 – FTIR spectrum of sizing following 500h of simulated sunlight exposure.

4.3.4 Ablated sizing

As a companion to Chapter 4, it is worthwhile to discuss the characteristics of deposited sizing following ultrafast laser ablation. This spectrum is shown in Figure 4-7. While highly similar to the neat sizing overall, there are some small but important changes. First, there is a peak evolution at 1580 and 1610 cm^{-1}, indicating graphitic and aromatic rings, a hallmark of thermal damage. Next, the peaks at 1530 and 1550 cm^{-1} are depleted, indicating some damage to the Amide II residue. The overall magnitudes of these changes are small, suggesting a highly surface effect (thus offering a proportionally small contribution to the overall spectrum). There is also an overall drop in intensity of the carbonyl, with a comparable increase in C-O-C, suggesting breakdown of the conjugated bond. The effects of ablation are not insignificant on the chemistry of the sizing.

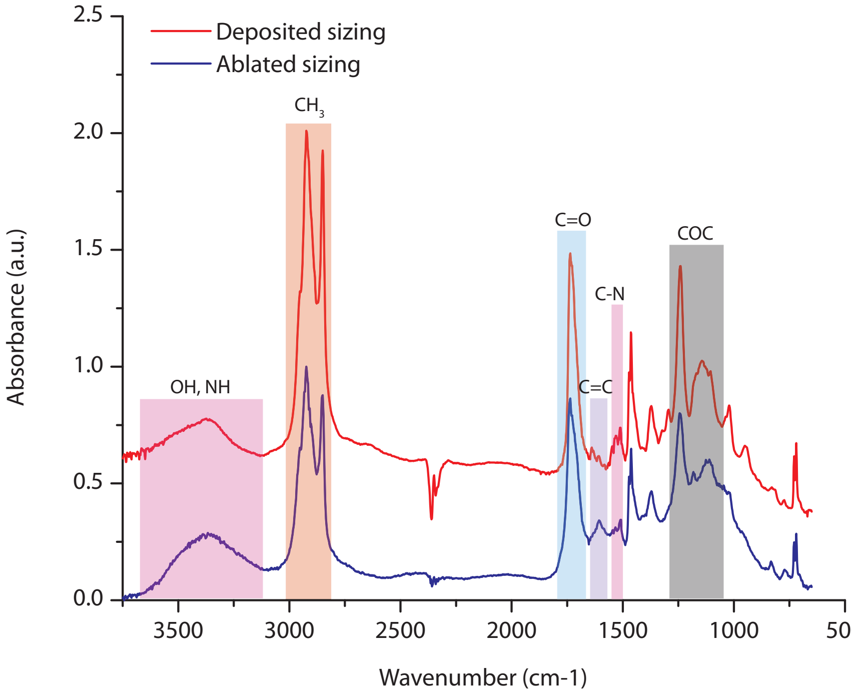

Figure 4-7 – FTIR spectra of sizing before and after ultrafast laser ablation (50mW, 3 pulses).

4.4 Conclusions

Investigation of the sizing material used for vinyl ester compatibility on Toray T700 fibers has revealed a number of vulnerabilities. The fiber sizing appears susceptible to premature curing, which would reduce its effectiveness at improving interfacial qualities. The chemistry of the sizing also contains numerous conjugated bonds, which are vulnerable to photodegradation after short time spans in inadequately-protected composites. The sizing may also be removed from the composite fairly readily using methylene chloride, a primary component in paint remover; as such, while a coating may shield the sizing material from UV radiation, solvent penetration when that coating is removed will also threaten the integrity of the composite.

4.5 References

[1] Hirano N, Tsuchiya A, Honma M. Carbon fiber bundles containing water-soluble polyurethane sizing agents. Toray Industries, Inc., Japan . 2011. p. 71pp.

[2] Saito M, Miyazaki M, Inoue H. Carbon fibers sized with a sizing agent for reinforcing plastics. Tonen Co., Ltd., Japan . 1991. p. 12 pp.

[3] Allred RE, Hoyt Haight AE, Gosau JM, Wesson SP. Aqueous-based emulsion reactive finishes for improving carbon/vinyl ester interfacial bonding. International SAMPE Symposium and Exhibition. 2005;50:741-56.

[4] Allred RE, Wesson SP, Hoyt Haight AE, Whitehead JW. Reactive finishes for improved interfacial properties in carbon/vinyl ester laminates. International SAMPE Symposium and Exhibition. 2004;49:2059-72.

[5] Allred RE, Wesson SP, Shin EE, Inghram L, McCorkle L, Papadopoulos D, et al. The influence of sizings on the durability of high-temperature polymer composites. High Performance Polymers. 2003;15:395-419.

[6] Keene LT, Vasquez MJ, Clayton CR, Halada GP. Failure of navy coating systems 2: failure pathways of artificially weathered navy coating systems applied to chromate conversion coated AA2024-T3 substrates. Progress in Organic Coatings. 2005;52:187-95.

[7] Keene LT, Halada GP, Clayton CR. Failure of navy coating systems 1: chemical depth profiling of artificially and naturally weathered high-solids aliphatic poly(ester-urethane) military coating systems. Progress in Organic Coatings. 2005;52:173-86.

[8] Hare CH. Paint Film Degradation: Mechanisms and Control. Pittsburgh: SSPC: The Society for Protective Coatings; 2001.

Chapter 5: Femtosecond Ablation of Carbon Fiber Composite Materials

5.1 Introduction

Lasers have been employed as a means of material preparation for some time, given their ability to execute a high precision cut through a variety of materials. Such lasers operate at long pulse durations (or continuous wave) and function by a photothermal process, leading to the melting and vaporization of material [1, 2]. While these lasers perform adequately in homogenous systems, composite materials present additional challenges due to significant differences in the thermal ablation threshold of materials [3, 4]. This often results in poor quality effects at the ablation site, and extensive thermal damage to the material in the vicinity. A somewhat more recent development is that of ultrafast lasers, with pulse durations on the order of femtoseconds. This ultrashort pulse results in rapid ionization of the impacted material, followed by avalanche ionization and subsequent electrostatic removal of this ionized material [5]. The upshot of this is the controlled removal of a small volume of material per laser pulse, with (theoretically) no thermal damage to the surrounding regions; the total duration of the pulse is short relative to the electron-phonon interaction time, thus minimizing any thermal interactions [6]. This technique has previously been used in depth profiling coatings in this laboratory [7].

Numerous morphological changes have been described in a range of samples subject to femtosecond ablation. The formation of periodic surface structures is common in semiconductors, polymers, and metals [8-12]. While studies have focused predominantly on pure materials, difficulties in the machining of composites has also been revealed, owing to a general mismatch in the ablation threshold of components [13]. Although such challenges exist for some systems, many polymeric systems have been shown to be well-suited to micromachining by ultrafast ablation [10, 14-16]. The excellent repeatability of processing is highly desirable for microchannels and micro-patterning [17-20].

While the ablation characteristics of individual polymers and likely fillers (such as graphite) [21-24] have been investigated, the area of femtosecond ablation as it pertains to composite materials has received only minor attention [7, 13]. The ability to machine such composites at high precision without deleterious effects to integrity or durability would be of great utility in the design of military systems. Furthermore, given the ability to remove extremely small amounts of material per pulse at low fluences [25], the technique could be adapted to the study of nano-scale interphase regions, such as those found in composites between fiber sizing and matrix resin [26].

5.2 Materials and methods

5.2.1 Sample materials

Samples were produced using Derakane MOMENTUM 411-350 vinyl ester resin in a VARTM system, with appropriate promoters as per the manufacturer's instructions. Samples were then cured for 2 h at 120 °C to fully harden. Toray T700 carbon fibers sized with system "F0E" were used in composite samples; this sizing is designed to maximize compatibility with vinyl ester resins. Some samples were exposed to artificial sunlight in a Q-Panel Q-Sun 1000 chamber, with a radiation intensity of 0.7W/m^2 at 340nm, simulating summer noontime sunlight, for 1000 hours; it has been noted elsewhere [27] that the effects of ultraviolet radiation have an observable effect on the IR spectra of BPA-based polycarbonate materials after just 400h. Other samples were heated in a furnace at temperatures ranging from 190 °C to 250 °C for 15, 30 and 60 minutes; all temperatures are well in excess of the cured resin T_g = 120 °C.

5.2.2 Laser ablation

Ablation was performed using a Spectra-Physics Spitfire Pro Ti:Sapphire CPA laser system, with a pulse duration of 130 fs at λ = 800 nm and ν = 1000 Hz, providing a horizontally-polarized beam with Gaussian line shape. Utilizing a focusing lens of f = 400 mm, a spot size ($1/e^2$) of 40 μm was achieved with a Rayleigh range of 3mm, thus minimizing the effect of the change in focus as the distance to the sample increases with surface ablation. Pulse energy and number were varied to evaluate the ablation rate and threshold of samples.

5.2.3 Materials characterization

Spectroscopic analysis was performed using a Nicolet Almega dispersive Raman spectrometer with 785nm excitation laser and 10x and 100x objective lenses; and a Nicolet Magna 560 FTIR spectrometer with 15x Reflachromat objective and micro-ATR attachments. Further analysis was performed using a WiTec α-500 confocal Raman spectrometer with 532nm excitation source and 20x and 100x objective lenses. AFM analysis was performed in semi-contact mode to measure height and roughness at the site of ablation. Confocal laser microscopy was performed using a Leica TCS SP2, with excitation at 488 nm. Scanning electron microscopy was performed using a FEI LEO SEM equipped with a backscatter detector. Ablation depth was measured using a custom laser profilometer coupled to a 2-axis motion stage with software collecting data points every 2.5 μm of motion.

NEXAFS spectroscopic analysis was performed on beamline U7A at the National Synchrotron Light Source at Brookhaven National Laboratory. A grid bias voltage of 150V was used for surface sensitivity, with a spot size of less than 1 mm^2. Spectra were subsequently pre/post-edge normalized prior to curve fitting and analysis. Additional analysis was performed using the large-area LARIAT detector at this beamline, permitting hyperspectral acquisition of a large area sample (13 x 18 mm), with comparable post-processing.

5.3 Results

5.3.1 Laser ablation of neat resin

Unexposed vinyl ester resin provides a point of reference for evaluating the effects of simulated sunlight or thermal exposure on the ablation rate, as well as establishing a rate of ablation for composites. Figure 5-1 illustrates the effects of ablation on neat vinyl ester resin. Heterogeneous roughness is apparent at the site of ablation, which is detailed in the inset photo. Larger voids in the material, present as a result of the curing process, cause minor variations in the geometry of the ablated surface. Increasing the number of pulses leads to a visible increase in ablation depth. Ablation sites measure approximately 40 μm in diameter, which is consistent with the pre-determined beam size at the focal point.

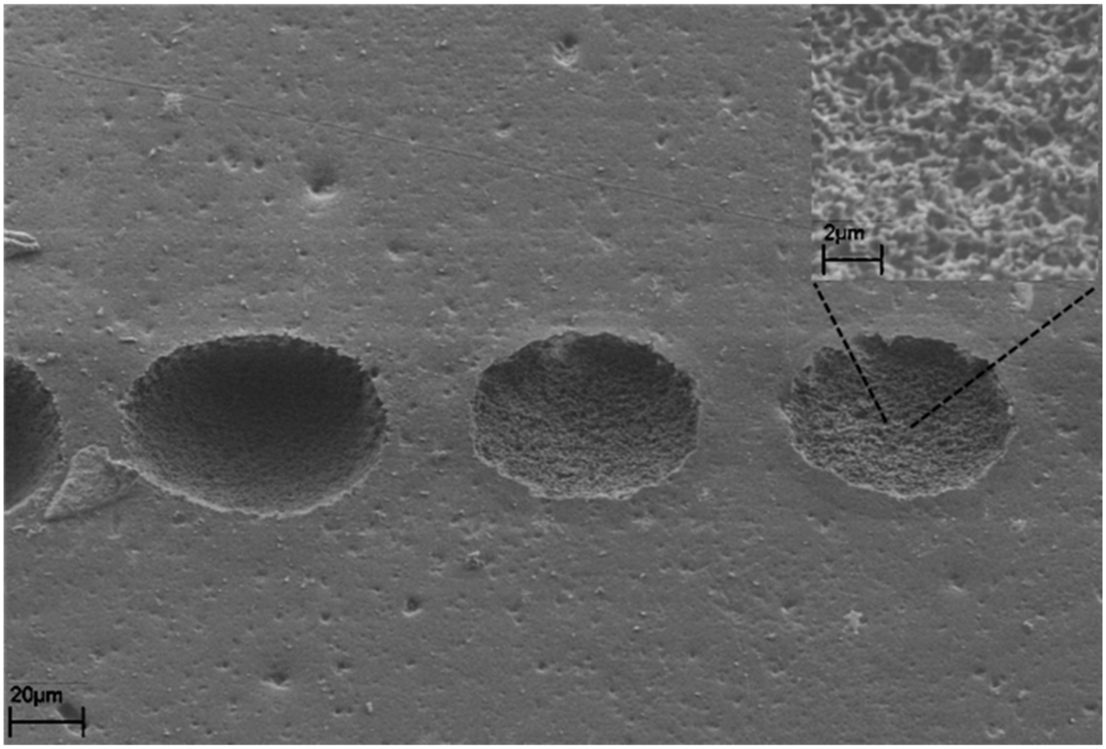

Figure 5-1 – SEM image of neat vinyl ester resin, ablated with (left to right) 32, 16, and 12 pulses at 100mW. Inset top right: magnified detailed view of the surface of a pit following ablation.

Texturing has been observed in ablated polymer systems elsewhere, both ordered [11] and non-ordered [28] in nature. Figure 5-2 presents a topographic image of an ablation site obtained by AFM. Over a large area (20 x 20 µm, approximately half the area of the ablation site) the ablation depth is fairly consistent, with pockets of variation attributable to pre-existing voids and imperfections in the sample. Analysis of a smaller area (5 x 5 µm) shows nano-scale roughness (on the order of 100 nm) in the porous structures seen remaining after ablation. This nano-rough texture appears consistently when material is ablated, regardless of fluence. As the number of pulses increases, the appearance of elevation at the edge of the crater develops, which has been observed in silicon to be caused by pressure shockwaves due to ablation [29].

In addition to nano-texturing, the floor of the crater also shows evidence of larger pores. The presence of these pores in the neat resin is significant, as they will likely translate to the composite material. Generally speaking, such pores will be filled with unreacted volatile organics, which are liberated when the pore is opened. Should these pores form at or near the interface of a fiber in the full composite, the interfacial adhesion will be weakened, and the pores will create a vulnerable location for mechanical failure.

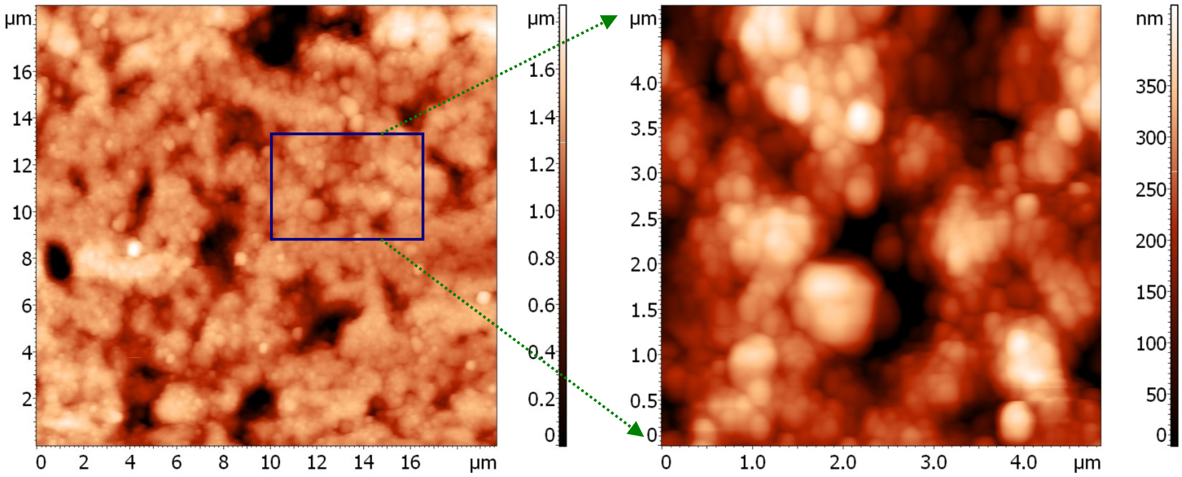

Figure 5-2 – (left) AFM tapping-mode surface map of ablated resin. (right) A higher-resolution image of the selected region.

In Figure 5-3, a comparison of ablation depths relative to the number of pulses applied at a selection of pulse energies is shown. Given the diameter of the focal region of the beam, and the corresponding diameter of the craters, these energies range from 1.592 to 7.962 J/cm^2. The depth of ablation increases in a linear fashion through this energy range, which is expected in the ablation of polymers [30], and for energies of this magnitude. The etch rate per pulse appears to remain roughly constant at higher energies, but demonstrates a reduced rate with increasing pulses at the highest energy. Ablation was not observed to occur (through SEM inspection, at any pulse count up to 256) at any tested energy below 20 µJ/pulse, which is accounted for by the poor absorbance of this material at the wavelength of the laser and the resulting impact on ablation threshold [4]. Exposure to UV radiation does not appear to impact the ablation rate, demonstrating the independence of ablation from sample chemistry. The absorbance of the resin at the wavelength of the laser is not expected to increase with exposure, which is in agreement with this outcome.

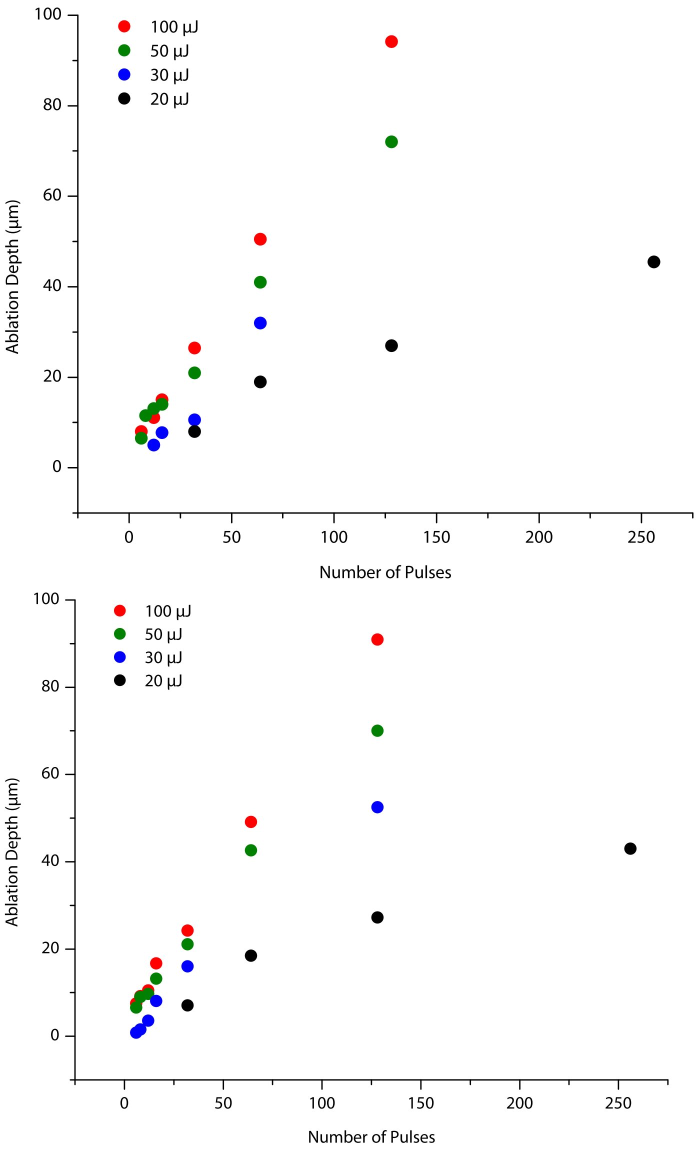

Figure 5-3 – Ablation depth as a function of number of pulses at different pulse energies for neat resin (top) and UV1000 resin (bottom).

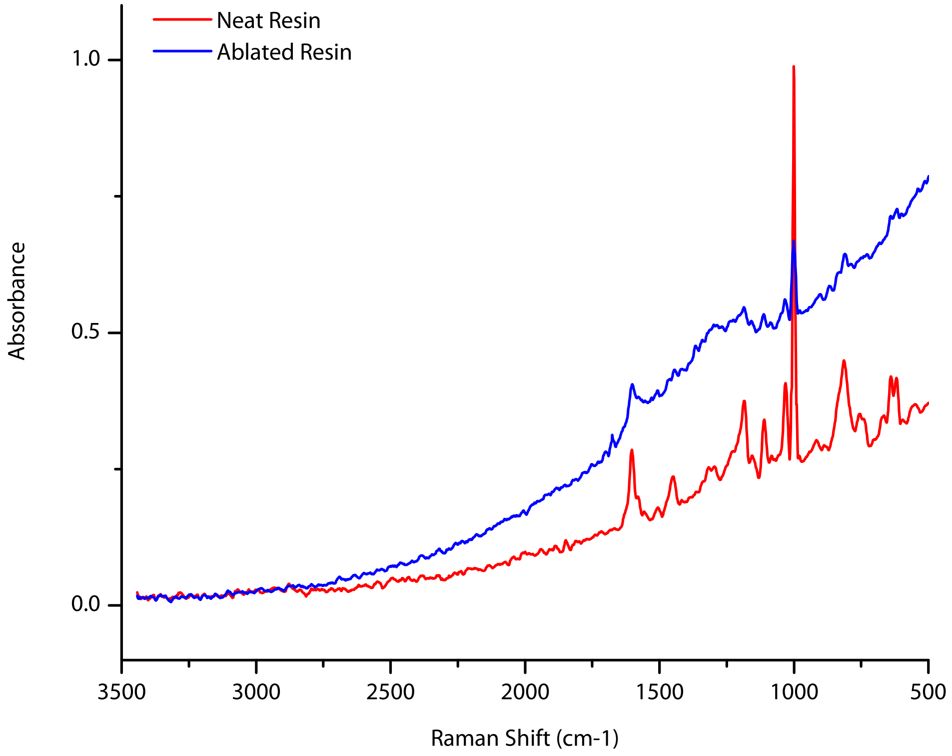

Figure 5-4 – Raman spectra of neat and ablated vinyl ester resin.

Chemical analysis of the ablated resin region was performed at a variety of depths of analysis. In Figure 5-4, the Raman spectra of the resin both before and after ablation are presented. Ablation serves to dramatically increase the degree of fluorescence in the spectrum. This fluorescence masks the intensity of the normal spectral features, but it is clear that there has been no effect on the peak positions as a result of ablation. The fluorescence effect is not expected for a purely athermal mechanism that produces no chemical change in the material.

For this technique to be useful in chemical depth profiling, it must demonstrate consistent ablation without alteration of the chemical composition. In Figure 5-5, ATR-FTIR spectra were taken in UV-exposed vinyl ester samples before and after ablation. There is a single noticeable change in the spectrum, showing a change in the height of a shoulder near 800 cm^{-1}; however, this shoulder change aligns with material undamaged by UV; the laser has removed the degraded material from the surface, exposing the pristine material beneath. To provide context, both Raman and ATR-FTIR techniques may have somewhat controllable depths of analyses, but these do not reach below 2 µm in our configurations. The electron escape depth for NEXAFS is on the order of a few nm [31], yielding an extremely surface-sensitive analysis which would not be detected with vibrational spectroscopic methods.

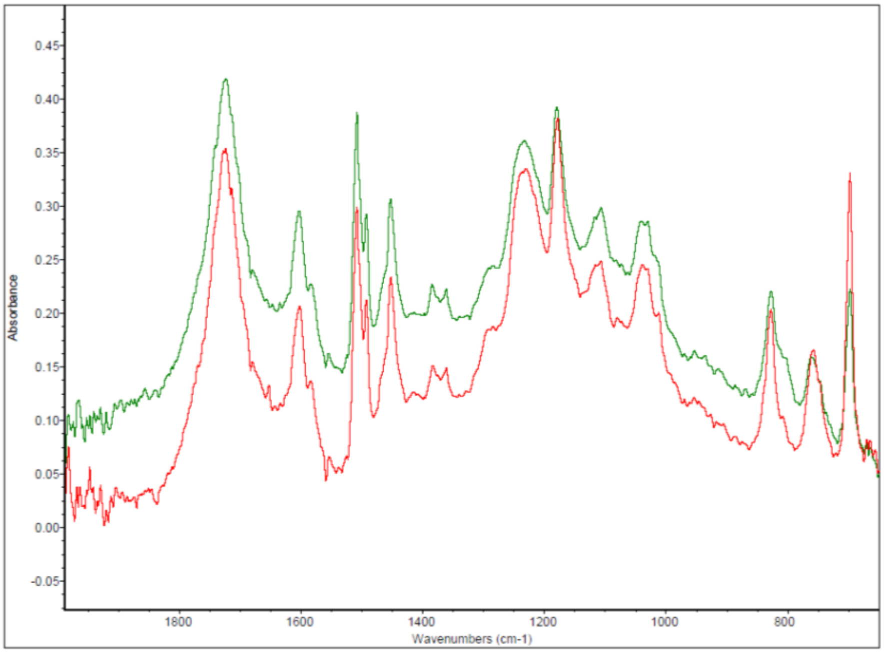

Figure 5-5 – ATR-FTIR of resin with 500 h UV, before ablation (red) and after 3-pulse ablation 50 mW (green).

In Figure 5-6, we present NEXAFS spectra from the undamaged resin system before and after ablation, wherein the laser was rastered across the surface with a spacing of slightly less than the diameter of ablation. The ablated region shows clear deviation from the unexposed region. There is a significant increase in the quantity of C=C (the peaks at ~285 eV) at the surface, and a decrease in the amount of C=O (the curve fit at 288.8 eV) relative to the adjacent features. The explanation is the deposition or formation of aromatic carbon molecules at the surface of the material. Each option leads to an intriguing implication.

The vinyl ester resin material is formed by the crosslinking of a bisphenol-based vinyl ester unit with an excess of styrene monomers. As a result, there is a substantial quantity of residual styrene remaining in the material after curing [32, 33]. The mobility of this styrene is extremely limited by the nature of the cross-linked network, yielding excellent retention. In thermally damaged samples (addressed in Chapter 5), the concentration of surface styrene is observed to increase through the use of NEXAFS, suggesting that the outgassed material re-deposits at the surface during thermal exposure. It is possible that a similar effect is seen here, where ablation leads to the rapid liberation of monomeric styrene trapped in the matrix and in observed pores, with subsequent deposition at the surface.

A second option is that the laser is creating aromatic carbon structures through material ejection, which deposit at the surface and at the edge of the crater. To support this point, the reader is referred to Figure 5-7, where we show the fluorescence image of an ablated region at the surface. In the shallowest ablation pit at right, there is some increase in fluorescence seen on the floor of the crater. We have discussed a relationship between thermal damage and fluorescence in Chapter 5, and literature cited therein links fluorescence to the presence of conjugated bonds (such as aromatic carbon or carbonyls), which would be present in the case of styrene. Around each pit, and with increasing intensity as the number of pulses increases (right to left), there is a narrow right of very high fluorescence at the rim of the crater, with some relatively large individual particles. This suggests that ejected material has been chemically modified in some way which results in increased fluorescence. There may be a secondary process occurring after ablation which produces these changes, but no chemical information on this debris is available – the area is too small for x-ray analysis, and the layer is too thin for vibrational analysis.

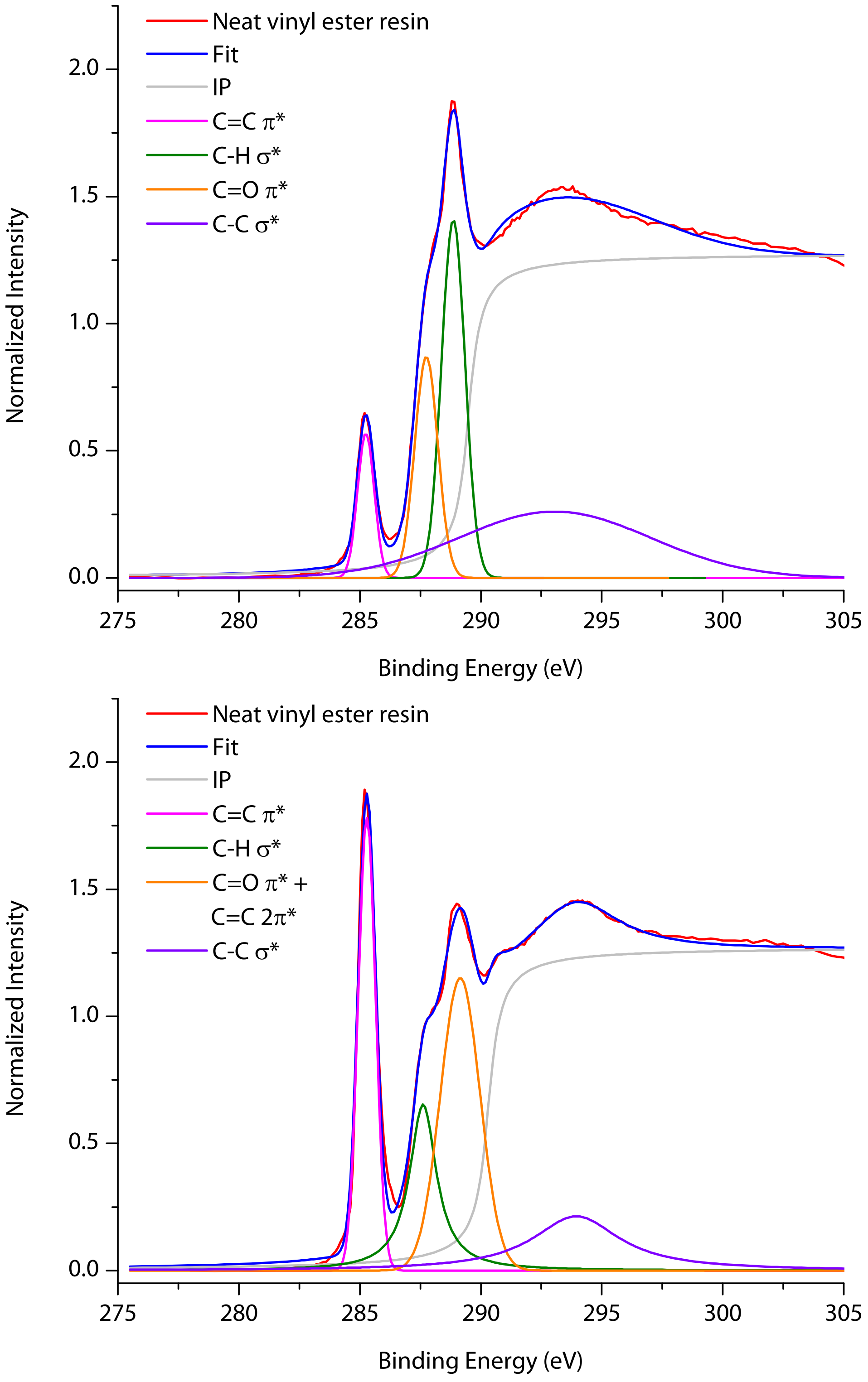

Figure 5-6 – NEXAFS spectra of neat (top) and ablated (bottom) vinyl ester resin

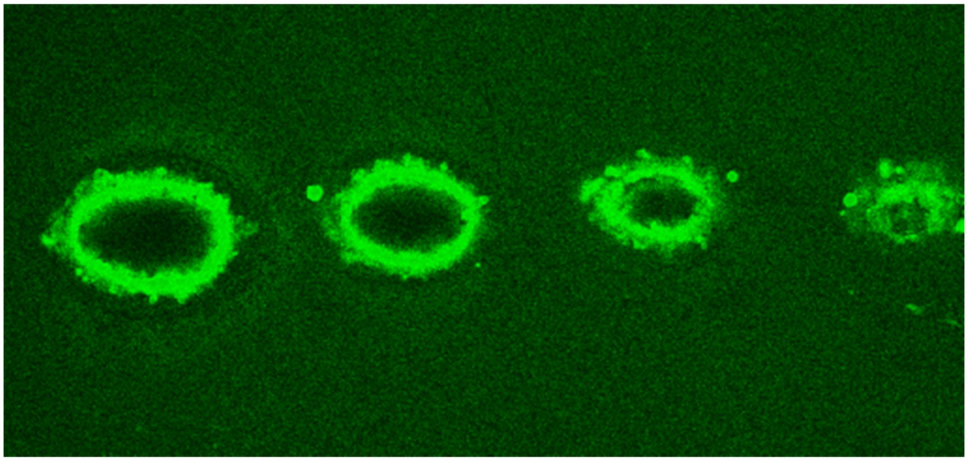

Figure 5-7 – Confocal laser microscopy image of ablated VE resin, showing increased fluorescence at and around the site of ablation

5.3.2 Laser ablation of woven carbon fibers

Woven carbon fibers were ablated separately to evaluate laser effects. As a result of rough bulk sample attachment to the stage, ablation led to fracture and ejection of material from the impacted carbon fibers, leaving only some of the impacted material to examine. In Figure 5-8, the ablated ends of these fibers are shown. There are signs of fiber breakage which appear to indicate a concussive mechanism rather than complete ablation and subsequent severing. Fibers also show evidence of distinct patterns. On many fibers nearer the top surface, there is an ordered striation effect apparent on the fibers near the site of breakage. The striations seen on the ablated fibers are oriented perpendicular to the polarization of the laser, and have a spacing of approximately 600 nm, which is consistent with such patterning seen in metal samples using a similar laser [34], and with striations generated in polyamide fibers [35]. The longitudinal striations seen further away from the surface ablation likely appear due to surface polishing of the polymer. Their spacing and ordering are not consistent with those seen on surface fibers. More distant fibers show evidence of striation along the direction of their orientation, related to the nature of the manufacturing process used in their creation [36]. These distant fibers also show evidence of the transverse striations seen on higher fibers.

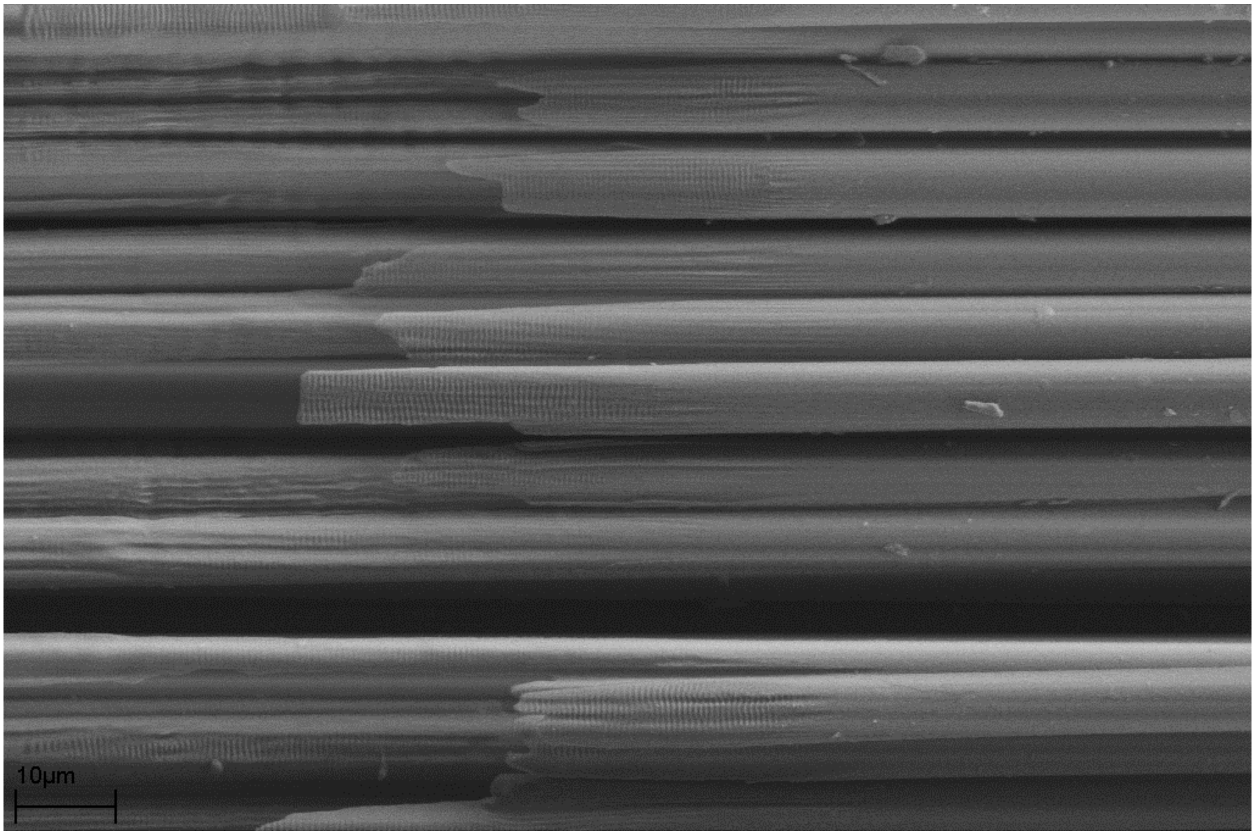

Figure 5-8 – Ablated bare fibers, 250uJ pulse energy. Perpendicular striation has a measured spacing of 600nm.

5.3.3 Low-energy ablation regime of carbon fiber composites

Carbon fiber reinforced vinyl ester composites are the primary system of interest in this project, but such samples also provide additional insight into the ablation parameters of bare fibers and resin. In Figure 5-9, we present the outcome of ablation on a fully-formed composite material at 100 μJ pulse energy, with pits each receiving 3 pulses; the magnified view of a single pit in Figure 5-10 comes from the use of the same parameters in another part of the sample. From the overview, it is apparent that not only does the presence of carbon fibers effect the removal of material, but that composite materials themselves are grossly heterogeneous. Several cracks, both large and small, appear to radiate from the sites of ablation parallel to the direction of the fibers; these cracks range in length from 100 μm to over 500 μm. Ablation geometries at the point of laser impingement lack the uniform crater shape seen in Figure 5-1. Instead, ablated regions show highly irregular borders with resin lifting. As seen in Figure 5-10, these delamination effects form on the scale of 10 μm or larger, and occur predominantly where carbon fibers are nearest the surface. These surface fibers show no evidence of surface striation seen in the bare fibers of Figure 5-8, nor are they seen in material subjected to a higher number of pulses (Figure 5-9, horizontal ablation at top of figure). This suggests that there may be a minimum threshold energy required to generate striations.

Femtosecond laser ablation operates on the principle of Coulombic explosion, which leads to a forcible electrostatic repulsion of ablated material [6]. Explosions with a subsequent increase in pressure have been theorized and observed in the literature [37], and internal shockwaves radiating from the point of pulse impact have been observed to be of sufficient intensity to cause shape change in ablated silicon [29]. From these observations, it is not difficult to suggest that this delamination effect comes from shockwave propagation down carbon fibers, with subsequent vibrations leading to a loss of adhesion. The voids in the matrix observed earlier would facilitate matrix disbondment, and lead to more dramatic shockwave effects.

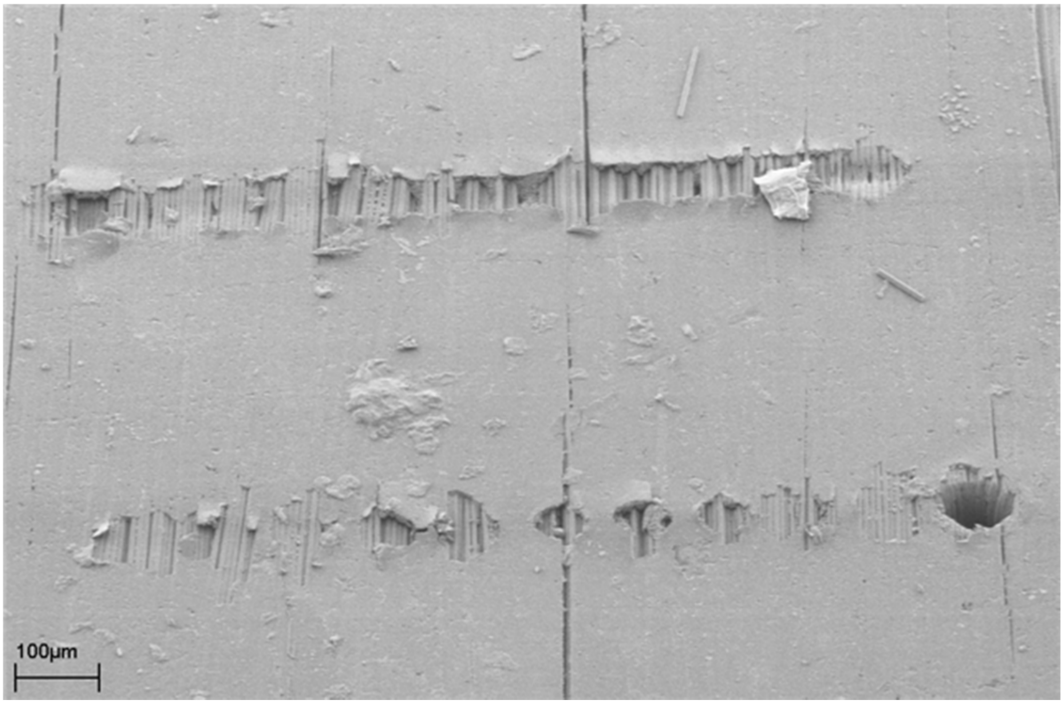

Figure 5-9 – Carbon fiber composite following ablation at 3mW; pits were formed by 3 pulses, while the line (top of image) was generated by scanning the laser across the sample. An orientation pit at the bottom right was made using 1000 pulses.

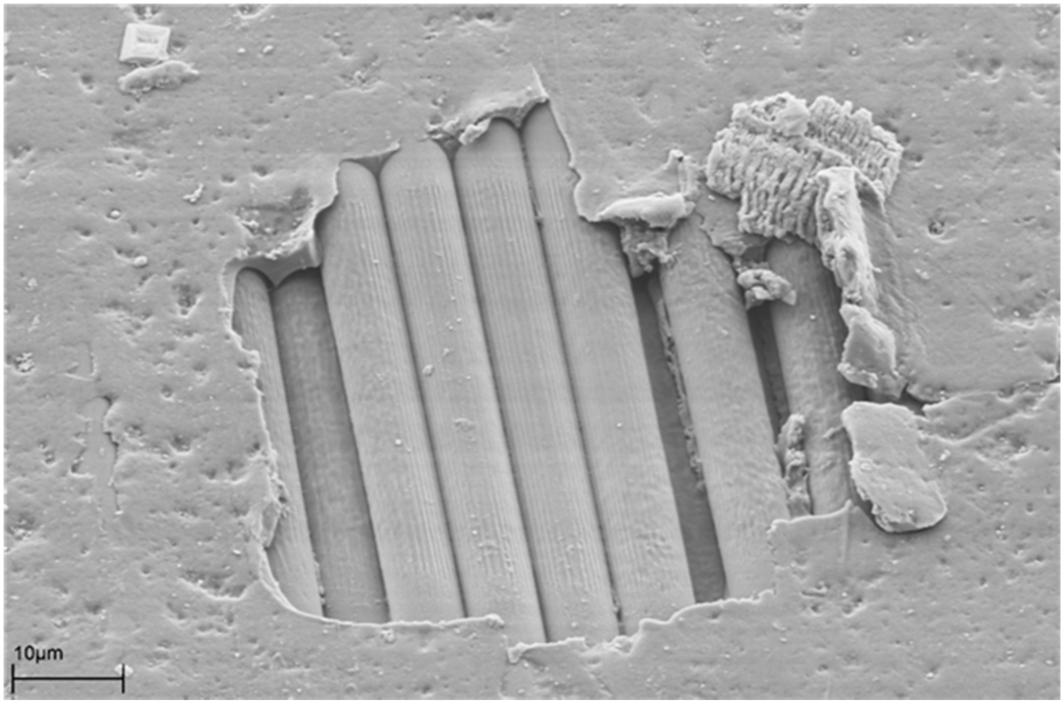

Figure 5-10 – Magnified view of a single ablation pit (100 mW, 3 pulses) with an ablated depth less than 5 µm.

5.3.4 High-energy ablation regime of CFVE composites

In addition to the lower-fluence regime used to attempt to remove resin preferentially from around fibers, higher energies were employed to evaluate higher rates of machining through the full material. In Figure 5-11, one such hole is shown, where ablation was performed at 1 W. The longitudinal striations of individual carbon fibers appear to run together down the walls of the ablated region. These striations match the dimensions of those seen on bare ablated fibers, which we attributed to laser interactions. There also appears to be a laminar patchwork effect on the wall, indicative of material redeposition. In Figure 5-12 we examine this patchwork in greater detail, where the image more clearly demonstrates the spacing of the major striation pattern. More significantly, the texture of the wall is that of many finely-pointed cones oriented in the direction of the beam. Such self-organized spikes have been witnessed in the ablation of tungsten [38], where they are observed to form at a minimum threshold ablation energy and pulse count. These authors attribute this growth to a picosecond-timescale liquid transition with subsequent heterogeneous nucleation at the ablated surface, which is not an unprecedented transition in graphite [24].

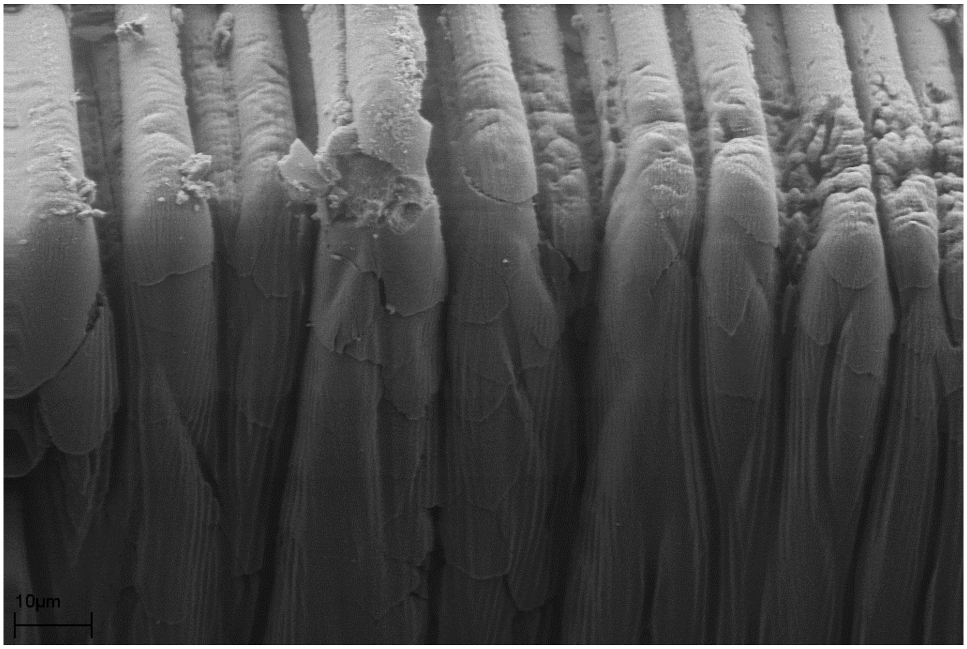

Figure 5-11 – Walls of ablation pit performed at high power (1W) for several seconds to achieve complete penetration.

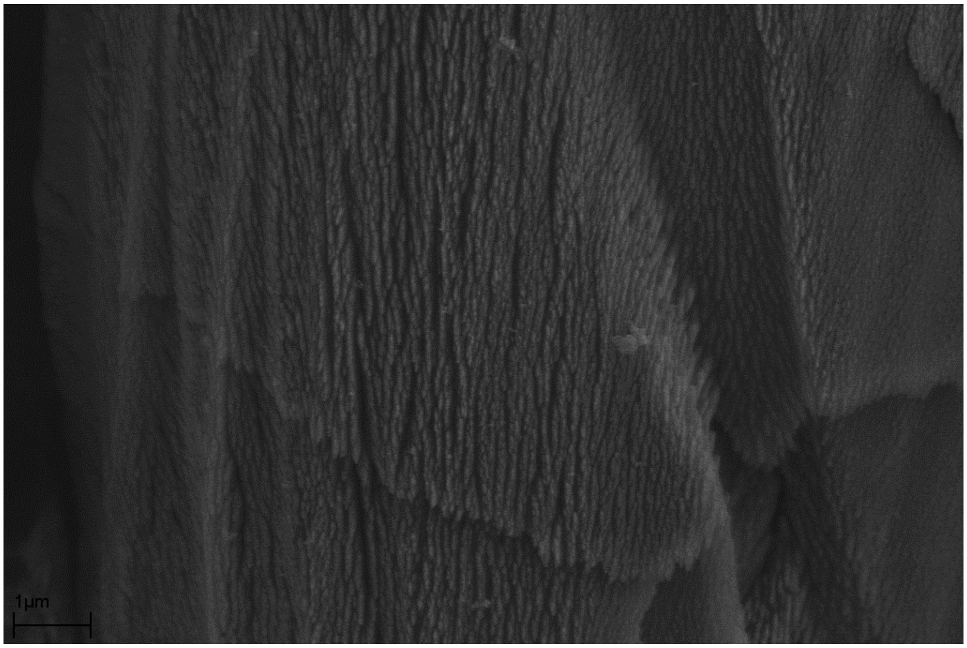

Figure 5-12 – Magnified view of ablated fibers from Figure 11. Pointed structures suggest nucleation of graphite.

Even higher energies lead to additional signs of secondary effects. Figure 5-13 reveals the effects of ablation at high power (1.4 W) with enough pulses to fully penetrate the material (between 2000 and 4000 pulses). There is a region of polished carbon fibers at the surface around the ablation crater, indicative of sufficient fluence to ablate polymer but not graphite. In Figure 5-14 we examine the far inside wall of the crater, which shows a tightly-spaced striation pattern on the scale of that seen in the ablated fibers earlier. With these fibers oriented perpendicular to the neat fibers at the time of ablation, we may definitively conclude that the striations are due to laser interactions rather than being related to the fiber manufacturing process. Figure 5-15 provides an enhanced view of ablated fibers from the far right side of the crater, demonstrating a high degree of consistency in the ablation striations, even on surfaces not oriented normal to the laser beam. In Figure 5-16 we see the effect of the ablation shockwave, with a high degree of resin separation from multiple fibers near the surface. It is also evident that increased pulse energies do not lead to striation formation in the resin. Some fibers here show only partial development of striation with partial polishing, demonstrating the radial dependency on distance from the center of the beam (and thus the crater) at which the fluence drops below the threshold of ablation.

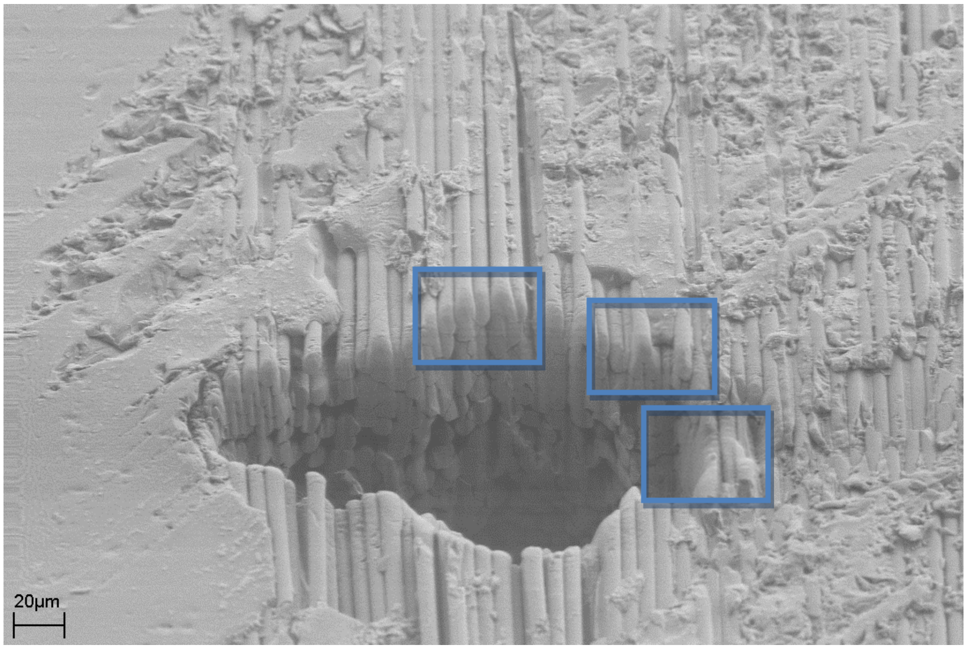

Figure 5-13 – Neat carbon fiber composite ablated at 1.4 W to achieve full penetration.

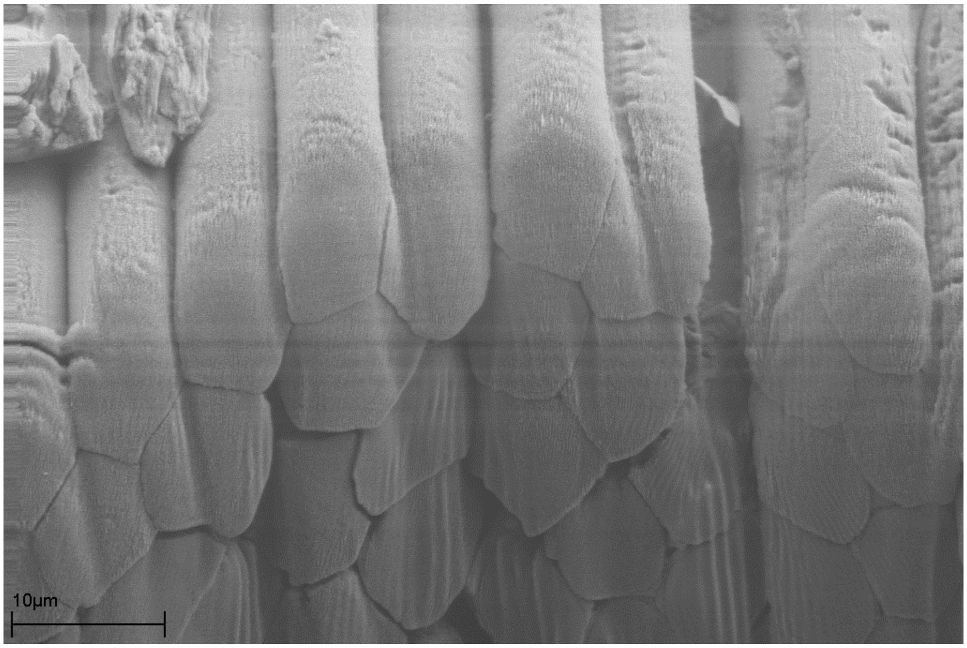

Figure 5-14 – Magnified view of the far wall of the ablated composite.

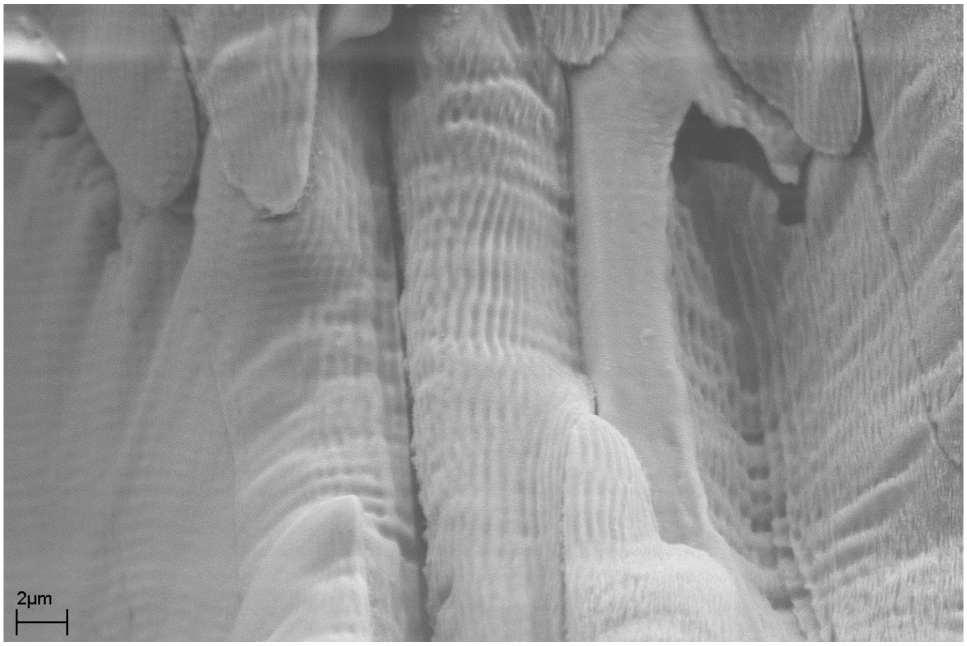

Figure 5-15 – Magnified view of the right side of the ablation site, showing significant damage to carbon fibers near the periphery.

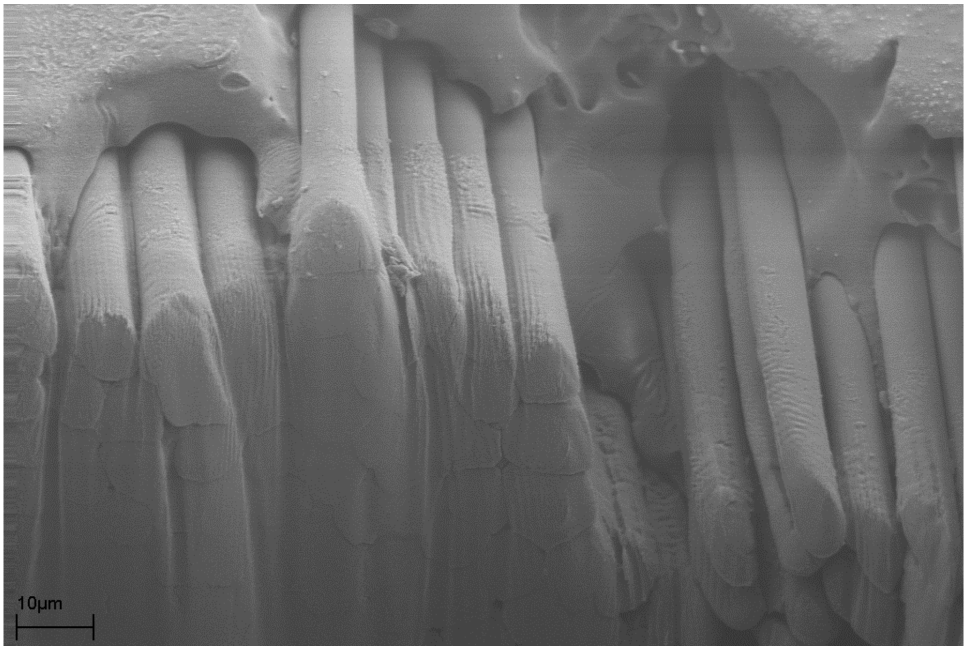

Figure 5-16 – Magnified view of ablated matrix (top right of ablation site) showing fiber-matrix disbanding and voids in the resin material.

Also of note in this figure is the visibility of pores in the resin, which from this perspective appear in fairly close proximity to the fiber. We earlier suggested that such pores would lead to enhanced fiber disbondment, and this effect is noticeable in the center of this figure. Carbon fiber sizing treatments form a coating of generally uniform thickness [39], but which does not necessarily completely cover the fiber [40], leaving a large area of surface-treated bare fiber to interact with the matrix resin. It has been demonstrated that bare carbon fiber inhibits the curing of vinyl ester resin due to surface functionalities [41], which would account for the development of voids due to a lack of curing. These observations provide additional context for Figure 5-9, with very long cracks suggesting poor matrix curing and wetting to the fiber. The presence of these voids so close to the surface of the composite (from Figure 5-16, approximately 10 μm) indicates an obvious vulnerability in the composite material to damage from UV radiation, heat, water, and other chemical infiltration, and a prime origination site for the development of a surface blister due to osmotic pressure from within.

5.3.5 High-energy ablation of weathered composites

For laser ablation to be useful in the analysis of exposed or damaged composites, it is desirable for the ablation characteristics to remain the same as undamaged samples. In Figure 5-17, we show a full-thickness ablation conducted to match that shown in an undamaged sample. There is evidence of appreciable polishing at the outer edges of the crater, indicating a ring of fluence above the threshold for ablation of resin, but below that of carbon fiber. What is remarkable from this experiment is the formation of a second halo of debris around the polished region, shown in Figure 5-18. The debris appears to consist of small particles of diameter 10 μm or less, which are irregularly deposited within approximately 60 μm of the polished zone; the amount of debris in this sample is significantly higher than in non-exposed composites, and the shape and nature of the debris is also changed. Rather than the relatively clean ablation of resin and fiber seen in neat samples, the material deposits in a large number of small particles, suggesting that the mechanism by which debris is generated is affected by the properties of the material. UV exposure of resin causes several chemical changes, among which include chain cleavage, surface oxidation, and the outgassing of unreacted styrene monomers which function as plasticizers *in situ*. The combination of these effects produces an increase in hardness, but a drop in the ultimate strain and toughness of the resin, along with embrittlement [42]. This change in mechanical properties seems the most likely cause for changed material deposition, as it is most likely related to the shockwave generated during ablation.

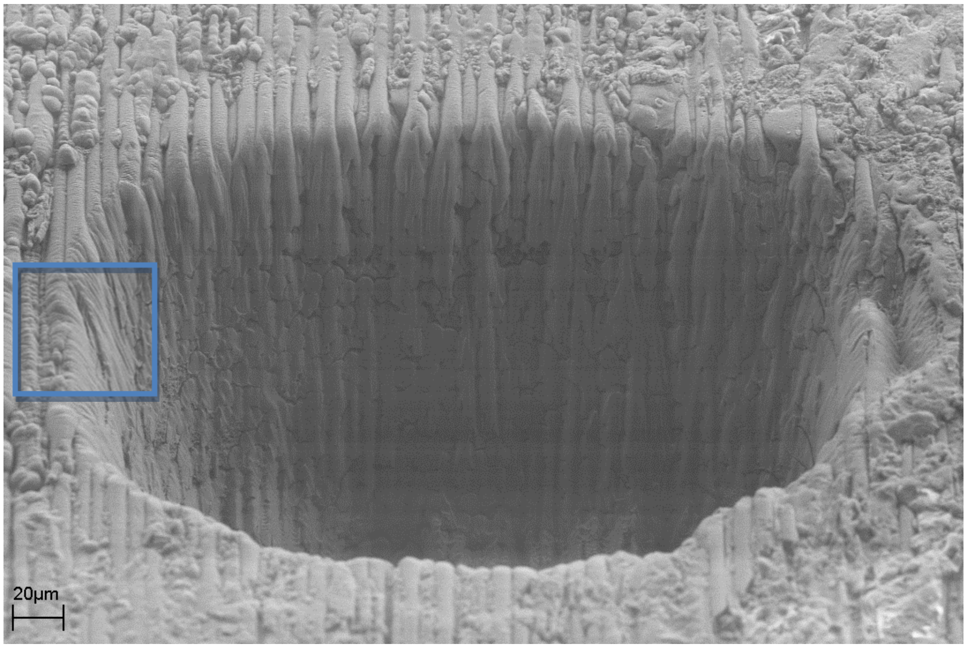

Figure 5-17 – Laser ablation of composite material after 1000 h accelerated weathering exposure.

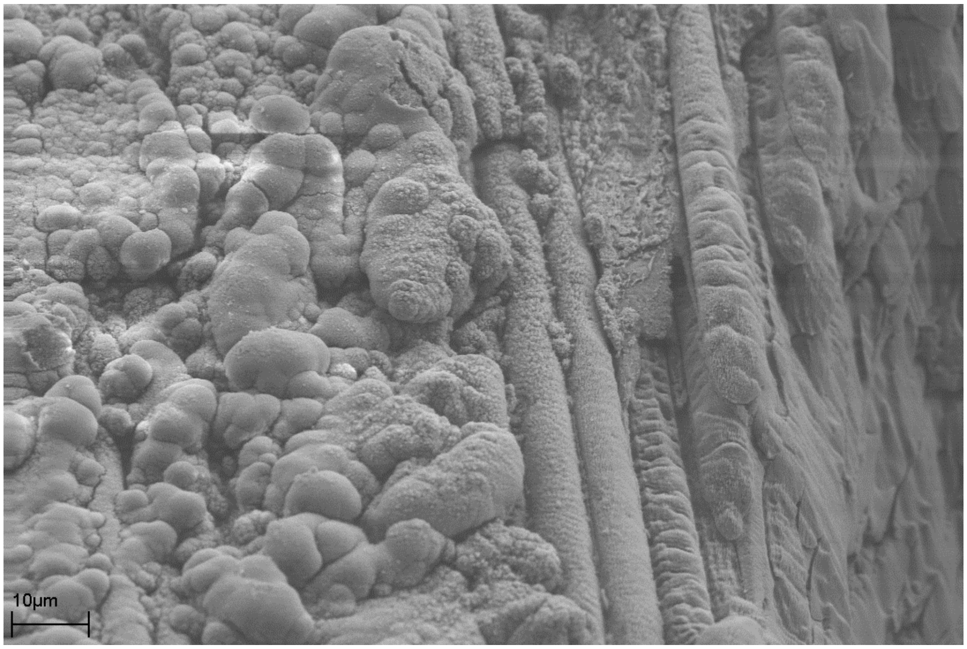

Figure 5-18 – Close-up of deposited materials along the left side of the ablation site shown above.

5.4 Conclusions

Ultrafast laser ablation has demonstrated the ability to remove the small quantities of material required to expose the chemistry and structure of the fiber/matrix interface. Both Raman spectroscopy and confocal microscopy have demonstrated enhanced laser-induced fluorescence at and around the site of ablation, which points to a modified surface chemistry potentially indicating thermal damage. NEXAFS spectroscopy has also indicated an increased amount of aromatic carbon at the site of ablation, apparently indicative of evacuated and redeposited monomeric styrene remaining in the material. The delamination and mechanical effects observed in the material several microns from the ablation site illustrate the additional system complexities involved when etching a composite, and reveals inherent weaknesses in the interfacial adhesion of the composite system. The porosity observed in the matrix near the polymer demonstrates a likely contributory effect to the resultant failure in adhesion after ablation. This more-extensive failure in the sample could be exploited to facilitate chemical analysis of the interfacial region away from the ablation site and styrene coating. The smoothed region at the edge of the crater indicates that machining at high energies may result in a secondary ablation process by virtue of fluences outside the $1/e^2$ beam radius. Redeposited material appears more extensively at the edge of the ablation crater in samples exposed to UV, which suggests that the chemical and mechanical changes caused by this process affect the mechanism of material ejection.

5.5 References

[1] D.X. Hammer, G.D. Noojin, R.J. Thomas, C.E. Clary, B.A. Rockwell, C.A. Toth, W.P. Roach, Intraocular laser surgical probe for membrane disruption by laser-induced breakdown, Appl. Opt., 36 (1997) 1684-1693.

[2] R. Fardel, M. Nagel, T. Lippert, F. Nueesch, A. Wokaun, B.S. Luk'yanchuk, Influence of thermal diffusion on the laser ablation of thin polymer films, Applied Physics A: Materials Science & Processing, 90 (2008) 661-667.

[3] P.E. Dyer, S.T. Lau, G.A. Oldershaw, D. Schudel, An investigation of xenon chloride (XeCl) laser ablation of poly(ether ether ketone) (PEEK)-carbon fiber composite, Journal of Materials Research, 7 (1992) 1152-1157.

[4] L. Torrisi, A. Borrielli, D. Margarone, Study on the ablation threshold induced by pulsed lasers at different wavelengths, Nuclear Instruments & Methods in Physics Research, Section B: Beam Interactions with Materials and Atoms, 255 (2007) 373-379.

[5] B.C. Stuart, M.D. Feit, S. Herman, A.M. Rubenchik, B.W. Shore, M.D. Perry, Optical ablation by high-power short-pulse lasers, Journal of the Optical Society of America B: Optical Physics, 13 (1996) 459-468.

[6] J. Longtin, Nonlinear phenomena in laser-material interactions, Annual Review of Heat Transfer, 14 (2005) 419-438.

[7] L.T. Keene, T. Fiero, C.R. Clayton, G.P. Halada, D. Cardoza, T. Weinacht, On the use of femtosecond laser ablation to facilitate spectroscopic depth profiling of heterogeneous polymeric coatings, Polym. Degrad. Stab., 89 (2005) 393-409.

[8] F. Costache, M. Henyk, J. Reif, Surface patterning on insulators upon femtosecond laser ablation, Applied Surface Science, 208–209 (2003) 486-491.

[9] J. Reif, F. Costache, M. Henyk, S.V. Pandelov, Ripples revisited: non-classical morphology at the bottom of femtosecond laser ablation craters in transparent dielectrics, Applied Surface Science, 197–198 (2002) 891-895.

[10] Q. Bian, S. Chen, B.-T. Kim, N. Leventis, H. Lu, Z. Chang, S. Lei, Micromachining of polyurea aerogel using femtosecond laser pulses, Journal of Non-Crystalline Solids, 357 (2011) 186-193.

[11] S. Baudach, J. Bonse, W. Kautek, Ablation experiments on polyimide with femtosecond laser pulses, Applied Physics A: Materials Science & Processing, 69 (1999) S395-S398.

[12] Y. Yang, J. Yang, L. Xue, Y. Guo, Surface patterning on periodicity of femtosecond laser-induced ripples, Applied Physics Letters, 97 (2010) 141101-141103.

[13] P. Moreno, C. Mendez, A. Garcia, I. Arias, L. Roso, Femtosecond laser ablation of carbon reinforced polymers, Appl. Surf. Sci., 252 (2006) 4110-4119.

[14] A.A. Serafetinides, M. Makropoulou, E. Fabrikesi, E. Spyratou, C. Bacharis, R.R. Thomson, A.K. Kar, Ultrashort laser ablation of PMMA and intraocular lenses, Applied Physics A: Materials Science & Processing, 93 (2008) 111-116.

[15] C.R. Mendonca, S. Orlando, G. Cosendey, M. Winkler, E. Mazur, Femtosecond laser micromachining in the conjugated polymer MEH–PPV, Applied Surface Science, 254 (2007) 1135-1139.

[16] M. Okoshi, N. Inoue, Femtosecond laser ablation of polyethylene, Japanese Journal of Applied Physics, Part 2: Letters, 42 (2003) L36-L38.

[17] M.Y. Xu, S.A. Hosseini, H. Zhang, S.M. Eaton, L.D. Lilge, P.R. Herman, Heat Accumulation Effects in Femtosecond Laser Ablation of ITO Thin Films for DEP Trapping Devices, in: Conference on Lasers and Electro-Optics/Quantum Electronics and Laser Science Conference and Photonic Applications Systems Technologies, Optical Society of America, 2007, pp. CFR3.

[18] C. De Marco, R. Suriano, M. Levi, S. Turri, S. Eaton, G. Cerullo, R. Osellame, Femtosecond laser fabrication and characterization of microchannels and waveguides in methacrylate-based polymers, Microsyst Technol, 18 (2012) 183-190.

[19] R. Suriano, A. Kuznetsov, S.M. Eaton, R. Kiyan, G. Cerullo, R. Osellame, B.N. Chichkov, M. Levi, S. Turri, Femtosecond laser ablation of polymeric substrates for the fabrication of microfluidic channels, Applied Surface Science, 257 (2011) 6243-6250.

[20] H. Jeon, R. Schmidt, J.E. Barton, D.J. Hwang, L.J. Gamble, D.G. Castner, C.P. Grigoropoulos, K.E. Healy, Chemical Patterning of Ultrathin Polymer Films by Direct-Write Multiphoton Lithography, Journal of the American Chemical Society, 133 (2011) 6138-6141.

[21] N.L. Vasily, M.P. Sergey, D.O. Elena, I.K. Sergey, F.B. Alexey, Single-shot and single-spot measurement of laser ablation threshold for carbon nanotubes, Journal of Physics D: Applied Physics, 46 (2013) 052002.

[22] A. Kaplan, M. Lenner, C. Huchon, R.E. Palmer, Nonlinearity and time-resolved studies of ion emission in ultrafast laser ablation of graphite, Applied Physics A: Materials Science & Processing, 92 (2008) 999-1004.

[23] M. Lenner, A. Kaplan, R.E. Palmer, Nanoscopic Coulomb explosion in ultrafast graphite ablation, Applied Physics Letters, 90 (2007) 153119/153111-153119/153113.

[24] K. Sokolowski-Tinten, S. Kudryashov, V. Temnov, J. Bialkowski, d.L.D. von, A. Cavalleri, H.O. Jeschke, M.E. Garcia, K.H. Bennemann, Femtosecond laser-induced ablation of graphite, Springer Ser. Chem. Phys., 66 (2001) 425-427.

[25] D. Pietroy, Y. Di Maio, B. Moine, E. Baubeau, E. Audouard, Femtosecond laser volume ablation rate and threshold measurements by differential weighing, Opt. Express, 20 (2012) 29900-29908.

[26] H. Al-Moussawi, E.K. Drown, L.T. Drzal, The silane/sizing composite interphase, Polymer Composites, 14 (1993) 195-200.

[27] M. Diepens, P. Gijsman, Outdoor and accelerated weathering studies of bisphenol A polycarbonate, Polymer Degradation and Stability, 96 (2011) 649-652.

[28] S. Baudach, J. Bonse, J. Krüger, W. Kautek, Ultrashort pulse laser ablation of polycarbonate and polymethylmethacrylate, Applied Surface Science, 154–155 (2000) 555-560.

[29] S. Panchatsharam, B. Tan, K. Venkatakrishnan, Femtosecond laser-induced shockwave formation on ablated silicon surface, Journal of Applied Physics, 105 (2009) 093103.

[30] A.J. Lee, J.M. Dawes, M.J. Withford, Investigation of femtosecond laser induced thermal ablation of polyethylene, Journal of Laser Applications, 20 (2008) 154-159.

[31] K.E. Sohn, M.D. Dimitriou, J. Genzer, D.A. Fischer, C.J. Hawker, E.J. Kramer, Determination of the Electron Escape Depth for NEXAFS Spectroscopy, Langmuir, 25 (2009) 6341-6348.

[32] S. Crawford, C.T. Lungu, Influence of temperature on styrene emission from a vinyl ester resin thermoset composite material, Science of The Total Environment, 409 (2011) 3403-3408.

[33] J. La Scala, C. Ulven, J. Orlicki, R. Jain, G. Palmese, U. Vaidya, J. Sands, Emission modeling of styrene from vinyl ester resins, Clean Techn Environ Policy, 9 (2007) 265-279.

[34] Y. Tang, J. Yang, B. Zhao, M. Wang, X. Zhu, Control of periodic ripples growth on metals by femtosecond laser ellipticity, Opt. Express, 20 (2012) 25826-25833.

[35] F. Bedoui, N.S. Murthy, F.M. Zimmermann, Enhancement of fiber-matrix adhesion by laser ablation-induced surface micro corrugation, J. Mater. Sci., 43 (2008) 5585-5590.

[36] S.M. Lee, Handbook of Composite Reinforcements, Wiley, 1992.

[37] E.N. Glezer, E. Mazur, Ultrafast-laser driven micro-explosions in transparent materials, Applied Physics Letters, 71 (1997) 882-884.

[38] Q.-Z. Zhao, S. Malzer, L.-J. Wang, Self-organized tungsten nanospikes grown on subwavelength ripples induced by femtosecond laser pulses, Opt. Express, 15 (2007) 15741-15746.

[39] R.E. Allred, A.E. Hoyt Haight, J.M. Gosau, S.P. Wesson, Aqueous-based emulsion reactive finishes for improving carbon/vinyl ester interfacial bonding, International SAMPE Symposium and Exhibition, 50 (2005) 741-756.

[40] R.E. Allred, S.P. Wesson, E.E. Shin, L. Inghram, L. McCorkle, D. Papadopoulos, D. Wheeler, J.K. Sutter, The influence of sizings on the durability of high-temperature polymer composites, High Performance Polymers, 15 (2003) 395-419.

[41] S.P. Tweed-Kent, Understanding Cure Inhibition in Carbon Fiber Reinforced Vinyl Ester Resin Composites, in: Materials Science and Engineering, The Pennsylvania State University, 2008.

[42] A.W. Signor, M.R. VanLandingham, J.W. Chin, Effects of ultraviolet radiation exposure on vinyl ester resins: characterization of chemical, physical and mechanical damage, Polymer Degradation and Stability, 79 (2002) 359-368.

Chapter 6: Thermally Damaged Vinyl Ester Composites: Relating Matrix Chemistry with Laser Fluorescence Yield

This project represents a collaborative effort between this author, Dr. William Scott of Computer Interface Instrumentation, Inc., and Mr. Guy Connelly of Connelly Applied Research, under the supervision of PI Dr. Richard Granata. Dr. Scott and Mr. Connelly were responsible for obtaining laser fluorescence measurements, as detailed in the chapter. No claim is made by this author on these results. These results have not yet been published, and are included herein as the outcome of private communications in the process of preparing a manuscript.

6.1 Introduction

Composite materials have found use in a variety of military applications. Over the course of their lifetimes, such materials can be subjected to varying degrees of thermal exposure at or above their recommended service temperature. Long-term studies have addressed the mechanical failure of thermally degraded composites [1, 2], particularly those employed in aircraft, which are subjected to high temperatures and stresses. Thermal exposure has been found to result in mass loss, which has been directly attributed to the outgassing of residual volatile components [3-5]. The relationship between thermal exposure and mechanical property degradation in epoxy composites has also been observed through FTIR, and it has been shown that FTIR may serve as an adequate indicator of damage in some systems [6]. Low-temperature thermal exposure (up to 50 °C) has also been shown to lead to extensive outgassing of unreacted styrene monomers over timescales on the order of 100 hours [7]. Laser-induced fluorescence has been shown to be a viable means of detecting low levels of thermal damage in composites made from epoxy resins [8, 9]. These studies simply ascribe fluorescence to the presence of ring structures formed during curing or degradation, without further investigation. In these resin systems, increasing fluorescence has been correlated with a loss of mechanical strength resulting from thermal exposure at temperatures well above their service limit. The localization of thermal damage is also possible through fluorescent imaging. A relationship between thermal damage and the degradation of mechanical properties has been established, as well as a relationship to dielectric properties [10].

The most accurate means of evaluating the degradation of a composite is through destructive testing of its mechanical properties. Changes in the strength, fracture mechanics, and thermal properties provide a direct measurement of the effects of exposure [2]. Non-destructive testing offers a way to measure the degree of degradation without damage. Methods such as X-radiography, ultrasound, and thermography provide quantitative information on the extent of defects present in the material [11]. However, these methods each have their own limitations, with the ultimate limitation on all being that they are unable to observe effects which have not yet resulted in cracks or delamination in the material. These techniques are essentially blind to small chemical changes which may significantly impact the performance of the composite. No such chemical model of thermal damage has yet been directly related to fluorescence. This study attempts to provide such insights through the application of vibrational spectroscopy and NEXAFS.

While vibrational spectroscopy has long provided for the majority of chemical analysis of polymers and polymer composites (e.g. [12, 13]), X-ray-based surface analysis can demonstrate changes and degradation before their effects have manifested deeper in the material. It has been shown that while UV degradation is best measured after hundreds or thousands of hours by even the relatively near-surface sensitive ATR-FTIR technique (1-2 μm), effects have been observed at a depth of tens of nanometers after just 100 hours using XPS, which is sensitive to surface changes on the order of nanometers in depth [14]. The spectroscopic complement to XPS, Near Edge X-ray Absorption Fine Structure (NEXAFS) spectroscopy is capable of probing the bonding states of molecules using monochromatic x-ray absorption. It is not only capable of determining the chemical composition of the surface, but because the x-rays are polarized can also offer information on changes in molecular orientation, which is directly relevant to the optical performance of a polymer [15].

In this chapter, we aim to probe the structure-property relationships in vinyl ester resin in a light thermal exposure regime, below the range of rapid thermal degradation. Scientifically we will study the link between chemical and mechanical property changes and thermal exposure, and determine how laser-induced fluorescence resulting from thermal exposure is related to these properties. The ultimate goal will be to understand the utility of laser-induced fluorescence as an analytical tool in thermal degradation of structural composites.

6.2 Materials and methods

Samples were produced using Derakane MOMENTUM 411-350 vinyl ester resin in a VARTM system. The samples were cured at 120 °C for 2 h to harden, in accordance with the manufacturer's recommendations. In the reinforced samples, Toray T700 carbon fibers with Toray "F0E" fiber sizing were used for compatibility with the resin. Samples were later heated in a furnace at temperatures between 177 and 274 °C for between 15 and 60 minutes in order to produce a variety of exposure conditions. Samples were also produced without carbon fibers for spectroscopic analysis.

Laser-induced fluorescence (LIF) analysis was performed using a custom-made system, comprehensively described elsewhere [9]. Briefly, a laser excitation source with wavelength 532 nm was combined with fiber optics and a spectrometer to analyze the fluorescent signature. The excitation and collection fibers were bundled into a probe head to allow analysis of a region of diameter 400 μm. A high-pass filter at 570 nm was used to reject scattered laser light. This instrument is highly sensitive to surface fluorescence.

Vibrational spectroscopic analysis was performed using a Nicolet Almega dispersive Raman spectrometer with 785 nm excitation laser and 10x and 100x objective lenses, for bulk spectroscopic analysis; and a Nicolet Magna 560 FTIR spectrometer with a diamond micro-ATR attachment, for surface vibrational analysis (to a depth of ~2 μm). Further Raman analysis was also conducted using a WiTec α-500 confocal Raman spectrometer with 20x and 100x objective lenses, in order to attempt depth profiling.

NEXAFS spectroscopic analysis was performed on beamline U7A at the National Synchrotron Light Source at Brookhaven National Laboratory. A grid bias voltage of 150V was used for surface sensitivity, yielding a depth of analysis on the order of several nm [16], while scanning the C1s absorption region between 270 and 330 eV. Spectra were subsequently normalized to the incident current to account for synchrotron beam decay prior to curve fitting and analysis. Custom software was written to calculate the dichroic ratio of selected molecular bonds in each sample, utilizing data collected at 3 angles (20, 55, and 90 degrees relative to the plane of the sample) [15]. The dichroic ratio describes the rough degree and direction of orientation of specific bonds in the material; changes in ordering seen by this method can be attributed to structural changes or surface depositions.

Dynamic mechanical analysis was performed using a Perkin Elmer 8000 DMA in single cantilever mode, with oscillations at a fixed frequency of 1 Hz while scanning across a temperature range from room temperature to the point of sample failure and decoupling, which occurred as high as 400 °C.

6.3 Results

6.3.1 Spectroscopic analysis of thermal damage

In this low temperature exposure regime (that is, below 300 °C), thermo-oxidative degradation has previously been found to be a slow process as measured by GC-MS [3]. as measured by Figure 6-1 shows a set of ATR-FTIR spectra for samples exposed at 210 °C for 15, 30 and 60 minutes. The carbonyl peak centered at 1725cm^{-1} begins to show a minor decrease in overall intensity (on the order of 15%) with a slight broadening at higher wave number after 30 minutes, with a more pronounced effect at 60 minutes. This appears to be the development of a small shoulder at 1745 cm^{-1}, indicative of an ester carbonyl without hydrogen bonds. It seems unlikely that this shoulder would be attributed to the breakage of styrene crosslinks in the matrix, as unsaturation of the alpha carbon nearest the carbonyl would lead to a decrease in frequency [17]. Accordingly, we explain this evolution as a decrease in the degree of hydrogen bonding of the carbonyl in the polymer. The effect seen is very weak, indicating that both the initial and final degrees of hydrogen bonding are extremely low. A significant increase is seen in the peak at 698 cm^{-1}, related to an out-of-plane C-H vibration in monosubstituted aromatic rings, while increases in peaks at 1580 and 1606 cm^{-1} indicate a growth of C=C aromatic vibrations [17]. With styrene making up a significant part of this vinyl ester resin mixture, we conclude that these changes are due to increased migration of unreacted styrene into the near-surface region for outgassing as a result of thermal exposure above the T_g of the resin. Styrene has been shown to outgas substantially from vinyl ester resin long after curing, particularly at elevated temperatures [5, 7].

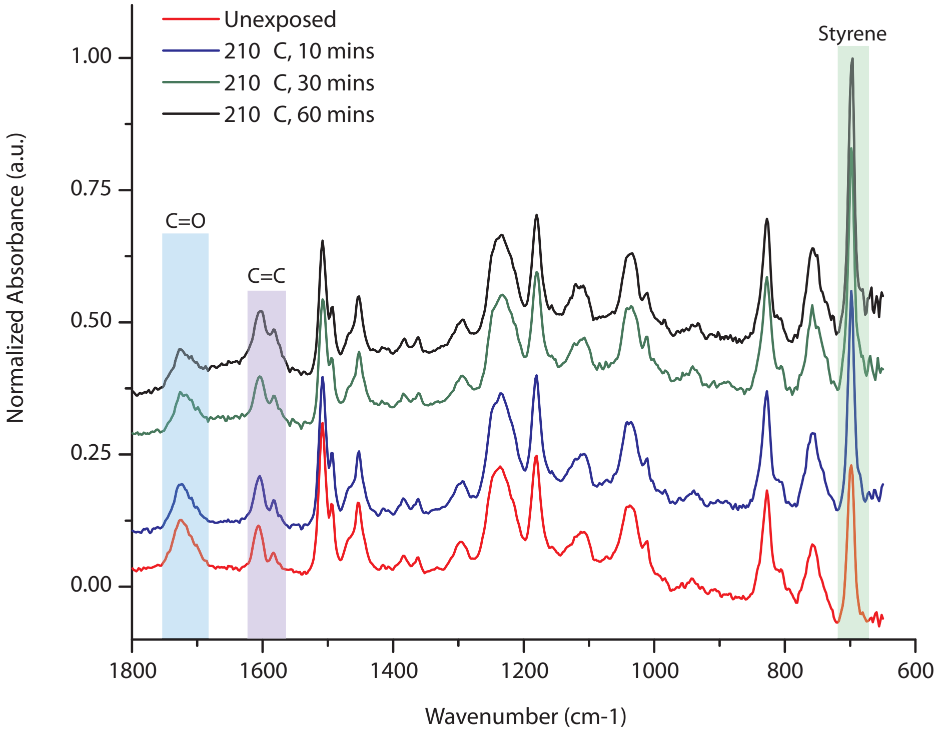

Figure 6-1 – FTIR spectra of vinyl ester resin before thermal exposure, and after exposure at 210 °C for 10, 30, and 60 minutes**.**

This assertion is further corroborated through Raman spectroscopy. In Figure 6-2, the Raman spectra from the same samples are shown. The evolution of a peak shoulder is seen at 1580 cm^{-1}, corresponding to aromatic C=C as is seen by FTIR. There is also a significant increase in background fluorescence with increasing exposure temperature and time. Due to the fluorescence and changes in surface morphology caused by exposure, it is difficult to discern changes to the peak at 1000 cm^{-1}, indicative of C=C ring breathing, which would further confirm the presence of styrene at the surface. The increase in fluorescence leads to masking of the chemical information in the spectrum. However, the laser-induced fluorescence observed on this instrument provides a qualitative look at laser-induced fluorescence.

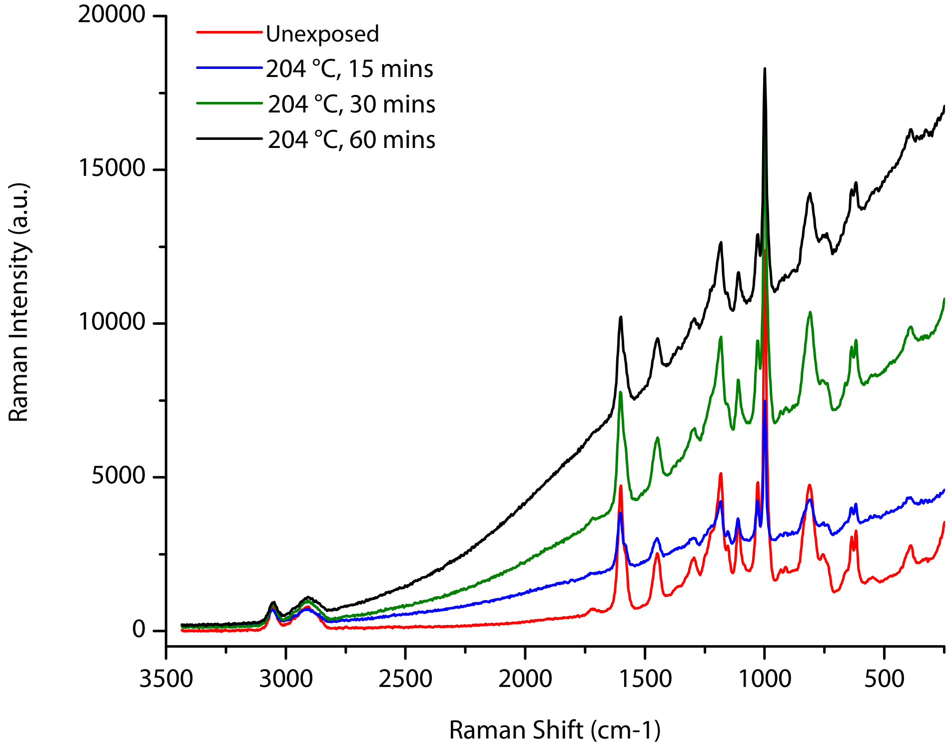

Figure 6-2 – Raman spectra of vinyl ester resin unexposed and heat treated for 15, 30 and 60 minutes.

NEXAFS spectroscopy of damaged composites provides a highly surface-sensitive view of the material, with the ability to evaluate the degree of orientation in polymers at the surface. This information is important to the detection of any thermally-induced structural changes. As seen in the undamaged sample curve-fit in Figure 6-3, the lowest-binding energy peak centered at 285.2 eV (C1s-π* C=C, henceforth described as C=C π*) is attributed both to the mono-substituted styrene ring and the di-substituted aromatic rings of the vinyl ester backbone. Additional peaks fit at 287.8 eV (C-H σ*, for the polymer chains) and 288.9 eV (C=O π*) for carbonyl. Peaks above the edge are σ* sp^2 hybridized C=C and σ* C-C-C absorptions, at ~293 and ~300 eV, respectively [18]. The π* transition is generally a sharp one, while σ* transitions are substantially broader due to the changing bond length as a function of nuclear vibrations, which leads to asymmetry [19].

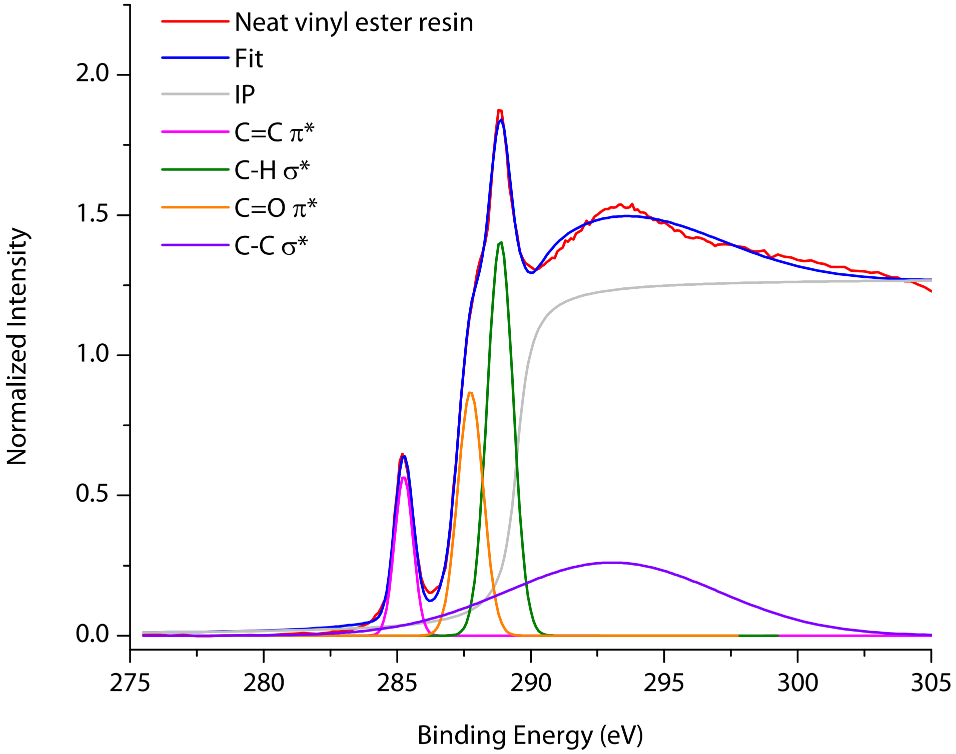

Figure 6-3 – NEXAFS partial electron yield spectrum peak deconvolution and fit of neat vinyl ester prior to thermal exposure.

Following varying degrees of exposure, there are significant changes to the spectrum, as can be seen in Figure 6-4. The peak at 285.2 eV shows a substantial increase with increasing exposure temperature and time; with the spectrum normalized on a per-atom basis, this indicates an increased quantity of aromatic ring structures at the surface. When considered with the ATR-FTIR shown above, this suggests not only a subsurface increase in the concentration of styrene, but also surface adsorption as a result of outgassing. At the highest tested sample exposure (246 °C, 60 mins), the spectrum undergoes a noticeable change. There is also a slight shift in the peak at 288.9 eV to 289.1 eV. Consistent with the separation between peaks seen in the spectrum of polystyrene elsewhere in the literature , we attribute this new location to the π^*_2 absorption commonly seen in aromatic systems [15, 19], with its broader width evidence of the contribution from the neighboring C=O peak of the underlying resin. We attribute this to the continued build-up of deposited styrene, which has become thick enough (several nm) to dominate the spectrum.

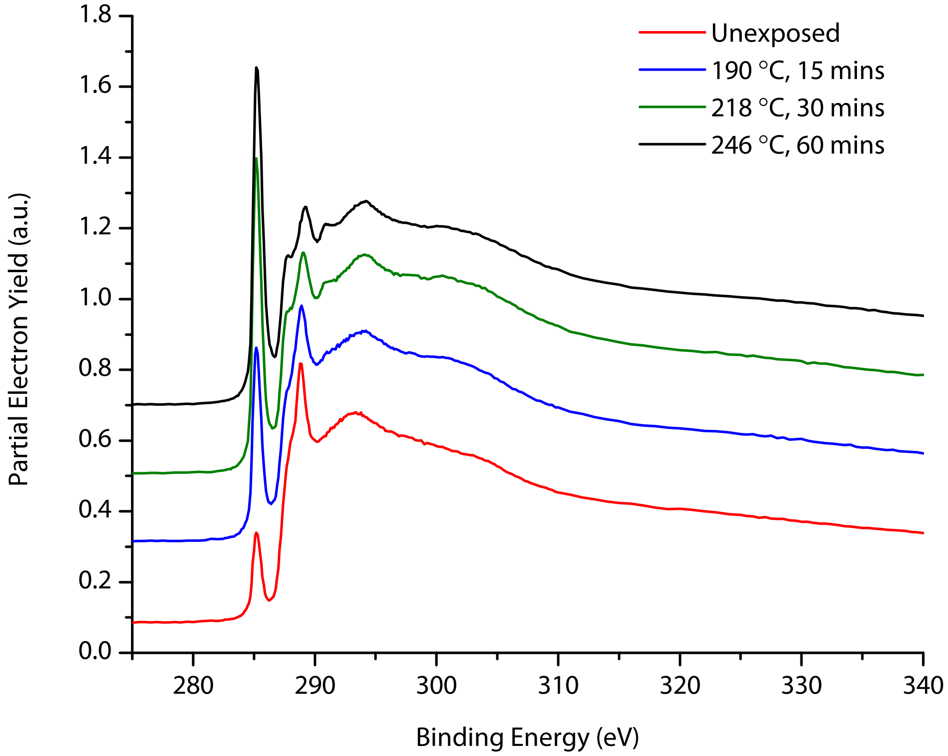

Figure 6-4 – NEXAFS partial electron yield spectra of thermally damaged vinyl ester resin with increasing temperature and time.

In Figure 6-5 we present the NEXAFS spectrum of a sample subjected to conditions severe enough to cause thermal damage. After exposure at 275 °C for 150 minutes, the intensity of the aromatic C=C π* peak decreases below that of the unexposed sample, and the center of the peak at 289.1 eV shifts back to 288.9 eV, suggesting a lack of adsorbed styrene at the surface, to which we had previously assigned this shift. The peak for C-H σ * increases relative to the aromatic as well, which suggests an increase in the ratio of long polymer chains to aromatic rings in the surface region. The restored intensity of the σ* absorbance at 293 eV demonstrates the increased surface density of polymer backbone bonding, in the absence of styrene dilution. In this temperature range, thermo-oxidative degradation occurs much more quickly, and serves to break the styrene crosslinks of the resin matrix and thus decrease the amount of fixed aromatic carbon in the surface region (not to be confused with the adsorbed styrene on top of the surface). Other authors have discussed the rate of styrene diffusion through the matrix, and have determined that the rate is slowed tremendously in the cured resin due to matrix crosslinking [7]. By raising the temperature of the material well beyond its T_g (120 °C), polymeric segmental dynamics have increased sufficiently to permit additional diffusion. While the rate of diffusion has increased drastically, surface ruptures must still form to permit outgassing of the material; hence, the resultant formation of significant pore structures often seen following thermal exposure [20].

The model used by La Scala in [5] describes 3 main processes controlling styrene outgassing: a diffusion-controlled region, a transition region, and an evaporation-controlled region. Although we have studied much shorter timescales in our systems, the temperatures examined are also significantly higher. We believe that this model remains valid for our systems, based on qualitative observations. Given the high temperatures, both the rate of evaporation and internal diffusion must be very high, with build-up in the surface transitional region acting to limit diffusion.

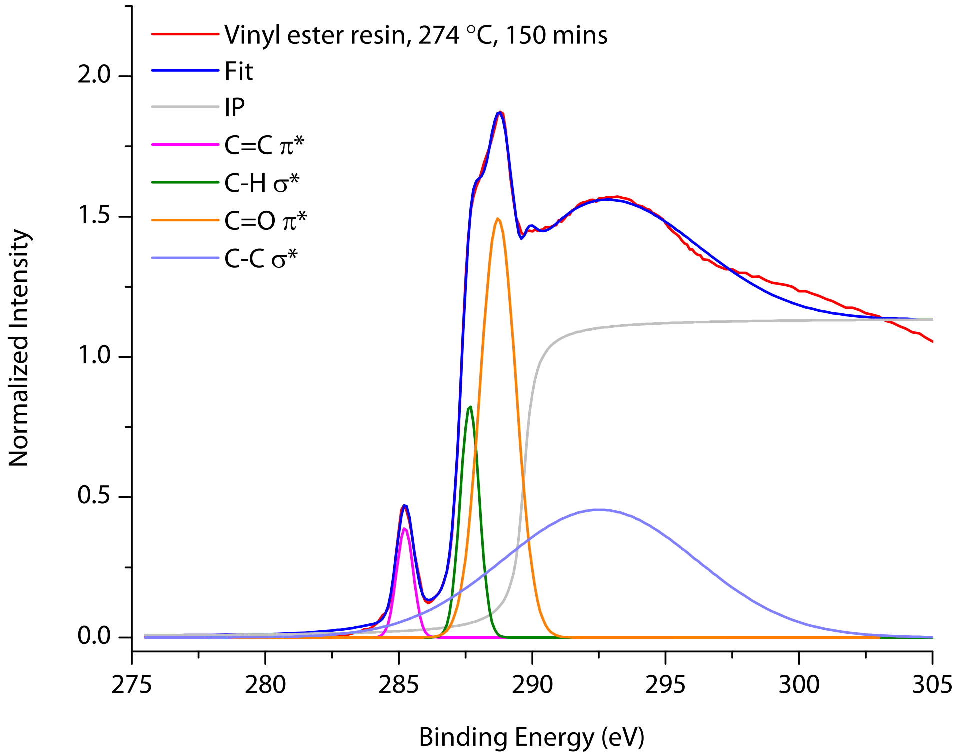

Figure 6-5 – NEXAFS partial electron yield spectrum and curve fits of vinyl ester resin at exposure at 274 °C for 150 minutes.

Dichroic ratio data suggests orientation of the adsorbed styrene at the surface. In Table 6-1, the dichroic ratio of fitted peaks from the resin before and after exposure at 246 °C for 30 mins is presented. Prior to thermal exposure, there is some weak orientation of the aromatic ring bound in the matrix with the ring itself standing perpendicular to the surface, indicated by a negative DR value with a magnitude of 0.1; after heating, this ordering effect is lost, which is due to the disordered arrangement of styrene monomers deposited at the surface. The orientation effect of the carbonyl becomes more pronounced in the direction perpendicular to the plane of the sample, as does the degree of in-plane orientation of the polymer chain as seen by C-C-C σ*. These changes are overall suggestive of chain relaxation and reorientation relative to the surface; in concert with the absorption results presented above, this also suggests the beginnings of the development of an oxidized layer at the surface. Other DR values are listed in this table, but must be disregarded due to quality of fit – a linear fit with an R^2 value less than 0.9 was chosen as a minimum threshold to describe a genuinely ordered system, in light of the relatively few angles (3) at which the spectrum was measured.

VE Unexposed				
Peak (eV)	285.2	287.8	288.8	293.8
R^2	0.9788	0.9411	0.9981	0.9334
Dichroic Ratio	**-0.10189**	**0.03757**	**0.05878**	**0.07826**
VE 246 °C 60min				
Peak (eV)	285.2	287.8	288.8	293.8
R^2	0.1931	0.0612	0.9705	0.9201
Dichroic Ratio	0.1782	0.02075	**0.15715**	**0.33447**

Table 6-1 - Dichroic ratio information for unexposed and thermally exposed resins. Usable dichroic ratio values are presented in bold, with their R^2 values highlighted in green.

6.3.2 Laser induced fluorescence following thermal exposure

Having established substantial chemical changes at the surface of the material through its thermal aging process, the LIF technique was used to collect information on the intensity and wavelength shift of the fluorescence signature from the sample following exposure. Due to the presence of carbon fibers within the sample, we can readily state that the fluorescence observed comes from the resin coating of the sample above the top layer of the fiber weave.

Figure 6-6 shows a plot of (non-normalized) fluorescence signals from samples exposed for 30 minutes at a range of temperatures. There is a general increase in the overall fluorescence intensity with higher temperatures; of note is the significant jump in intensity between exposures at 205 °C and 220 °C. Figure 6-7 shows the same collection of spectra following normalization; it is clear that the curve for fluorescence intensity widens to a higher wavelength as a function of exposure. As with overall intensity, the width increases significantly between exposures at 205 °C and 220 °C. This suggests a transition point in the mechanism responsible for the increase in fluorescence. This phenomenon tracks with the increase in the peak area indicating aromatic C=C (at 285.2 eV) in the NEXAFS spectra presented previously, suggesting the aromatic ring of mobile styrene as the cause for both fluorescence intensity and broadening. In Figure 6-8, the increase in half-maximum wavelength is plotted for all exposure temperatures and times. The increased shift is evident across all exposure times.

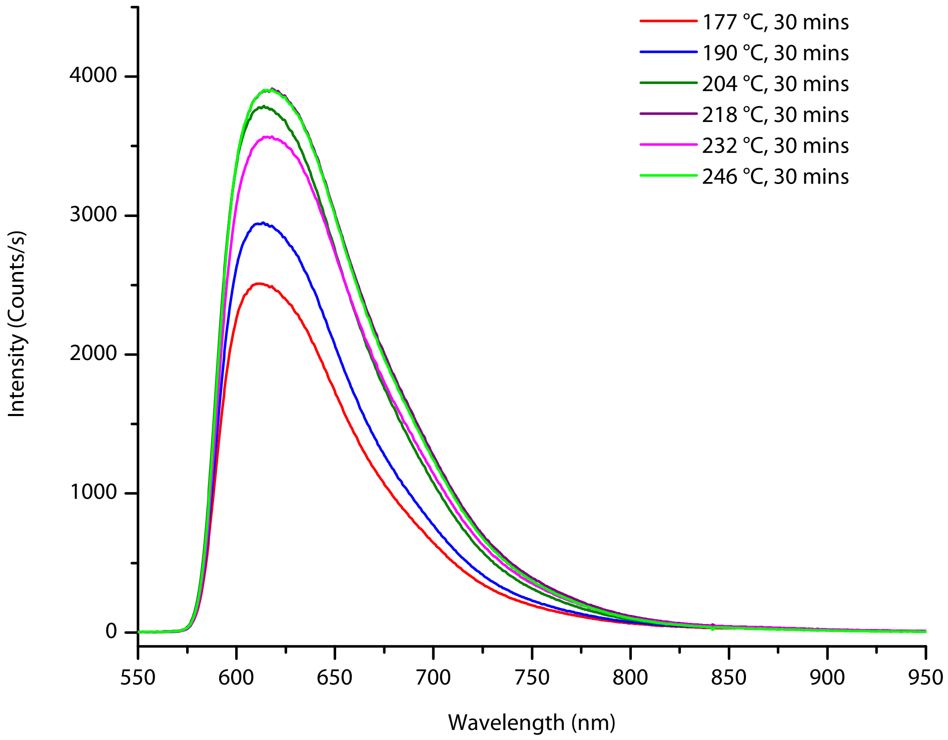

Figure 6-6 – Non-normalized laser-induced fluorescence spectra of CFVE composites exposed for constant times to a range of temperatures above T_g.

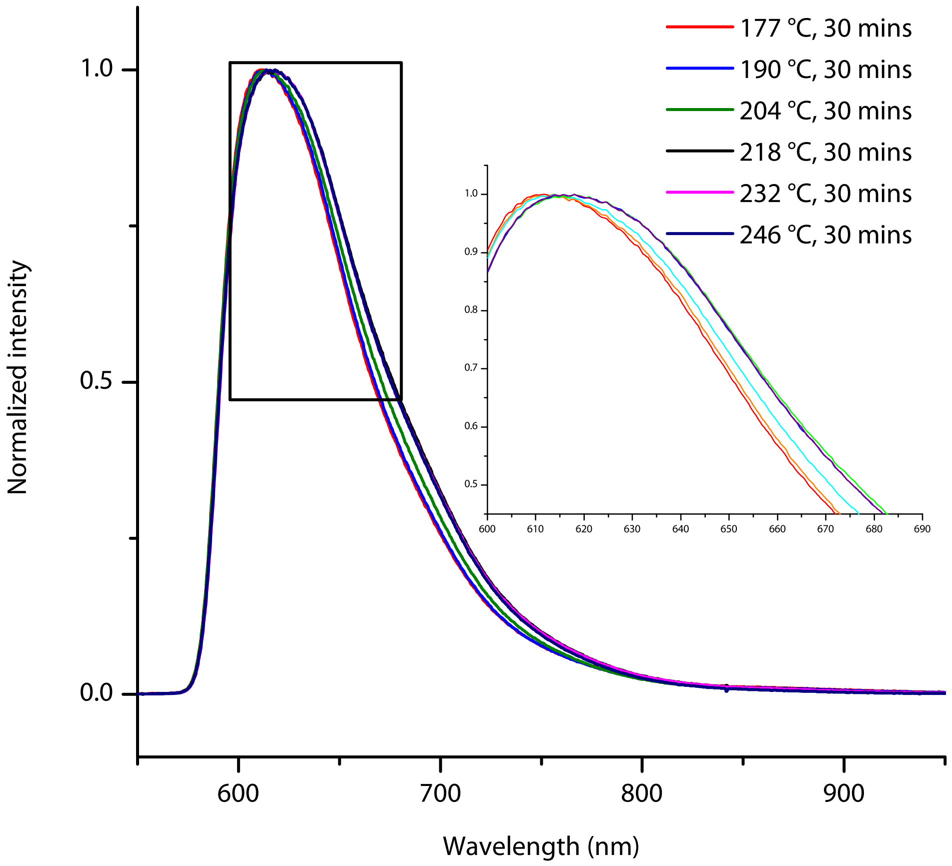

Figure 6-7 – Normalized laser-induced fluorescence spectra of CFVE composites exposed for constant times to a range of temperatures above T_g. Inset: magnified view of the peak region.

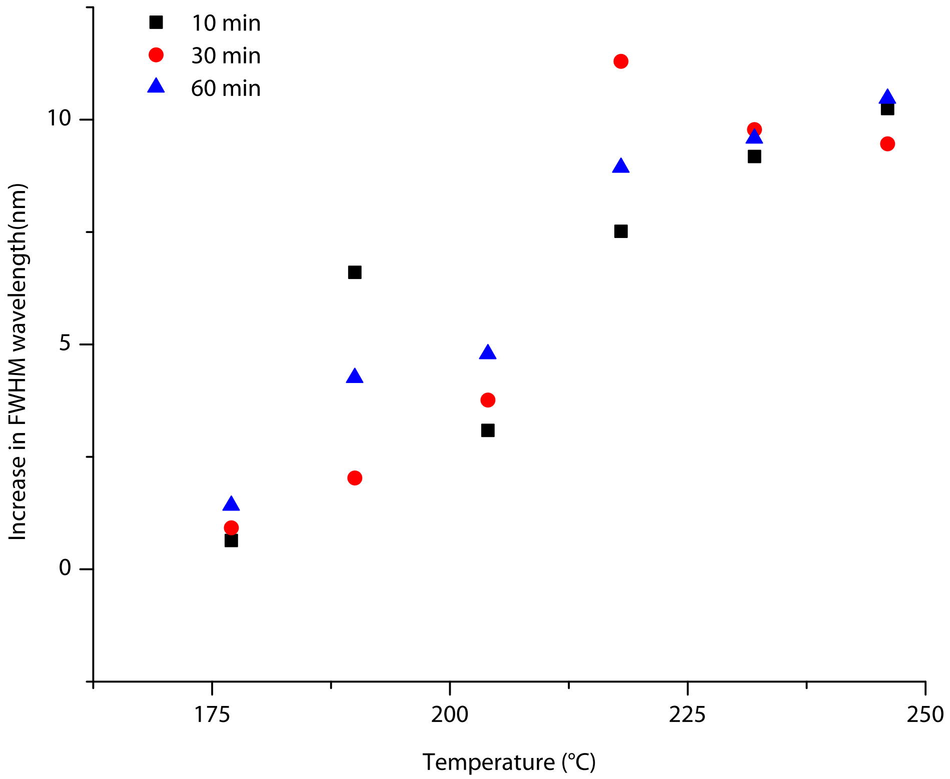

Figure 6-8 – Broadening of FWHM in laser-induced fluorescence spectra following exposure at t = 10, 30, and 60 minutes. This figure not discussed Note inconsistencies in the order of the FWHM data.

It is interesting to note the apparent equivalence of different thermal exposure conditions. From Figure 8, it is easy to see that shifts in the FWHM may correspond to a given exposure temperature and duration, as well as another higher-temperature, shorter-duration set of conditions. Although the data does show deviations due to inherent heterogeneity, it appears that this pattern holds generally at lower temperatures (up to 205 °C). This equivalence would serve well in the use of this technique in field-based non-destructive testing.

6.3.3 Mechanical testing of exposed composites

The spectroscopic methods employed above assess the chemistry of the surface and near-surface regions to depths on the order of microns. In order to gauge the mechanical effects of thermal exposure, we must investigate the bulk mechanical properties. Figure 6-9 presents the values of the storage modulus (the energy stored due to elastic motion during vibration) after exposure as a function of temperature and time. Analysis of the storage modulus shows an initial increase of roughly 10%, followed by a comparable decrease at exposure to higher temperatures and longer times. This data correlates to a decrease in this modulus after the laser fluorescence intensity reaches a maximum value.

This initial increase in storage modulus may be considered as an increase in material stiffness. At the lower range of thermal exposure in this system, styrene is observed to be migrating to the surface of the sample; La Scala measured outgassing at lower temperatures, but found an exponential increase in styrene outgassing rates as a function of temperature [5] Additionally, we have demonstrated above that a high-temperature exposure for 150 minutes leads to a significant depletion of the amount of detectable styrene at the surface, suggesting a fairly rapid outgassing process. Accordingly, in line with the changes to the storage mechanism, we propose that the initial increase is caused primarily by a loss of plasticizer, due to sample heating above T_g. The subsequent drop in storage modulus may indicate the onset of thermal decomposition and chain scission, demonstrating a critical threshold value for damage.

An alternative explanation could lie at the fiber/matrix interface. Plasticizer is distributed throughout the matrix, and in Chapter 5 we describe the presence of large voids (indicating uncured reaction products) in fairly close proximity to the fibers. These unreacted organics would become pressurized with heating, which could lead to a blistering effect due to osmotic pressure which may impact the interfacial surface. This breakdown in fiber/matrix interfacing would lead to a reduced ability to transfer stress from the matrix to the fiber, and thus a lower storage modulus. No supporting evidence is available to support this theory, other than the above-noted formation of surface blisters as a result of thermal damage in [20].

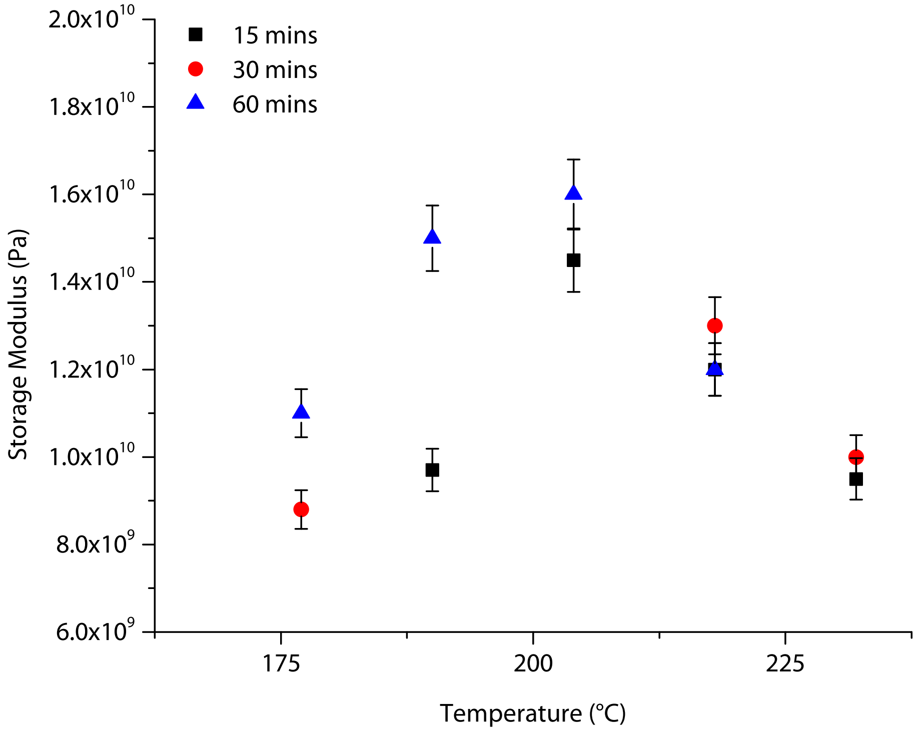

Figure 6-9 – Changes in storage modulus at room temperature as a function of time and temperature of exposure.

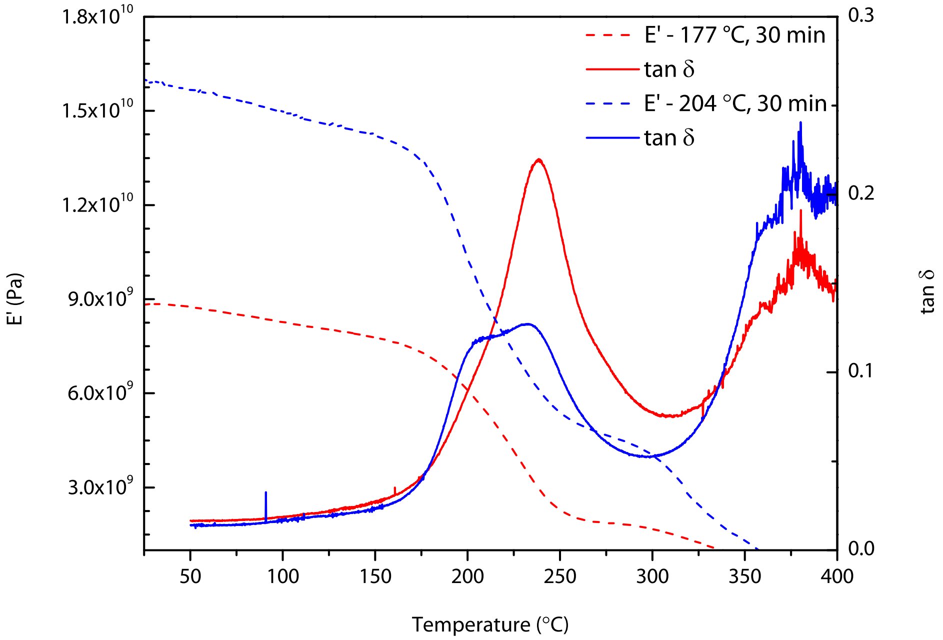

Figure 6-10 - DMA curve comparison showing storage modulus and tan δ for exposures at two different conditions.

Figure 6-10 demonstrates the evolution of the storage modulus and the tan δ curve , which measures the damping properties of the material. Under minimal exposure conditions, there is a single peak in tan δ, indicative of a single damping transition during oscillation directly related to T_g, demonstrating a single phase transition. Following thermal exposure, there is an evolution of a second damping mode peak at a temperature approximately 50 °C lower than the main transition.

This second peak appears to occupy a significant quantity of the total integrated area of tan delta, suggesting a significant quantity of contributing material. This peak has evolved in a sample where the storage modulus has reached its maximum value (204 °C, 30 mins), likely hinting at the origin of the subsequent decline. If we consider the plasticizer concentration model as the cause, then this curve suggests the development of essentially a two-phase material, with styrene-rich and styrene-poor regions. The difficulty of assigning this comes from the high degree of fiber loading in the composite (as seen in ablated cross-sections in Chapter 5), which suggests that the interphase chemistry between fiber sizing and matrix resin is the more likely region of interest. A plausible understanding of this two-phase system would then come from considering the interphase to be either rich or poor in plasticizer, which would certainly impact the mechanical properties of the interphase. Sizing itself is likely to act as a plasticizer in the matrix, in order to resiliently transfer energy from matrix to fiber without breakage. Additional plasticization would lead to a depressed T_g and lower elastic modulus, as is seen in this figure.

At higher exposures (e.g. 220 °C, 30mins), the new peak of tan delta does grow larger than is seen here. We have assigned the cause of the increase in storage modulus in this shown exposure to an overall loss of plasticizer in the sample, but it is not unreasonable to then attribute the second damping mode to styrene-rich regions due to the diffusion path through the resin of the sample. With such a high degree of fiber loading, the path of diffusion is limited and restricted, which offers the opportunity for gradients to build up in the interphase region around fibers.

The second explanation for this second damping mode is the beginnings of interfacial failure on a large scale in the sample. Reduced adhesion does contribute to a lowering of the observed temperature of the tan delta peak, and in light of the observed voids and demonstrated surface blistering, this theory represents a somewhat simpler explanation for the development. The contradiction in this model comes from the increased storage modulus at "mid-range" exposures such as the one discussed here, since adhesion failure would not contribute to an increase in storage modulus; rather, the opposite should occur. It is possible that both of these models partially describe the mechanism in play.

6.4 Conclusions

Low-grade thermal exposure has been shown to have an impact on mechanical performance in CFVE composites. From vibrational and x-ray spectroscopic analysis, it appears that this thermal damage results in significant migration of unreacted styrene monomers from the bulk of the sample to the surface, and requires either higher temperature exposure or longer exposure times at lower temperatures for adequate thermal damage to breach the surface and permit egress. Based on the principles of fluorescence, this suggests that laser-induced fluorescence measurements are exciting and detecting the aromatic rings of the monomer prior at the surface, with a different mechanism for fluorescence occurring after outgassing, due to surface thermo-oxidation. The changes in mechanical properties observed after thermal damage suggest the evolution of a second "phase" of resin with a lower T_g, which could be accounted for by the development of styrene-rich and styrene-poor regions in the resin and interphase, where the plasticization effect of styrene results in a change to T_g. A second interpretation for mechanical degradation is that voids containing unreacted components are pressurizing and bursting, leading to the beginnings of interfacial failure.

6.5 References

[1] Sorathia U, Dapp T. Structural performance of glass/vinyl ester composites at elevated temperatures. SAMPE Journal. 1997;33:53-8.

[2] Martin R. Ageing of Composites. 1st ed. Cambridge, England: Woodhead Publishing Limited; 2008.

[3] Hiltz JA. Low-temperature thermal degradation studies of styrene-crosslinked vinyl ester and polyester resins. Def. Res. Establ. Atl.,Dartmouth,NS,Can.; 1988. p. 39 pp.

[4] Regnier N, Mortaigne B. Analysis by pyrolysis/gas chromatography/mass spectrometry of glass fiber/vinylester thermal degradation products. Polym Degrad Stab. 1995;49:419-28.

[5] La Scala J, Ulven C, Orlicki J, Jain R, Palmese G, Vaidya U, et al. Emission modeling of styrene from vinyl ester resins. Clean Techn Environ Policy. 2007;9:265-79.

[6] Rein A, Seelenbinder J. Thermal Damage in Composites - Correlation of Short Beam Shear Data with Fourier Transform Infrared Spectroscopy. Application Note 204. 2009:1-2.

[7] Crawford S, Lungu CT. Influence of temperature on styrene emission from a vinyl ester resin thermoset composite material. Science of The Total Environment. 2011;409:3403-8.

[8] Fisher WG, Storey JME, Sharp SL, Janke CJ, Wachter EA. Nondestructive inspection of graphite-epoxy composites for heat damage using laser-induced fluorescence. Appl Spectrosc. 1995;49:1225-31.

[9] Kulowitch P, Scott WR. Detection of thermal damage in epoxy-based composites using laser pumped fluorescence. Nondestructive Characterization of Materials XI, Proceedings of the International Symposium, 11th, Berlin, Germany, June 24-28, 2002. 2003:545-53.

[10] Chatterjee A. Thermal degradation analysis of thermoset resins. Journal of Applied Polymer Science. 2009;114:1417-25.

[11] Scott IG, Scala CM. A review of non-destructive testing of composite materials. NDT International. 1982;15:75-86.

[12] Signor AW, VanLandingham MR, Chin JW. Effects of ultraviolet radiation exposure on vinyl ester resins: characterization of chemical, physical and mechanical damage. Polymer Degradation and Stability. 2002;79:359-68.

[13] Yang XF, Vang C, Tallman DE, Bierwagen GP, Croll SG, Rohlik S. Weathering degradation of a polyurethane coating. Polymer Degradation and Stability. 2001;74:341-51.

[14] Keene LT, Halada GP, Clayton CR. Failure of navy coating systems 1: chemical depth profiling of artificially and naturally weathered high-solids aliphatic poly(ester-urethane) military coating systems. Progress in Organic Coatings. 2005;52:173-86.

[15] Lenhart JL, Fischer DA, Chantawansri TL, Andzelm JW. Surface Orientation of Polystyrene Based Polymers: Steric Effects from Pendant Groups on the Phenyl Ring. Langmuir. 2012;28:15713-24.

[16] Sohn KE, Dimitriou MD, Genzer J, Fischer DA, Hawker CJ, Kramer EJ. Determination of the Electron Escape Depth for NEXAFS Spectroscopy. Langmuir. 2009;25:6341-8.

[17] Socrates G. Infrared Characteristic Group Frequencies: Tables and Charts. 2nd ed. Chichester: John Wiley & Sons; 1994.

[18] Obst M, Grathwohl P, Kappler A, Eibl O, Peranio N, Gocht T. Quantitative High-Resolution Mapping of Phenanthrene Sorption to Black Carbon Particles. Environmental Science & Technology. 2011;45:7314-22.

[19] Stöhr J. NEXAFS Spectroscopy: Springer; 1992.

[20] Goodrich T, Lattimer B. Microscopic behavior of composite materials during heating and cooling. Proceedings of the 17th international conference on composite materials2009. p. 27-31.

Chapter 7: Physicochemical investigation of chemical paint removers I: Interactions of methylene chloride with polyurethane coatings

The content of this chapter is taken directly and completely from a manuscript submitted (though not yet accepted) with the same title to the journal Progress in Organic Coatings by this author. This work represents a collaborative effort between Stony Brook University and the Naval Research Laboratory in determining the mechanism of action of methylene chloride in coatings removal. Co-authors on this manuscript are Ms. Kelly Watson, Dr. James Wynne, Dr. James Yesinowski, and the dissertation advisor, Dr. Clive Clayton.

Ms. Watson and Dr. Wynne contributed TGA, DSC, and vapor entrapment GC-MS results to this work; Dr. Yesinowski contributed solid-state NMR findings. In combination with our spectroscopic results obtained through XPS, Raman, and ATR-FTIR analysis, we have been able to elucidate the function of methylene chloride in the coating through investigation both while the coating is swollen with solvent and after it has dried and relaxed. No claim is made by this author on the results or work provided by these collaborators. Portions of this work have been included in US Navy memorandum report #NRL/MR/6120—11-9368, on which the author, dissertation advisor, and outside committee member are all co-authors.

7.1 Introduction

Chemical paint strippers based on methylene chloride and phenol are widely used to remove polymeric coatings. These strippers are highly effective, inexpensive and have minimal impact on the substrate. However, environmental and health concerns have dictated a need to find suitable replacements. This is a significant issue in the restoration of historic artwork and furniture, where careful design of solvent systems through the use of Hansen solubility parameters is employed in removing coatings while protecting the delicate substrate [1]. Unfortunately, efforts to replace solvent based paint removers in military applications have only produced less effective alternatives [2]. Methods such as solid particle blasting and laser ablation [3] create their own hazards: particle blasting produces toxic dust, laser ablation requires protection from the laser, and both are more cumbersome and expensive than solvent-based removal. Efforts to replace methylene chloride and phenol by other components in solvent-based paint strippers have been largely unsuccessful. The subsequent solvent systems are often less effective, as is seen with alkali or acid based mixtures [4].

There are few published studies in the scientific literature on the mechanism or mechanisms by which methylene chloride and other components of paint strippers work to remove polymeric coatings. The conclusion has been that solvent-based paint removing formulations wet the paint surface and then penetrate the layers to the underlying substrate by diffusion through the coating [5, 6]. Small molar volume solvents, *i.e.* water and methylene chloride, are presumed to penetrate the coating by more easily fitting into spaces between the polymer chains and diffusing through these spaces and channels. A recent paper by Croll [7] discusses the current state of knowledge and considers the effect that swelling by solvents has on "the cohesive and adhesive properties of a cross-linked polymer network." In this work, the Flory-Rehner and the Griffith equations are used to estimate the reduction in strength and resistance to fracture caused by swelling. The swelling effects of vapor-phase methylene chloride in polyurethanes was noted by Volkov [8] using FTIR, where an increase in the amount of free (relative to hydrogen-bonded) carbonyl groups was observed, suggesting that this swelling can occur by interfering with inter-chain hydrogen bonding.

The solvent penetration into cross-linked polymeric networks that is a key aspect of the paint-stripping process is related to an area that has received some attention, the permeation of small molecules, usually gaseous, through polymer membranes. In particular, the ability of a small molecule to enter a polymer matrix presupposes the existence of some “unoccupied volume” (the term “free volume” is also used, although its definition may vary), i.e. cavities consisting of open space outside the van der Waals radii of the atoms of the polymer [9-12]. Theoretical simulations of polymer chains having a given packing density have yielded histograms of the percentage of free volume vs. the volume of the maximum-size sphere fitting in the cavity. As an example of such results, for polypropylene 20° below its T_g of -20 °C the largest cavity volume thus calculated is ca. 27 Å^3 (corresponding to a diameter of 3.7 Å), although a more representative volume of 9 Å^3 (corresponding diameter 2.6 Å) represents the approximate median point in terms of free volume fraction available [12]. These dimensions can be compared to those of the methylene chloride molecule, which closely approximates a prolate ellipsoid in shape [13]. The effective radius along the Cl-Cl vector direction is 3.3 Å, and thus two axes in the molecule present a long dimension of twice this radius, or 6.6 Å. A comparison of this dimension with those calculated from the free volumes [12, 14] demonstrates that even though methylene chloride may be a “small” molecule, it is too large to fit into the existing free volume cavities (of this polymer at least), and thus must exert its effect by a dynamic process of swelling the polymer to create more space for solvent molecules. However, the connectedness of such cavities through “throats” or “necks” to form a percolation pathway is also crucially important, and it is likely that polymer dynamics also plays a role by modulating the size of such openings to transiently allow a small molecule to penetrate. Once this process has begun, at least in the case of liquid solvents, one expects a continuing expansion of the polymer by the swelling that facilitates further penetration by the solvent molecules. The ability of molecules to penetrate into a polymer can be predicted by comparing their Hansen solubility parameters, where solvents and polymers with similar values are more likely to be compatible. Given the relatively complex interactions that may occur between the polar methylene chloride molecule and polyurethane, these Hansen values must be used over the simpler Hildebrand solubility parameters [15]. As one might expect given its effectiveness, the Hansen solubility parameters of methylene chloride ($\boldsymbol{\delta_d}$**:** 18.2 $MPa^{0.5}$ $\boldsymbol{\delta_p}$**:** 6.3 $MPa^{0.5}$ $\boldsymbol{\delta_h}$**:** 6.1 $MPa^{0.5}$) [16] are very similar to those of polyurethane ($\boldsymbol{\delta_d}$**:** 18.0 $MPa^{0.5}$ $\boldsymbol{\delta_p}$**:** 6.3 $MPa^{0.5}$ $\boldsymbol{\delta_h}$**:** 6.3 $MPa^{0.5}$) [17].

This paper begins to fill the knowledge gap regarding the molecular-level interactions important to the action of paint strippers by using a combination of techniques to characterize the interaction of methylene chloride with model polyurethane topcoats. Model paint-removing systems, based upon those currently in use, are constructed to permit analysis of solvent-polymer interactions with a minimum of interference. One of the crucial changes taking place during this solvent-induced swelling process is the transition from a glassy polymer (i.e. one below its glass transition temperature T_g) to an elastomer (or rubbery state) above T_g, with small irreversible changes to T_g occurring. Differential Scanning Calorimetry (DSC) was used to monitor this change, and solid-state proton (^1H) Nuclear Magnetic Resonance (NMR) spectroscopy to follow the increase in the polymer segmental dynamics associated with the transition to an elastomeric state. Vibrational spectroscopy (specifically FTIR and Raman) was used to survey for chemical changes in the polymer resulting from the solvent swelling. Solid-state deuterium (^2H) NMR of isotopically-labeled methylene chloride (CD_2Cl_2) was used to specifically observe this component and to obtain information about its physical state in the topcoat polymer network. Finally, XPS identified heterogeneous coating characteristics of a commonly-used cellulosic stabilizer that may serve an important function.

7.2 Materials and Methods

7.2.1 Chemicals and Coatings

All chemicals were reagent grade and used without further purification. Mixtures were prepared by weight percent according to Table 7-1.

	Compound	Methylene Chloride (MC)	Ethanol	Water	Phenol	Methocel
	Commercial Paint stripper[a]	60.7	5.8	7.8	15.8	1.2
A	Methylene Chloride	100	---	---	---	---
B	MC and EtOH	91	9	---	---	---
C	MC, EtOH and Water	82	8	10	---	---

Table 7-1 – List of control formulations by weight percent

[a] Contains also toluene (1.3%), sodium petroleum sulfonate (5.5%) and paraffin wax (1.9%). Methocel F4M PRG (cellulose ether, DowWolff Cellulosics) is used to enhance solvent phase miscibility and viscosity.

Current military coatings were selected for study, in the form of two polyurethane topcoats, based upon military specifications MIL-DTL-53039 (coating PU-1) and MIL-PRF-85285 (coating PU-2). The coatings were unsupported free films, with a final thickness of approximately 127 μm (5 mils) (see Table 7-2). For ease of analysis, coatings used in this study were clear films, without pigments, fillers and pigment related dispersion and wetting agents. Antifoaming agents were retained to facilitate sample preparation. Current formulations were used based on the same raw materials and binder ratios used in the commercial product. However, the solvent ratios were altered to compensate for the change in surface tension, viscosity and other properties resulting from the removal of the pigments and other components. Initial application using conventional spray equipment and settings failed due to the high viscosity of the formulations; a drawdown mechanism for creating coatings also failed as creating films of the approximate 102 µm (4 mil) thickness in one application trapped too many bubbles in the coating as it cured. All formulas were ultimately sprayed in multiple layers on release paper allowing 16-24 hour cure time between each layer and a final seven day cure time. This minimized bubble formation and created coatings of the desired thickness. The clear coatings were prepared on release paper and subsequently removed for evaluation.

Coating	Coating Type	Military Specification	Final thickness (mm)	Specific coating description
Sample PU-1	Polyurethane	MIL-DTL-53039	0.13	Single component aliphatic polyurethane topcoat
Sample PU-2	Polyurethane	MIL-PRF-85285	0.13	Two component high solids polyurethane topcoat

Table 7-2 – List of coatings prepared for analysis.

7.2.2 Solvent Exposure of Coatings for Thermal and Spectroscopic Analysis

Approximately two centimeter squares of each coating were cut and placed into individual scintillation vials. To each vial the respective solvent or solvent mixture was added until the coating was completely covered (~10 mL). After exposure periods of either two hours or two days, the liquid was decanted, the surface of the coating rinsed with 5 mL EtOH to remove any impurities that may have been extracted and remained on the surface, and the coating allowed to air dry in the vial for >2 weeks. Caution was taken to ensure that the vial did not contain any solvent droplets and that the coating was completely dry before testing. For the spectroscopic study of swollen coatings, square samples were exposed to solution for several hours, then removed and analyzed immediately without drying.

7.2.3 Differential Scanning Calorimetry (DSC)

Differential scanning calorimetry (DSC) was performed on a TA Instruments Q20 DSC with the DSC Refrigerated Cooling System (RCS) and a purge gas of nitrogen set to 50 mL/min. Samples of approximately 1-2 mg were placed into TA Instrument Tzero aluminum pans, with an empty aluminum pan used as reference. Samples were analyzed twice from -90 °C to 150 °C at 20 °C/min. All data reported were taken from the second scan. Glass transition temperatures were found using the TA Universal Analysis program.

7.2.4 Thermogravimetric Analysis (TGA)

Thermogravimetric analysis (TGA) was done on a TA Instruments Q50 TGA using a platinum sample pan. The analysis was carried out in the presence of oxygen with breathing air used as the sample purge gas. Nitrogen was used as the purge gas for the balance. Data were recorded from ambient temperature to 700 °C at 5 °C/min. Plots of percent weight loss versus temperature were made to analyze the data.

7.2.5 FTIR-ATR

FTIR spectra were recorded on a Thermo Scientific Nicolet 6700 FTIR spectrometer equipped with a Smart Performer ATR attachment using a germanium crystal and constant pressure tower, and also with a Smart iTR attachment using a zinc selenide crystal and constant pressure tower. A DTGS detector collected 64 scans of the sample. Data acquisition and analyses were performed using the Thermo Scientific OMNIC software suite.

7.2.6 Raman spectroscopy

Raman analysis was carried out using a Nicolet Almega dispersive spectrometer coupled to an Olympus microscope with 10x and 100x objective lenses, and also using a WiTec α-500 confocal Raman microspectrometer with 20x and 100x objective lenses. The sample was scanned 128 times using a 1s collection time, with the spectra analyzed using the Thermo Scientific OMNIC software suite. Samples were placed on quartz slides to reduce background interference. In the case of the solvated coatings, samples were placed on a quartz slide with additional solvent, then covered with a second quartz slide to maintain sample geometry and to direct solvent evaporation away from the objective. Additional solvated samples were analyzed by having the sample adhere to the inner face of a quartz cuvette, which was then capped and placed horizontally for analysis. Efforts were made to minimize sample heating while performing the analysis.

7.2.7 XPS

X-ray photoelectron spectra were obtained using a VG ESCA-3 Mk. II system under ultra-high vacuum (10^{-9} Torr ≡ 10^{-7} Pa). X-rays were generated from a magnesium anode at 6 kV with a filment current of 20 mA. A pass energy of 20 eV was applied to emitted photoelectrons for analysis. Scans for each region were executed with a spacing of 0.1 eV and a 100ms dwell time; each scan was repeated 50 times and co-added, using the VGX900i control program. Spectra were calibrated using the adventitious carbon peak at 284.5 eV. Analysis was performed using the CasaXPS software package.

7.2.8 Vapor Entrapment

Vapor above a coating in an air tight vial (the headspace) was injected into the GCMS after the vial had been heated at approximately 80 ^{0}C for 30 minutes. The GCMS system was an

Agilent 7890A gas chromatograph equipped with an Agilent 5975C mass selective detector operating in electron ionization mode and an Agilent 7693A autoinjector. The column utilized was an Agilent HP-5MS (5% phenyl) methylpolysiloxane film. The carrier gas was helium with a flow rate of 1 $mL \cdot min^{-1}$. The injection volume was 10 μL with a split injection ratio of 50:1. The temperature program has an initial temperature of 35 °C for one minute, then 10 °C per minute ramp to 90 °C with a three minute post run hold at 250 °C. The injection port temperature, MS quad temperature, and source temperature were 220 °C, 150 °C and 230 °C, respectively. The detector was set to scan a mass range from 20 to 500 *m/z*.

7.2.9 Solid state proton (^1H) and deuterium (^2H) NMR

The ^1H NMR results were obtained on a Bruker DMX-500 spectrometer using a non-spinning high-power ^1H probe with a horizontal 5 mm solenoidal coil containing the glass sample tube with film. Proton NMR spectra and ^1H relaxation times were obtained at 500 MHz (11.7 T field). Measurements of the spectra yield a full-linewidth at half-height (HHLW), the spin-lattice relaxation time (T_1) and the spin-lattice relaxation time in the rotating frame ($T_{1\rho}$), and were made as a function of temperature to allow comparison of the dynamics induced by an increased temperature with dynamics induced by solvent activity. ^1H NMR studies were done on coating PU-1 before and after a five minute exposure to methylene chloride.

The ^1H spin-lattice relaxation times (T_1) were measured using a saturation-recovery pulse sequence with typically a dozen different recovery delays, and fitting the recovery curve of the peak intensity to a single-exponential recovery curve with time constant T_1 (using Origin Pro 7.0). The intensities of static ^1H NMR peaks vs. spin-lock times (typically nine values) in a spin-locking pulse sequence were fit using Origin to a single-exponential decay curve with a decay time constant $T_{1\rho}$. Measurements were repeated at different temperatures and for different samples.

All of the ^2H NMR spectra (nuclear spin I=1) were acquired at 76 MHz on a Varian/Agilent NMR spectrometer at 11.7 T, using a high-power static probe with a 5 mm horizontal solenoidal coil and 2.75 μs 90° pulses. Spectra of the isotopically-labeled methylene chloride (CD_2Cl_2) were obtained using a quadrupolar-echo pulse sequence ("ssecho1d" provided by Varian) in order to be able to detect any extremely wide (>200 kHz) "powder-pattern" spectra characteristic of ^2H in the absence of molecular motions. An error was discovered in the phase-cycling of this manufacturer-supplied program after all experiments were completed. The phases of the last two (out of eight) phase cycles had the phases of the second pulse interchanged from the correct values, which produced two phase cycles where the two pulses were not orthogonal to each other as they should be. However, because the spectra were obtained exactly on-resonance, the net effect of this error was relatively minimal: a reduction of the acquired signal amplitude to 75% of what it should have been, and some loss in the artifact-removal properties of the phase-cycling. These effects do not affect the data analysis and conclusions presented later.

7.3 Results and discussion

7.3.1 Changes in thermal properties

Upon removal from solvent immersion (exposure) all coatings remained intact, though polymer solvation was evident from the lack of rigidity in all samples. Some shape deformation was observed; coatings which curled during exposure then retained the curled shape after removal of the solvents. Coatings retained their transparency or opacity after exposure; an increase in transparency was observed heterogeneously in samples exposed to solvent mixture C.

It is generally thought that paint removal involves the softening of the applied coating, which occurs not only through chemical degradation but also through polymer swelling [18]. Thermal data regarding phase behavior of the coating could suggest the nature of effects resulting from exposure. The glass transition temperatures obtained by DSC are given in Table 7-3. In both coatings, exposure to (A), (B), and (C) show a modest reduction (by 5-22 °C) in T_g from the unexposed control coating. Given the compositions of each mixture and its subsequent effect, it seems that methylene chloride is primarily responsible for this reduction of T_g. Longer exposure times did not lead to further depression of T_g.

Exposure Time	**Solvent System**	T_g (°C) Coating PU-1	T_g (°C) Coating PU-2
	Control (unexposed)	87±3	51±2
2 hour exposure	Methylene Chloride (A)	67±2	46±4
	Methylene Chloride and Ethanol (B)	67±4	44±3
	Methylene Chloride, Ethanol and Water (C)	70±3	45±5
Multiday exposure	Methylene Chloride (A)	72±1	44±3
	Methylene Chloride and Ethanol (B)	65±2	41±0
	Methylene Chloride, Ethanol and Water (C)	70±4	43±3

Table 7-3 – DSC results of coatings exposed to control solvent solutions, over short and long exposure periods.

7.3.2 Solvent persistence in coatings

Thermogravimetric analysis (TGA) was performed on all exposed coatings, with an unexposed coating serving as control. As seen in Figure 7-1, each coating exposed to (A), (B), and (C) shows a similar TGA curve that mimics the shape of that of the unexposed coating, except with a stronger weight loss by 150 °C. TGA shows significant and reproducible weight loss at low (<200 °C) temperatures indicative of solvent outgassing. The observed solvent outgassing did not begin until well above the boiling point of the solvents present, thus suggesting solvent-polymer interactions.

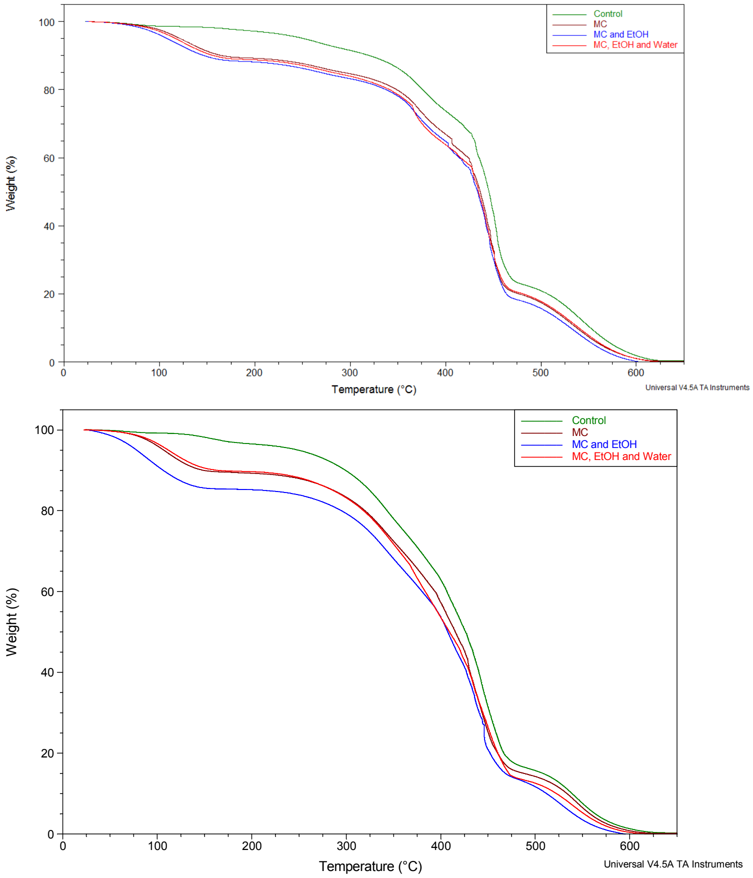

Figure 7-1 – TGA of PU-1 (top) and PU-2 (bottom), following exposure to solvent mixtures.

7.3.3 NMR of polymer-solvent interactions

In order to obtain molecular level information about the effects of solvents upon clear coatings using a very different spectroscopic approach, solid-state proton (^{1}H) and deuterium (^{2}H) NMR were employed. The ^{1}H NMR results provide information about the segmental dynamics of the polymer chains in the topcoat as a function of temperature and solvent exposure [19]. However, labeling the solvent with deuterium provides greater selectivity (because of the low natural-abundance of ^{2}H, 0.015%) as well as greater sensitivity to and theoretical interpretability of molecular dynamics and orientation due to the dominance of the large nuclear quadrupole interaction. This is exemplified by ^{2}H NMR studies of D_2O in epoxy [20] and in strained and unstrained nylon [21] and of deuterated small organic molecules used to probe stress/strain effects in polymers [22, 23] including d_5-phenol in nylon [24]. The ^{2}H NMR results provide molecular-level information about the solvent molecule itself, by relying upon isotopic-labeling of the methylene chloride.

7.3.3.1 Proton NMR

The ^{1}H NMR results from the unexposed sample of coating PU-1 were compared with those from the same sample exposed to methylene chloride for 5 minutes at 20 °C and then blotted dry. Figure 7-2 shows T_1 as a function of temperature for the film before and after exposure to methylene chloride, as well as the T_1 for the neat solvent alone. The T_1 of neat methylene chloride is long because it is an isotropic liquid with a short (*ca.* 1 ps) rotational correlation time [25], whereas the T_1 of the unexposed polymer film is significantly shorter and typical of non-rigid polymers. The near-equality of the two T_1 values of the polyurethane sample exposed to methylene chloride to those in the starting polyurethane film at the same two temperatures indicates that methylene chloride is in intimate atomic-scale contact with the polymer, since the proton NMR signal from the methylene chloride component contributes to the overall spectrum of the exposed sample (see Inset). This contact results in the methylene chloride having significant proton-proton dipolar coupling to the polyurethane polymer, which equalizes T_1 values by the process of spin-diffusion. There is no evidence whatsoever for free methylene chloride in liquid-like pools of any size, which would yield a sharper proton NMR peak than seen in the Inset to Figure 7-2, and one with a longer T_1.

The proton NMR spectra of the polyurethane topcoat clearcoat film (coating PU-1) are shown in the inset of Figure 7-2 – Proton NMR T_1 vs. temperature of clear-coat topcoat film PU-1 before (black circles) and after (red triangles) 5-minute exposure to methylene chloride at 20 °C. Also shown is the T_1 of neat methylene chloride (blue square). Inset: Proton NMR spectra of clear-coat topcoat film PU-1 at 296 K (blue dotted) and 363 K (red dashed-dotted) and methylene-chloride exposed film at 296 K (solid magenta).. The spectrum obtained at 296 K (23 °C) is greatly broadened by homonuclear dipolar interactions (around 50 kHz half-height linewidth), as expected for a crosslinked polymer with only limited segmental dynamics (the T_g from Table 7-3 was 87 °C). Heating the sample to near the T_g (363 K, or 90 °C) results in a substantial reduction in the linewidth due to greatly increased segmental dynamics that partially average out the dipolar interactions. Similarly, exposure to methylene chloride for 5 minutes at 20 °C results in a spectrum at 296 K that is greatly narrowed by an increase in the segmental dynamics, similar to the effects of increasing temperature alone. The line shape after exposure to methylene chloride also has the appearance of a sharper and a broader component added together, the former of which is still far broader than would be the case for purely liquid-like pools of methylene chloride. As discussed above, it is reasonable to attribute the sharper component to methylene chloride that is so strongly dipolar-coupled to nearby polymer protons that it shares the same T_1 relaxation time, again indicating that the solvent molecules are not in a free liquid state. Short exposure to methylene chloride results in significant polymer segmental motions at room temperature that resemble what occurs in the polyurethane alone after raising the temperature by approximately 70 ^{0}C, as seen in the inset to Figure 7-2.

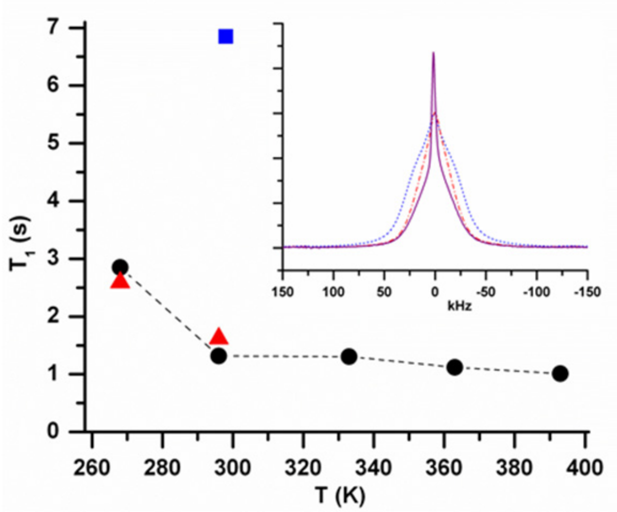

Figure 7-2 – Proton NMR T_1 vs. temperature of clear-coat topcoat film PU-1 before (black circles) and after (red triangles) 5-minute exposure to methylene chloride at 20 °C. Also shown is the T_1 of neat methylene chloride (blue square). Inset: Proton NMR spectra of clear-coat topcoat film PU-1 at 296 K (blue dotted) and 363 K (red dashed-dotted) and methylene-chloride exposed film at 296 K (solid magenta).

The $T_{1\rho}$ experiments as summarized in Figure 7-3 were conducted on this same polyurethane film before and after exposure to methylene chloride. For the unexposed film, the steep drop in $T_{1\rho}$ values above the maximum around 330 K can be interpreted as due to the activation of relatively slow motions on an approximately 15 μs time scale (the optimum time scale for $T_{1\rho}$ relaxation at the RF field strength used in the measurement). In an untreated coating these motions will begin to increase near the T_g of the coating (87 °C, or 360 K, from Table 7-3). Short exposure of the coating to methylene chloride allows these motions to occur at temperatures well below the T_g, as judged by the shorter $T_{1\rho}$ values at two temperatures after exposure to methylene chloride. This suggests that exposure to methylene chloride and the resultant swelling may be equivalent to raising the temperature in an unexposed coating by many tens of degrees. Here, a strong decrease in the $T_{1\rho}$ relaxation time results from exposure to methylene chloride, comparable to the depression seen at temperatures above the glass transition.

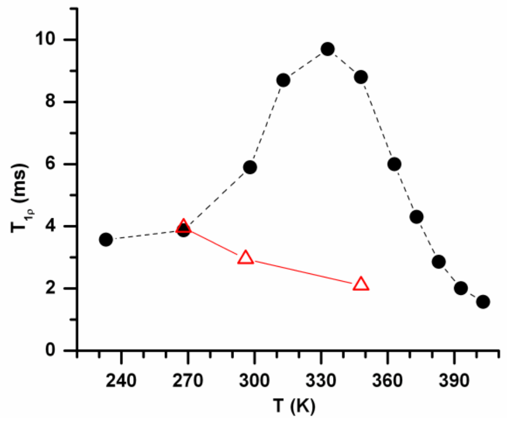

Figure 7-3 – Proton NMR T1ρ vs. temperature for polyurethane clear-coat PU-1 film before (solid black circles) and after 5-minute exposure to methylene chloride at 20 °C (open red triangles, showing the $T_{1\rho}$ behavior of the broad component in the spectrum only).

7.3.3.2 Deuterium NMR of polymer-solvent interactions

The deuterium NMR spectra of coating PU-1 clear film after a 10 minute exposure to deuterated methylene chloride (CD_2Cl_2) are shown in Figure 7-4. The narrow linewidth at room temperature (24 °C) indicates rapid rotational motion that largely averages out the ^{2}H nuclear quadrupole coupling constant of CD_2Cl_2, which has been reported to be 170 kHz at 77 K[26]. This motion occurs on a time scale shorter than 6 μs, the inverse of the static quadrupole coupling constant. The narrow HHLW of 1.4 kHz corresponds to 18 ppm, which seems to be rather broader than would be expected to arise from the free-liquid solvent.

Cooling the sample to 0 °C resulted in a broader spectrum that could be fitted very well to a Lorentzian line shape with a HHLW = 6.30 kHz, broader than the linewidth at 24 °C. The T_2 value was measured to be 67.2 μs, as shown in Figure 7-4 (middle inset). This value corresponds to a homogeneous linewidth of 4.74 kHz ($=1/[\pi T_2]$). The difference of 1.6 kHz from the (larger) measured linewidth again seems too large to be accounted for by broadening due to magnetic susceptibility or field inhomogeneities. It may be due to a distribution of small residual quadrupolar splittings that somehow do not result in a deviation from a Lorentzian line shape. This explanation might also account for the 1.4 kHz HHLW observed at 24 °C.

The measured T_2 is many orders of magnitude shorter than the ~3 s value expected for pure CD_2Cl_2 (the ^2H T_1 of CD_2Cl_2 containing 9 mole % CH_2Cl_2 has been measured to be ~3 s at 300 K, and $T_2=T_1$ for an isotropic liquid) [25]. The relevant equation for the full HHLW of the Lorentzian in the motionally-narrowed regime is $\Delta\omega 02\ \tau c / \pi$ (in Hz), where $\Delta\omega 02$ is the second moment (in angular frequency units) characterizing the rigid solid linewidth and τc the rotational correlation time [27]. The latter depends upon the molecule or particle size and the viscosity of the medium, and has been measured to be 0.82 ps from ^2H NMR of CD_2Cl_2 [25]. If we use this rotational correlation time and crudely estimate the root second moment $\sqrt{}\Delta\omega 02$ from the measured quadrupole coupling constant as $(170{,}000 \mathrm{x} 2\pi)$, then we obtain a HHLW for the free liquid of the order of 0.3 Hz. Thus, the measured T2 and corresponding broad homogeneous linewidth indicate that the CD_2Cl_2 molecule in the coating PU-1 clear film at 0 °C has a rotational correlation time more than four orders of magnitude greater than its value in neat CD_2Cl_2. Although one cannot assign a meaningful viscosity to the surrounding polymer matrix, it is clear that the rotational tumbling of the CD_2Cl_2 molecule is being restricted, quite plausibly by some sort of electric dipole-electric dipole interaction with polar groups on the polymer. The fact that the spectrum is not that of an immobilized solvent molecule indicates that the interaction energy is relatively weak compared to the thermal energy (kT, = 2.5 kJ/mol at 300 K).

The spectrum at a reduced temperature (-27 °C) of deuterated methylene chloride after swelling the coating is significantly broader than the spectra obtained at either 24 °C or 0 °C (note the different frequency scale in Figure 7-4). The HHLW is 14.1 kHz, but also apparent is an even broader peak at the base. The increase in linewidths suggests two different possibilities, or a combination of both. There may be a further degree of restriction to the rotational motion of the solvent molecules upon further cooling from 0 °C, and there may possibly exist two or more different environments, assuming that the linewidths are largely determined by $1/(\pi T_2)$. The alternative possibility is that there may be a distribution of residual quadrupolar coupling constants due to increased ordering at lower temperatures of the CD_2Cl_2 in the anisotropic polymer matrix.

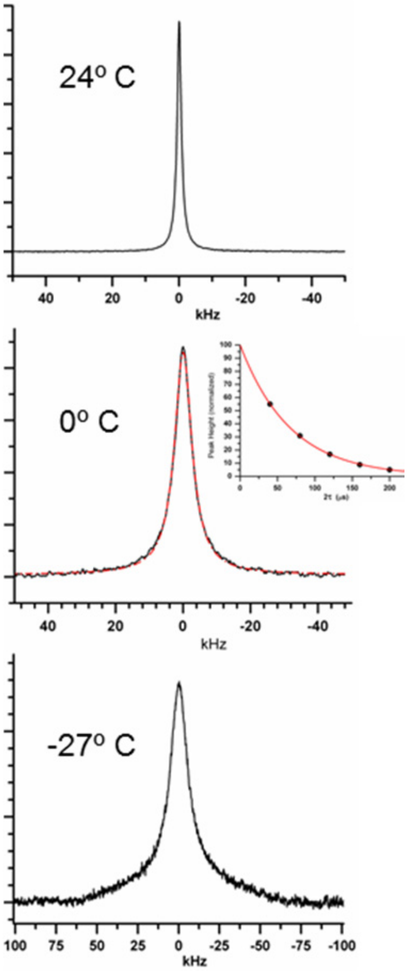

Figure 7-4 – Deuterium quadrupole-echo NMR spectra obtained at indicated temperatures of polyurethane clear-coat PU-1 film exposed to CD_2Cl_2 (d_2-methylene chloride) for 10 minutes at 20 °C, resulting in a 34.9% weight increase. The middle spectrum (solid black) has a Lorentzian fit (red dashed-dotted line) with a full HHLW = 6.30 kHz; the inset shows the single-exponential fit of peak intensity as a function of the total quadrupolar-echo delay time of 2τ to a T_2 decay time of 67.2 μs.

7.3.4 Raman spectra of solvent-polymer interactions

Vibrational spectroscopy offers further, and more detailed, evidence of the molecular association between methylene chloride molecules and chemical groups in the polyurethane film that is indicated by ^1H and ^2H NMR. Raman spectra of coatings PU-1 and PU-2 taken immediately following 1 hour exposure to methylene chloride are presented in Figure 7-5. With analysis performed immediately after removal from solvent, there is a significant effect observed in the carbonyl region of the spectrum. In coatings PU-1 and PU-2, the main carbonyl peak occurs at 1758 cm^{-1}, with the latter demonstrating an additional shoulder peak at 1735 cm^{-1}; as a result of exposure, spectra from both coatings evolve into a broad band centered around 1680 cm^{-1} and 1700 cm^{-1}, respectively. These evolved peaks suggest an increase in hydrogen bonding to the carbonyl group. Based on the chemistry of these coatings, the peak at 1758 cm^{-1} corresponds to free carbonyls found in urea [28]. The shoulder peak at 1735 cm^{-1} in coating PU-2 indicates carbonyl from the polyester cross-linker of the system. Fitted peaks at 1685 cm^{-1} are tentatively assigned to hydrogen-bonded carbonyls. Upon solvent exposure, a number of new peaks can be fit; these peaks are relatively broad compared to those found in the unexposed sample. These peaks cover a wide range from 1715 - 1635 cm^{-1}, all within the range expected for hydrogen-bound carbonyls. Their specific assignment is difficult without a thorough discussion of the specific coating chemistries. Given the number of additional peaks which form, and their energy displacement from those of the unexposed coatings, it is reasonable to suggest that more than one configuration of hydrogen bonding is occurring, with bonds forming between the carbonyl group and one or more solvent molecules. This bonding can explain the restriction on molecular tumbling in methylene chloride seen by NMR, discussed in 7.3.3.

Raman spectroscopy has been found to be sensitive to the solvation of carbonyl groups at resonant Raman excitation wavelengths (266nm) [29], but these effects are far less prominent at higher excitation wavelengths; specifically, no shift in the position of Amide I has been noted to be caused purely by solvation. Other research into the effects of solvent interactions on the Raman spectra of carbonyl groups [30, 31] has shown some decrease in the wavenumber for the excitation of this vibration, though not to the extent we observe, thus suggesting a stronger interaction in our system. The evolved peaks are observed to diminish and disappear after approximately 20 minutes, which corresponds to significant evaporation and outgassing of the solvent over this time. Given the irreversible curling seen in the samples following exposure, it seems that the increased segmental dynamics seen via NMR has permitted some degree of polymer chain rearrangement within the coating. Methylene chloride is able to dissociate from the carbonyl over a relatively short timeframe, indicating a low binding energy relative to kT, which is in line with predictions made from NMR, discussed in 7.3.3.

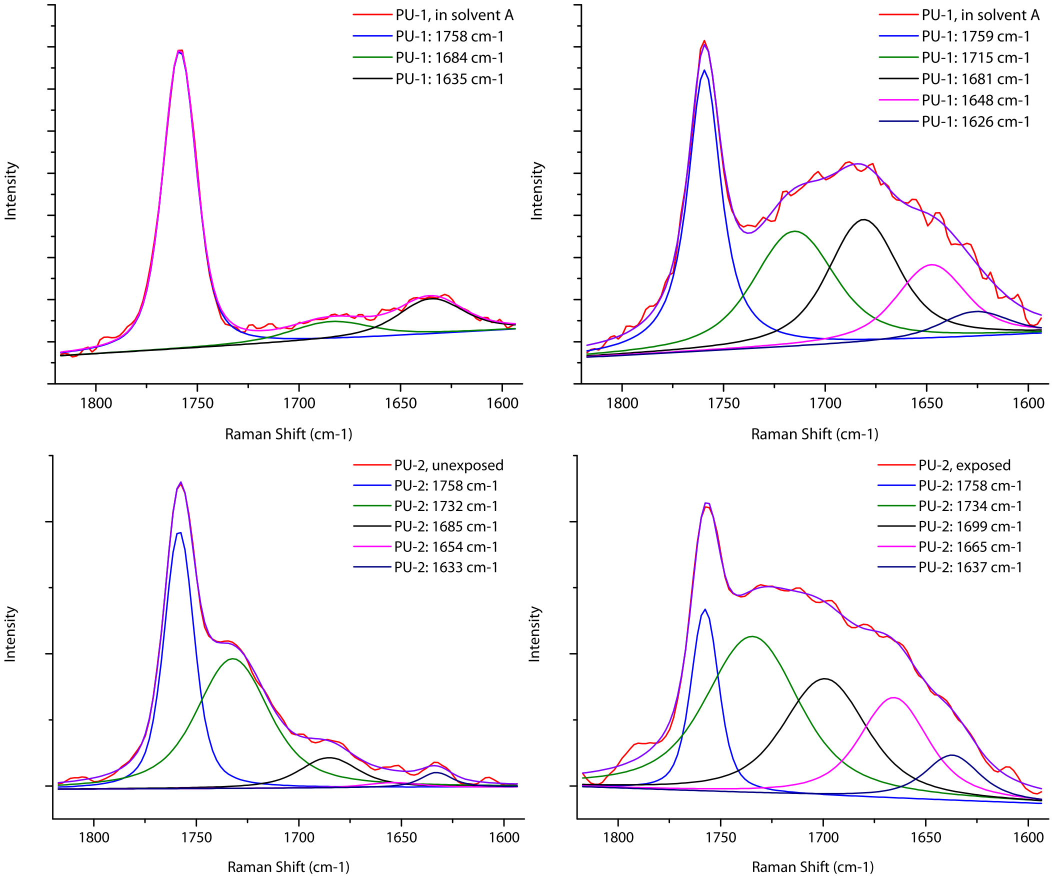

Figure 7-5 – Raman spectra of coatings PU-1 (top) and PU-2 (bottom) before and immediately following 1-hour exposure to solvent system A, with fitted peaks for the carbonyl region.

7.3.5 Deposition of stabilizer in solvent system C

Following exposure to solvent systems A and B, and after extensive drying (approximately 1 month, to ensure maximum solvent evaporation), neither coating system shows any observable chemical change through ATR-FTIR or Raman spectroscopy (as seen in Figure 7-6 and Figure 7-7). The lack of any significant changes in peak positions or intensities after exposure and drying indicate the absence of irreversible chemical changes. As noted in section 3.4, broadening of the carbonyl peak, which can be seen in wet samples, disappears after drying with no residual effect. While there are morphological changes (seen as curling of the free-standing film), likely due to chain rearrangement in order to relieve internal strain, these did not lead to any chemical modification; this suggests that the role of these solvents lies purely in dilation and transport of other active ingredients. Solvent system C causes a chemical change detectable only through the use of more surface-sensitive methods (confocal Raman and ATR-FTIR). Visually, the translucent clear coatings develop a heterogeneous distribution of spots which appear to make the coating more transparent. Surface spectra collected in these regions indicate the deposition of a very thin (2 μm or less, as determined by confocal Raman microspectroscopy) layer of methylcellulose, which is the component used to thicken and compatibilize solvent system C; the attenuation of the coating spectrum is incomplete, as seen by the persistent carbonyl peak in the spectrum, suggesting incomplete coverage of the sample area. Methylcellulose is used in the fully-formulated paint remover as well, for the same purposes as it is used here. Through these vibrational spectroscopic methods, it is easy to see that there are significant deposits of this material in visible regions.

XPS was employed to evaluate the extent of coverage by methylcellulose across the surface of the coating following exposure. Given the shallow depth of analysis (10 nm), the spectrum from uncoated areas should be distinct. As seen in Figure 7-8, it appears that the material is wide-spread across the surface of the exposed coating. Peaks present in the unexposed coating show a strong presence of **C**-N (286.1 eV) and **C**=O (289.4 eV), in line with expectations for this polyurethane. Following exposure, the peak for **C**-N is eliminated, and the N1s spectrum as a whole is almost completely removed. The signature of **C**=O is also heavily attenuated. A new peak is formed at 287.1 eV, indicative of **C**-O-C found in methylcellulose. The extent of N1s attenuation resulting from exposure suggests a very consistent deposition across the surface. Scanning electron microscopy reveals the deposition of material on the surface as a localized conformal coating with visibly different surface morphology (Figure 7-9).

This thin film of methylcellulose does not lead to a significant change in T_g, which is not surprising for such a deposit. It is interesting that the deposits lead to an increase in clarity on the coating, suggesting a smooth conformal coating. The heterogeneous distribution of such deposits suggests a localized vulnerability leading to enhanced nucleation for deposition. The presence of the thin film across the surface suggests that it might function as a barrier, wherein the methylcellulose could act to aid in solvent retention by the polymer.

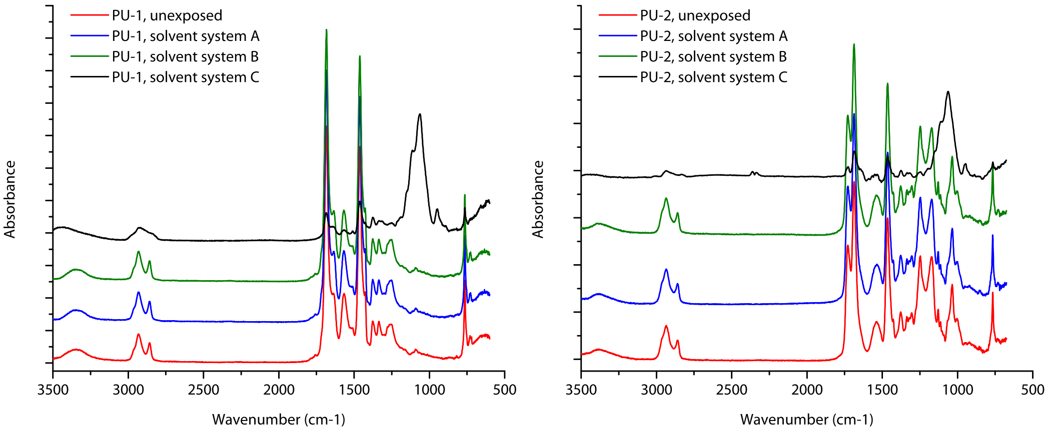

Figure 7-6 – ATR-FTIR spectra of coatings PU-1 and PU-2 unexposed, and after 2-hour exposure with subsequent extensive drying to solvents A, B and C. Regions studied after exposure to system C were selected to include areas of visually-observed clarity. The spectra were obtained after extensive drying (1 month).

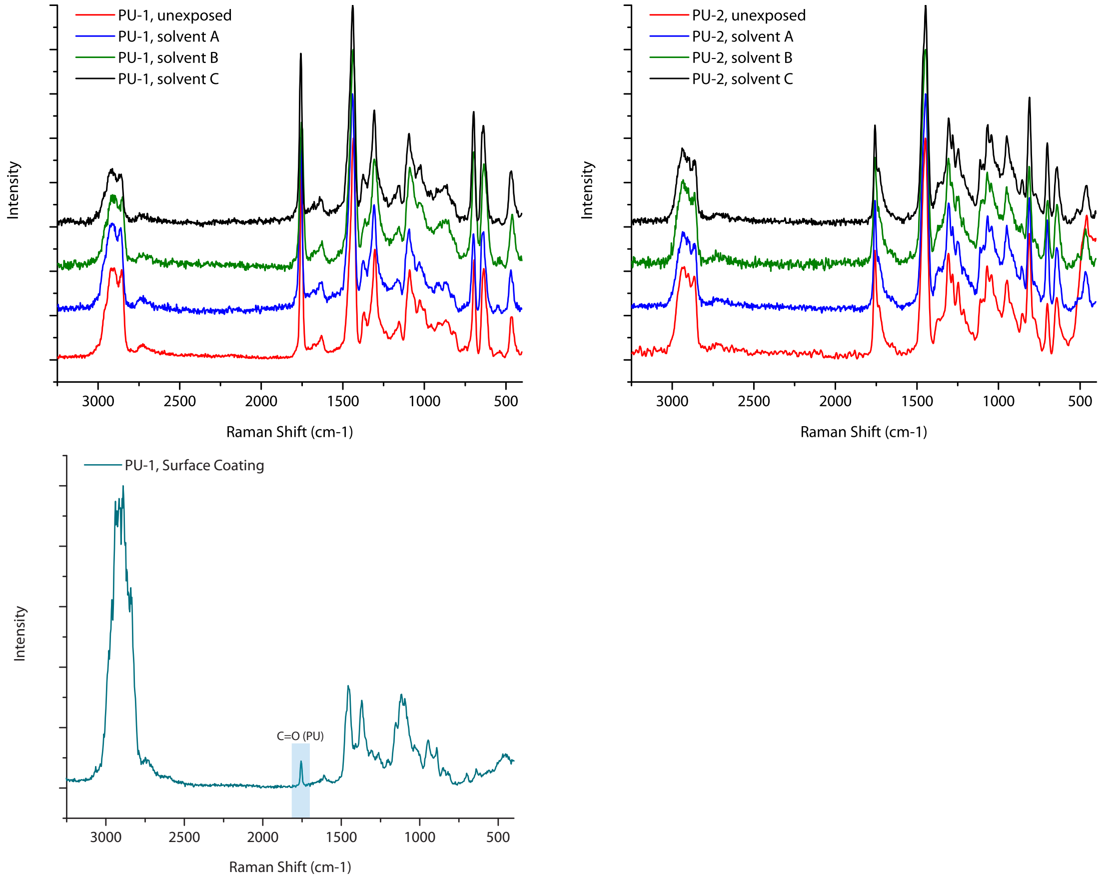

Figure 7-7 – (top) Raman spectra of PU-1 (left) and PU-2 (right), unexposed and after 2-hour exposure to solvents A, B and C; (bottom) confocal Raman surface spectrum of clear regions, indicating deposition of methylcellulose. The spectra were obtained after extensive drying (1 month).

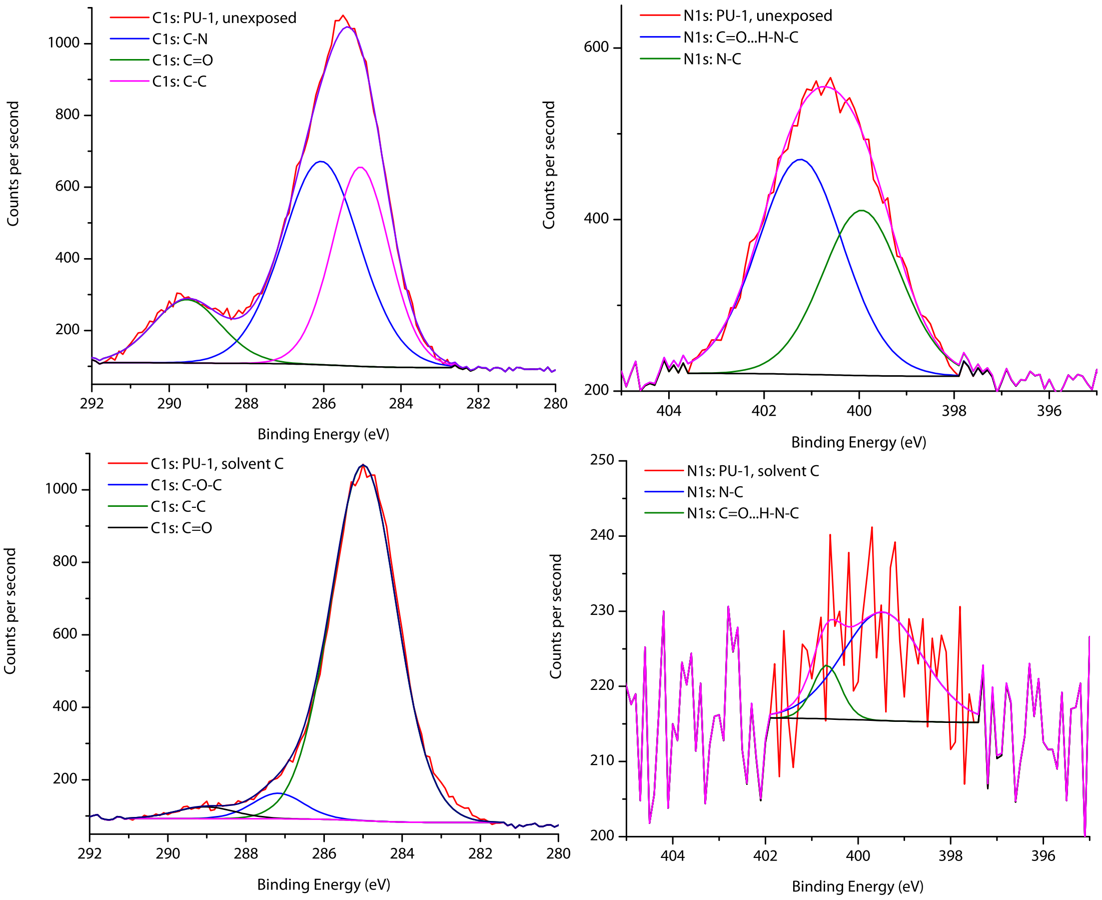

Figure 7-8 – XPS (C1s and N1s) of PU-1 unexposed (top) and PU-1 after exposure to solvent system C for 2 hrs (bottom). Individual curve fits are included.

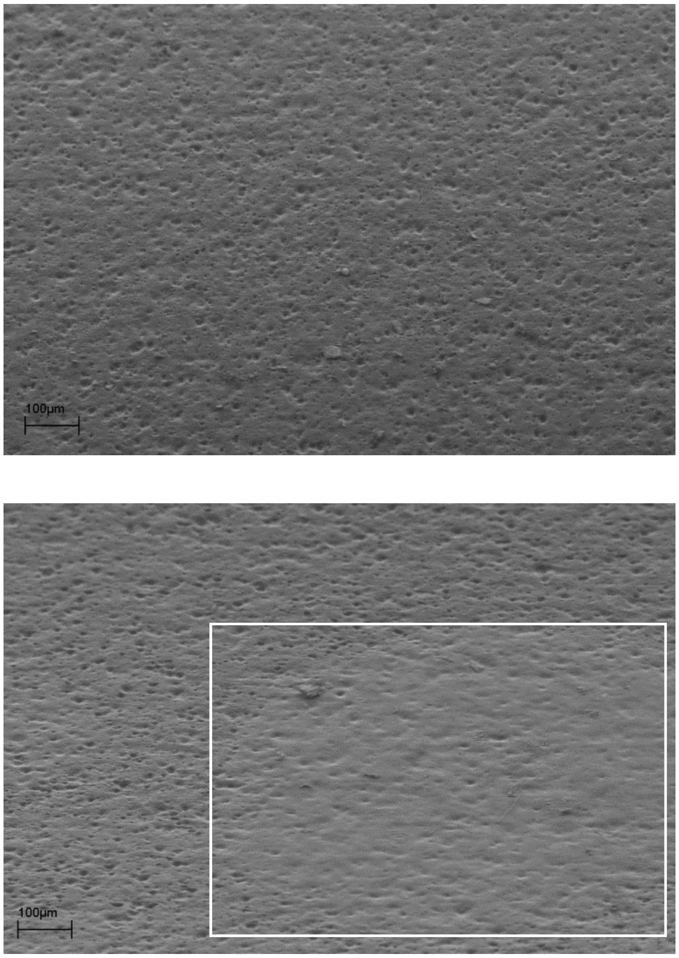

Figure 7-9 – Electron micrographs of coating PU-2 clear film exposed to (top) solvent system A and (bottom) solvent system C. A rectangular box highlights the area of apparent Methocel buildup.

7.4 Conclusions

Polyurethane coatings have been found to show a small but systematic depression in their glass transition temperature as a result of exposure to methylene chloride. The addition of ethanol and water to the methylene chloride did not seem to contribute further to this depression. Methylene chloride and ethanol were both found to enter the coating and remain trapped until being released thermally, and the addition of ethanol and water do not seem to contribute to an increase in solvent absorption.

Proton NMR spectroscopy suggests intimate polymer-methylene chloride contact through the similarity of T_1 values of unexposed and exposed coatings containing methylene chloride, and further indicate the absence of liquid-like pools of methylene chloride. The observed linewidths and $T_{1\rho}$ values show that this intimate contact increases polymer segmental dynamics similarly to elevating the temperature of the polymer closer to T_g. Analysis of the deuterium NMR spectra and T_2 values over a range of temperatures indicates that the methylene chloride solvent is highly restricted in its rotation, but not immobilized, with a rotational correlation time at 0 °C over four orders of magnitude greater than that in the free liquid. At lower temperatures the molecule may exhibit a low degree of partial ordering (showing small residual quadrupole couplings), but the interaction with the polymer seems to be relatively weak, less than 2.5 kJ/mol.

Raman spectroscopy of methylene chloride-saturated coatings shows solvation effects at the carbonyl group that suggest a temporary decoupling or screening of the hydrogen bond responsible for polymer crosslinkage, but further demonstrates that this interference is reversible as the concentration of solvent decreases. This solvation effect leads to the restriction of motion of methylene chloride. The addition of hydroxypropyl methylcellulose as a thickening agent and solvent compatibilizer has the additional effect of forming a heterogeneous thin film on the sample, which adheres to the rough surface of the coating.

It appears that methylene chloride serves to soften the polyurethane coating by diffusing into the coating and associating weakly at the carbonyl, serving to disrupt inter-chain linkage and permit additional swelling, which facilitates further solvent diffusion. With methylene chloride serving to "open the door," other components of the fully-formulated paint removing solution can execute further attack. The next paper in this sequence will examine the effects of additional components of paint removers in light of these findings.

7.5 References

[1] S. Rivers, N. Umney, Conservation of Furniture, Butterworth Heinemann, Oxford, England, 2003.

[2] J. Durkee, Cleaning times: Paint stripping: It's just like parts cleaning, Metal Finishing, 107 (2009) 49-51.

[3] E. Groshart, Finishing in the green: Paint stripping—Without methylene chloride, Metal Finishing, 95 (1997) 55-57.

[4] S. Arndt, R. Canum, Overview of chemical paint strippers: The ongoing development of safer solvent paint removers has yielded versatile, user-friendly products, Metal Finishing, 105 (2007) 49-50.

[5] V. Del Nero, C. Siat, M.J. Marti, J.M. Aubry, J.P. Lallier, N. Dupuy, J.P. Huvenne, Mechanism of paint removing by organic solvents, in: The proceedings of the 53rd international meeting of physical chemistry: Organic coatings, AIP, Paris, France, 1996, pp. 469-476.

[6] K.R. Stone, J. Springer Jr., Review of solvent cleaning in aerospace operations and pollution prevention alternatives, Environmental Progress, 14 (1995) 261-265.

[7] S.G. Croll, Application of the Flory-Rehner equation and the Griffith fracture criterion to paint stripping, J. Coat. Technol. Res., 7 (2010) 49-55.

[8] V.P.N.s. Volkov, K.V.; Sotnikova, E.N; Apukhtina, N.P.; Potepun, L.I., IR-Spectroscopic Investigation of Molecular Interactions in Segmented Polyurethanes, Zhurnal Prikladnoi Spektroskopii, 36 (1982) 787-792.

[9] P. Gotthardt, A. Gruger, H.G. Brion, R. Plaetschke, R. Kirchheim, Volume change of glassy polymers by sorption of small molecules and its relation to the intermolecular space, Macromolecules, 30 (1997) 8058-8065.

[10] S. Misra, W.L. Mattice, Atomistic Models of Amorphous Polybutadienes. 3. Static Free Volume, Macromolecules, 26 (1993) 7274-7281.

[11] C. Nagel, E. Schmidtke, K. Gunther-Schade, D. Hofmann, D. Fritsch, T. Strunskus, F. Faupel, Free volume distributions in glassy polymer membranes: Comparison between molecular modeling and experiments, Macromolecules, 33 (2000) 2242-2248.

[12] S. Arizzi, P.H. Mott, U.W. Suter, Space Available to Small Diffusants in Polymeric Glasses - Analysis of unoccupied Space and Its' Connectivity, J. Polym. Sci. Pt. B-Polym. Phys., 30 (1992) 415-426.

[13] P.N. Brier, A. Perry, Neutron Inelastic-Scattering Measurements and Liquid Dynamics of CH2CL2, Advances in Molecular Relaxation and Interaction Processes, 13 (1978) 1-46.

[14] V.M. Shah, S.A. Stern, P.J. Ludovice, Estimation of the free volume in polymers by means of a Monte Carlo technique, Macromolecules, 22 (1989) 4660-4662.

[15] N.M.K. Lamba, K.A. Woodhouse, S.L. Cooper, Polyurethanes in Biomedical Applications, Taylor & Francis, 1997.

[16] A.F.M. Barton, CRC handbook of solubility parameters and other cohesion parameters, CRC Press, 1983.

[17] A. Latnikova, D.O. Grigoriev, H. Möhwald, D.G. Shchukin, Capsules Made of Cross-Linked Polymers and Liquid Core: Possible Morphologies and Their Estimation on the Basis of Hansen Solubility Parameters, The Journal of Physical Chemistry C, 116 (2012) 8181-8187.

[18] T. Wollbrinck, The Composition of Proprietary Paint Strippers, Journal of the American Institute for Conservation, 32 (1993) 43-57.

[19] S. Schlick, Z. Gao, S. Matsukawa, I. Ando, E. Fead, G. Rossi, Swelling and Transport in Polyisoprene Networks Exposed to Benzene−Cyclohexane Mixtures: A Case Study in Multicomponent Diffusion, Macromolecules, 31 (1998) 8124-8133.

[20] L.W. Jelinski, J.J. Dumais, A.L. Cholli, T.S. Ellis, F.E. Karasz, Nature of the water-epoxy interaction, Macromolecules, 18 (1985) 1091-1095.

[21] L.S. Loo, R.E. Cohen, K.K. Gleason, Deuterium nuclear magnetic resonance of deuterium oxide in nylon 6 under active uniaxial deformation, Polymer, 41 (2000) 7699-7704.

[22] B. Deloche, E.T. Samulski, Short-range nematic-like orientational order in strained elastomers: a deuterium magnetic resonance study, Macromolecules, 14 (1981) 575-581.

[23] P.T. Callaghan, E.T. Samulski, Biaxial Deformation of a Polymer Network Measured via Deuteron Quadrupolar Interactions, Macromolecules, 36 (2003) 724-735.

[24] L.S. Loo, R.E. Cohen, K.K. Gleason, Deuterium Nuclear Magnetic Resonance of Phenol-d5 in Nylon 6 under Active Uniaxial Deformation, Macromolecules, 32 (1999) 4359-4364.

[25] D.E. Oreilly, E.L. Yasaitis, E.M. Peterson, Self-Diffusion Coefficients and Rotational Correlation Times in Polar Liquids. IV. Dichloromethane and Pyridine, J. Chem. Phys., 57 (1972) 890-&.

[26] J.L. Ragle, K.L. Sherk, Deuteron Quadrupole Coupling in Some Solid Chlorinated Hydrocarbons, J. Chem. Phys., 50 (1969) 3553-&.

[27] J.P. Yesinowski, High-resolution NMR spectroscopy of solids and surface-adsorbed species in colloidal suspension: phosphorus-31 NMR spectra of hydroxyapatite and diphosphonates, Journal of the American Chemical Society, 103 (1981) 6266-6267.

[28] G. Socrates, Infrared Characteristic Group Frequencies: Tables and Charts, 2nd ed., John Wiley & Sons, Chichester, 1994.

[29] N.E. Triggs, J.J. Valentini, An Investigation of Hydrogen Bonding in Amides Using Raman Spectroscopy, Journal of Physical Chemistry, 96 (1992) 6922-6931.

[30] F. Terenziani, A. Painelli, D. Comoretto, Solvation Effects and Inhomogeneous Broadening in Optical Spectra of Phenol Blue, Journal of Physical Chemistry A, 104 (2000) 11049-11054.

[31] V. Ramakrishnan, A. Sarua, M. Kuball, A.F. Abdullah, Solvent dependent study of carbonyl vibrations of 3-phenoxybenzaldehyde and 4-ethoxybenzaldehyde by Raman spectroscopy and ab initio calculations, J. Raman Spectrosc., 40 (2009) 921-935.

Chapter 8: Physicochemical investigation of chemical paint removers II: Role and mechanism of phenol on the removal of polyurethane coatings

This chapter represents a continuation of the work from Chapter 7, involving the same collaborative group effort. TGA, DSC, and GC-MS vapor entrapment results were obtained by Ms. Kelly Watson and Dr. James Wynne and contributed towards a manuscript on this topic for submission to Progress in Organic Coatings, which is currently in production. No claim is made by this author on these results. As in Chapter 7, portions of this work have been included in US Navy memorandum report #NRL/MR/6120—11-9368, on which the author and dissertation advisor are co-authors, and the outside committee member is first author. The reproduction herein of findings from this report is authorized by the lead author.

8.1 Introduction

The formulation of chemical paint removers is of significant environmental relevance in military applications. A significant amount of waste is produced in a paint removal operation, with much of it contaminated by methylene chloride and phenol, both solvents with significant negative environmental and physiological side-effects. In order to reduce the impact of paint removal operations a new, less-hazardous paint remover must be formulated. Other methods, including laser ablation and sand-blasting, incur significant expense and show reduced utility [1].

In the previous chapter we discussed the chemical changes caused by the presence of methylene chloride in model military coatings. In short, it was found that methylene chloride appears to solvate the carbonyl groups responsible for cross-linkage, leading to polymer swelling. This solvation effect is demonstrated through Raman peak broadening of the carbonyl peak, through non-liquid dynamics of methylene chloride within the saturated coating by ^{1}NMR, and by increased polymer segmental dynamics by the same method. However, while methylene chloride softens the coating during exposure, after evaporation there is minimal effect on coating T_g. This suggests the primary purpose of phenol as a degradative agent. Methocel, which was included for solvent miscibility and solution thickening, was also found to deposit at the surface as a conformal coating, which may contribute to solvent retention.

Extensive studies have been undertaken concerning the degradation of military coatings by water [2], accelerated weathering [3-8], and physical aging [9]. Literature on paint stripping generally comes from the art conservation and furniture restoration field [10]. The main study of the suitability of a solvent for polymer coating removal has been through the use of Hansen solubility parameters, which provide a quantifiable metric for the types and strength of interactions a solvent may produce [11]. More recently, paint stripping has been modeled and interpreted by Croll from a mechanical standpoint, with the Flory-Rehner equation and Griffith fracture criteria used to interpret removal from the perspective of the cohesive and adhesive properties of the polymer [12].   Others have described the role of substrate receptor group density on adhesion [13-15], providing a chemical framework to disbondment.

In the absence of phenol, the remaining components of the MIL-PRF-81294 paint remover failed to demonstrate significant depression of T_g after sample drying. While these solvents may prove effective while saturating the coating, they lack the “staying power” which comes about in the fully-formulated stripper. In this paper, we will discuss the effects of phenol in combination with the other model formulation components on model military coatings, in order to elucidate the mechanism that allows phenol to cause irreversible damage to the coating.

8.2 Materials and methods

8.2.1 Chemicals and coatings

All chemicals were reagent grade and used without further purification. Mixtures were prepared by weight percent according with Table 8-1.

Solution	Compound	Methylene Chloride	Ethanol	Water	Phenol	Methocel
	Commercial Paint stripper[a]	60.6	5.8	7.8	15.8	1.2
D	MC, EtOH, H_2O, PhOH	67	6	9	18	1.2
E	EtOH, PhOH	0	27	0	73	0
F	MC, PhOH	79	0	0	21	0

Table 8-1 – List of control formulations by weight percent.

[a]Contains also, Toluene (1.3%), sodium petroleum sulfonate (5.5%) and paraffin wax (1.9%). Methocel is used to enhance solvent phase miscibility and viscosity.

Current military coatings were selected for study, in the form of two polyurethane topcoats, based upon military specifications MIL-DTL-53039 (coating PU-1) and MIL-PRF-85285 (PU-2). The coatings were unsupported free films, with a finial thickness of approximately 5 mils (see Table 8-2). The simplification of the otherwise complex coating system was prepared to allow for ease of analysis. Coatings used in this study were clear films, without pigments, fillers and pigment related dispersion and wetting agents. Antifoaming agents were retained to facilitate sample preparation. Current formulations were used based on the same raw materials and binder ratios used in the commercial product. However, the solvent ratios were altered to compensate for the change in surface tension, viscosity and other properties resulting from the removal of the pigments and other components. Initial application using conventional spray equipment and settings failed due to the high viscosity of the formulations; a drawdown mechanism for creating coatings also failed as creating films of the approximate 4 mil thickness in one application trapped too many bubbles in the coating as it cured. All formulas were ultimately sprayed in multiple layers on release paper allowing 16-24 hour cure time between each layer and a final seven day cure time. This minimized the presence of bubbles and created coatings of the desired thickness. The clear coatings were prepared on release paper and subsequently removed for evaluation.

Coating	Coating Type	Military Specification	Finial thickness (mm)	Specific coating description
PU-1	Polyurethane	MIL-DTL-53039	0.13	single component aliphatic polyurethane CARC topcoat
PU-2	Polyurethane	MIL-PRF-85285	0.13	two component high solids 2.8 VOC polyurethane topcoat

Table 8-2 – List and description of prepared coatings.

8.2.2 Sample exposure

Approximately two centimeter squares of each coating were cut and placed into individual scintillation vials. To each vial was added the respective solvent or solvent mixture until the coating was completely covered (~10 mL). After exposure periods of two hours and two days respectively, the liquid was decanted, the surface of the coating rinsed with 5 mL EtOH to remove any impurities that may have been extracted and remain on the surface, and the coating allowed to air dry in the vial for >2 weeks. Caution was taken to ensure that the vial did not contain any solvent droplets and that the coating was completely dry before testing. In the case of solvated coatings, square samples were prepared and exposed overnight, then immediately removed for analysis without deliberate drying.

8.2.3 Differential Scanning Calorimetry (DSC)

Differential scanning calorimetry (DSC) was performed on a TA Instruments Q20 DSC with the DSC Refrigerated Cooling System (RCS) and a purge gas of nitrogen set to 50 mL/min. Samples of approximately 1-2 mg were placed into TA Instruments Tzero Aluminum pans, with an empty aluminum pan was used as reference. Samples were analyzed from -90 °C to 150 °C at 20 °C/min twice. All data reported was taken from the second ramp. Glass transition temperatures were found using TA Universal Analysis program.

8.2.4 Thermogravimetric Analysis (TGA)

Thermogravimetric analysis (TGA) was done on a TA Instruments Q50 TGA using a platinum sample pan. The analysis was carried out in the presence of oxygen with breathing air used as the sample purge gas. Nitrogen was used as the purge gas for the balance. Data were recorded from ambient temperature to 700 °C at 5 °C/min. Plots of percent weight loss versus temperature were made to analyze the data.

8.2.5 FTIR-ATR

FTIR spectra were recorded on a Thermo Scientific Nicolet 6700 FTIR spectrometer equipped with a Smart Performer ATR attachment using a germanium crystal and constant pressure tower, and also with a Nicolet iS-50 FTIR spectrometer equipped with a Smart iTR attachment using zinc selenide and diamond crystals with a constant pressure tower. A DTGS or MCT/A detector collected 64 scans of the sample. Data acquisition and analysis was performed using the Thermo Scientific OMNIC software suite.

8.2.6 Raman spectroscopy

Raman analysis was carried out using a Nicolet Almega dispersive spectrometer coupled to an Olympus microscope with 10x and 100x objective lenses, and also using a WiTec α-500 confocal Raman microspectrometer with 20x and 100x objective lenses. The sample was scanned 128 times using a 1s collection time, with the spectra analyzed using the Thermo Scientific OMNIC software suite. Samples were placed on quartz slides to reduce background interference.

8.2.7 XPS

X-ray photoelectron spectra were obtained using a VG ESCA-3 Mk. II system under ultra-high vacuum (10^{-9} Torr ≡ 10^{-7} Pa). X-rays were generated from a magnesium anode at 6 kV with a filament current of 20 mA. A pass energy of 20 eV was applied to emitted photoelectrons for analysis. Scans for each region were executed with a spacing of 0.1 eV and a 100ms dwell time; each scan was repeated 50 times and co-added, using the VGX900i control program. Spectra were calibrated using the adventitious carbon peak at 284.5 eV. Analysis was performed using the CasaXPS software package.

8.2.8 Vapor entrapment

Vapor above a coating (headspace) in an air tight vial was injected into the GCMS after the vial had been heated at approximately 80 ^{0}C for 30 minutes. The GCMS system was an Agilent 7890A gas chromatograph equipped with an Agilent 5975C mass selective detector operating in electron ionization mode and an Agilent 7693A autoinjector. The column utilized was an Agilent HP-5MS (5% phenyl) methylpolysiloxane film. The carrier gas was helium with a flow rate of 1 $\text{mL}\cdot\text{min}^{-1}$. The injection volume was 10 μL with a split injection ratio of 50:1. The temperature program has an initial temperature of 35 °C for one minute, then 10 °C per minute ramp to 90 °C with a three minute post run hold at 250 °C. The injection port temperature, MS quad temperature, and source temperature were 220 °C, 150 °C and 230 °C, respectively. The detector was set to scan a mass range from 20 to 500 *m/z*.

8.3 Results and discussion

8.3.1 Thermal properties

In Table 8-3, the changes in T_g due to exposure to the prepared phenol solvent mixtures is shown. Phenol produces significant, irreversible deterioration of the coating. The addition of phenol leads to T_g depressions of well over 50 °C, which results in a soft, easily-torn coating at room temperature. In the case of coating PU-2, the clear coating became so swollen and soft that removal of the coating from solution was impossible. One would expect that solvent system D would lead to decomposition in the fully-formulated coating as well, or at least lead to the greatest T_g depression. We explain this based on the nature of the coating: fully-formulated PU-2 has a glass transition temperature of 0 °C, indicating that it is highly flexible in the presence of fillers. We speculate that these fillers serve to provide some minimal flexible cohesion which is unaffected by phenol; further, this cohesion would be further supported by the methylcellulose film deposited on the coating.

	PU-1 Polyurethane Topcoat		**PU-2 Polyurethane Topcoat**	
(* Denotes use of methocel for solution compatibility)	**Clear coating**	**Fully formulated coating**	**Clear coating**	**Fully formulated coating**
Control	**87**	**60**	**51**	**0**
MC/EtOH/Water/PhOH*	**-11**	**-8**	**DECOMP**	**-38**
EtOH/PhOH	**-9**	**-13**	**-25**	**-45**
MC/PhOH	**-4**	**-2**	**-30**	**-54**

Table 8-3 – T_g information for clear and fully-formulated coatings exposed to phenol-containing solutions.

8.3.2 Solvent persistence

The exposed coatings acquire a light purple tint (shown in Figure 8-1) as a result of exposure, indicative of the presence of impure solid phenol. Coatings also produce a strong odor of phenol after several months of drying, indicating solvent retention. Small samples of exposed coatings were heated in sealed vials, and the subsequent headspace gas was analyzed using GC-MS, where the presence of phenol was confirmed.

Figure 8-1 – Clear coating PU-1 (MIL-53039) after exposure to solvent system D for 2h with subsequent drying, showing a purple tint indicative of impure solid phenol.

Thermogravimetric analysis (TGA) was performed on all exposed coatings, with an unexposed coating serving as control. Curves are presented in Figure 2, with phenol-containing solvent results overlaid against those from solvent blends without phenol. Following exposure to solvent mixtures containing phenol, each coating shows a significant weight drop before 125 °C. The boiling point of phenol is well above this point (181 °C), which suggests that phenol is causing significant chain scission within the sample.

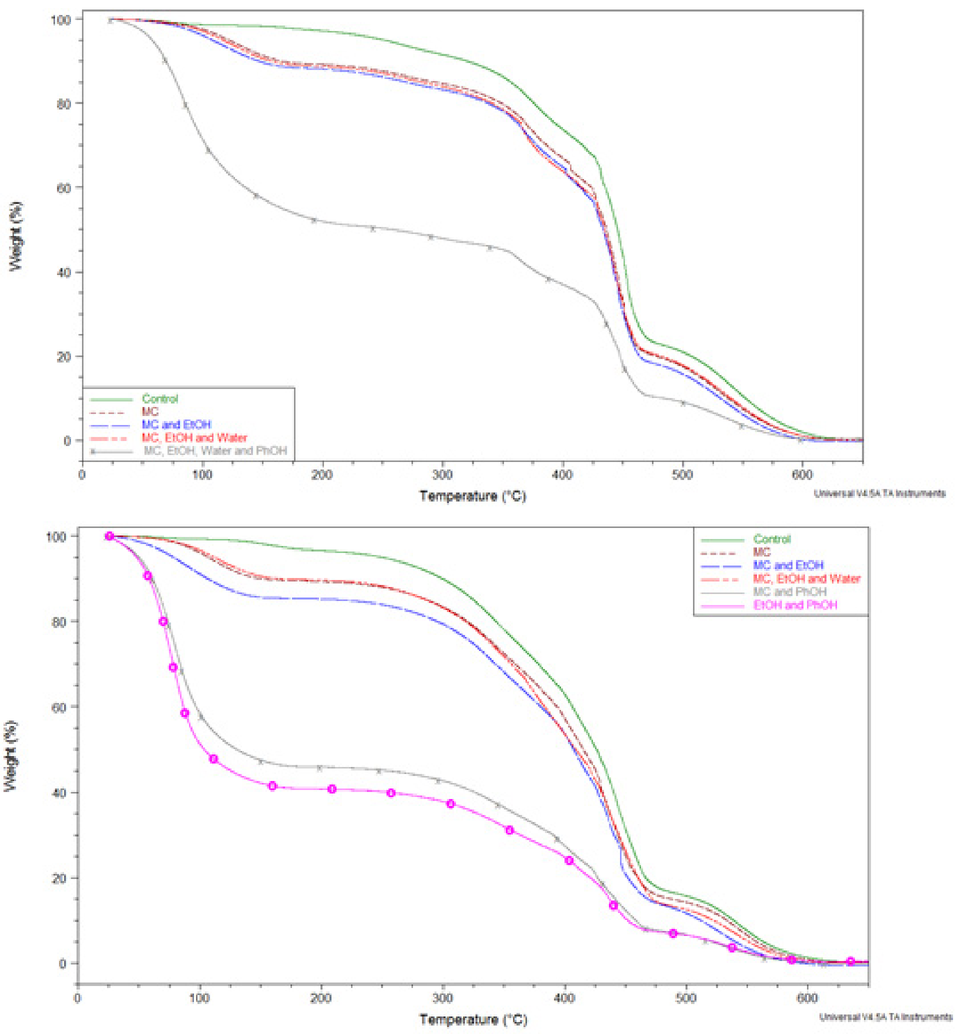

Figure 8-2 – TGA curves of coatings PU-1 (top) and PU-2 (bottom) exposed to solvent systems D, E, and F; as well as systems A, B, and C from past work.

8.3.3 Spectroscopy of exposed polyurethanes – solvent system D

Polyurethane is observed to degrade significantly after exposure to phenol-containing solvent mixtures. In Figure 8-3, we present ATR-FTIR spectra of coating PU-1 exposed to mixture D, which causes the greatest T_g depression in this system. There is spectral evidence of significant residue of hydroxypropyl methylcellulose on the surface of the material, as mentioned in the previous chapter; this masks many changes which occur in the coating. The spectrum demonstrates significant attenuation of the polyurethane binder, with the primary signatures coming from methylcellulose and phenol. It is difficult to evaluate chemical changes in these samples with such a shallow depth of analysis.

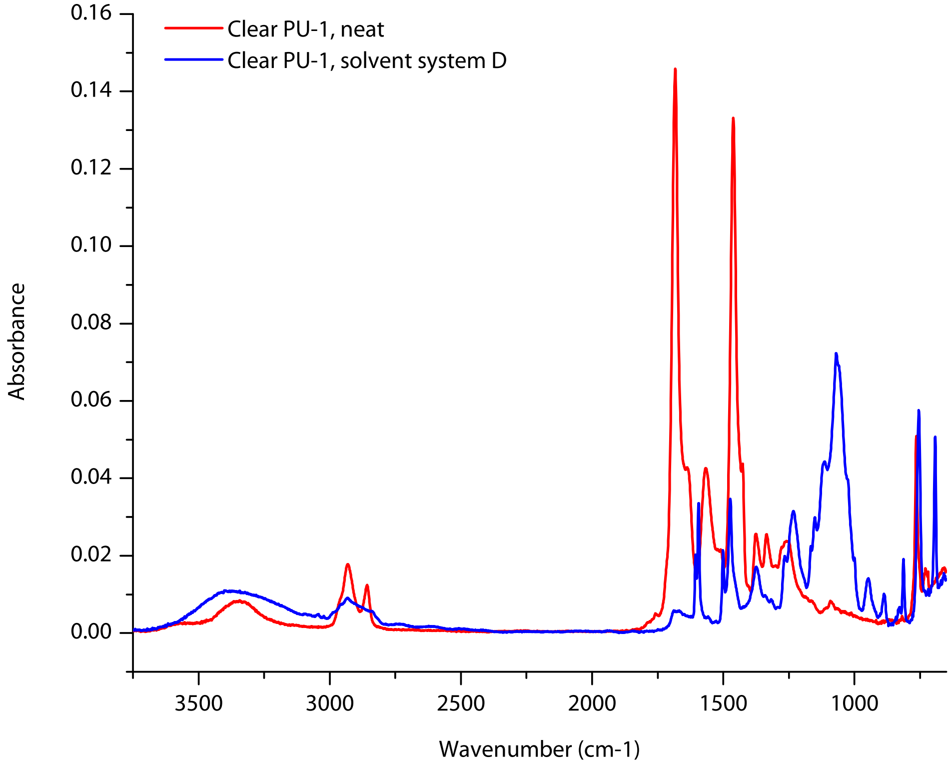

Figure 8-3 – ATR-FTIR spectra of clear coating PU-1 before and after exposure to solvent system D.

In Figure 8-4, the complementary spectrum from Raman analysis is presented. Herein, we see the similar evolution of C-O-C due to methylcellulose, in addition to the numerous persistent peaks due to phenol. The spectra were normalized using the peak at 1462 cm^{-1} relating to CH_2 stretching, in which we do not expect any change to occur. The peak at 1000 cm^{-1} is caused by aromatic ring breathing, and its growth is attributable to the presence of phenol. The overall difficulty in this analysis arises because the most likely chemical changes in the coating are generally masked by similar bonds in methylcellulose and phenol.

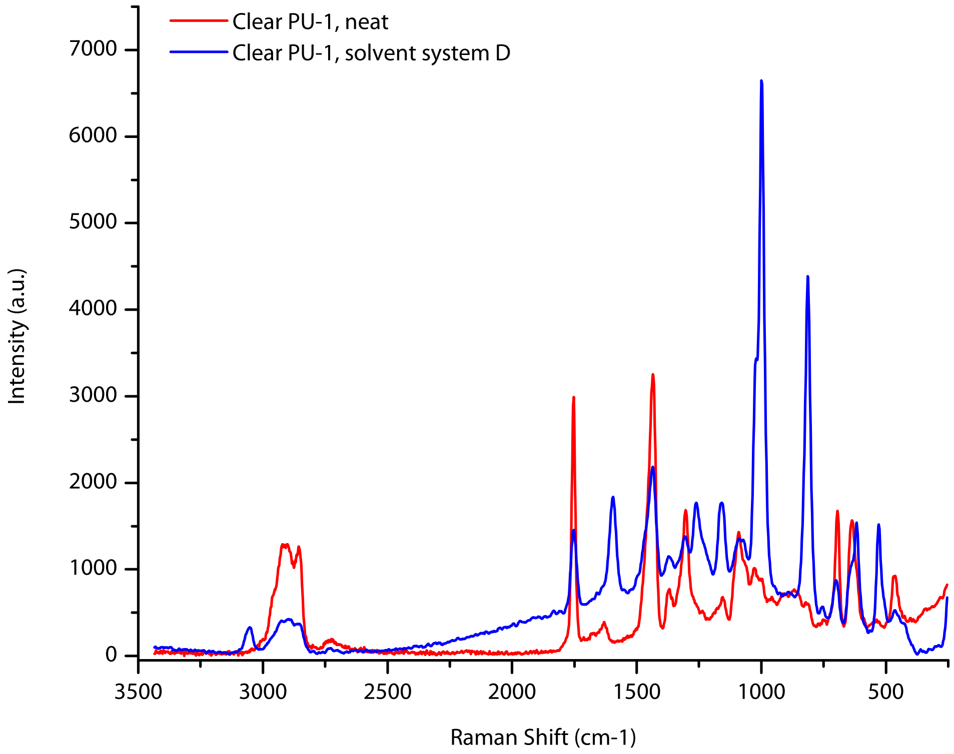

Figure 8-4 – Raman spectra of clear 53039 before and after exposure to solvent system D.

XPS spectra of coatings exposed to solvent system D are dominated by the presence of methylcellulose at the surface, rendering a more detailed chemical investigation difficult. In Figure 8-5, we present a comparison of the XPS C1s spectrum between the neat coating, the coating after exposure to solvent system C (from the previous chapter), and the coating after exposure to solvent system D. The spectral features after each exposure are quite similar, although the peak indicating C=O is slightly strong after exposure in system D, possibly because of degradation of the coating leading to breaches in the conformal film of methylcellulose.

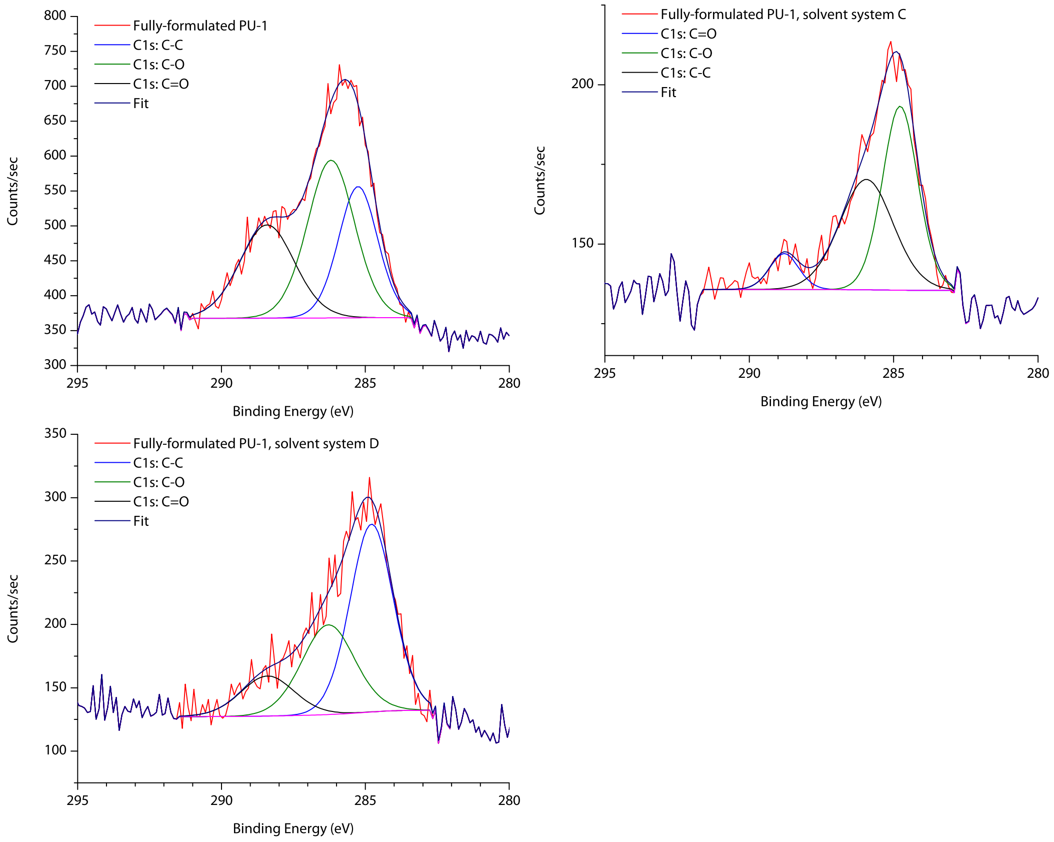

Figure 8-5 – XPS C1s spectra of fully-formulated PU-1 unexposed (top left), exposed to solvent system C (top right), and exposed to solvent system D (below right).

8.3.4 Spectroscopy of exposed polyurethanes – solvent system F

In order to isolate the effects of phenol, coatings were exposed to a solvent system without methylcellulose; while this system is marginally less effective than solvent system D, the interactions of phenol are likely to be similar in nature. The ATR-FTIR spectra of clear system PU-2 before and after exposure to solvent system F are shown in Figure 8-6, with an enhanced view of the fingerprint region in Figure 8-7; the preponderance of phenol in the sample does skew the peak intensities of the polymer, rendering quantitative analysis difficult. Several changes in the spectrum are immediately obvious. The carbonyl peak has undergone broadening and splitting, indicative of a change in the degree of hydrogen bonding. The larger peak at 1684 cm^{-1} must be attributable to hydrogen-bound urethane carbonyl [16], and the shoulder at 1728

cm^{-1} indicates ester carbonyl from the polyester-polyol extender [7]. The peak at 1645 cm^{-1} indicates hydrogen-bound urea [17](resulting from the polyisocyanate form of HDI, which is in the form of a biuret for this application, and from the inevitable formation of urea as a result of isocyanate-water reactions) [18]. After exposure, the hydrogen-bound urethane peak splits into two peaks at 1670 and 1687 cm^{-1}. Based on the splitting pattern, we propose that the peak at 1687 cm^{-1} corresponds to hydrogen-bound urethane carbonyl as before (and thus shifted to a small degree thanks to steric effects of the presence of phenol), and that 1670 cm^{-1} corresponds to a urethane carbonyl vibration near a chain end, of the form NR_2-CO-O-Ar (resembling phenyl carbamate). The carbonyl position for phenyl carbamate occurs slightly above 1700 cm^{-1} (reference spectra from Sigma, need citation); given the usual pattern of roughly 20-25 cm^{-1} shift depending on the degree of hydrogen bonding [19], it is reasonable to suggest this position as a possible location. A new shoulder forms at 1265 cm^{-1}; it is recognized that aryl monosubstitution increases the wavenumber in asymmetric C-O-C stretching vibrations [20], thus further supporting the phenyl carbamate model. The Amide II peak centered at 1540 cm^{-1} is significantly decreased, and reduces into 2 peaks at 1530 and 1555 cm^{-1}, which might plausibly be attributed to the aromatic substitution undergone. The DSC data presented above supports this notion, as the strongly depressed T_g value indicated in Table 8-3 suggests some measure of polymer chain cleavage to so severely impact the material. We propose that this change occurs as a result of nucleophilic attack, as explained schematically in Figure 8-8, due to the weak acidity of the phenol molecule. One important note: one would expect that a peak for C-OH might appear at 953 cm^{-1}, but none is present. The peaks which correspond to O-H stretching around 3370 – 3500 cm^{-1} do increase in intensity, but this is also influenced by the presence of unbound phenol, as noted through GC/MS headspace analysis discussed earlier. Generally, the presence of both residual phenol and existing esters mask many changes we would otherwise hope to detect in the coating, but the occurrence of carbonyl peak splitting and the development of a new C-O-C shoulder suggest this reaction mechanism. By eliminating the presence of methylcellulose, we confirm that these changes are caused by a chemical reaction, rather than cellulosic deposition at the surface as seen with stabilized solvent blends.

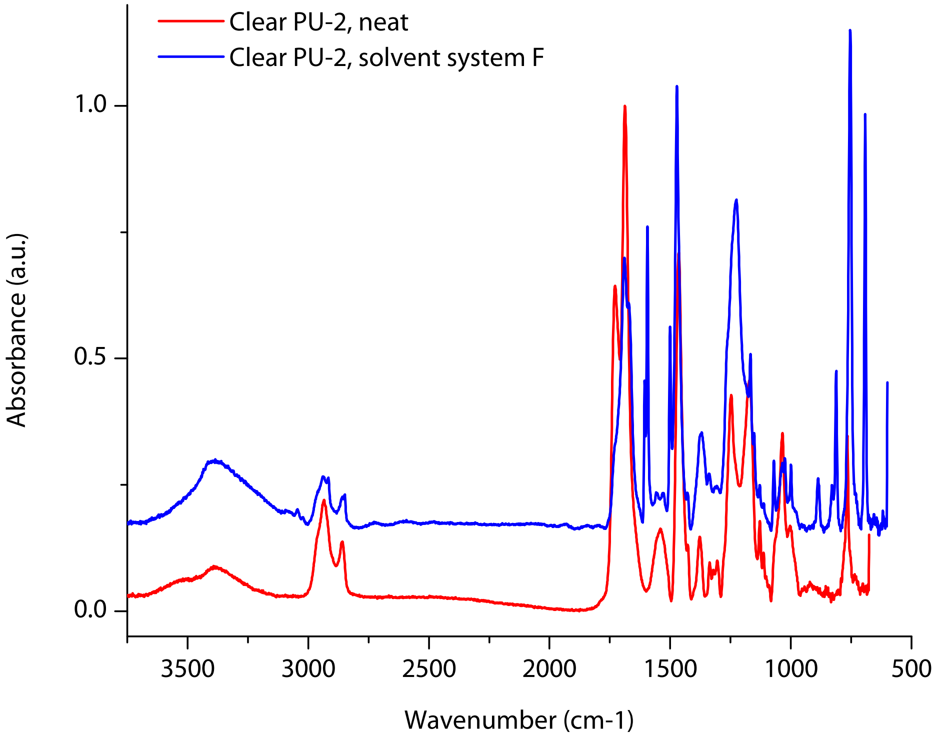

Figure 8-6 – ATR-FTIR of clear PU-2 before and after exposure to solvent system F for 2h.

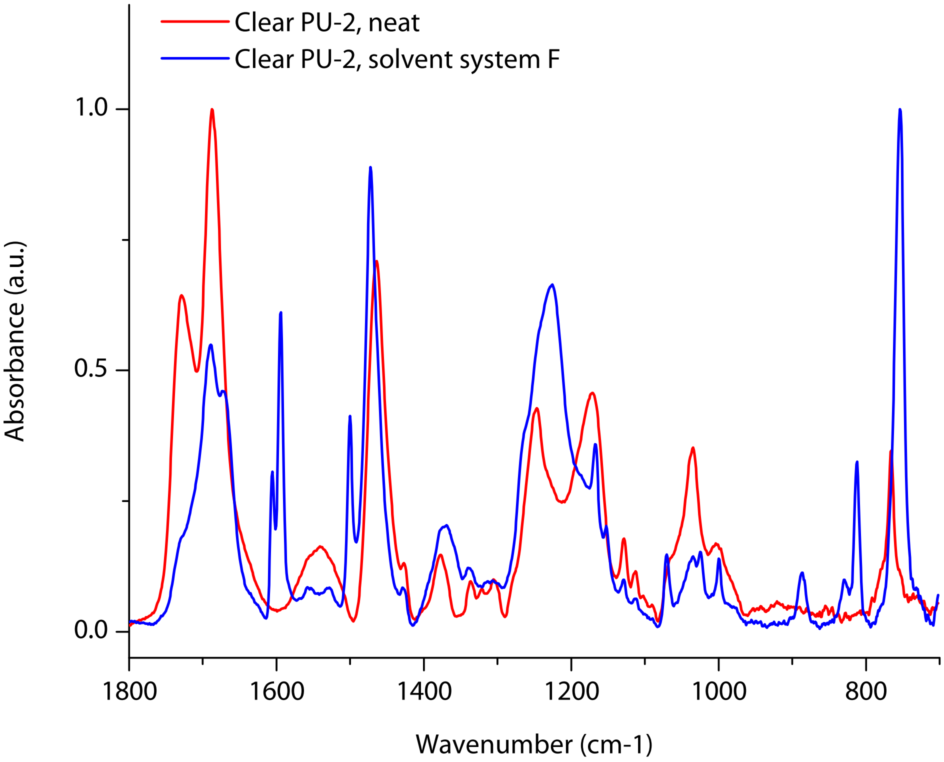

Figure 8-7 – ATR-FTIR spectrum of PU-2 before and after exposure to solvent system F, highlighting the organic fingerprint region.

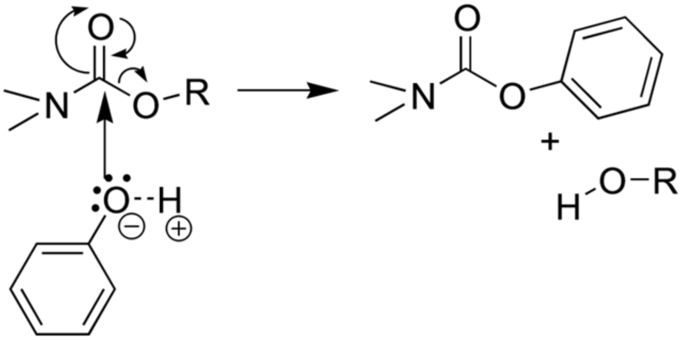

Figure 8-8 – Proposed nucleophilic attack of phenol in polyurethane.

A comparable effect is observable in coating PU-1, presented in Figure 8-9 and Figure 8-10. The carbonyl peak at 1683 cm^{-1} is split into two peaks at 1687 and 1670 cm^{-1}, suggesting the same mechanism seen in PU-2. It is more straightforward to resolve the shoulder at 1265 cm^{-1} in this sample, as it is not crowded by the presence of other C-O-C polyester peaks due to the extender polymer chosen (here, usually polyethylene or a derivative), although the presence of phenol does still generate several peaks nearby. From the thermal data, we know that the degradative performance of phenol is enhanced by the addition of a small amount of water. This seems likely to be due to the enhanced acidity of phenol in the presence of water. The Raman spectrum of this exposure (Figure 8-11) is dominated by the presence of phenol, and as it is not as sensitive as FTIR to the changes observed in this degradation, does not shed any additional light on the situation.

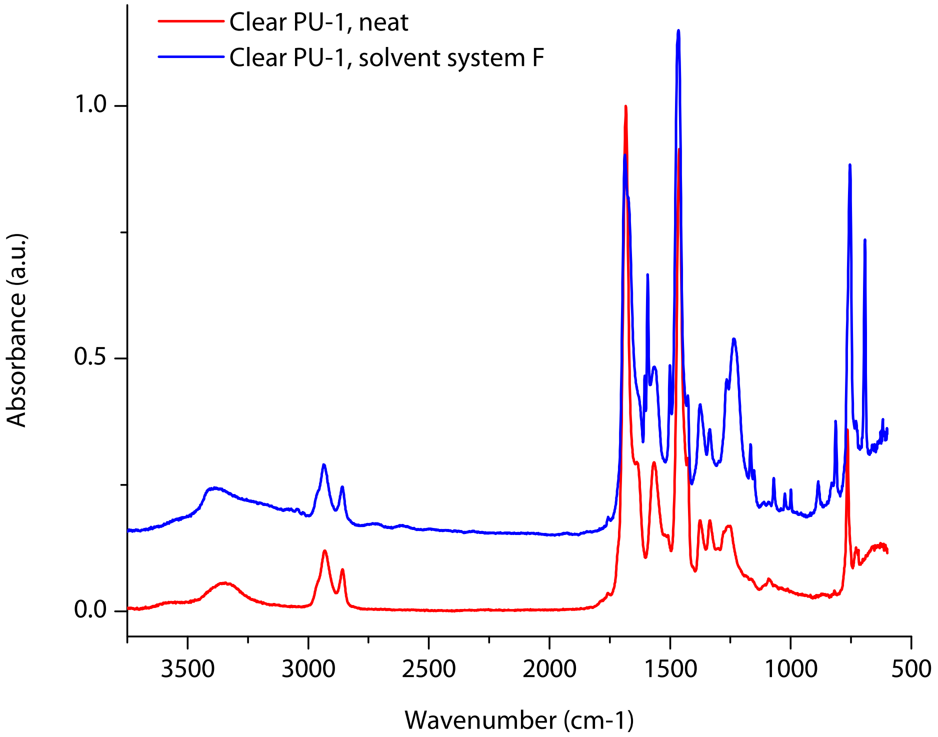

Figure 8-9 – ATR-FTIR spectra of clear PU-1 before and after exposure to solvent system F for 2h.

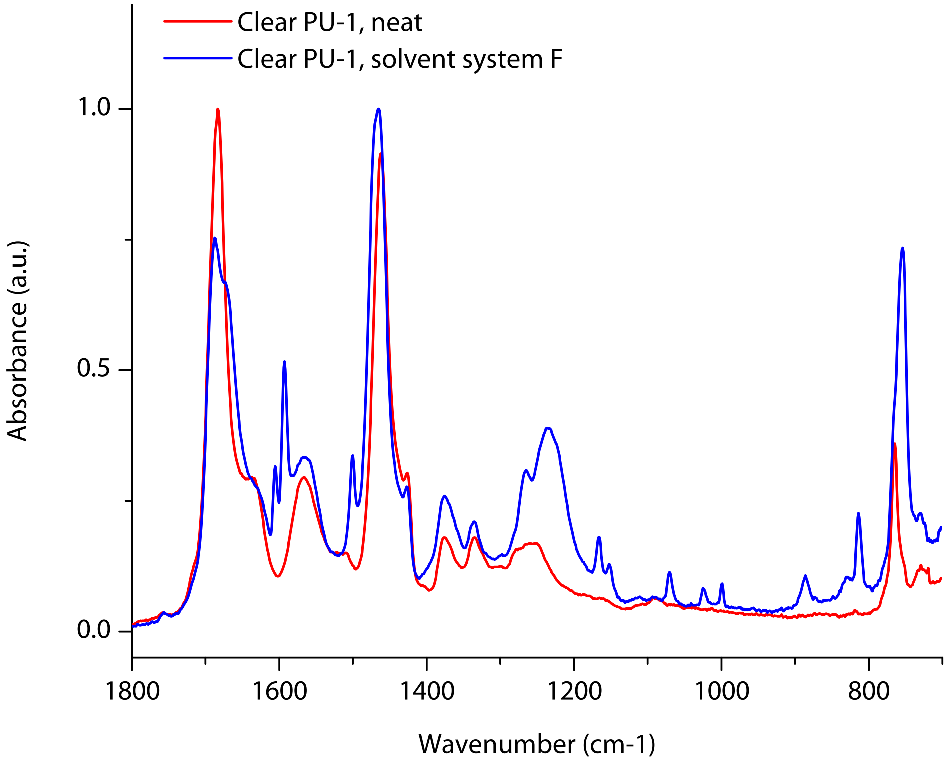

Figure 8-10 – ATR-FTIR spectra of clear PU-1 before and after exposure to solvent system F for 2h, highlighting the organic fingerprint region.

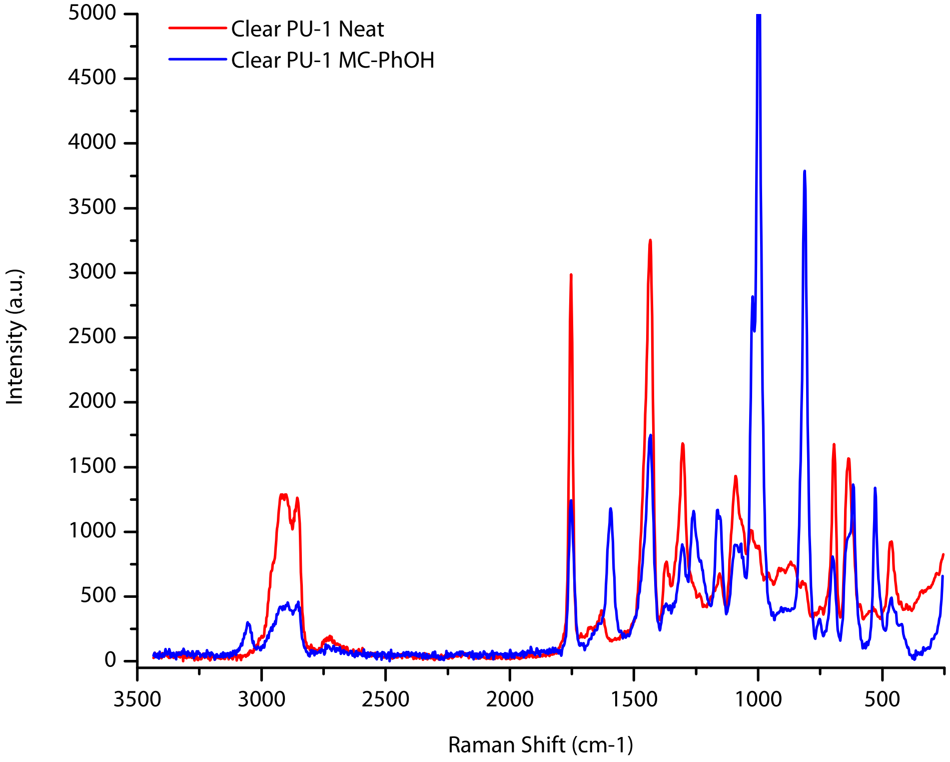

Figure 8-11 – Raman spectra of clear PU-1 before and after exposure to solvent system F.

The apparent degradation mechanism of fully-formulated coatings does not differ greatly from their clear-formulated counterparts. In Figure 8-12 and Figure 8-13 we show the spectra of fully-formulated PU-1 before and after exposure. The exposed coating is softer and more flexible, leading it to make better contact with the ATR crystal than the brittle control coating, which manifests as a smoother spectrum. The same broadening effect of the carbonyl peak, ether shoulder evolution, and increase in amine are all apparent in these spectra, which indicates that the addition of fillers does not alter the chemical mechanism of degradation. However, in the thermal data, we do note that while the magnitude of T_g depression is higher in the clear-formulated coatings, the fully-formulated version of PU-2 is decreased to a lower overall temperature. Given its already-low T_g (0 °C), there must be several additives or fillers further plasticizing the coating.

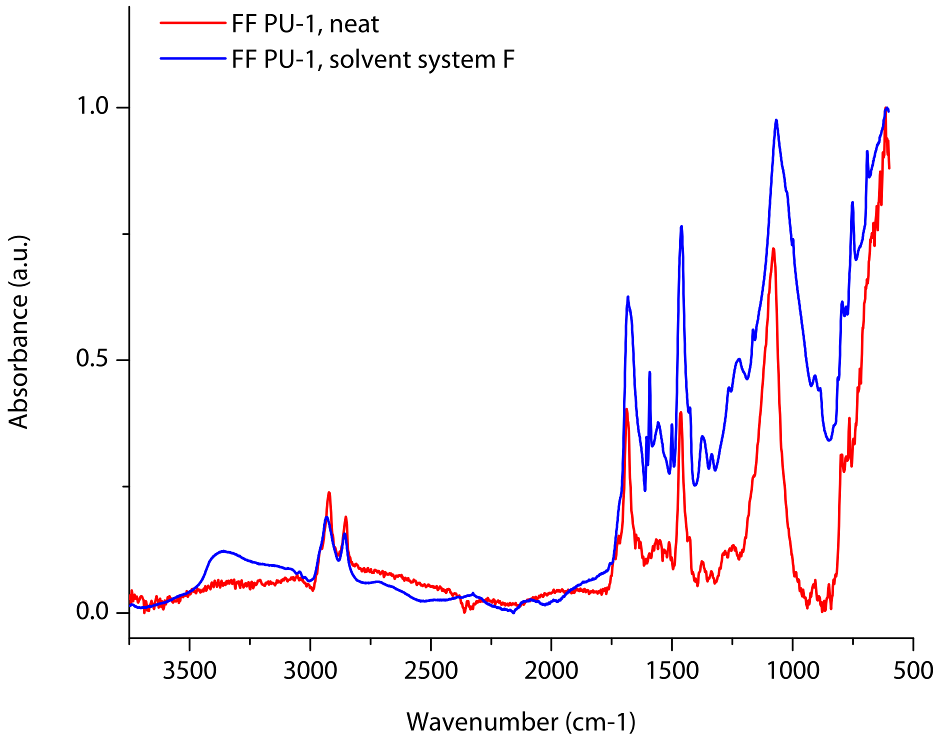

Figure 8-12 – ATR-FTIR spectra of fully-formulated PU-1 before and after exposure to solvent system F for 2h.

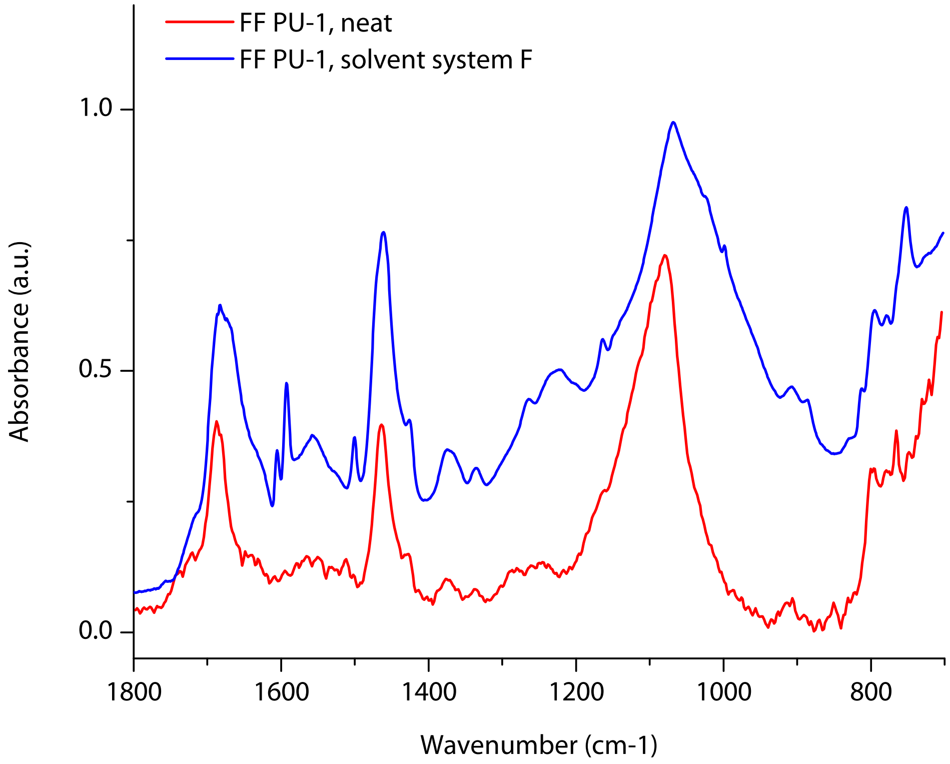

Figure 8-13 – ATR-FTIR spectra of fully-formulated PU-1 before and after exposure to MC-PhOH solvent for 2h, magnified to highlight the organic fingerprint region.

8.4 Conclusions

The addition of phenol to a model paint stripping solution results in significant, irreversible depression of T_g in exposed military coating systems. Phenol is retained in the sample for months after exposure, and can be detected by GC-MS analysis and a simple odor test. There is significant mass loss from the exposed coating at much lower temperature than can simply be accounted for by phenol sublimation, suggesting that a chemical reaction by phenol is resulting in chain scission and subsequent removal of the shortened chains. ATR-FTIR spectroscopy highlights a change in the degree and type of carbonyl/amine hydrogen bonding of the coating, as well as the development of a new aromatic ether peak, which allows us to suggest a model for degradation based on nucleophilic attack of the urethane linkage by the weakly-acidic phenol molecule. The presence of methylcellulose stymies attempts to evaluate material chemistry, as these solutions appear to deposit a thicker and more consistent coating during exposure, which attenuates the ATR-FTIR signal.

8.5 References

[1] Groshart E. Finishing in the green: Paint stripping—Without methylene chloride. Metal Finishing. 1997;95:55-7.

[2] Yang XF, Tallman DE, Croll SG, Bierwagen GP. Morphological changes in polyurethane coatings on exposure to water. Polymer Degradation and Stability. 2002;77:391-6.

[3] Croll SG, Skaja AD. Quantitative spectroscopy to determine the effects of photodegradation on a model polyester-urethane coating. Journal of Coatings Technology. 2003;75:85-94.

[4] Yang XF, Li J, Croll SG, Tallman DE, Bierwagen GP. Degradation of low gloss polyurethane aircraft coatings under UV and prohesion alternating exposures. Polymer Degradation and Stability. 2003;80:51-8.

[5] Yang XF, Tallman DE, Bierwagen GP, Croll SG, Rohlik S. Blistering and degradation of polyurethane coatings under different accelerated weathering tests. Polymer Degradation and Stability. 2002;77:103-9.

[6] Yang XF, Vang C, Tallman DE, Bierwagen GP, Croll SG, Rohlik S. Weathering degradation of a polyurethane coating. Polymer Degradation and Stability. 2001;74:341-51.

[7] Keene LT, Halada GP, Clayton CR. Failure of navy coating systems 1: chemical depth profiling of artificially and naturally weathered high-solids aliphatic poly(ester-urethane) military coating systems. Progress in Organic Coatings. 2005;52:173-86.

[8] Keene LT, Vasquez MJ, Clayton CR, Halada GP. Failure of navy coating systems 2: failure pathways of artificially weathered navy coating systems applied to chromate conversion coated AA2024-T3 substrates. Progress in Organic Coatings. 2005;52:187-95.

[9] Croll SG, Shi X, Fernando BMD. The interplay of physical aging and degradation during weathering for two crosslinked coatings. Progress in Organic Coatings. 2008;61:136-44.

[10] Rivers S, Umney N. Conservation of Furniture. Oxford, England: Butterworth Heinemann; 2003.

[11] Hansen CM. Hansen Solubility Parameters: A User's Handbook, Second Edition: Taylor & Francis; 2007.

[12] Croll SG. Application of the Flory-Rehner equation and the Griffith fracture criterion to paint stripping. J Coat Technol Res. 2010;7:49-55.

[13] Lee I, Wool RP. Polymer Adhesion vs. Substrate Receptor Group Density. Macromolecules. 2000;33:2680-7.

[14] Hinder SJ, Watts JF, Lowe C. Interface analysis and compositional depth profiling by XPS of polymer coatings prepared using ultralow-angle microtomy. Surf Interface Anal. 2004;36:1032-6.

[15] Hinder SJ, Lowe C, Maxted JT, Perruchot C, Watts JF. Intercoat adhesion failure in a multilayer organic coating system: An X-ray photoelectron spectroscopy study. Progress in Organic Coatings. 2005;54:20-7.

[16] Coleman MM, Skrovanek DJ, Hu J, Painter PC. Hydrogen bonding in polymer blends. 1. FTIR studies of urethane-ether blends. Macromolecules. 1988;21:59-65.

[17] Marcos-Fernández A, Lozano AE, González L, Rodríguez A. Hydrogen Bonding in Copoly(ether−urea)s and Its Relationship with the Physical Properties. Macromolecules. 1997;30:3584-92.

[18] MaterialScience B. The Chemistry of Polyurethane Coatings: A General Reference Manual. In: MaterialScience B, editor. Pittsburgh, PA: Bayer; 2005.

[19] Irusta L, Iruin JJ, Fernández-Berridi MJ, Sobkowiak M, Painter PC, Coleman MM. Infrared spectroscopic studies of the self-association of ethyl urethane. Vibrational Spectroscopy. 2000;23:187-97.

[20] Socrates G. Infrared Characteristic Group Frequencies: Tables and Charts. 2nd ed. Chichester: John Wiley & Sons; 1994.

Chapter 9: NEXAFS Analysis of Polyurethane Coatings

9.1 Introduction

In the two previous chapters, we have discussed at length the nature of chemical changes in polyurethane coatings as observed by vibrational spectroscopy. In these chapters, we observed that exposure to methylene chloride alone (solvent system A) produced no detectable chemical changes in the coating. The limitations of the techniques employed in these chapters comes from their depths of analysis – vibrational techniques measure a minimum of 1 μm of thickness, thereby masking any surface changes with a signal from the near-surface bulk region. In order to accurately assess chemical changes at the surface, a surface-sensitive technique such as NEXAFS must be employed in order to provide a sufficiently shallow depth of analysis.

XPS also provides this shallow analysis, and was employed in the earlier discussion, but this method is not sensitive to the pi-bonding states of C=C molecules [1]. Even with monochromatic x-rays, the only signals related to these peaks are shake-up satellites, from which little information can be garnered. Because of its higher sensitivity to local chemical environment, NEXAFS makes a compelling tool for assessing small changes in surface chemistry which may result from solvent exposure. Further, the polarization of the x-ray beam means that we may be able to make qualitative statements concerning the surface orientation of bonds in the material, through calculation of the dichroic ratio. Additionally, a qualitative estimate of surface region density may be made through proper spectral manipulation, in order to gauge the effects of swelling on polymer rearrangement, and the effect of phenol ingress at the surface. The implementation of NEXAFS which is best suited to this application comes in the form of a large area detector which collects 480,000 spectra over an area greater than 1 cm^2. These collected spectra may be used to generate images of the sample, enabling the rapid investigation of trends in surface chemistry.

9.2 Methods

Near Edge X-ray Absorption Fine Structure (NEXAFS) spectroscopy was performed on beamline U7A at the National Synchrotron Light Source at Brookhaven National Laboratory to study the carbon and oxygen K edges of unexposed and exposed coatings. A grid bias voltage of 150V was used, which provides surface selectivity on the order of a few nm, with a spot size of less than 1 mm^2. Spectra were subsequently pre-/post-edge normalized prior to curve fitting and analysis. Additional analysis was performed using the LARIAT detector at this beamline with a bias voltage of 100V, enabling hyperspectral acquisition of a large area sample (12x15mm), with comparable post-processing. Software for hyperspectral analysis from this detector was used to select regions of interest in each sample for further fitting and analysis. This software was also used to generate pseudocolored images of the sample, utilizing the integrated area of a selected peak to determine intensity. Whereas XPS binding energies are based on ejection from discrete orbitals, and thus are consistent across samples, the energy required for an orbital transition depends more on the local chemical environment of the bond being probed, leading to greater variation in binding energy. As such, reference values for NEXAFS peaks were selected on the basis of the best possible fit with the local chemical environment for each peak. An X-ray absorption transition in a given bond is described in general as (*e.g.*) C1s-π^* (C=C), indicating the ground and ultimate excited states of the electron along with the bond in which the electron is excited; for simplicity, we will concisely describe such a transition as C=C π^*. Due to beam time limitations, spectra were obtained only for selected samples.

Curve fitting was performed over a range from 284 eV (to capture the pre-edge baseline) to 302.5 eV. This region was selected in order to define the maximum number of peaks available. The ionization potential of carbon was modeled as an exponential step at approximately 290 eV with a width of 1 eV or less; given the different chemistries involved in the coating, we thought it best to allow a small degree of flexibility in the fit to account for variations in chemistry, though the position and width were very consistent across samples. The pre/post edge correction process used performs two tasks. First, the pre-edge is subtracted to remove the overall background, providing the correct intensity of the spectrum. The post-edge correction, which sets the long-tail end of the data to an intensity of 1, provides normalization of the data. The intensity of the post-ionization edge jump is directly related to the number of atoms which are absorbing x-rays [2]. By using only pre-edge correction, we may assess the overall density of the surface region of interest, within the sampling volume. Using both pre- and post-edge correction, spectral changes indicate differences in functional group density [3]. While more precise measurements have indicated that the change in number density of atoms will change the electron escape depth from this technique [4], leading to a variability in sample depth, we will use this information to provide only a qualitative estimate of increase or decrease in number density at the surface as a result of solvent exposure.

9.3 Results and discussion

9.3.1 NEXAFS spectroscopy of control coatings

Spectra were obtained for each coating system prior to exposure. The included figures show the collected spectra for each fully-formulated system from different selected areas of interest, along with pseudocolored images of these coatings where relevant. Spectra presented here come from measurements taken at 55 degrees, which is the “magic angle” to eliminate orientation effects [2]. We will discuss the ramifications of different angles of takeoff in a later section.

NEXAFS spectra of more complex molecules may be considered using a "building block" scheme, where the spectra of smaller components are combined to generate peak position information of the larger system. The challenge in our analysis here arises from not knowing the specific chemistry of the system under investigation. Numerous assumptions have been made concerning the presence, concentration, and composition of several additives, and these represent the best fit available based on the author's knowledge of such additives and their role in coating formulation.

It is immediately apparent that the coating surface is chemically heterogeneous, with differing relative concentrations of some moieties at different positions; with a lateral resolution on the order of tens of microns, it is not implausible that this suggests the development of regions which are rich in one domain (either hard or soft), given that domains of this scale have been viewed by other members of this research group in other coating systems. As an example, Figure 9-1 shows an image map of the surface pseudocolored for the integrated intensity of C=C with pre/post normalization; several lighter and darker spots can be seen. Given the aliphatic nature of MIL-PRF-85285 (termed PU-2), the peak exhibited by the outward-facing surface shown in Figure 9-2 for C1s-π^* C=C peak (285.4 eV, peak A) must be attributed to an additive in the polymer; we suspect that this is due to the presence of UV stabilizing compounds, which might consist of a benzophenone-based molecule or similar. A single curve fit for this peak is slightly too broad for this technique (FWHM = 0.8 eV), so we have chosen to fit this as two peaks at 285.2 and 285.7 eV (dubbed A1 and A2), with somewhat more reasonable FWHM values (~0.6 eV) for a peak at this binding energy. Since the fitted peaks are dissimilar in area, with A1 generally being larger than A2, we are confident in this assignment. The very weak features at the nitrogen K edge (not shown) suggest that the chosen stabilizer for this coating does not contain azole functionality. The small peak at 286.7 eV (B) corroborates the prediction of a molecule resembling benzophenone, as it corresponds to the transition seen in a carbonyl which links two aromatic rings. Other peaks in the carbon K edge spectrum are related to C-H σ* (288 eV, C) absorptions from the long chains of the polyisocyanates and polyesters [5], and to C=O π* (289.4 eV, D) absorptions due to the polyisocyanates – this peak fits well for the types of urea linkages seen at the heart of many structures commonly employed in the formation of polyisocyanates from HDI [6]. We believe the peak fit at 290.7 eV (E) to be the aggregate of several peaks: the C=O π* and C-N σ* transitions arising from urethanes, a C-O σ* transition, and the C=C 2π* transition; while the literature states that the carbonyl peak should be closer to 290 eV, and this single peak is somewhat overly broad for this assignment, there is a significant challenge in obtaining proper fit information for the ionization edge area between 290 and 291 eV, so we have chosen to under-fit the curve [7]. Further peaks at ~293, ~296, and ~299 eV (F, G, H) are σ* transitions which relate to C-C, C-C-/C-O, and C=C, respectively [8]. The positions and assignments of these peaks are presented in Table 1, and shall form the basis of assignments for all other systems discussed.

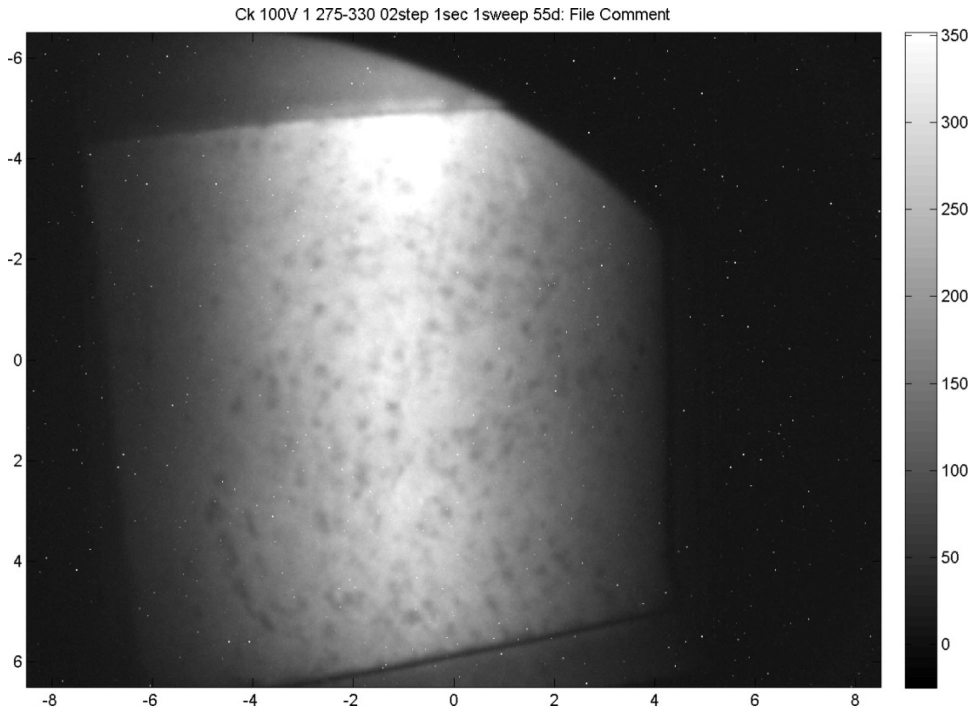

Figure 9-1 – NEXAFS pseudocolored image map of unexposed MIL-PRF-85285 selected for integrated C=C intensity.

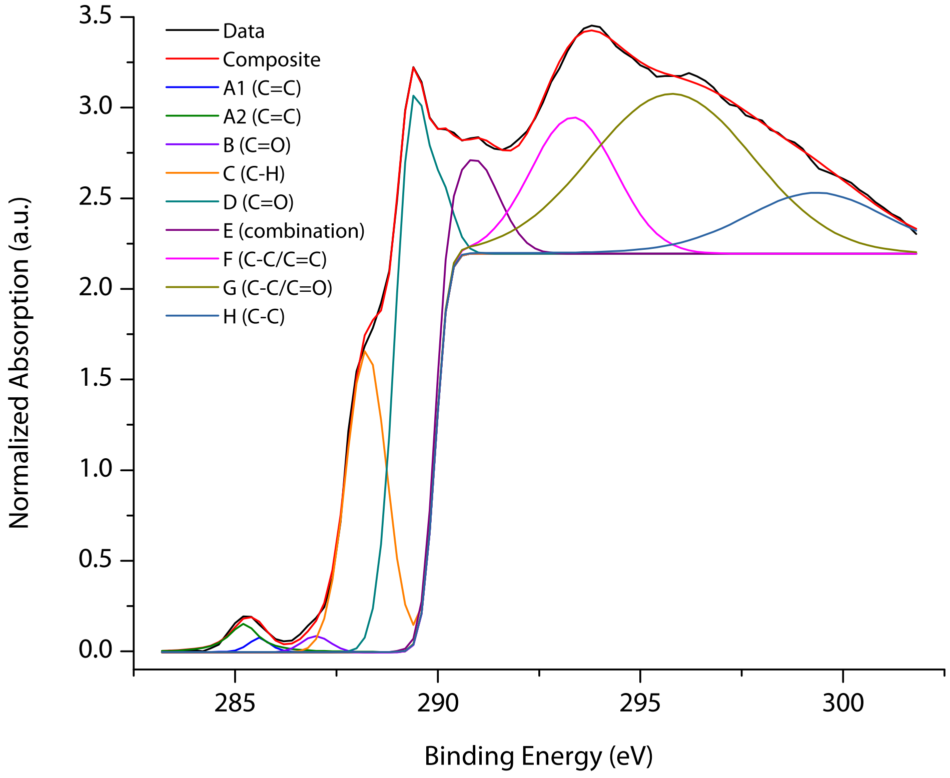

Figure 9-2 – NEXAFS C K-edge spectrum of unexposed, fully-formulated MIL-PRF-85285 (blue color), top surface.

Label	**Binding Energy (eV)**	**Structure**
A	285.2, 285.7	C-H π* of aromatic C=C
B	286.8	C=O π*
C	288	C-H σ*
D	289.5	C=O π*
E	290.7	C=O π*, C-N σ*, C-O σ*, C=C 2π*
F	293	C-C/C=C σ*
G	296	C-C/C=O σ*
H	299	C-C σ*

Table 9-1 – Labels and assignments of NEXAFS C K-edge peak fits for polyurethane coatings

The substrate-facing and surface-facing sides of the coating do not exhibit the same spectrum. In Figure 9-3, we show the substrate-facing side of the coating, following removal from release paper. The A peaks are appreciably stronger at this surface than on the top surface, by roughly 40%. Along with the increase in aromatics, peak B shows an increase in intensity, which suggests migration of a stabilizer to this surface. Peak C is much stronger than at the top surface, leading it to stand distinctly in the curve, and peaks D and E are now roughly equal in spectral height. The σ* peak F is broader here, and peak G is largely indistinct; these bonds are related to the polymer chain, and therefore suggest that while different functional groups may have segregated preferentially to this interface, so too have aliphatic chains.

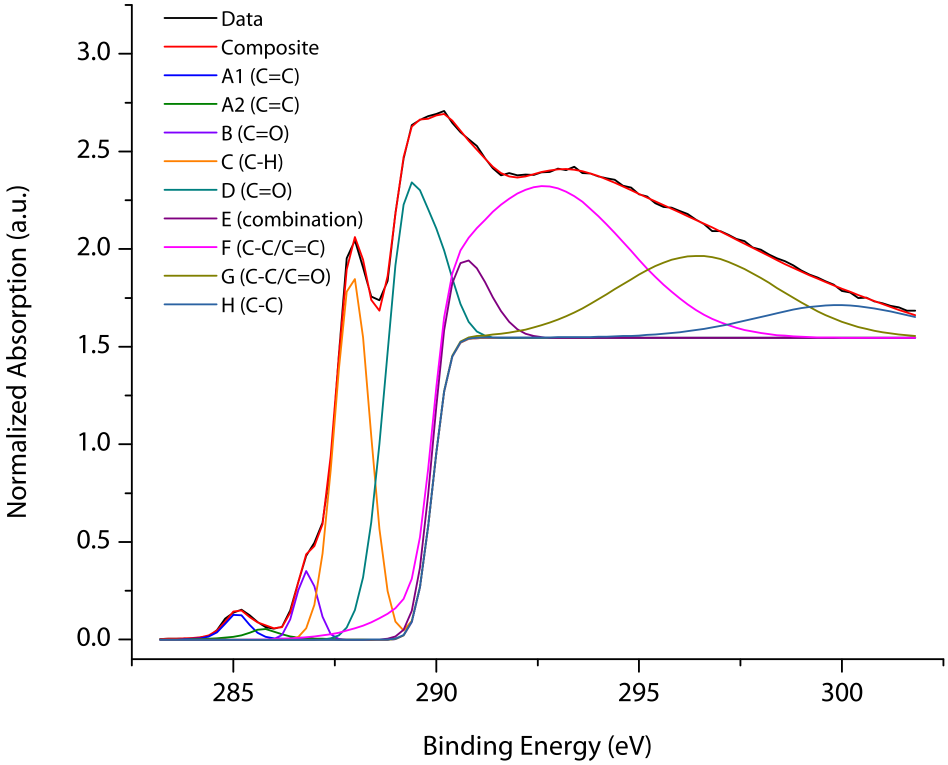

Figure 9-3 – NEXAFS C K-edge spectrum of unexposed, fully-formulated MIL-PRF-85285 (blue color), bottom surface.

In Figure 9-4, we present the NEXAFS spectrum of clear-formulated MIL-PRF-85285, top surface, with no pigmentation or fillers added. While the structure of the spectrum is similar to the pigmented system, the parameters for peak fits demonstrate that there are major differences. The C=C π* aromatic peak remains, but whereas in the first spectrum the lower-energy peak (A1) was larger than the higher-energy peak (A2), the opposite is now true, and the fit quality is poorer. Peak B remains largely unaffected, suggesting a similar stabilizer concentration may be employed. We conclude that in addition to indicating a stabilizer, the aromatic peak is also related to the pigmentation or fillers used. Peaks C and D remain as before, as expected for components of the resin itself. Peak E increases relative to the adjacent carbonyl (peak D), but this occurs heterogeneously across the surface; some areas show a low spectral feature at this binding energy. This may suggest that complete mixing of the clear-formulated coating is more problematic than initially thought, or that microscale domain separation is occurring between the hard and soft segments of the system. Further heterogeneity is seen in peaks F, G, and H, which relate to the polymer chains.

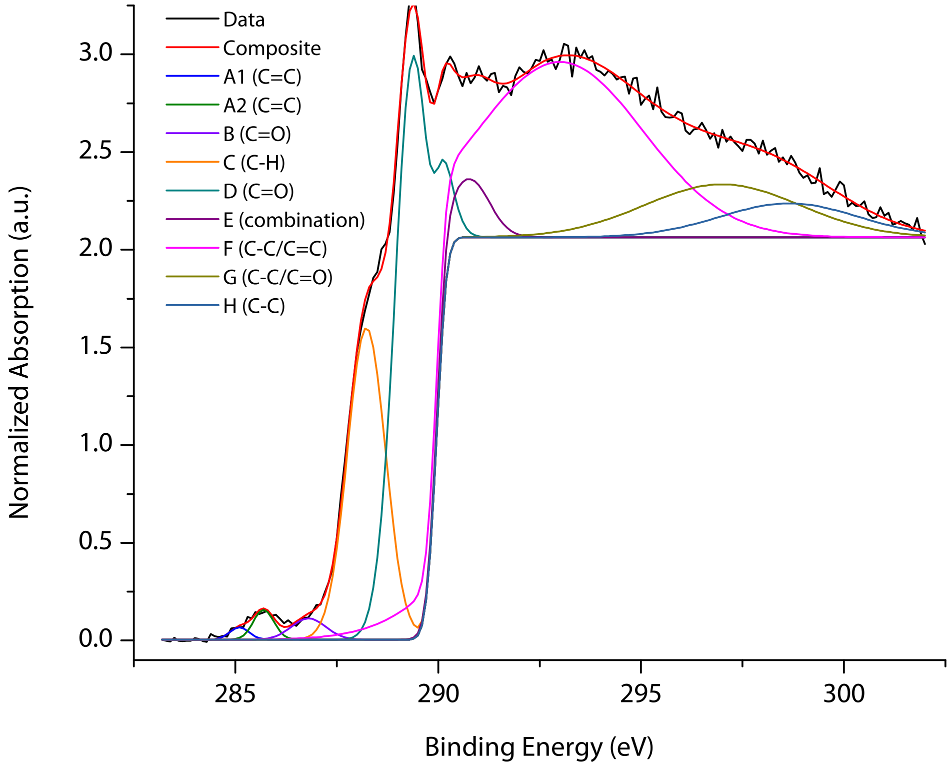

Figure 9-4 – NEXAFS C K-edge spectrum of unexposed, clear-formulated MIL-PRF-85285, top surface.

In Figure 9-5, we present the NEXAFS spectrum of clear-formulated MIL-PRF-85285, bottom surface, with no pigmentation or fillers added. It is immediately obvious that the surface of this sample does not compare well to its pigmented counterpart. The amount of aromatic carbon at the surface is 2-3 times higher here than is seen in the fully-formulated coating at the same surface, and is much more heterogeneously distributed. Peak B is diminished, which suggests another, unrecognized source of this aromatic material. The other most significant change to this spectrum is the unusual contribution of carbonyl in peak D. We speculate that the PVF release paper used interacts in some way with different components of the coating, leading to preferential segregation of certain additives and components at the wetting surface, with a sufficient effect on composition to lead to a minor shift in the ionization potential. The interplay between peaks D and E at the edge contributes to an odd fitting of the feature. With the FWHM of peaks constrained to resemble those observed in the literature, the contribution of carbonyl generates an additional visible feature just at the edge, which does not appear to be caused by a different chemical contribution.

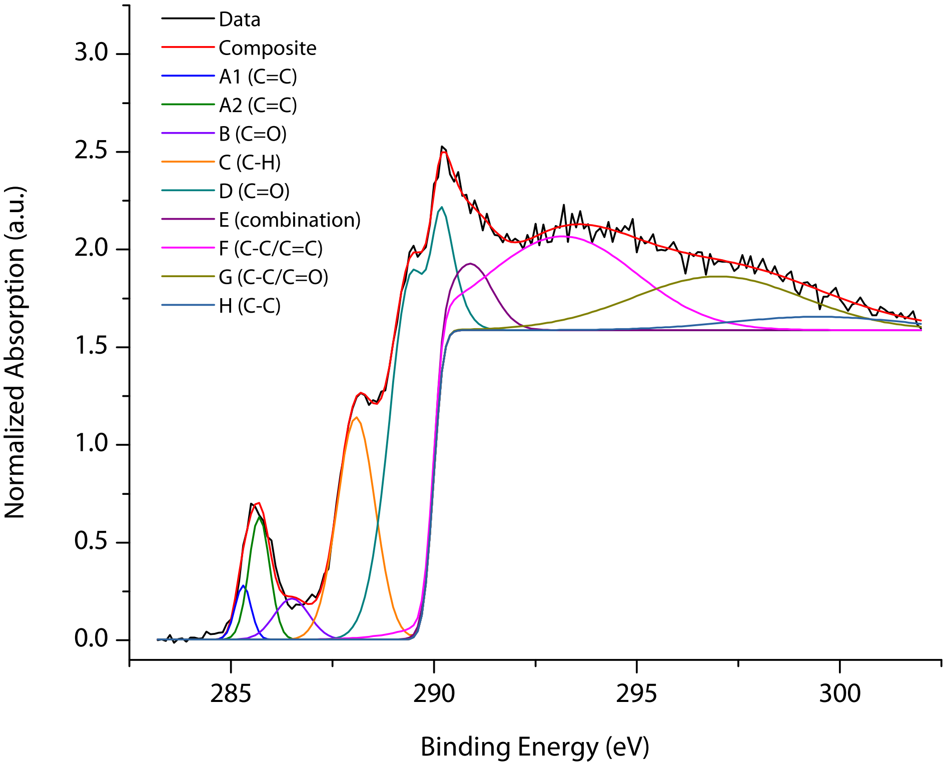

Figure 9-5 – NEXAFS C K-edge spectrum of unexposed, clear-formulated MIL-PRF-85285, bottom surface.

9.3.2 NEXAFS spectroscopy of exposed coatings

Coatings were analyzed after a droplet of the paint stripper solvent component was applied to the surface and subsequently dried. The pseudocolored image of this exposure, selecting for the presence of C=C, is shown in

Figure 9-6, and clearly demonstrates the location of the center of the droplet and the maximum diameter of exposure through the depletion of this moiety. Although the image gives the appearance of significant surface deformation, the ripples in the intensity are largely indicative of chemical changes, as far as can be determined. Spectra at the far edges of the sample are consistent with the unexposed sample, showing that the solvent did not diffuse to these regions. Broadly, there are two regimes of interest due to exposure: the center of the droplet, and the halo around the droplet. Interrogation of these two regions reveals markedly different spectra.

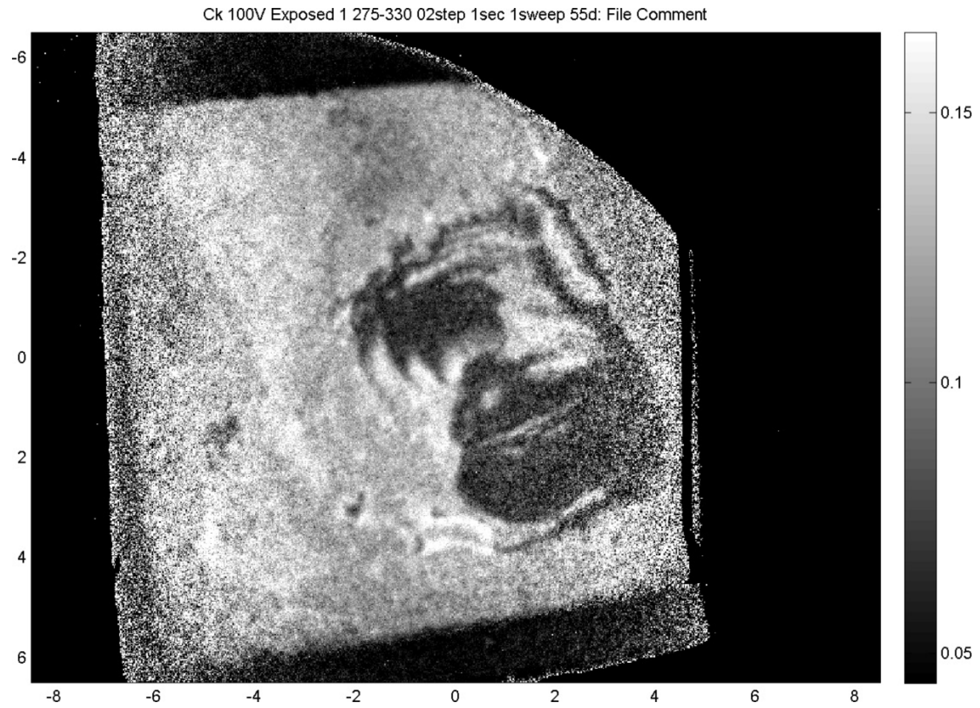

Figure 9-6: Pseudocolored hyperspectral image of MC-exposed, fully-formulated MIL-PRF-85285, top surface, with brightness linked to C=C π* peak area.

In Figure 9-7, we present the NEXAFS spectra from the center of the region of application of methylene chloride to the surface. In the center, the A peaks indicating aromatic C=C have decreased. It appears that the aromatic-based additive has been displaced by the solvent, suggesting its solubility in methylene chloride. The amount of peak C decreases slightly relative to the amount of peak D, and peak G becomes somewhat less pronounced, suggesting an effect on the polymer chains. Peak D shows a small shift to lower binding energy (by about 150 meV, which is within the experimental precision of the instrument), which could be due to changes in the local steric environment about the carbonyl as a result of polymer swelling and rearrangement; we have discussed this swelling in an earlier chapter. The intensity of peak E drops slightly, particularly as relating to its contribution around 290.1 eV. Analysis of the halo region (Figure 9-8) reveals that the aromatic additive depleted from the center of the droplet has been redeposited here; the overall intensity of this peak increases by roughly 50%.

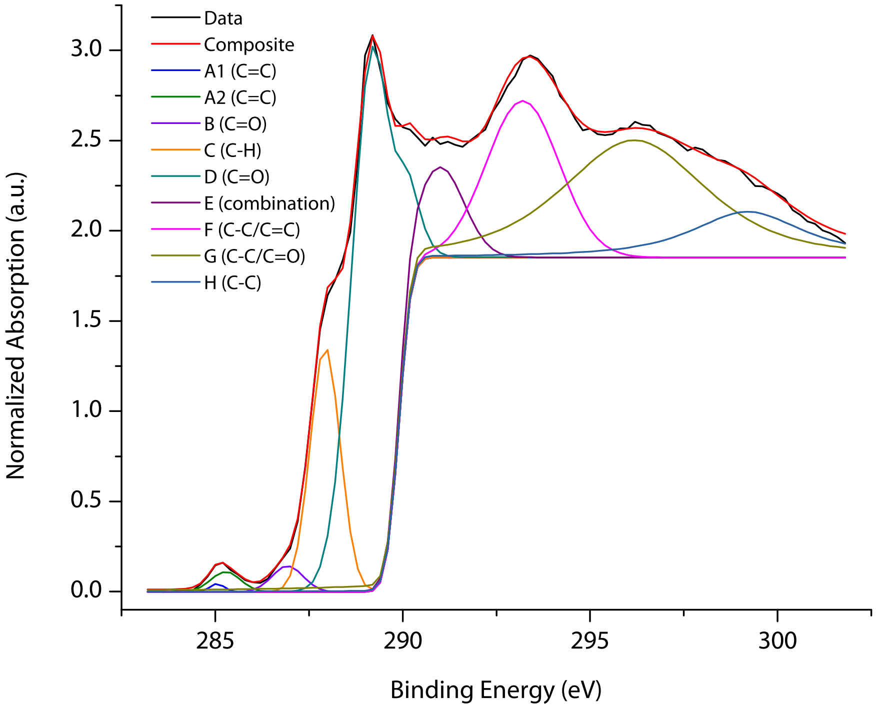

Figure 9-7 – NEXAFS C K-edge spectrum of MC-exposed, fully-formulated MIL-PRF-85285, top surface, within the area of the methylene chloride droplet.

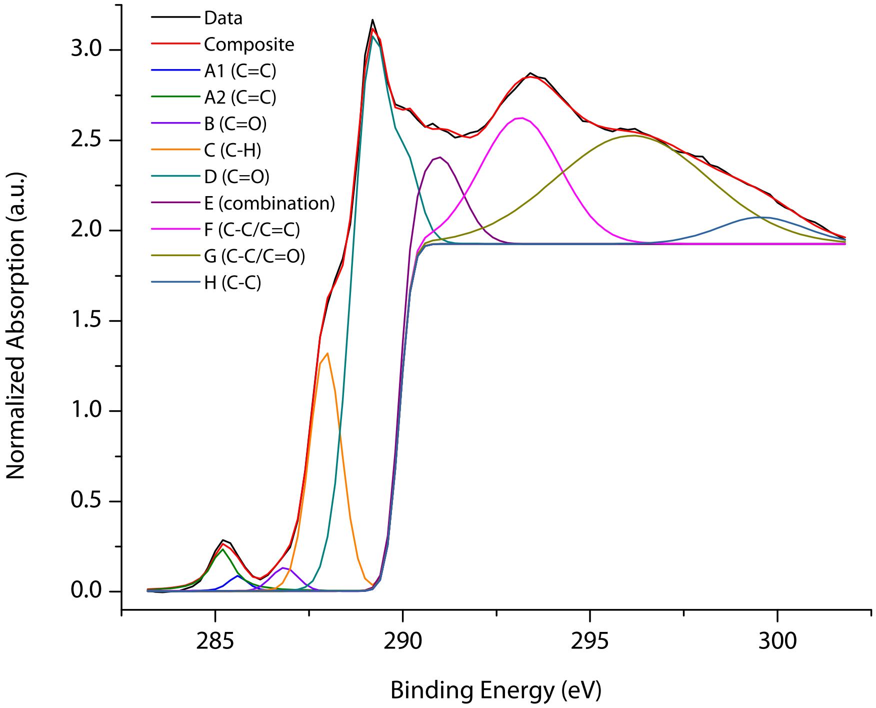

Figure 9-8 – NEXAFS C K-edge spectrum of MC-exposed, fully-formulated MIL-PRF-85285, top surface, in the halo-like ring around the outer perimeter of the methylene chloride droplet.

Previously, this group had proposed a model of methylene chloride solvation of the carbonyl in polyurethane, with a subsequent chain rearrangement as a result of increased polymer segmental dynamics. Based on changes to peaks C and G, we can conclude that the solvent has had some effect on polymer chain configuration, validating that model. As compared to the spectrum of the unexposed coating, the overall intensity has dropped, indicating a slightly lower overall density of functional groups in the coating (on the order of 5%).

Figure 9-9 provides the same pseudocolored image corresponding to peak A for exposure on the bottom surface of the coating. In Figure 9-10, we show the spectrum following exposure within the area of the droplet, while Figure 9-11 provides the spectrum of the ring around the droplet center, seen as a darker region in the image. Unlike the top coating, the concentration of C=C increases at the center of the droplet. Peak B shows some decrease in both the droplet and ring. The intensity of peak C is somewhat negatively impacted relative to the height of peak D, and in the ring region peak G is less distinctive, which again speaks to a change in polymer chain configuration. Peaks E and D remain in roughly their original proportion in the droplet region, but peak D is diminished in the ring around the sample. It is likely that we are seeing the preferential segregation of an unknown filler in the ring of the droplet

Figure 9-9 – Pseudocolored hyperspectral image of MC-exposed, fully-formulated MIL-PRF-85285, bottom surface, with brightness linked to C=C π* peak area.

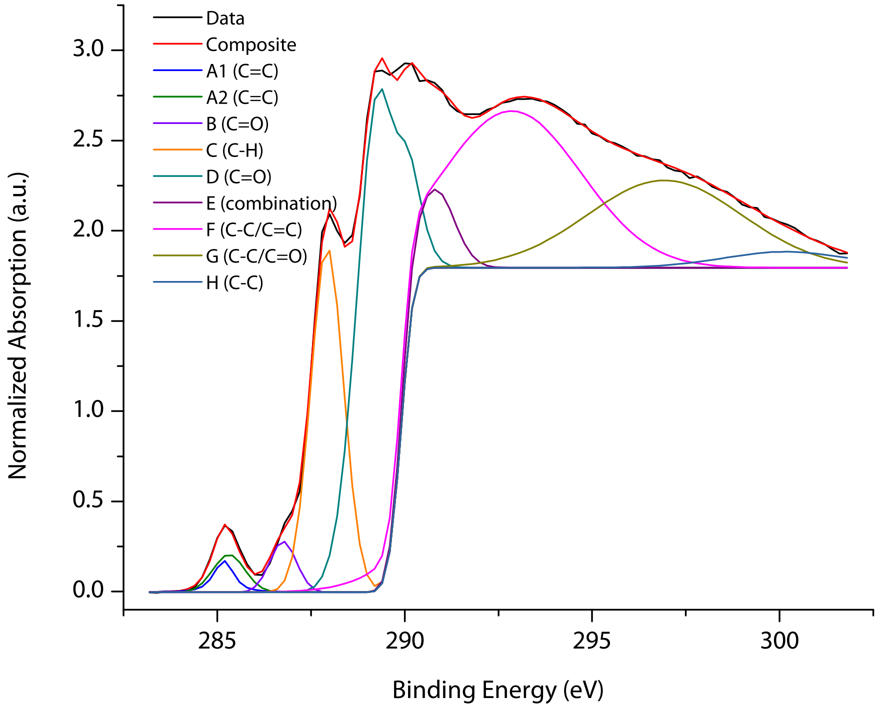

Figure 9-10 – NEXAFS C K-edge spectrum of MC-exposed, fully-formulated MIL-PRF-85285, bottom surface, within the area of the methylene chloride droplet.

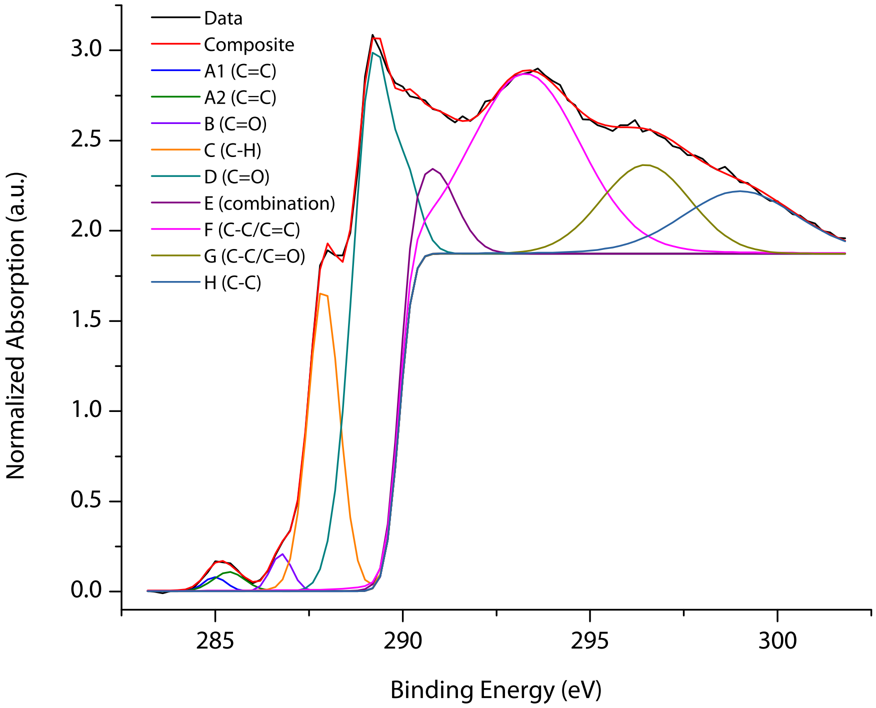

Figure 9-11 – NEXAFS C K-edge spectrum of MC-exposed, fully-formulated MIL-PRF-85285, bottom surface, in the halo-like ring around the outer perimeter of the methylene chloride droplet.

In Figure 9-12, we present a pseudocolored image of both the bottom (left) and top (right) surfaces of coating 85285 after exposure by a droplet of liquid phenol (91% PhOH, 9% H_2O), with coloration linked to the area of peak A. Figure 9-13 and Figure 9-14 show the spectra of these droplet regions as taken from the top and bottom surfaces, respectively. The significant changes occur in peaks A and E, both of which may be attributed to aromatic π* transitions (π* and 2π*, respectively). Through these changes, we confirm that part of peak E relates to the presence of aromatics.

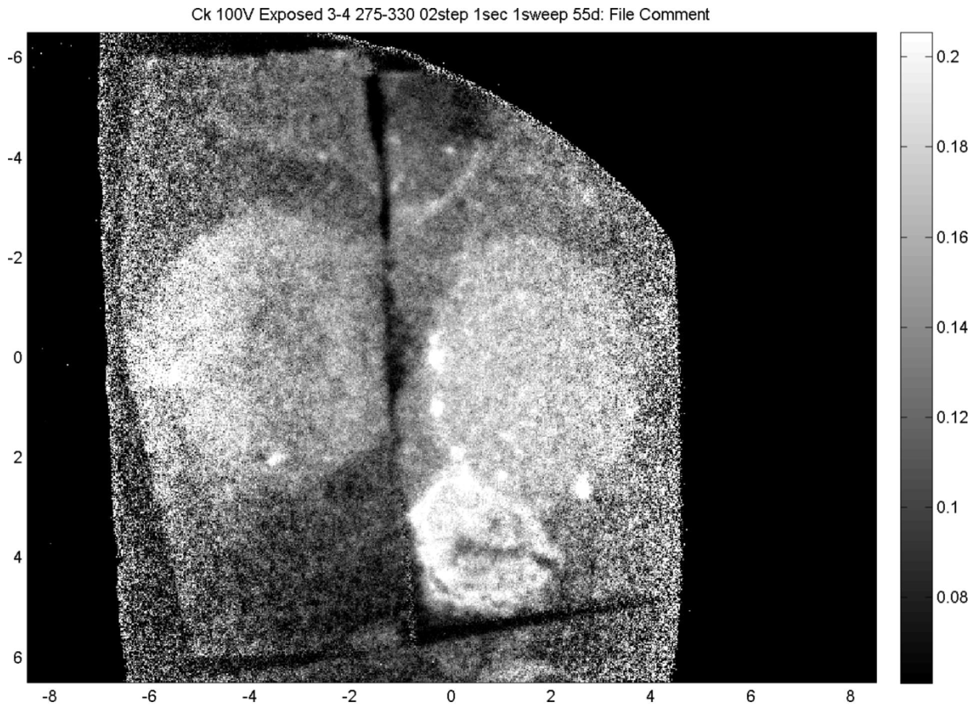

Figure 9-12 – Pseudocolored hyperspectral image of PhOH/H_2O-exposed, fully-formulated MIL-PRF-85285, bottom surface (left) and top surface (right), with brightness linked to C=C π* peak area.

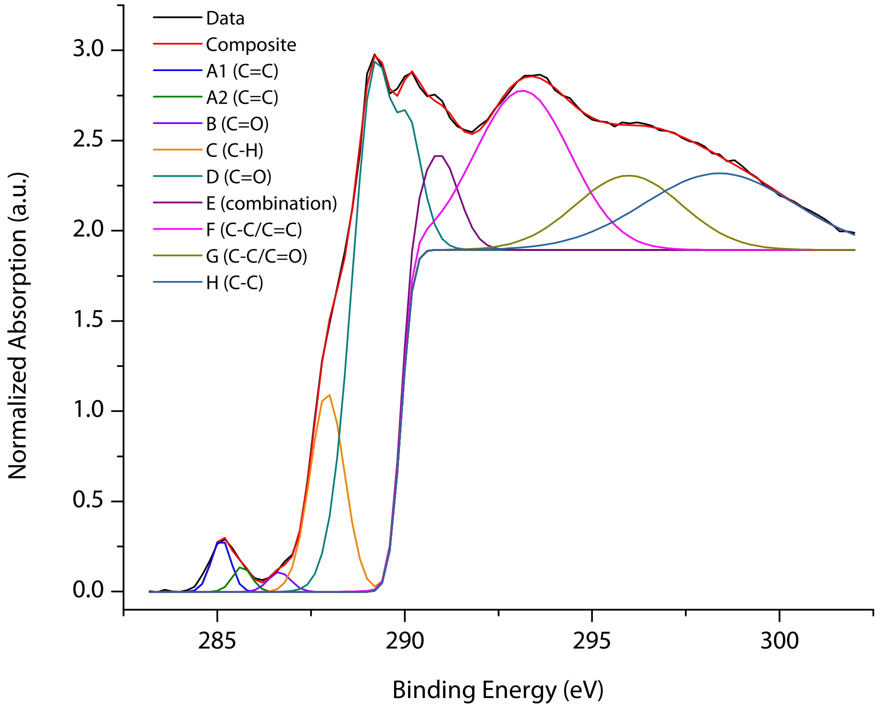

Figure 9-13 – NEXAFS C K-edge spectrum of PhOH/H_2O-exposed, fully-formulated MIL-PRF-85285, top surface, in the region of the droplet.

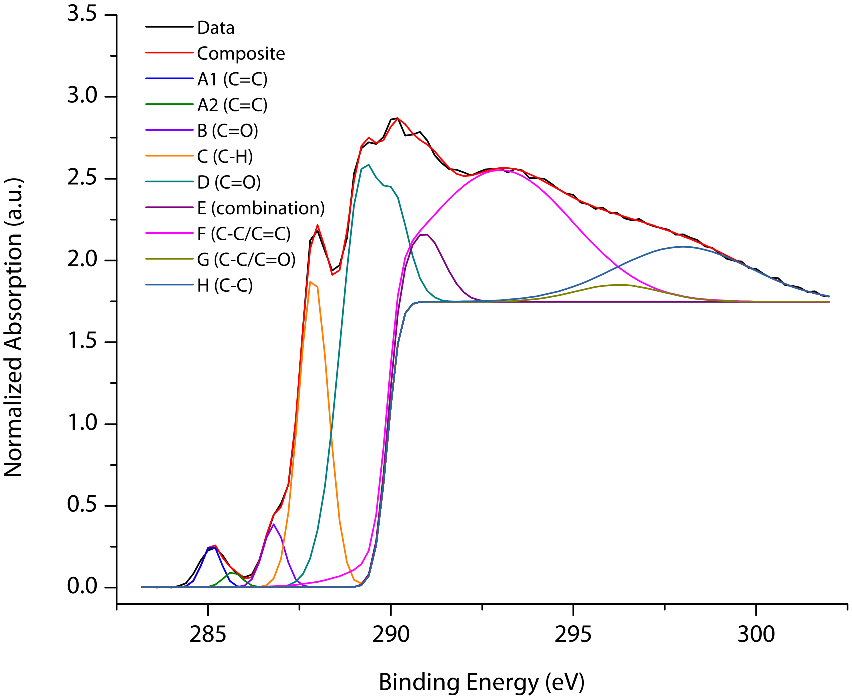

Figure 9-14 – NEXAFS C K-edge spectrum of PhOH/H_2O-exposed, fully-formulated MIL-PRF-85285, bottom surface, in the region of the droplet.

From our thermal analyses, we know that methylene chloride and phenol in combination serve to produce a significant decrease in the T_g of the coating (see Table 8-1). Having also established that the presence of Methocel produces a conformal coating thick enough to dominate the x-ray spectrum, we have analyzed the surfaces of this coating after exposure to methylene chloride/ethanol/phenol. These spectra, seen in Figure 9-15 and Figure 9-16, demonstrate the persistent effects of these solvents due to exposure. We know from past work on this project that significant amounts of phenol remain in the sample, giving it a purple tint and persistent odor for years after exposure. There is no major increase in the peaks at region A, which is surprising given the aforementioned phenol retention, and unusually suggests a removal of unreacted phenol, and the absence of aromatic rings chemically bound to polymer chains at the surface. Peak E increases dramatically in these spectra, such that it is the dominant feature at and around the ionization potential step. Further, the “double-peak” feature of Peak D has once again led to a stronger second peak, due to another minor shift in the ionization potential, which suggests a more significant change in surface chemistry. Additionally, the proportional change in height of the ionization edge makes it difficult to remain consistent with regards to the significance of peak areas from previous samples. Given the reaction mechanism proposed in Chapter 8, we must conclude that the increase in Peak E is due primarily to a contribution from aromatic C-O σ*. This is unusual, in light of the findings of no substantial change in Peaks A.

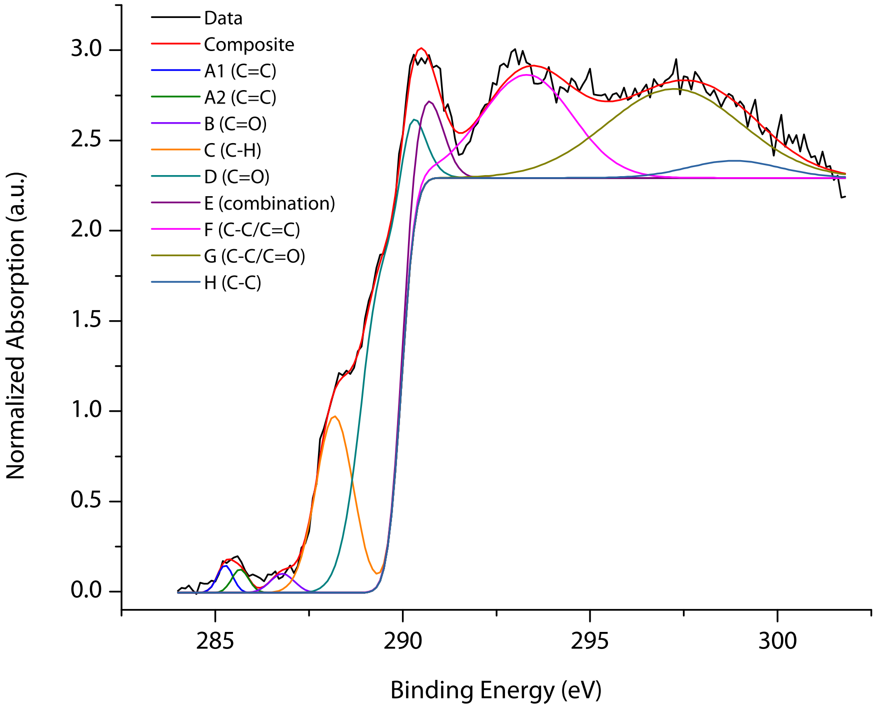

Figure 9-15 – NEXAFS C K-edge spectrum of MC/EtOH/PhOH-exposed, fully-formulated MIL-PRF-85285, top surface.

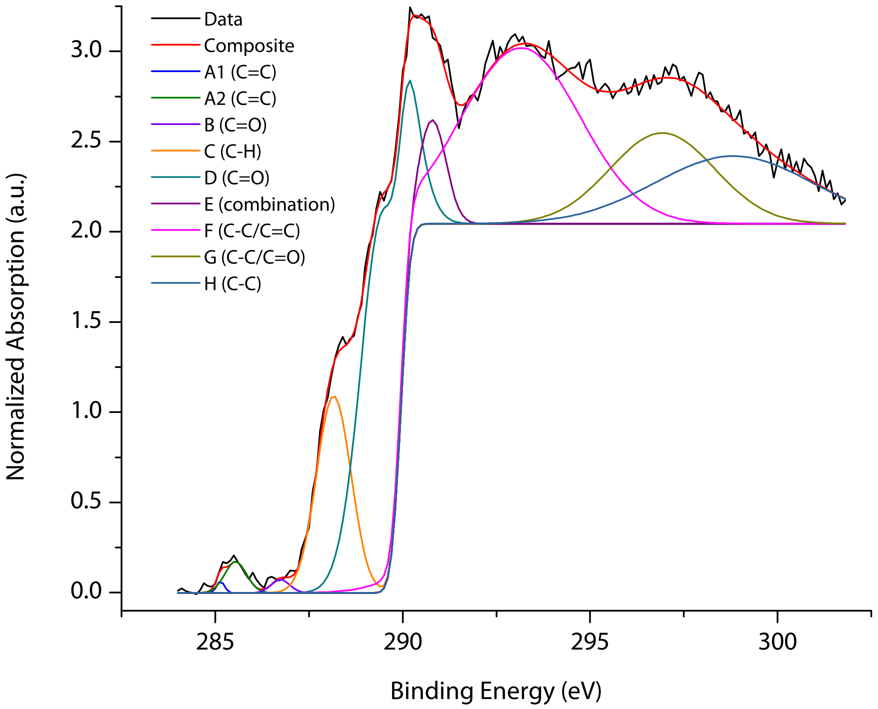

Figure 9-16 – NEXAFS C K-edge spectrum of MC/EtOH/PhOH-exposed, fully-formulated MIL-PRF-85285, bottom surface.

9.3.3 Density changes from exposure

By examining only pre-edge corrected spectra, we can make qualitative statements regarding the density of the sample within the depth of analysis of the region of interest. In order to eliminate orientation factors which might influence the intensity, the only spectra analyzed in this fashion were those collected at 55 degrees. Prior to exposure, these samples have been measured to have a roughness on the order of 2 μm, which will play a role in the results obtained. By averaging over a large area (on the order of 1 mm^2 or greater) and by analyzing several areas, we hope to eliminate the issue roughness might cause. As such, only large changes may be used to infer effects.

In Figure 9-17 we present a pre-edge-corrected pseudocolored image of an unexposed coating of 85285, both top and bottom faces, integrated over the post-edge region in order to highlight changes in total density. It is immediately apparent that the density is far more heterogeneous across the top surface than the bottom, which manifests in the heterogeneous distribution of functional groups seen earlier. It is likely that the homogenous bottom surface provides benefits to substrate adhesion. This analysis provides interesting insight into the model of curing in this coating system. These changes in density across the sample suggest a number of more complex solvent diffusion parameters as a result of differences in polymer density and density of functionalities. This could suggest vulnerabilities in the coating to penetration by paint removers.

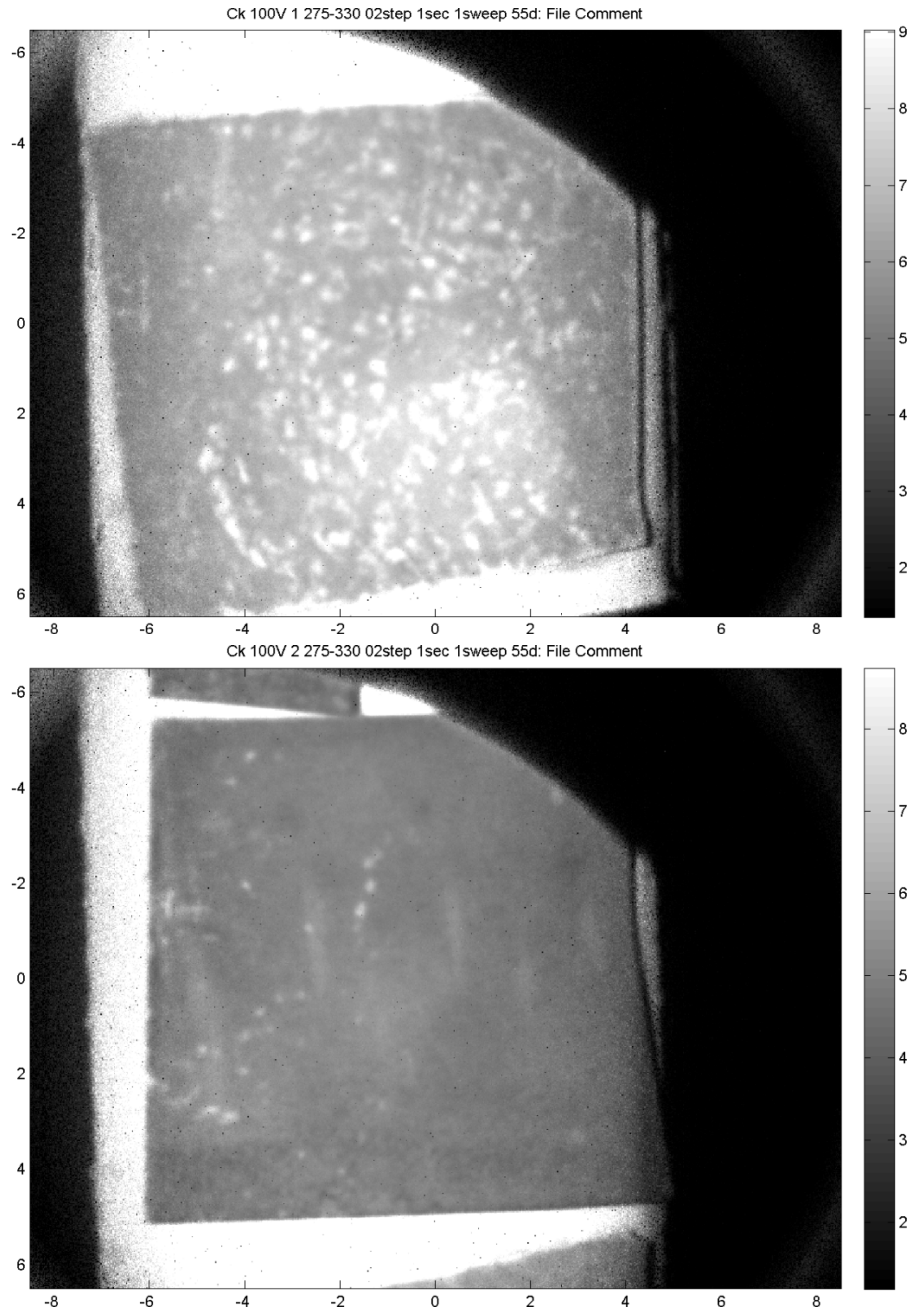

Ck 100V 1 275-330 02step 1sec 1sweep 55d: File Comment

Ck 100V 2 275-330 02step 1sec 1sweep 55d: File Comment

Figure 9-17 – Pseudocolored NEXAFS images of fully-formulated 85285 (top) top and (bottom) bottom surfaces, pre-edge normalized, with intensity from integration over 290 - 305 eV.

9.3.4 Dichroic ratio changes from solvent exposure

Methylene chloride exposure has been demonstrated to cause changes in local surface concentration of coating additives, and to lead to changes in the density of functional groups in the surface region. The solvation mechanism was described in Chapter 7 to impact polymer chain segmental mobility, which would lead to rearrangements of the existing bonds. In Table 9-2, we demonstrate the effects of solvent exposure at the top surface of the coating by examining the coating prior to exposure, and the ring region at the edge of the droplet. In this analysis, we have chosen an R^2 fit value of 0.85 to be the minimum value for a “good fit” indicating physical significance. Prior to solvent exposure, the top surface does not show significant orientation, with only the C-H bonds of C=C aromatics showing some semblance of weak ordering normal to the surface. After exposure, there is a significant increase in the amount of orientation at the surface, in terms of both degree of ordering and affected bonds. In particular, the carbonyl peak shows a very strong orientational preference in the plane of the coating. The order in the polymer backbone chains is unaffected by exposure.

PU-2 Top, unexposed							
Peak (eV)	C=C π*	C=O π*	C-H σ*	C=O π*	C-O σ*	C-C σ*	C-C σ*
R^2	0.9143	0.6505	0.2885	0.3409	0.0469	0.2939	0.2938
DR	**0.0555**	-0.2039	0.0037	-0.0027	0.0031	0.0003	-0.0003
PU-2 Top, ring around droplet							
Peak (eV)	C=C π*	C=O π*	C-H σ*	C=O π*	C-O σ*	C-C σ*	C-C σ*
R^2	0.9893	0.9615	0.9640	0.8989	0.8306	0.1961	0.1492
DR	**0.2849**	**-1.1418**	**0.0489**	**0.0332**	**0.4167**	0.0123	-0.001

Table 9-2 - Dichroic ratios of molecular bonds in methylene chloride-exposed polyurethane, top surface.

In Table 9-3, we present the dichroic ratio data for solvent exposure to the bottom surface of the coating. The initial orientation of the material differs significantly at the bottom surface, again highlighting the difference between the top and bottom surfaces of the coating. Several bonds show a fit value between 0.8 and 0.85, which are lower than our self-imposed fit threshold, but suggest a likely orientation effect. Following solvent exposure, these fit values increase significantly, as is seen in the top surface. The degree of change in orientation of the carbonyl bond is much lower at this surface, suggesting that the curing process or additives may be constraining the ability of the chains to rotate to permit in-chain reorientation.

PU-2 Bottom, Unexposed							
Peak (eV)	C=C	C=O	C-H	C=O	C-O	C-C	C-C
R^2	0.9979	0.9775	0.8024	0.8439	0.8465	0.7569	0.5210
DR	**-0.1413**	**-0.0368**	**-0.0789**	**0.0645**	**-0.1190**	0.0055	-0.0202
PU-2 Bottom, droplet center							
Peak (eV)	C=C	C=O	C-H	C=O	C-O	C-C	C-C
R^2	0.9603	0.9961	0.9938	0.9846	0.8936	0.4739	0.5294
DR	**-0.0382**	**-0.2549**	**-0.0403**	**-0.2049**	**-0.1443**	0.0885	-0.0101

Table 9-3 - Dichroic ratios of molecular bonds in methylene chloride-exposed polyurethane, bottom surface.

9.4 Conclusions

While methylene chloride was previously shown to cause no significant change which could be resolved through Raman, ATR-FTIR, or large-area XPS, a more focused study with a surface-sensitive, high-resolution imaging technique has revealed that there are subtle changes. With adequate lateral resolution of an exposed region, we can see that the local concentration of coating additives is affected by the addition of solvent. The extraction and diffusion of such additives during exposure could contribute to the rate of infiltration of paint removing solvents. Methylene chloride has also been demonstrated to lead to polymer chain rearrangement and reordering, which is behavior consistent with the model of carbonyl solvation and inter-chain cross-linkage separation previously posited. While the degree of order induced is low compared to many other measured systems, the values are not unusual for a bulk system [3]. The changes to ordering differ between the outward-facing and substrate-facing surfaces of the coating, suggesting appreciably different near-surface molecular arrangements in addition to the observed chemical compositions. While additives and stabilizers have been suggested based on the interpretation of spectral features, these cannot be confirmed.

9.5 References

[1] Leiro JA, Heinonen MH, Laiho T, Batirev IG. Core-level XPS spectra of fullerene, highly oriented pyrolitic graphite, and glassy carbon. Journal of Electron Spectroscopy and Related Phenomena. 2003;128:205-13.

[2] Stöhr J. NEXAFS Spectroscopy: Springer; 1992.

[3] Lenhart JL, Fischer DA, Chantawansri TL, Andzelm JW. Surface Orientation of Polystyrene Based Polymers: Steric Effects from Pendant Groups on the Phenyl Ring. Langmuir. 2012;28:15713-24.

[4] Sohn KE, Dimitriou MD, Genzer J, Fischer DA, Hawker CJ, Kramer EJ. Determination of the Electron Escape Depth for NEXAFS Spectroscopy. Langmuir. 2009;25:6341-8.

[5] Urquhart SG, Hitchcock AP, Smith AP, Ade HW, Lidy W, Rightor EG, et al. NEXAFS spectromicroscopy of polymers: overview and quantitative analysis of polyurethane polymers. Journal of Electron Spectroscopy and Related Phenomena. 1999;100:119-35.

[6] Urquhart SG, Smith AP, Ade HW, Hitchcock AP, Rightor EG, Lidy W. Near-Edge X-ray Absorption Fine Structure Spectroscopy of MDI and TDI Polyurethane Polymers. The Journal of Physical Chemistry B. 1999;103:4603-10.

[7] Kuznetsova A, Popova I, Yates JT, Bronikowski MJ, Huffman CB, Liu J, et al. Oxygen-Containing Functional Groups on Single-Wall Carbon Nanotubes: NEXAFS and Vibrational Spectroscopic Studies. Journal of the American Chemical Society. 2001;123:10699-704.

[8] Sedlmair J. Soft X-Ray Spectromicroscopy of Environmental and Biological Samples: Universitätsverlag Göttingen; 2011.

Chapter 10: Conclusions and Future Work

10.1 Conclusions

10.1.1 Composites

Sizing has been extracted from commercial carbon fibers and deposited for analysis. Several functional groups have been observed, which suggest the chemistry of this material is similar but not identical to those found in patent disclosures by the manufacturer. Sizing removal from the fiber was performed using using methylene chloride, which is a common primary component in military paint removers, thus indicating the potential vulnerability of painted composites to chemical damage by solvent ingress during the depainting process. Accelerated weathering has been shown to cause cleavage at the Amide II linkage in the sizing, as well as leading to restrictions in molecular vibration likely due to curing. Damage has been observed after a relatively short exposure time, highlighting the importance of proper protection of composite materials from UV exposure.

Ultrafast laser ablation has been used to perform shallow and full-depth material removal from neat resin and composites. The pressure shockwave due to ablation has been observed to cause raised edges of ablation craters in neat resin, and significant disbondment of carbon fibers from the matrix. A nanoporous texture develops at the site of ablation, which further reveals a number of larger pores inherent to the material. These pores are also found in the composite material not far from the fiber/matrix interface, which represents a significant vulnerability in the composite to fiber disbondment and interphase attack by penetrating solvents. Further, these pores reduce the protection of the interphase from UV radiation, to which the sizing has been proven susceptible. Laser interactions with the carbon fiber differ from those with the resin, with striations and cone-like structures developing on the surface of the fiber. Material chemistry at the site of ablation appears unchanged via vibrational spectroscopy, but surface-sensitive techniques observe a strong increase in the amount of styrene at the ablated surface, suggesting that residual styrene monomers in the resin are being expelled and redeposited at the surface.

Low-grade thermal damage (above the glass transition temperature) has been found to cause numerous observable changes in vinyl ester and CFVE composites. Laser-induced fluorescence shows a repeatable shift in both wavelength and peak width which may be easily measured by a portable NDT device. Vibrational spectroscopy indicates the migration and concentration of unreacted styrene monomers from the bulk to a region nearer the surface, while x-ray analysis places a layer of styrene on the surface following outgassing. Mechanical testing shows an initial increase in elastic modulus from exposure, followed by a subsequent decrease, most likely due to the loss of styrene acting as a plasticizer in the material. The evolution of a second damping peak in DMA analysis suggests that the material properties are significantly impacted by this styrene migration, leading to a change in the material elasticity.

10.1.2 Coatings

Methylene chloride has been found to swell polyurethane coatings by solvating the carbonyl bond, which is responsible for inter-chain hydrogen bonding. By separating these bonds, the coating is rendered soft and easier to remove while the solvent is present. The solvent preferentially solvates the carbonyl, leading to peak dilation seen through Raman spectroscopy. Proton NMR spectroscopy indicates that the methylene chloride molecules are in close contact with the polymer, leading to increased segmental dynamics. The solvent has been found to evaporate from the coating enough to end swelling after just minutes, but residual solvent has been found to outgas weeks after exposure with suitable thermal treatment. Methylene chloride produces no irreversible chemical changes in the coating, but is observed by NEXAFS spectroscopy to cause displacement of additives to the coating, as well as leading to polymer chain reordering at the surface, with a slight reduction in surface polymer density.

This swelling also facilitates the ingress of other components of the mixture. Phenol enters the swollen coating and appears to react with the urethane ether linkage via nucleophilic substitution, thus causing polymer chain cleavage with aromatic ring attachment. Additional phenol becomes intercalated within the matrix, leading to very slow outgassing which lasts years. This scission combines with the steric effects of phenol to effectively (and irreversibly) depress the T_g of the exposed coating. Water appears to enhance this effect, leading to lower T_g, likely by increasing the acidity of phenol *in situ*. The result of this would be a higher degree of chain scission. Ethanol functions as a carrier solvent for phenol to facilitate infiltration, and is retained much like methylene chloride. Hydroxypropyl methylcellulose, previously believed to act only as a thickener and phase stabilizer, deposits at the surface and casts a conformal coating across the sample. Based on contact angle measurements and observations of solvent infiltration times, this coating slows the transfer of solvents, leading to improved retention after application to the coating.

10.2 Future work

While we have established the durability of sizing, and others have elucidated the durability of matrix resins, the specific chemical durability of the interphase region is yet to be analyzed. Employing ultrafast laser ablation and small-area, surface-sensitive tools of analysis, the interphase-bearing resin may be removed from the fiber and subjected to analysis in order to determine the effects of degradation.

The NEXAFS imaging detector employed here has demonstrated significant utility in the analysis of coatings, which can also be applied to composites. The ability to discern local polymer orientation information across a coating would be of great use in further investigations, particularly those involving carbon fiber sizing. A detector with higher lateral resolution (currently under construction at the NSLS) could enable the study of sizing on bare fibers, as well as analysis of the interphase. The data reduction software for this detector allows for the generation of dichroic ratio image maps, providing orientation information which may be correlated to other visible changes. Scanning Transmission X-ray Microscopy (STXM) provides NEXAFS data with a much smaller spot size (on the order of 50 nm), which would permit full chemical mapping of the fiber-sizing interphase region.

Additional work is required in the study of coatings in order to design a highly-effective paint removal system. Although we have explained the mechanisms of action by which current solvents function in fresh coatings, exposure to UV radiation and heat has been demonstrated to have a significant effect on polymer chemistry, which may lead to changes in efficacy of the mechanisms indicated. By understanding how these chemical changes impact solvent performance, we may better contribute design parameters to the next generation of solvents, and evaluate and elucidate their performances in much the same way we have in this work.

Substrates for painting have commonly been made of metal, but newer systems employ composite materials, which must also be painted and repainted. The interactions of paint removing solvents have been shown to cause significant degradation in polyurethane, but their impact on composite resins is not well understood. Given the susceptibility of fiber sizing to dissolution by methylene chloride, this suggests a significant vulnerability in the composite material, which is likely to crack down to the point of adhesion, which is found mere microns from the surface.

10.3 Closing remarks

We have demonstrated the utility of highly complementary spectroscopic methods in elucidating polymer systems. By developing highly detailed molecular models, we have been able to comprehensively describe chemical changes undergone by a polymer in response to external forms of degradation. This suite of techniques may be applied to a range of other polymer systems to explain a host of phenomena.

References

Chapter 2:

[1] C.H. Hare, Paint Film Degradation: Mechanisms and Control, SSPC: The Society for Protective Coatings, Pittsburgh, 2001.

[2] D. Bello, S.R. Woskie, R.P. Streicher, Y. Liu, M.H. Stowe, E.A. Eisen, M.J. Ellenbecker, J. Sparer, F. Youngs, M.R. Cullen, C.A. Redlich, Polyisocyanates in occupational environments: A critical review of exposure limits and metrics, American Journal of Industrial Medicine, 46 (2004) 480-491.

[3] J. Colmenares-Angulo, S. Zhao, C. Young, A. Orlov, The effects of thermal spray technique and post-deposition treatment on the photocatalytic activity of TiO2 coatings, Surface and Coatings Technology, 204 (2009) 423-427.

[4] C.H. Hare, Protective Coatings: Fundamentals of Chemistry and Composition, SSPC: The Society for Protective Coatings, Pittsburgh, 1998.

[5] Z.W. Wicks Jr., F.N. Jones, S.P. Pappas, Organic Coatings: Science and Technology, 2nd ed., Wiley-Interscience, New York, 1999.

[6] J.G. Lundin, S.L. Giles, R.F. Cozzens, J.H. Wynne, Analysis of surface segregating additives for self-decontaminating coatings, in, American Chemical Society, 2013, pp. COLL-280.

[7] N.C. Blacker, P.H. Findlay, D.C. Sherrington, Synthesis of CuII-complexed polymers and use as catalysts in the hydrolytic decontamination of sarin nerve agent, Polym. Adv. Technol., 12 (2001) 183-196.

[8] R.A. Brizzolara, D.M. Stamper, The effect of covalent surface immobilization on the bactericidal efficacy of a quaternary ammonium compound, Surf. Interface Anal., 39 (2007) 559-566.

[9] N. Grover, I.V. Borkar, C.Z. Dinu, R.S. Kane, J.S. Dordick, Laccase- and chloroperoxidase-nanotube paint composites with bactericidal and sporicidal activity, Enzyme Microb. Technol., 50 (2012) 271-279.

[10] R.R. Pant, J.L. Buckley, P.A. Fulmer, J.H. Wynne, D.M. McCluskey, J.P. Phillips, Hybrid siloxane epoxy coatings containing quaternary ammonium moieties, J. Appl. Polym. Sci., 110 (2008) 3080-3086.

[11] A.J. Russell, J.A. Berberich, G.F. Drevon, R.R. Koepsel, Biomaterials for mediation of chemical and biological warfare agents, Annu. Rev. Biomed. Eng., 5 (2003) 1-27.

[12] J.H. Wynne, P.A. Fulmer, D.M. McCluskey, N.M. Mackey, J.P. Buchanan, Synthesis and Development of a Multifunctional Self-Decontaminating Polyurethane Coating, ACS Appl. Mater. Interfaces, 3 (2011) 2005-2011.

[13] A. Turner, Marine pollution from antifouling paint particles, Mar Pollut Bull, 60 (2010) 159-171.

[14] R. Parks, M. Donnier-Marechal, P.E. Frickers, A. Turner, J.W. Readman, Antifouling biocides in discarded marine paint particles, Mar Pollut Bull, 60 (2010) 1226-1230.

[15] A. Turner, N. Singh, J.P. Richards, Bioaccessibility of metals in soils and dusts contaminated by marine antifouling paint particles, Environ Pollut, 157 (2009) 1526-1532.

[16] A. Turner, H. Pollock, M.T. Brown, Accumulation of Cu and Zn from antifouling paint particles by the marine macroalga, Ulva lactuca, Environ Pollut, 157 (2009) 2314-2319.

[17] F. Fay, D. Carteau, I. Linossier, M. Delbury, K. Vallee-Rehel, Joint-action of antifouling substances in copper-free paints, Colloids Surf., B, 102 (2013) 569-577.

[18] E.K. Oikonomou, Z. Iatridi, M. Moschakou, P. Damigos, G. Bokias, J.K. Kallitsis, Development of Cu2+- and/or phosphonium-based polymeric biocidal materials and their potential application in antifouling paints, Progress in Organic Coatings, 75 (2012) 190-199.

[19] F. Natalio, R. Andre, A.F. Hartog, B. Stoll, K.P. Jochum, R. Wever, W. Tremel, Vanadium pentoxide nanoparticles mimic vanadium haloperoxidases and thwart biofilm formation, Nat. Nanotechnol., 7 (2012) 530-535.

[20] S. Krishnan, R. Ayothi, A. Hexemer, J.A. Finlay, K.E. Sohn, R. Perry, C.K. Ober, E.J. Kramer, M.E. Callow, J.A. Callow, D.A. Fischer, Anti-Biofouling Properties of Comblike Block Copolymers with Amphiphilic Side Chains, Langmuir, 22 (2006) 5075-5086.

[21] R.J. Klein, D.A. Fischer, J.L. Lenhart, Thermal and Mechanical Aging of Self-Assembled Monolayers as Studied by Near Edge X-ray Absorption Fine Structure, Langmuir, 27 (2011) 12423-12433.

[22] J.D. Weir, R.G. Pirich, D.J. Leyble, L.G. Chorosinski, J.D. Gardner, Jr., S. Chu, Self-cleaning coating for protection against hazardous biopathogens and toxic chemical agents utilizing both super-hydrophobic effects and suitable oxide interfaces, in, Northrop Grumman Systems Corporation, USA . 2011, pp. 4pp.

[23] D.o. Defense, COATING, ALIPHATIC POLYURETHANE, SINGLE COMPONENT, CHEMICAL AGENT RESISTANT, in, Aberdeen, MD, 2011.

[24] D.o. Defense, COATING: POLYURETHANE, AIRCRAFT AND SUPPORT EQUIPMENT, in, NAWCAD, Lakehurst, NJ, 2012.

[25] L.T. Keene, G.P. Halada, C.R. Clayton, Failure of navy coating systems 1: chemical depth profiling of artificially and naturally weathered high-solids aliphatic poly(ester-urethane) military coating systems, Progress in Organic Coatings, 52 (2005) 173-186.

[26] L.T. Keene, M.J. Vasquez, C.R. Clayton, G.P. Halada, Failure of navy coating systems 2: failure pathways of artificially weathered navy coating systems applied to chromate conversion coated AA2024-T3 substrates, Progress in Organic Coatings, 52 (2005) 187-195.

[27] S.G. Croll, A.D. Skaja, Quantitative spectroscopy to determine the effects of photodegradation on a model polyester-urethane coating, Journal of Coatings Technology, 75 (2003) 85-94.

[28] A.D. Skaja, S.G. Croll, Quantitative ultraviolet spectroscopy in weathering of a model polyester–urethane coating, Polymer Degradation and Stability, 79 (2003) 123-131.

[29] X.F. Yang, J. Li, S.G. Croll, D.E. Tallman, G.P. Bierwagen, Degradation of low gloss polyurethane aircraft coatings under UV and prohesion alternating exposures, Polymer Degradation and Stability, 80 (2003) 51-58.

[30] X.F. Yang, D.E. Tallman, G.P. Bierwagen, S.G. Croll, S. Rohlik, Blistering and degradation of polyurethane coatings under different accelerated weathering tests, Polymer Degradation and Stability, 77 (2002) 103-109.

[31] X.F. Yang, D.E. Tallman, S.G. Croll, G.P. Bierwagen, Morphological changes in polyurethane coatings on exposure to water, Polymer Degradation and Stability, 77 (2002) 391-396.

[32] X.F. Yang, C. Vang, D.E. Tallman, G.P. Bierwagen, S.G. Croll, S. Rohlik, Weathering degradation of a polyurethane coating, Polymer Degradation and Stability, 74 (2001) 341-351.

[33] L.T. Keene, T. Fiero, C.R. Clayton, G.P. Halada, D. Cardoza, T. Weinacht, On the use of femtosecond laser ablation to facilitate spectroscopic depth profiling of heterogeneous polymeric coatings, Polym. Degrad. Stab., 89 (2005) 393-409.

[34] G. Socrates, Infrared Characteristic Group Frequencies: Tables and Charts, 2nd ed., John Wiley & Sons, Chichester, 1994.

[35] J. De Gelder, P. Vandenabeele, F. Govaert, L. Moens, Forensic analysis of automotive paints by Raman spectroscopy, Journal of Raman Spectroscopy, 36 (2005) 1059-1067.

[36] J.H. Wynne, K.E. Watson, J.P. Yesinowski, C.N. Young, C.R. Clayton, N. Nesteruk, J. Kelley, T. Braswell, Report on Scientific Basis for Paint Stripping: Mechanism of Methylene Chloride Based Paint Removers, in, Naval Research Laboratory, Washington, DC, 2011.

[37] DoD, MIL-R-81294D: REMOVER, PAINT, EPOXY, POLYSULFIDE, AND POLYURETHANE SYSTEMS, in, 1999.

[38] J. Durkee, Cleaning times: Paint stripping: It's just like parts cleaning, Metal Finishing, 107 (2009) 49-51.

[39] E. Groshart, Finishing in the green: Paint stripping—Without methylene chloride, Metal Finishing, 95 (1997) 55-57.

[40] S.G. Croll, Application of the Flory-Rehner equation and the Griffith fracture criterion to paint stripping, J. Coat. Technol. Res., 7 (2010) 49-55.

[41] C.M. Hansen, Hansen Solubility Parameters: A User's Handbook, Second Edition, Taylor & Francis, 2007.

[42] A.F.M. Barton, CRC handbook of solubility parameters and other cohesion parameters, CRC Press, 1983.

[43] A. Latnikova, D.O. Grigoriev, H. Möhwald, D.G. Shchukin, Capsules Made of Cross-Linked Polymers and Liquid Core: Possible Morphologies and Their Estimation on the Basis of Hansen Solubility Parameters, The Journal of Physical Chemistry C, 116 (2012) 8181-8187.

[44] P.A. Schweitzer, Mechanical and Corrosion-Resistant Properties of Plastics and Elastomers, 1 ed., Marcel Dekker, New York, 2000.

[45] D.D.L. Chung, Composite Materials: Science and Applications, Springer London, 2010.

[46] A.B. Strong, Fundamentals Of Composites Manufacturing: Materials, Methods and Applications, Society of Manufacturing Engineers, 2008.

[47] F. Santiago, A.N. Mansour, R.N. Lee, XPS study of sizing removal from carbon fibers, Surface and Interface Analysis, 10 (1987) 17-22.

[48] H. Al-Moussawi, E.K. Drown, L.T. Drzal, The silane/sizing composite interphase, Polymer Composites, 14 (1993) 195-200.

[49] C.L. Weitzsacker, M. Bellamy, P.M.A. Sherwood, Studies of the Effect of Size on Carbon Fiber Surfaces, Journal of Vacuum Science and Technology A, 12 (1994) 2392 - 2397.

[50] C.M.I. Laot, Spectroscopic Characterization of Molecular Interdiffusion at a Poly(Vinyl Pyrrolidone) / Vinyl Ester Interface, in: Chemical Engineering, Virginia Polytechnic Institute and State University, Blacksburg, 1997.

[51] L.T. Weng, C. Poleunis, P. Bertrand, V. Carlier, M. Sclavons, P. Franquinet, R. Legras, Sizing removal and functionalization of the carbon fiber surface studied by combined TOF SIMS and XPS, Journal of Adhesion Science and Technology, 9 (1995) 859-887.

[52] H. Oyama, J.P. Wightman, Surface characterization of PVP [poly(vinylpyrrolidone)-sized and oxygen plasma-treated carbon fibers, Surface and Interface Analysis, 26 (1998) 39-55.

[53] G.E. Hammer, L.T. Drzal, Graphite fiber surface analysis by x-ray photoelectron spectroscopy and polar/dispersive free energy analysis, Applications of Surface Science (1977-1985), 4 (1980) 340-355.

[54] A. Proctor, P.M.A. Sherwood, X-ray photoelectron spectroscopic studies of carbon fiber surfaces. III - Industrially treated fibers and the effect of heat and exposure to oxygen, Surface and Interface Analysis, 4 (1982) 212-219.

[55] A. Proctor, P.M.A. Sherwood, X-ray photoelectron spectroscopic studies of carbon fiber surfaces. I. Carbon fiber spectra and the effects of heat treatment, Journal of Electron Spectroscopy and Related Phenomena, 27 (1982) 39-56.

[56] G. Bogoeva-Gaceva, D. Burevski, A. Dekanski, A. Janevski, The effect of surface treatment on the interfacial properties in carbon fiber epoxy matrix composites, Journal of Materials Science, 30 (1995) 3543-3546.

[57] N.S. Broyles, S.V.D. K. N. E. Verghese, H. Li, R. M. Davis, J. J. Lesko and J. S. Riffle, Fatigue performance of carbon fibre/vinyl ester composites: the effect of two dissimilar polymeric sizing agents, Polymer, 39 (1998) 3417-3424.

[58] M.A.F. Robertson, M.B. Bump, K.E. Verghese, S.R. McCartney, J.J. Lesko, J.S. Riffle, I.C. Kim, T.H. Yoon, Designed interphase regions in carbon fiber reinforced vinyl ester matrix composites, Journal of Adhesion, 71 (1999) 395-416.

[59] R.E. Allred, S.P. Wesson, E.E. Shin, L. Inghram, L. McCorkle, D. Papadopoulos, D. Wheeler, J.K. Sutter, The influence of sizings on the durability of high-temperature polymer composites, High Performance Polymers, 15 (2003) 395-419.

[60] L.T. Drzal, K.J. Hook, R.K. Agrawal, Enhanced chemical bonding at the fiber-matrix interphase in microwave processed composites, Materials Research Society Symposium Proceedings, 189 (1991) 449-454.

[61] J.L. Koenig, F. Fondeur, Modern spectroscopic analysis of composite interphases, Adhes. Soc., Proc. Sixteenth Annu. Meet. Int. Symp. Interphase, (1993) 303-305.

[62] C.D. Arvanitopoulos, J.L. Koenig, Infrared spectral imaging of the interphase of epoxy-glass fiber-reinforced composites under wet conditions, Applied Spectroscopy, 50 (1996) 11-18.

[63] C.D. Arvanitopoulos, J.L. Koenig, FT-IR microspectroscopic investigation of the interphase of epoxy resin-glass fiber-reinforced composites, Applied Spectroscopy, 50 (1996) 1-10.

[64] C.L. Weitzsacker, M. Xie, L.T. Drazal, Using XPS to investigate fiber/matrix chemical interactions in carbon-fiber-reinforced composites, Surface and Interface Analysis, 25 (1997) 53-63.

[65] C. Perruchot, J.F. Watts, C. Lowe, R.G. White, P.J. Cumpson, Angle-resolved XPS characterization of urea formaldehyde-epoxy systems, Surf. Interface Anal., 33 (2002) 869-878.

[66] A. Al-Ostaz, H. Al-Moussawi, L.T. Drzal, Characterization of the interphase in glass sphere reinforced polymers, Composites, Part B: Engineering, 35B (2004) 393-412.

[67] A.C. Prickett, P.E. Vickers, P.A. Smith, J.F. Watts, The interphase chemistry of carbon fiber composite materials, Adhesion '99, International Conference on Adhesion and Adhesives, 7th, Cambridge, United Kingdom, Sept. 15-17, 1999, (1999) 369-373.

[68] R.E. Allred, A.E. Hoyt Haight, J.M. Gosau, S.P. Wesson, Aqueous-based emulsion reactive finishes for improving carbon/vinyl ester interfacial bonding, International SAMPE Symposium and Exhibition, 50 (2005) 741-756.

[69] R.E. Allred, S.P. Wesson, A.E. Hoyt Haight, J.W. Whitehead, Reactive finishes for improved interfacial properties in carbon/vinyl ester laminates, International SAMPE Symposium and Exhibition, 49 (2004) 2059-2072.

[70] N.S. Broyles, Thermoplastic Sizings: Effects on Processing, Mechanical Performance, and Interphase Formation in Pultruded Carbon Fiber/Vinyl-Ester Composites, in: Chemical Engineering, Virginia Polytechnic Institute and State University, Blacksburg, VA, 1999, pp. 328.

[71] P. Bartolomeo, J.F. Chailan, J.L. Vernet, Dielectric investigation of interphase formation in composite materials. Part 1. Ionic conductivity and permittivity exploration, Journal of Polymer Science, Part B: Polymer Physics, 38 (2000) 2154-2161.

[72] D. Cho, Y. Choi, J.-H. Chang, L.T. Drzal, Interphase sizing temperature effect of LaRC PETI-5 on the dynamic mechanical thermal properties of carbon fiber/BMI composites, Composite Interfaces, 13 (2006) 215-229.

[73] Y. Yang, C.-X. Lu, X.-L. Su, G.-P. Wu, X.-K. Wang, Effect of nano-SiO2 modified emulsion sizing on the interfacial adhesion of carbon fibers reinforced composites, Materials Letters, 61 (2007) 3601-3604.

[74] J. Liu, H. Ge, J. Chen, D. Wang, H. Liu, The preparation of emulsion type sizing agent for carbon fiber and the properties of carbon fiber/vinyl ester resin composites, Journal of Applied Polymer Science, 124 (2012) 864-872.

[75] L.W. Jelinski, J.J. Dumais, A.L. Cholli, T.S. Ellis, F.E. Karasz, Nature of the water-epoxy interaction, Macromolecules, 18 (1985) 1091-1095.

[76] J.-L. Gardette, B. Mailhot, J. Lemaire, Photooxidation mechanisms of styrenic polymers, Polymer Degradation and Stability, 48 (1995) 457-470.

[77] A.W. Signor, M.R. VanLandingham, J.W. Chin, Effects of ultraviolet radiation exposure on vinyl ester resins: characterization of chemical, physical and mechanical damage, Polymer Degradation and Stability, 79 (2002) 359-368.

[78] S. Agrawal, A. Mishra, J.S.P. Rai, Effect of diluents on the decomposition behavior of vinyl ester resin, J. Appl. Polym. Sci., 87 (2003) 1952-1956.

[79] B.G. Kumar, R.P. Singh, T. Nakamura, Degradation of carbon fiber-reinforced epoxy composites by ultraviolet radiation and condensation, Journal of Composite Materials, 36 (2002) 2713-2733.

[80] L. Wu, K. Murphy, V.M. Karbhari, J.S. Zhang, Short-term effects of sea water on E-glass/vinylester composites, J. Appl. Polym. Sci., 84 (2002) 2760-2767.

[81] V.M. Karbhari, S. Zhang, E-Glass/Vinylester Composites in Aqueous Environments - I: Experimental Results, Applied Composite Materials, 10 (2003) 19-48.

[82] K.-B. Shin, C.-G. Kim, C.-S. Hong, Correlation of accelerated aging test to natural aging test on graphite-epoxy composite materials, Journal of Reinforced Plastics and Composites, 22 (2003) 849-861.

[83] A. Kootsookos, A.P. Mouritz, Seawater durability of glass- and carbon-polymer composites, Composites Science and Technology, 64 (2004) 1503-1511.

[84] Y. Miyano, M. Nakada, N. Sekine, Accelerated testing for long-term durability of GFRP laminates for marine use, Composites, Part B: Engineering, 35B (2004) 497-502.

[85] K.N.E. Verghese, N.S. Broyles, J.J. Lesko, R.M. Davis, J.S. Riffle, Pultruded Carbon Fiber/Vinyl Ester Composites Processed with Different Fiber Sizing Agents. Part II: Enviro-Mechanical Durability, J. Mater. Civ. Eng., 17 (2005) 334-342.

[86] A.P. Mouritz, A.G. Gibson, Fire properties of polymer composite materials, Springer London, Limited, 2006.

[87] B.C. Ray, Temperature effect during humid aging on interfaces of glass and carbon fibers reinforced epoxy composites, Journal of Colloid and Interface Science, 298 (2006) 111-117.

[88] R. Martin, Ageing of Composites, 1st ed., Woodhead Publishing Limited, Cambridge, England, 2008.

Chapter 3:

[1] Socrates G. Infrared Characteristic Group Frequencies: Tables and Charts. 2nd ed. Chichester: John Wiley & Sons; 1994.

[2] Tian J, Liu J, He W, Hu Z, Yao X, Chen X. Probing the Binding of Scutellarin to Human Serum Albumin by Circular Dichroism, Fluorescence Spectroscopy, FTIR, and Molecular Modeling Method. Biomacromolecules. 2004;5:1956-61.

[3] Janssen A, Niederer JPM, Hoëlderich WF. Investigation of rhodium complexes in micro- and mesoporous materials by computer modeling, FTIR, and 31P MAS NMR. Catalysis Letters. 1997;48:165-71.

[4] Atkins P, de Paula J. Physical Chemistry. 8th ed. New York: W. H. Freeman and Co.; 2006.

[5] Gauglitz G, Vo-Dinh T. Handbook of Spectroscopy: Wiley; 2006.

[6] Raman CV. A New Radiation. Indian Journal of Physics. 1928;2:387-98.

[7] Ferraro JR. Introductory Raman spectroscopy. 2nd ed. ed. Academic Press: Amsterdam ;; 2003.

[8] Moulder JF, Stickle WF, Sobol PE, Bomben KD. Handbook of X-ray Photoelectron Spectroscopy. 2nd ed. Eden Prairie, MN, USA: Physical Electronics, Inc.; 1995.

[9] Teo BK, Joy DC. EXAFS spectroscopy, techniques and applications. Plenum Press: New York; 1981.

[10] Stöhr J. NEXAFS Spectroscopy: Springer; 1992.

[11] Francis JT, Hitchcock AP. Inner-shell spectroscopy of p-benzoquinone, hydroquinone, and phenol: distinguishing quinoid and benzenoid structures. The Journal of Physical Chemistry. 1992;96:6598-610.

[12] Tinone MCK, Tanaka K, Maruyama J, Ueno N, Imamura M, Matsubayashi N. Inner-shell excitation and site specific fragmentation of poly(methylmethacrylate) thin film. The Journal of Chemical Physics. 1994;100:5988-95.

[13] Urquhart SG, Smith AP, Ade HW, Hitchcock AP, Rightor EG, Lidy W. Near-Edge X-ray Absorption Fine Structure Spectroscopy of MDI and TDI Polyurethane Polymers. The Journal of Physical Chemistry B. 1999;103:4603-10.

[14] Dhez O, Ade H, Urquhart SG. Calibrated NEXAFS spectra of some common polymers. Journal of Electron Spectroscopy and Related Phenomena. 2003;128:85-96.

[15] Lenhart JL, Fischer DA, Chantawansri TL, Andzelm JW. Surface Orientation of Polystyrene Based Polymers: Steric Effects from Pendant Groups on the Phenyl Ring. Langmuir. 2012;28:15713-24.

[16] Lam RSK, Metzler RA, Gilbert PUPA, Beniash E. Anisotropy of Chemical Bonds in Collagen Molecules Studied by X-ray Absorption Near-Edge Structure (XANES) Spectroscopy. ACS Chemical Biology. 2011;7:476-80.

[17] Nishikida K, Nishio E, Hannah RW. Selected Applications of Modern Ft-Ir Techniques: Kodansha and Gordon and Breach; 1995.

[18] White JR, Turnbull A. Weathering of polymers: mechanisms of degradation and stabilization, testing strategies and modeling. Journal of Materials Science. 1994;29:584-613.

[19] Klein RJ, Fischer DA, Lenhart JL. Thermal and Mechanical Aging of Self-Assembled Monolayers as Studied by Near Edge X-ray Absorption Fine Structure. Langmuir. 2011;27:12423-33.

[20] Holch F. Investigation of Intermolecular Interaction in Organic Thin Films by means of NEXAFS Spectroscopy. Wurzburg: Julius–Maximilians Universität Würzburg; 2009.

[21] Hemraj-Benny T, Banerjee S, Sambasivan S, Balasubramanian M, Fischer DA, Eres G, et al. Near-Edge X-ray Absorption Fine Structure Spectroscopy as a Tool for Investigating Nanomaterials. Small. 2006;2:26-35.

[22] Scholl A, Fink R, Umbach E, Mitchell GE, Urquhart SG, Ade H. Towards a detailed understanding of the NEXAFS spectra of bulk polyethylene copolymers and related alkanes. Chemical Physics Letters. 2003;370:834-41.

[23] Liu Y, Russell TP, Samant MG, Stöhr J, Brown HR, Cossy-Favre A, et al. Surface Relaxations in Polymers. Macromolecules. 1997;30:7768-71.

[24] Cerruti M, Rhodes C, Losego M, Efremenko A, Maria J-P, Fischer D, et al. Influence of indium–tin oxide surface structure on the ordering and coverage of carboxylic acid and thiol monolayers. Journal of Physics D: Applied Physics. 2007;40:4212.

[25] Li Z, Zhang L, Resasco DE, Mun BS, Requejo FG. Angle-resolved x-ray absorption near edge structure study of vertically aligned single-walled carbon nanotubes. Applied Physics Letters. 2007;90:103115-3.

[26] Banerjee S, Hemraj-Benny T, Sambasivan S, Fischer DA, Misewich JA, Wong SS. Near-Edge X-ray Absorption Fine Structure Investigations of Order in Carbon Nanotube-Based Systems†. The Journal of Physical Chemistry B. 2005;109:8489-95.

[27] Wallace WE, Fischer DA, Efimenko K, Wu W-L, Genzer J. Polymer Chain Relaxation: Surface Outpaces Bulk. Macromolecules. 2001;34:5081-2.

Chapter 4:

[1] Hirano N, Tsuchiya A, Honma M. Carbon fiber bundles containing water-soluble polyurethane sizing agents. Toray Industries, Inc., Japan . 2011. p. 71pp.

[2] Saito M, Miyazaki M, Inoue H. Carbon fibers sized with a sizing agent for reinforcing plastics. Tonen Co., Ltd., Japan . 1991. p. 12 pp.

[3] Allred RE, Hoyt Haight AE, Gosau JM, Wesson SP. Aqueous-based emulsion reactive finishes for improving carbon/vinyl ester interfacial bonding. International SAMPE Symposium and Exhibition. 2005;50:741-56.

[4] Allred RE, Wesson SP, Hoyt Haight AE, Whitehead JW. Reactive finishes for improved interfacial properties in carbon/vinyl ester laminates. International SAMPE Symposium and Exhibition. 2004;49:2059-72.

[5] Allred RE, Wesson SP, Shin EE, Inghram L, McCorkle L, Papadopoulos D, et al. The influence of sizings on the durability of high-temperature polymer composites. High Performance Polymers. 2003;15:395-419.

[6] Keene LT, Vasquez MJ, Clayton CR, Halada GP. Failure of navy coating systems 2: failure pathways of artificially weathered navy coating systems applied to chromate conversion coated AA2024-T3 substrates. Progress in Organic Coatings. 2005;52:187-95.

[7] Keene LT, Halada GP, Clayton CR. Failure of navy coating systems 1: chemical depth profiling of artificially and naturally weathered high-solids aliphatic poly(ester-urethane) military coating systems. Progress in Organic Coatings. 2005;52:173-86.

[8] Hare CH. Paint Film Degradation: Mechanisms and Control. Pittsburgh: SSPC: The Society for Protective Coatings; 2001.

Chapter 5:

[1] D.X. Hammer, G.D. Noojin, R.J. Thomas, C.E. Clary, B.A. Rockwell, C.A. Toth, W.P. Roach, Intraocular laser surgical probe for membrane disruption by laser-induced breakdown, Appl. Opt., 36 (1997) 1684-1693.

[2] R. Fardel, M. Nagel, T. Lippert, F. Nueesch, A. Wokaun, B.S. Luk'yanchuk, Influence of thermal diffusion on the laser ablation of thin polymer films, Applied Physics A: Materials Science & Processing, 90 (2008) 661-667.

[3] P.E. Dyer, S.T. Lau, G.A. Oldershaw, D. Schudel, An investigation of xenon chloride (XeCl) laser ablation of poly(ether ether ketone) (PEEK)-carbon fiber composite, Journal of Materials Research, 7 (1992) 1152-1157.

[4] L. Torrisi, A. Borrielli, D. Margarone, Study on the ablation threshold induced by pulsed lasers at different wavelengths, Nuclear Instruments & Methods in Physics Research, Section B: Beam Interactions with Materials and Atoms, 255 (2007) 373-379.

[5] B.C. Stuart, M.D. Feit, S. Herman, A.M. Rubenchik, B.W. Shore, M.D. Perry, Optical ablation by high-power short-pulse lasers, Journal of the Optical Society of America B: Optical Physics, 13 (1996) 459-468.

[6] J. Longtin, Nonlinear phenomena in laser-material interactions, Annual Review of Heat Transfer, 14 (2005) 419-438.

[7] L.T. Keene, T. Fiero, C.R. Clayton, G.P. Halada, D. Cardoza, T. Weinacht, On the use of femtosecond laser ablation to facilitate spectroscopic depth profiling of heterogeneous polymeric coatings, Polym. Degrad. Stab., 89 (2005) 393-409.

[8] F. Costache, M. Henyk, J. Reif, Surface patterning on insulators upon femtosecond laser ablation, Applied Surface Science, 208–209 (2003) 486-491.

[9] J. Reif, F. Costache, M. Henyk, S.V. Pandelov, Ripples revisited: non-classical morphology at the bottom of femtosecond laser ablation craters in transparent dielectrics, Applied Surface Science, 197–198 (2002) 891-895.

[10] Q. Bian, S. Chen, B.-T. Kim, N. Leventis, H. Lu, Z. Chang, S. Lei, Micromachining of polyurea aerogel using femtosecond laser pulses, Journal of Non-Crystalline Solids, 357 (2011) 186-193.

[11] S. Baudach, J. Bonse, W. Kautek, Ablation experiments on polyimide with femtosecond laser pulses, Applied Physics A: Materials Science & Processing, 69 (1999) S395-S398.

[12] Y. Yang, J. Yang, L. Xue, Y. Guo, Surface patterning on periodicity of femtosecond laser-induced ripples, Applied Physics Letters, 97 (2010) 141101-141103.

[13] P. Moreno, C. Mendez, A. Garcia, I. Arias, L. Roso, Femtosecond laser ablation of carbon reinforced polymers, Appl. Surf. Sci., 252 (2006) 4110-4119.

[14] A.A. Serafetinides, M. Makropoulou, E. Fabrikesi, E. Spyratou, C. Bacharis, R.R. Thomson, A.K. Kar, Ultrashort laser ablation of PMMA and intraocular lenses, Applied Physics A: Materials Science & Processing, 93 (2008) 111-116.

[15] C.R. Mendonca, S. Orlando, G. Cosendey, M. Winkler, E. Mazur, Femtosecond laser micromachining in the conjugated polymer MEH–PPV, Applied Surface Science, 254 (2007) 1135-1139.

[16] M. Okoshi, N. Inoue, Femtosecond laser ablation of polyethylene, Japanese Journal of Applied Physics, Part 2: Letters, 42 (2003) L36-L38.

[17] M.Y. Xu, S.A. Hosseini, H. Zhang, S.M. Eaton, L.D. Lilge, P.R. Herman, Heat Accumulation Effects in Femtosecond Laser Ablation of ITO Thin Films for DEP Trapping Devices, in: Conference on Lasers and Electro-Optics/Quantum Electronics and Laser Science Conference and Photonic Applications Systems Technologies, Optical Society of America, 2007, pp. CFR3.

[18] C. De Marco, R. Suriano, M. Levi, S. Turri, S. Eaton, G. Cerullo, R. Osellame, Femtosecond laser fabrication and characterization of microchannels and waveguides in methacrylate-based polymers, Microsyst Technol, 18 (2012) 183-190.

[19] R. Suriano, A. Kuznetsov, S.M. Eaton, R. Kiyan, G. Cerullo, R. Osellame, B.N. Chichkov, M. Levi, S. Turri, Femtosecond laser ablation of polymeric substrates for the fabrication of microfluidic channels, Applied Surface Science, 257 (2011) 6243-6250.

[20] H. Jeon, R. Schmidt, J.E. Barton, D.J. Hwang, L.J. Gamble, D.G. Castner, C.P. Grigoropoulos, K.E. Healy, Chemical Patterning of Ultrathin Polymer Films by Direct-Write Multiphoton Lithography, Journal of the American Chemical Society, 133 (2011) 6138-6141.

[21] N.L. Vasily, M.P. Sergey, D.O. Elena, I.K. Sergey, F.B. Alexey, Single-shot and single-spot measurement of laser ablation threshold for carbon nanotubes, Journal of Physics D: Applied Physics, 46 (2013) 052002.

[22] A. Kaplan, M. Lenner, C. Huchon, R.E. Palmer, Nonlinearity and time-resolved studies of ion emission in ultrafast laser ablation of graphite, Applied Physics A: Materials Science & Processing, 92 (2008) 999-1004.

[23] M. Lenner, A. Kaplan, R.E. Palmer, Nanoscopic Coulomb explosion in ultrafast graphite ablation, Applied Physics Letters, 90 (2007) 153119/153111-153119/153113.

[24] K. Sokolowski-Tinten, S. Kudryashov, V. Temnov, J. Bialkowski, d.L.D. von, A. Cavalleri, H.O. Jeschke, M.E. Garcia, K.H. Bennemann, Femtosecond laser-induced ablation of graphite, Springer Ser. Chem. Phys., 66 (2001) 425-427.

[25] D. Pietroy, Y. Di Maio, B. Moine, E. Baubeau, E. Audouard, Femtosecond laser volume ablation rate and threshold measurements by differential weighing, Opt. Express, 20 (2012) 29900-29908.

[26] H. Al-Moussawi, E.K. Drown, L.T. Drzal, The silane/sizing composite interphase, Polymer Composites, 14 (1993) 195-200.

[27] M. Diepens, P. Gijsman, Outdoor and accelerated weathering studies of bisphenol A polycarbonate, Polymer Degradation and Stability, 96 (2011) 649-652.

[28] S. Baudach, J. Bonse, J. Krüger, W. Kautek, Ultrashort pulse laser ablation of polycarbonate and polymethylmethacrylate, Applied Surface Science, 154–155 (2000) 555-560.

[29] S. Panchatsharam, B. Tan, K. Venkatakrishnan, Femtosecond laser-induced shockwave formation on ablated silicon surface, Journal of Applied Physics, 105 (2009) 093103.

[30] A.J. Lee, J.M. Dawes, M.J. Withford, Investigation of femtosecond laser induced thermal ablation of polyethylene, Journal of Laser Applications, 20 (2008) 154-159.

[31] K.E. Sohn, M.D. Dimitriou, J. Genzer, D.A. Fischer, C.J. Hawker, E.J. Kramer, Determination of the Electron Escape Depth for NEXAFS Spectroscopy, Langmuir, 25 (2009) 6341-6348.

[32] S. Crawford, C.T. Lungu, Influence of temperature on styrene emission from a vinyl ester resin thermoset composite material, Science of The Total Environment, 409 (2011) 3403-3408.

[33] J. La Scala, C. Ulven, J. Orlicki, R. Jain, G. Palmese, U. Vaidya, J. Sands, Emission modeling of styrene from vinyl ester resins, Clean Techn Environ Policy, 9 (2007) 265-279.

[34] Y. Tang, J. Yang, B. Zhao, M. Wang, X. Zhu, Control of periodic ripples growth on metals by femtosecond laser ellipticity, Opt. Express, 20 (2012) 25826-25833.

[35] F. Bedoui, N.S. Murthy, F.M. Zimmermann, Enhancement of fiber-matrix adhesion by laser ablation-induced surface micro corrugation, J. Mater. Sci., 43 (2008) 5585-5590.

[36] S.M. Lee, Handbook of Composite Reinforcements, Wiley, 1992.

[37] E.N. Glezer, E. Mazur, Ultrafast-laser driven micro-explosions in transparent materials, Applied Physics Letters, 71 (1997) 882-884.

[38] Q.-Z. Zhao, S. Malzer, L.-J. Wang, Self-organized tungsten nanospikes grown on subwavelength ripples induced by femtosecond laser pulses, Opt. Express, 15 (2007) 15741-15746.

[39] R.E. Allred, A.E. Hoyt Haight, J.M. Gosau, S.P. Wesson, Aqueous-based emulsion reactive finishes for improving carbon/vinyl ester interfacial bonding, International SAMPE Symposium and Exhibition, 50 (2005) 741-756.

[40] R.E. Allred, S.P. Wesson, E.E. Shin, L. Inghram, L. McCorkle, D. Papadopoulos, D. Wheeler, J.K. Sutter, The influence of sizings on the durability of high-temperature polymer composites, High Performance Polymers, 15 (2003) 395-419.

[41] S.P. Tweed-Kent, Understanding Cure Inhibition in Carbon Fiber Reinforced Vinyl Ester Resin Composites, in: Materials Science and Engineering, The Pennsylvania State University, 2008.

[42] A.W. Signor, M.R. VanLandingham, J.W. Chin, Effects of ultraviolet radiation exposure on vinyl ester resins: characterization of chemical, physical and mechanical damage, Polymer Degradation and Stability, 79 (2002) 359-368.

Chapter 6:

[1] Sorathia U, Dapp T. Structural performance of glass/vinyl ester composites at elevated temperatures. SAMPE Journal. 1997;33:53-8.

[2] Martin R. Ageing of Composites. 1st ed. Cambridge, England: Woodhead Publishing Limited; 2008.

[3] Hiltz JA. Low-temperature thermal degradation studies of styrene-crosslinked vinyl ester and polyester resins. Def. Res. Establ. Atl.,Dartmouth,NS,Can.; 1988. p. 39 pp.

[4] Regnier N, Mortaigne B. Analysis by pyrolysis/gas chromatography/mass spectrometry of glass fiber/vinylester thermal degradation products. Polym Degrad Stab. 1995;49:419-28.

[5] La Scala J, Ulven C, Orlicki J, Jain R, Palmese G, Vaidya U, et al. Emission modeling of styrene from vinyl ester resins. Clean Techn Environ Policy. 2007;9:265-79.

[6] Rein A, Seelenbinder J. Thermal Damage in Composites - Correlation of Short Beam Shear Data with Fourier Transform Infrared Spectroscopy. Application Note 204. 2009:1-2.

[7] Crawford S, Lungu CT. Influence of temperature on styrene emission from a vinyl ester resin thermoset composite material. Science of The Total Environment. 2011;409:3403-8.

[8] Fisher WG, Storey JME, Sharp SL, Janke CJ, Wachter EA. Nondestructive inspection of graphite-epoxy composites for heat damage using laser-induced fluorescence. Appl Spectrosc. 1995;49:1225-31.

[9] Kulowitch P, Scott WR. Detection of thermal damage in epoxy-based composites using laser pumped fluorescence. Nondestructive Characterization of Materials XI, Proceedings of the International Symposium, 11th, Berlin, Germany, June 24-28, 2002. 2003:545-53.

[10] Chatterjee A. Thermal degradation analysis of thermoset resins. Journal of Applied Polymer Science. 2009;114:1417-25.

[11] Scott IG, Scala CM. A review of non-destructive testing of composite materials. NDT International. 1982;15:75-86.

[12] Signor AW, VanLandingham MR, Chin JW. Effects of ultraviolet radiation exposure on vinyl ester resins: characterization of chemical, physical and mechanical damage. Polymer Degradation and Stability. 2002;79:359-68.

[13] Yang XF, Vang C, Tallman DE, Bierwagen GP, Croll SG, Rohlik S. Weathering degradation of a polyurethane coating. Polymer Degradation and Stability. 2001;74:341-51.

[14] Keene LT, Halada GP, Clayton CR. Failure of navy coating systems 1: chemical depth profiling of artificially and naturally weathered high-solids aliphatic poly(ester-urethane) military coating systems. Progress in Organic Coatings. 2005;52:173-86.

[15] Lenhart JL, Fischer DA, Chantawansri TL, Andzelm JW. Surface Orientation of Polystyrene Based Polymers: Steric Effects from Pendant Groups on the Phenyl Ring. Langmuir. 2012;28:15713-24.

[16] Sohn KE, Dimitriou MD, Genzer J, Fischer DA, Hawker CJ, Kramer EJ. Determination of the Electron Escape Depth for NEXAFS Spectroscopy. Langmuir. 2009;25:6341-8.

[17] Socrates G. Infrared Characteristic Group Frequencies: Tables and Charts. 2nd ed. Chichester: John Wiley & Sons; 1994.

[18] Obst M, Grathwohl P, Kappler A, Eibl O, Peranio N, Gocht T. Quantitative High-Resolution Mapping of Phenanthrene Sorption to Black Carbon Particles. Environmental Science & Technology. 2011;45:7314-22.

[19] Stöhr J. NEXAFS Spectroscopy: Springer; 1992.

[20] Goodrich T, Lattimer B. Microscopic behavior of composite materials during heating and cooling. Proceedings of the 17th international conference on composite materials2009. p. 27-31.

Chapter 7:

[1] S. Rivers, N. Umney, Conservation of Furniture, Butterworth Heinemann, Oxford, England, 2003.

[2] J. Durkee, Cleaning times: Paint stripping: It's just like parts cleaning, Metal Finishing, 107 (2009) 49-51.

[3] E. Groshart, Finishing in the green: Paint stripping—Without methylene chloride, Metal Finishing, 95 (1997) 55-57.

[4] S. Arndt, R. Canum, Overview of chemical paint strippers: The ongoing development of safer solvent paint removers has yielded versatile, user-friendly products, Metal Finishing, 105 (2007) 49-50.

[5] V. Del Nero, C. Siat, M.J. Marti, J.M. Aubry, J.P. Lallier, N. Dupuy, J.P. Huvenne, Mechanism of paint removing by organic solvents, in: The proceedings of the 53rd international meeting of physical chemistry: Organic coatings, AIP, Paris, France, 1996, pp. 469-476.

[6] K.R. Stone, J. Springer Jr., Review of solvent cleaning in aerospace operations and pollution prevention alternatives, Environmental Progress, 14 (1995) 261-265.

[7] S.G. Croll, Application of the Flory-Rehner equation and the Griffith fracture criterion to paint stripping, J. Coat. Technol. Res., 7 (2010) 49-55.

[8] V.P.N.s. Volkov, K.V.; Sotnikova, E.N; Apukhtina, N.P.; Potepun, L.I., IR-Spectroscopic Investigation of Molecular Interactions in Segmented Polyurethanes, Zhurnal Prikladnoi Spektroskopii, 36 (1982) 787-792.

[9] P. Gotthardt, A. Gruger, H.G. Brion, R. Plaetschke, R. Kirchheim, Volume change of glassy polymers by sorption of small molecules and its relation to the intermolecular space, Macromolecules, 30 (1997) 8058-8065.

[10] S. Misra, W.L. Mattice, Atomistic Models of Amorphous Polybutadienes. 3. Static Free Volume, Macromolecules, 26 (1993) 7274-7281.

[11] C. Nagel, E. Schmidtke, K. Gunther-Schade, D. Hofmann, D. Fritsch, T. Strunskus, F. Faupel, Free volume distributions in glassy polymer membranes: Comparison between molecular modeling and experiments, Macromolecules, 33 (2000) 2242-2248.

[12] S. Arizzi, P.H. Mott, U.W. Suter, Space Available to Small Diffusants in Polymeric Glasses - Analysis of unoccupied Space and Its' Connectivity, J. Polym. Sci. Pt. B-Polym. Phys., 30 (1992) 415-426.

[13] P.N. Brier, A. Perry, Neutron Inelastic-Scattering Measurements and Liquid Dynamics of CH2CL2, Advances in Molecular Relaxation and Interaction Processes, 13 (1978) 1-46.

[14] V.M. Shah, S.A. Stern, P.J. Ludovice, Estimation of the free volume in polymers by means of a Monte Carlo technique, Macromolecules, 22 (1989) 4660-4662.

[15] N.M.K. Lamba, K.A. Woodhouse, S.L. Cooper, Polyurethanes in Biomedical Applications, Taylor & Francis, 1997.

[16] A.F.M. Barton, CRC handbook of solubility parameters and other cohesion parameters, CRC Press, 1983.

[17] A. Latnikova, D.O. Grigoriev, H. Möhwald, D.G. Shchukin, Capsules Made of Cross-Linked Polymers and Liquid Core: Possible Morphologies and Their Estimation on the Basis of Hansen Solubility Parameters, The Journal of Physical Chemistry C, 116 (2012) 8181-8187.

[18] T. Wollbrinck, The Composition of Proprietary Paint Strippers, Journal of the American Institute for Conservation, 32 (1993) 43-57.

[19] S. Schlick, Z. Gao, S. Matsukawa, I. Ando, E. Fead, G. Rossi, Swelling and Transport in Polyisoprene Networks Exposed to Benzene−Cyclohexane Mixtures: A Case Study in Multicomponent Diffusion, Macromolecules, 31 (1998) 8124-8133.

[20] L.W. Jelinski, J.J. Dumais, A.L. Cholli, T.S. Ellis, F.E. Karasz, Nature of the water-epoxy interaction, Macromolecules, 18 (1985) 1091-1095.

[21] L.S. Loo, R.E. Cohen, K.K. Gleason, Deuterium nuclear magnetic resonance of deuterium oxide in nylon 6 under active uniaxial deformation, Polymer, 41 (2000) 7699-7704.

[22] B. Deloche, E.T. Samulski, Short-range nematic-like orientational order in strained elastomers: a deuterium magnetic resonance study, Macromolecules, 14 (1981) 575-581.

[23] P.T. Callaghan, E.T. Samulski, Biaxial Deformation of a Polymer Network Measured via Deuteron Quadrupolar Interactions, Macromolecules, 36 (2003) 724-735.

[24] L.S. Loo, R.E. Cohen, K.K. Gleason, Deuterium Nuclear Magnetic Resonance of Phenol-d5 in Nylon 6 under Active Uniaxial Deformation, Macromolecules, 32 (1999) 4359-4364.

[25] D.E. Oreilly, E.L. Yasaitis, E.M. Peterson, Self-Diffusion Coefficients and Rotational Correlation Times in Polar Liquids. IV. Dichloromethane and Pyridine, J. Chem. Phys., 57 (1972) 890-&.

[26] J.L. Ragle, K.L. Sherk, Deuteron Quadrupole Coupling in Some Solid Chlorinated Hydrocarbons, J. Chem. Phys., 50 (1969) 3553-&.

[27] J.P. Yesinowski, High-resolution NMR spectroscopy of solids and surface-adsorbed species in colloidal suspension: phosphorus-31 NMR spectra of hydroxyapatite and diphosphonates, Journal of the American Chemical Society, 103 (1981) 6266-6267.

[28] G. Socrates, Infrared Characteristic Group Frequencies: Tables and Charts, 2nd ed., John Wiley & Sons, Chichester, 1994.

[29] N.E. Triggs, J.J. Valentini, An Investigation of Hydrogen Bonding in Amides Using Raman Spectroscopy, Journal of Physical Chemistry, 96 (1992) 6922-6931.

[30] F. Terenziani, A. Painelli, D. Comoretto, Solvation Effects and Inhomogeneous Broadening in Optical Spectra of Phenol Blue, Journal of Physical Chemistry A, 104 (2000) 11049-11054.

[31] V. Ramakrishnan, A. Sarua, M. Kuball, A.F. Abdullah, Solvent dependent study of carbonyl vibrations of 3-phenoxybenzaldehyde and 4-ethoxybenzaldehyde by Raman spectroscopy and ab initio calculations, J. Raman Spectrosc., 40 (2009) 921-935.

Chapter 8:

[1] Groshart E. Finishing in the green: Paint stripping—Without methylene chloride. Metal Finishing. 1997;95:55-7.

[2] Yang XF, Tallman DE, Croll SG, Bierwagen GP. Morphological changes in polyurethane coatings on exposure to water. Polymer Degradation and Stability. 2002;77:391-6.

[3] Croll SG, Skaja AD. Quantitative spectroscopy to determine the effects of photodegradation on a model polyester-urethane coating. Journal of Coatings Technology. 2003;75:85-94.

[4] Yang XF, Li J, Croll SG, Tallman DE, Bierwagen GP. Degradation of low gloss polyurethane aircraft coatings under UV and prohesion alternating exposures. Polymer Degradation and Stability. 2003;80:51-8.

[5] Yang XF, Tallman DE, Bierwagen GP, Croll SG, Rohlik S. Blistering and degradation of polyurethane coatings under different accelerated weathering tests. Polymer Degradation and Stability. 2002;77:103-9.

[6] Yang XF, Vang C, Tallman DE, Bierwagen GP, Croll SG, Rohlik S. Weathering degradation of a polyurethane coating. Polymer Degradation and Stability. 2001;74:341-51.

[7] Keene LT, Halada GP, Clayton CR. Failure of navy coating systems 1: chemical depth profiling of artificially and naturally weathered high-solids aliphatic poly(ester-urethane) military coating systems. Progress in Organic Coatings. 2005;52:173-86.

[8] Keene LT, Vasquez MJ, Clayton CR, Halada GP. Failure of navy coating systems 2: failure pathways of artificially weathered navy coating systems applied to chromate conversion coated AA2024-T3 substrates. Progress in Organic Coatings. 2005;52:187-95.

[9] Croll SG, Shi X, Fernando BMD. The interplay of physical aging and degradation during weathering for two crosslinked coatings. Progress in Organic Coatings. 2008;61:136-44.

[10] Rivers S, Umney N. Conservation of Furniture. Oxford, England: Butterworth Heinemann; 2003.

[11] Hansen CM. Hansen Solubility Parameters: A User's Handbook, Second Edition: Taylor & Francis; 2007.

[12] Croll SG. Application of the Flory-Rehner equation and the Griffith fracture criterion to paint stripping. J Coat Technol Res. 2010;7:49-55.

[13] Lee I, Wool RP. Polymer Adhesion vs. Substrate Receptor Group Density. Macromolecules. 2000;33:2680-7.

[14] Hinder SJ, Watts JF, Lowe C. Interface analysis and compositional depth profiling by XPS of polymer coatings prepared using ultralow-angle microtomy. Surf Interface Anal. 2004;36:1032-6.

[15] Hinder SJ, Lowe C, Maxted JT, Perruchot C, Watts JF. Intercoat adhesion failure in a multilayer organic coating system: An X-ray photoelectron spectroscopy study. Progress in Organic Coatings. 2005;54:20-7.

[16] Coleman MM, Skrovanek DJ, Hu J, Painter PC. Hydrogen bonding in polymer blends. 1. FTIR studies of urethane-ether blends. Macromolecules. 1988;21:59-65.

[17] Marcos-Fernández A, Lozano AE, González L, Rodríguez A. Hydrogen Bonding in Copoly(ether−urea)s and Its Relationship with the Physical Properties. Macromolecules. 1997;30:3584-92.

[18] MaterialScience B. The Chemistry of Polyurethane Coatings: A General Reference Manual. In: MaterialScience B, editor. Pittsburgh, PA: Bayer; 2005.

[19] Irusta L, Iruin JJ, Fernández-Berridi MJ, Sobkowiak M, Painter PC, Coleman MM. Infrared spectroscopic studies of the self-association of ethyl urethane. Vibrational Spectroscopy. 2000;23:187-97.

[20] Socrates G. Infrared Characteristic Group Frequencies: Tables and Charts. 2nd ed. Chichester: John Wiley & Sons; 1994.

Chapter 9:

[1] Leiro JA, Heinonen MH, Laiho T, Batirev IG. Core-level XPS spectra of fullerene, highly oriented pyrolitic graphite, and glassy carbon. Journal of Electron Spectroscopy and Related Phenomena. 2003;128:205-13.

[2] Stöhr J. NEXAFS Spectroscopy: Springer; 1992.

[3] Lenhart JL, Fischer DA, Chantawansri TL, Andzelm JW. Surface Orientation of Polystyrene Based Polymers: Steric Effects from Pendant Groups on the Phenyl Ring. Langmuir. 2012;28:15713-24.

[4] Sohn KE, Dimitriou MD, Genzer J, Fischer DA, Hawker CJ, Kramer EJ. Determination of the Electron Escape Depth for NEXAFS Spectroscopy. Langmuir. 2009;25:6341-8.

[5] Urquhart SG, Hitchcock AP, Smith AP, Ade HW, Lidy W, Rightor EG, et al. NEXAFS spectromicroscopy of polymers: overview and quantitative analysis of polyurethane polymers. Journal of Electron Spectroscopy and Related Phenomena. 1999;100:119-35.

[6] Urquhart SG, Smith AP, Ade HW, Hitchcock AP, Rightor EG, Lidy W. Near-Edge X-ray Absorption Fine Structure Spectroscopy of MDI and TDI Polyurethane Polymers. The Journal of Physical Chemistry B. 1999;103:4603-10.

[7] Kuznetsova A, Popova I, Yates JT, Bronikowski MJ, Huffman CB, Liu J, et al. Oxygen-Containing Functional Groups on Single-Wall Carbon Nanotubes: NEXAFS and Vibrational Spectroscopic Studies. Journal of the American Chemical Society. 2001;123:10699-704.

[8] Sedlmair J. Soft X-Ray Spectromicroscopy of Environmental and Biological Samples: Universitätsverlag Göttingen; 2011.